# 博士論文

# Impact of the Change in Temperature and Structural Distortion on the Spontaneous Polarization of Dielectric Interfaces and Ferroelectric Thin Films

(温度と構造歪みの変化が誘電体界面及び強誘電体薄膜中の自発分極に与える影響)

ニッタヤカセワッ　シリ

# Doctoral Dissertation

## Impact of the Change in Temperature and Structural Distortion on the Spontaneous Polarization of Dielectric Interfaces and Ferroelectric Thin Films

DISSERTATION SUBMITTED TO

DEPARTMENT OF MATERIALS ENGINEERING

SCHOOL OF ENGINEERING

THE UNIVERSITY OF TOKYO

FOR THE DEGREE OF DOCTOR OF PHILOSOPHY

Siri Nittayakasetwat

# Abstract

In this study, the main motivation is to investigate how spontaneous polarization ($P_s$) can control the material properties of a material. For a material to possess $P_s$, the material must have a net polarization even in an absence of an external electric field. This study focuses on the $P_s$ at dielectric interfaces and in ferroelectric (FE) thin films. In complementary metal-oxide-semiconductor (CMOS) and emerging non-volatile memory (NVM) memories, $P_s$ is important because $P_s$ in a gate dielectric determines the operating voltage of the device. This dissertation aims to find new methods to control the $P_s$ at dielectric interfaces and in FE-thin films.

Due to the aggressive miniaturization of gate dielectrics, dielectric interfaces have become an essential part that determines the overall performance of a device. It is known that at a dielectric interface, a layer of dipole moments (also known as interface dipole layer) can be formed and causes a shift in the operating voltage of the device. So far, the magnitude (also known as interface dipole layer strength, $\varphi_{\mathrm{dipole}}$) and the direction of an interface dipole layer are thought to be fixed with the choice of the material selection and the thermal annealing process. Hence, we extracted the temperature dependence of $\varphi_{\mathrm{dipole}}$ at several dielectric interfaces. We found that the $\varphi_{\mathrm{dipole}}$ is not fixed by the choice of materials selection and annealing process, but $\varphi_{\mathrm{dipole}}$ can also be controlled by the change in temperature. We also found that the magnitude of the temperature dependence can be universally explained using the concept of screening length.

The FE-thin film focused in this study is FE-$HfO_2$. FE-$HfO_2$ is a promising material that is a candidate to be the next material to be commercialized. Nevertheless, one of the remaining issues of FE-$HfO_2$ is the waking-up effect, which refers to the irreversible increase in the $P_s$ during the initial cycles of electric field cycling. To date, the mechanism and the origin of the waking-up effect have already been established but not well discussed. Studies suggest that the origin of the waking-up effect is closely related to the phase transformation to the orthorhombic (O) phase[1] driven by electric field cycling; however, the waking-up effect and the phase

[1] Orthorhombic phase is known to be the source of ferroelectricity in $HfO_2$.

transformation were not observed at the same scale. Therefore, the relationship between the waking-up effect and the phase transformation was not correctly represented. We clarified the origin of the waking-up effect by observing the two phenomena at the same scale. We found that the origin of the waking-up effect is the result of the phase transformation driven by electric field cycling.

Typically, it is unconventional for a phase transformation to take place without thermal annealing. Hence, the phase transformation must be governed by a phenomenon that has not yet been discussed. During structural characterization, we found an anomalous difference between the interplanar spacing ($d_{spacing}$) that is parallel and perpendicular to the surface of $HfO_2$ and attribute it to the structural distortion. We further investigated and clarified that structural distortion is a driving force that determines the amount of phase transformation to be driven by an electric field. Later, we also clarified that the anomalous structural distortion is originating from the rapid shrinkage in the volume of $HfO_2$ during the crystallization.

Normally, the thermodynamic stale phase in $HfO_2$ is regarded as the monoclinic (M) phase, but M-phase is non-FE. Although O-phase can become the stable phase in some circumstances, the phase transformation to the O-phase without thermal annealing is not kinetically feasible. We investigated the factors that accelerate the phase transformation to the O-phase without thermal annealing. We found that positive charges, the magnitude, and the time that the electric field was applied are important in the acceleration of the phase transformation to the O-phase.

To total, we found two new methods to control the $P_s$ at dielectric interfaces and in FE-thin films; that is through the change in the temperature and the structural distortion, respectively.

# Contents

# Table of Figures

# Table of Tables

# Chapter 1 Introduction

## 1.1 Polarization and Materials Properties

To engineer a material property of any matter, it is crucial to understand what determines them in the first place. The main motivation of this study is to investigate how polarization determines the material properties of a dielectric interface and ferroelectric thin films. In this section, we intend to differentiate macroscopic and microscopic polarization.

Whenever there is an unbalance in charge distribution, there is polarization. This definition holds true both in a microscopic and a macroscopic world. However, macroscopic and microscopic polarizations are not identical. A macroscopic polarization is like a material property and can be explained by the collection of microscopic polarization. On a microscopic scale, the polarization of material exists in the form of dipole moments, and the **macroscopic polarization ($\vec{P}$)** is simply the sum of individual **dipole moments ($\vec{p}$)** per unit volume,

$$\vec{P} = \sum \vec{p} = N_{\mathrm{m}} \alpha_{\mathrm{m}} \vec{E}_{\mathrm{loc}} \tag{1.1}$$

where $N_{\mathrm{m}}$, $\alpha_{\mathrm{m}}$, and $\vec{E}_{\mathrm{loc}}$ are the **number of dipole moments**, the **microscopic polarizability** of the dipole moment, and the **local electric field** that a dipole moment is experiencing, respectively. Generally, microscopic polarization can be categorized into 3 categories: ionic polarization, electronic polarization, and orientation polarization. The schematic of microscopic polarizations and their frequency dependence are shown in Fig. 1.1 and Fig. 1.2, respectively. Ionic and electronic polarization arises from the atomic bond bending/lengthening and uneven electron cloud distribution, respectively. Orientation polarizations arise from the orientation of molecules that has an asymmetric charge distribution, therefore, they are permanent dipole moments. In a dielectric material, the polarizability is mostly comprised of ionic and electronic polarizability, where the dipole moment originates from the displacement of charged ions and unbalance in atomic orbitals.

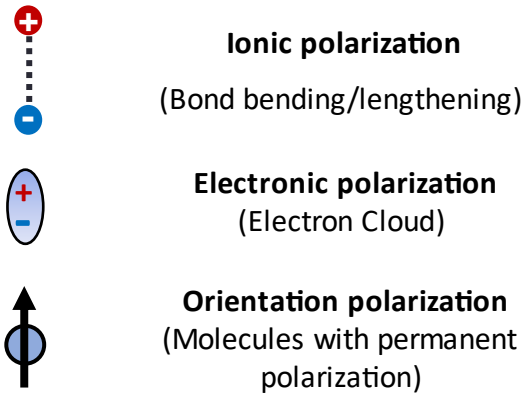


Fig. 1.1 Microscopic polarization (dipole moment) in materials.

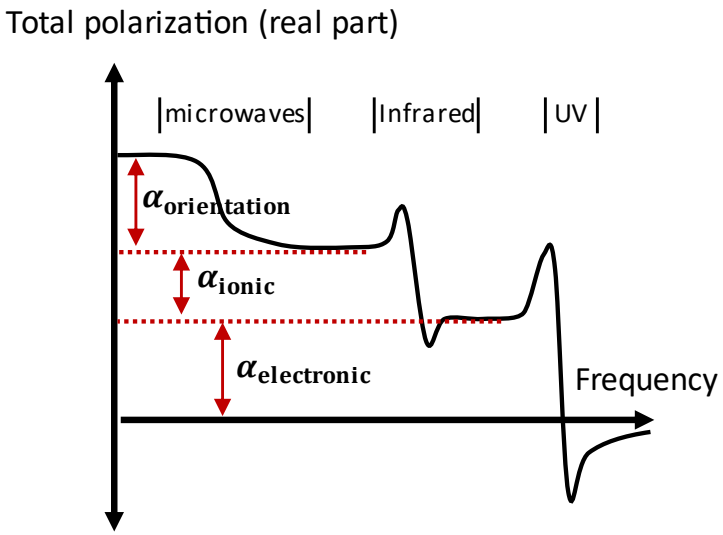


Fig. 1.2 Frequency dependence of several types of polarizability in materials. The figure is redrawn from ref [1].

A material property like the **dielectric constant (*k*)** of a high-*k* oxide is a classic and an excellent example of how macroscopic polarization can be explained by the collection of microscopic polarization. The term high-*k* oxides refer to oxides with a high dielectric constant (*k*), sometimes referred to as the relative permittivity ($\varepsilon$). Because the polarizability of a high-*k* material is comprised of electric and ionic polarizabilities, the dipole moments are randomly orientated; thus, no net polarization can be observed and is considered paraelectric. Fig. 1.3(a) shows an example of a paraelectric material in the absence of an electric field. However, under an electric field, these dipole moments can re-orientate themselves to compensate for the charges that accumulate at the surfaces. The ability of these individual dipole moments to compensate for the accumulated charges on a macroscopic scale is reflected by the dielectric

constant of a material. The schematic diagrams showing the ability for the dipole moments in $SiO_2$ and $Al_2O_3$ under the same electric field and thickness compensate the charges is reflected by its dielectric constant are shown in Fig. 1.3(b) and (c), respectively. Because the dipole moments of $Al_2O_3$ can compensate twice more charges than the dipole moments of $SiO_2$, the dielectric constant of $Al_2O_3$ ($k$≈8) is twice higher $SiO_2$ ($k$≈4). In other words, for $SiO_2$ to compensate the same number of charges as $Al_2O_3$, the thickness of $SiO_2$ has to be reduced by half.

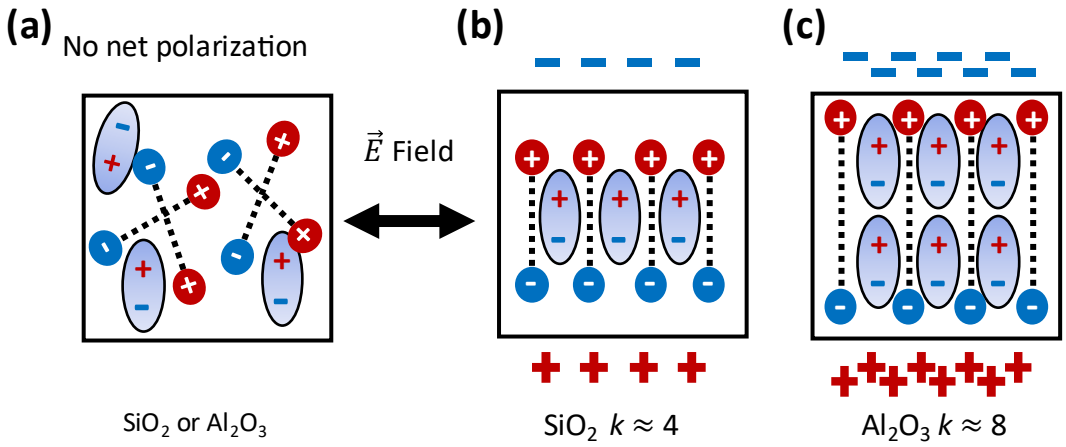


Fig. 1.3 (a) An example of randomly orientated dipole moments in a paraelectric material. The orientation dipole moments in (b) $SiO_2$ and (c) $Al_2O$ to counteract that accumulated charges under the influence of an electric field.

To mathematically relate a relationship between the macroscopic dielectric constant ($k$) and microscopic polarizability ($\alpha_m$) of a material, we derived the Clausius-Mossottoo relation as an example of the relationship between $k$ and $\alpha_m$. In a macroscopic world, the dielectric constant is described as the relationship between the dielectric displacement ($\vec{D}$) and the $\vec{P}$ of a material:

$$\vec{D} = \varepsilon_0 k \vec{E}_{app} = \vec{P} + \varepsilon_0 \vec{E}_{app}. \tag{1.2}$$

where $\varepsilon_0$ and $\vec{E}_{app}$is the permittivity of vacuum and the macroscopic applied electric field, respectively. Rearrange and solve for $\vec{P}$, we get

$$\vec{P} = \varepsilon_0 k \vec{E}_{app} - \varepsilon_0 \vec{E}_{app}$$

$$= \varepsilon_0 (k-1) \vec{E}_{app}. \tag{1.3}$$

Microscopically, the $\vec{E}_{\text{loc}}$ , in Eq. (1.1), can be approximated by the **Lorentz relation**, where the local electric field that is applied on a dipole moment is the sum of the macroscopic applied electric field ($\vec{E}_{\text{app}}$) and polarization of other dipole moments in the material,

$$\vec{E}_{loc} = \vec{E}_{\text{app}} + \frac{\vec{P}}{3\varepsilon_0}.$$

Since we know the relationship between $\vec{P}$ and *k* from Eq. (1.3), the equation becomes:

$$\begin{aligned} \vec{E}_{loc} &= \vec{E}_{\text{app}} + \frac{1}{3\varepsilon_0}(k-1)\vec{E}_{\text{app}} \\ &= \vec{E}_{\text{app}}\left(\frac{k+2}{3}\right) \end{aligned} \tag{1.4}$$

Now, we can relate *k* and $\vec{P}$ by substituting Eq. (1.4) into Eq. (1.1) to obtain

$$\vec{P} = N_{\text{m}}\alpha_{\text{m}}\vec{E}_{\text{app}}\left(\frac{k+2}{3}\right). \tag{1.5}$$

We can combine Eq. (1.3) and Eq. (1.5) to obtain the **Clausius-Mossotto relation**:

$$\frac{k-1}{k+1} = \frac{1}{3\varepsilon_0}N_{\text{m}}\alpha_{\text{m}}. \tag{1.6}$$

The Clausius-Mossotto relation demonstrates that a material property like a dielectric constant (*k*) can be explained by the collection of microscopic polarization (polarizability of dipole moments, $\alpha_{\text{m}}$ ). Note that that the relationship between the dielectric constant and the polarizability is not linear.

## 1.2 Spontaneous Polarization in Dielectric Interfaces

The type of polarization that we are focusing on in this study is the **spontaneous polarization** at (i) dielectric interfaces (this section) and in (ii) ferroelectric thin film (Section 1.3 ). To be a spontaneous polarization, the material must possess a net polarization even in an absence of an external electric field.

Due to the aggressive miniaturization of CMOS devices [2], [3], the interface of a gate dielectric has become a prominent factor that determines the properties of a gate dielectric. The spontaneous polarization at dielectric interfaces, or commonly also known as **interface dipole layers**, was first reported from an anomalous shift in the flatband voltage ($V_{fb}$) of Au/$HfLaO_x$/$SiO_2$/Si capacitors that are highly dependent on La-doping concentration near the $HfLaO_x$/$SiO_2$ interface region, as shown in Fig. 1.4 [4]. It was later supported the shift in the $V_{fb}$ is mainly the result of high-*k*/$SiO_2$ interfaces in bi-layer high-*k* dielectric stacks. Fig. 1.5 demonstrates that the high-*k* oxide layer that was in contact with $SiO_2$ is responsible for the shift in the $V_{fb}$ of a bilayer high-*k* dielectric MOS capacitors.

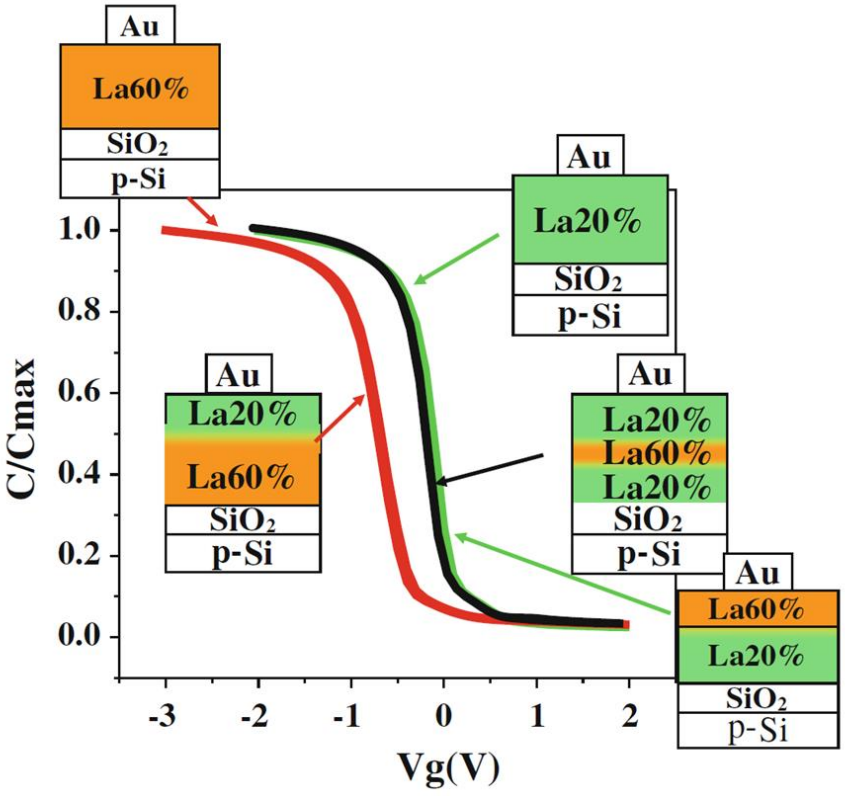


Fig. 1.4 C-V characteristics of MOS capacitors with $HfLaO_x$/$SiO_2$ gate dielectric at different doping concentration profiles in the $HfLaO_x$ layer [4].

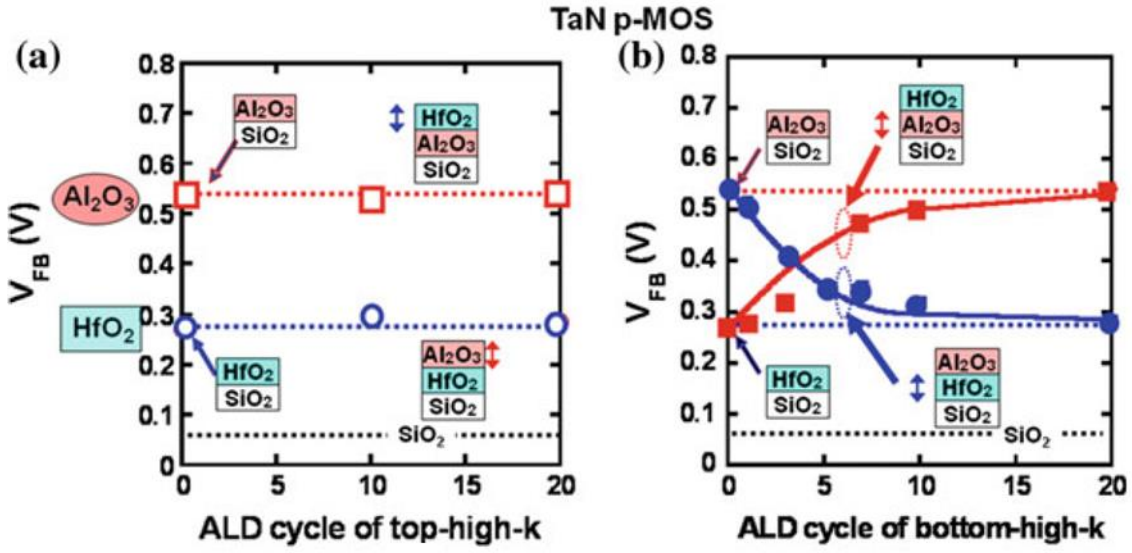


Fig. 1.5 The shift in $V_{fb}$ of high-*k*/$SiO_2$ dielectric bilayer MOS capacitors. The thicknesses of the (a) *top* and (b) *bottom* high-*k* layers were presented as a function of ALD cycles [5].

Unlike the electronic and ionic polarization in high-*k* materials, interface dipole layers (as the name has suggested) can only be found near the interface region of two dielectric layers and the polarity does not switch in response to the applied electric field. So far, the spontaneous polarization at dielectric interfaces is known to be determined by the choice of the material selection at the interface [6]–[8]. In some interfaces, interface dipole layers can be activated with specific annealing temperatures [9], [10]. Fig. 1.6 (a) and (b) illustrate how the polarity of an interface dipole layer can be switched by reversing the order of the dielectric layers. In addition, it has been experimentally demonstrated that the polarity of interfaces dipole layers can be switched by changing the materials at the interface [11]. Several models have already been purposed to explain the magnitude and the direction of the spontaneous polarization at interface dipole layers at room temperatur.[1] What is unknown and remains to be clarified is the effect of temperature on the spontaneous polarization at interface dipole layers. In Chapter 3, we will be investigating the temperature dependence of the spontaneous polarization at several interface dipole layers.

[1] Section 3.1.1 summarise several models the explain for formation mechanism of interface dipole layers.

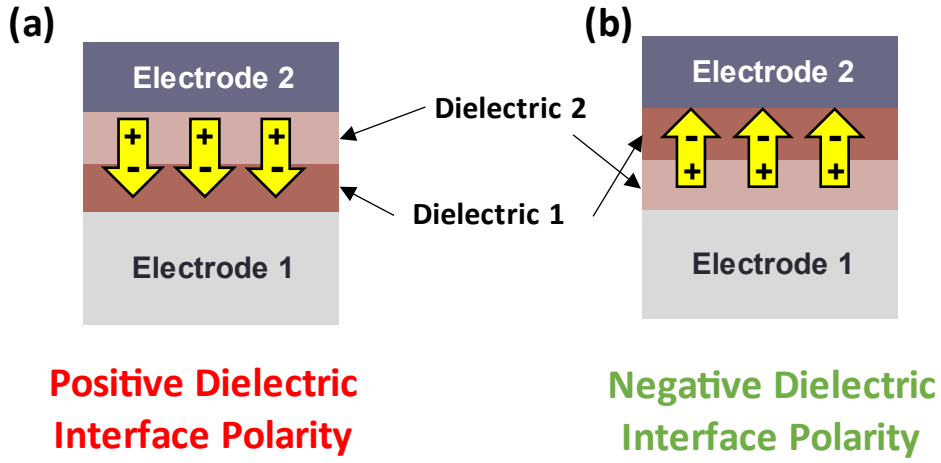


Fig. 1.6 (a) Positive and (b) negative polarity of an interface dipole layer. The polarity of an interface dipole layer can be controlled by the choice of materials selections at the interface.

## 1.3 Spontaneous Polarization in Ferroelectric Thin Films

Another class of materials that possess a spontaneous polarization is ferroelectric (FE) material. In contrast to the spontaneous polarization at dielectric interfaces, the polarities of the spontaneous polarization in FE materials can be reversed in response to an external electric field. Fig. 1.7 shows how to polarity of FE materials can be reversed by an electric field.

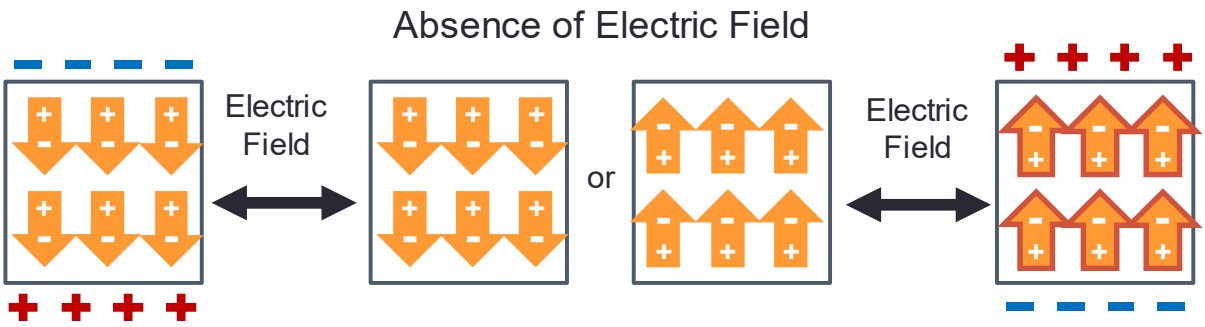


Fig. 1.7 In a ferroelectric material, a net polarization exists in the absence of an electric field. The direction of the net polarization can be reversed by applying an electric field in the opposite direction.

It is important to point out that a FE material is a sub-class of a dielectric material. Fig. 1.8 shows that a ferroelectric material is a sub-class of other materials. Piezoelectric and pyroelectric materials are materials that can induce an imbalance in electric charges in response to the change in mechanical stress and temperature, respectively. Thus, every FE material is also a dielectric material, but the vise-verser is not true. Hence, it is important to differentiate the dielectric and the FE responses when an electric field is applied to the materials.

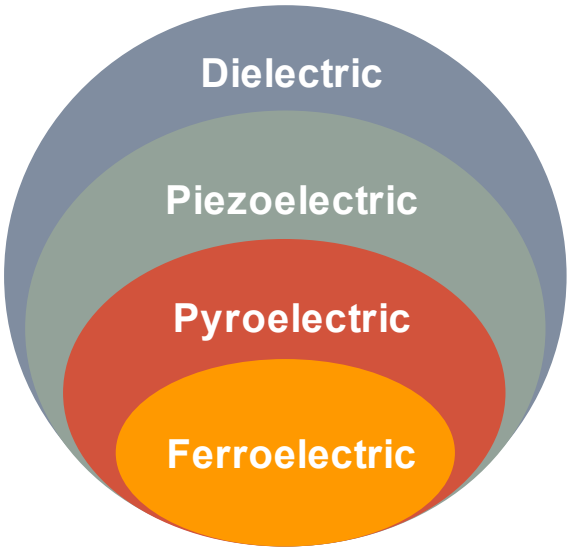


Fig. 1.8 Ferroelectric, pyroelectric, piezoelectric materials are sub-class of a dielectric material.

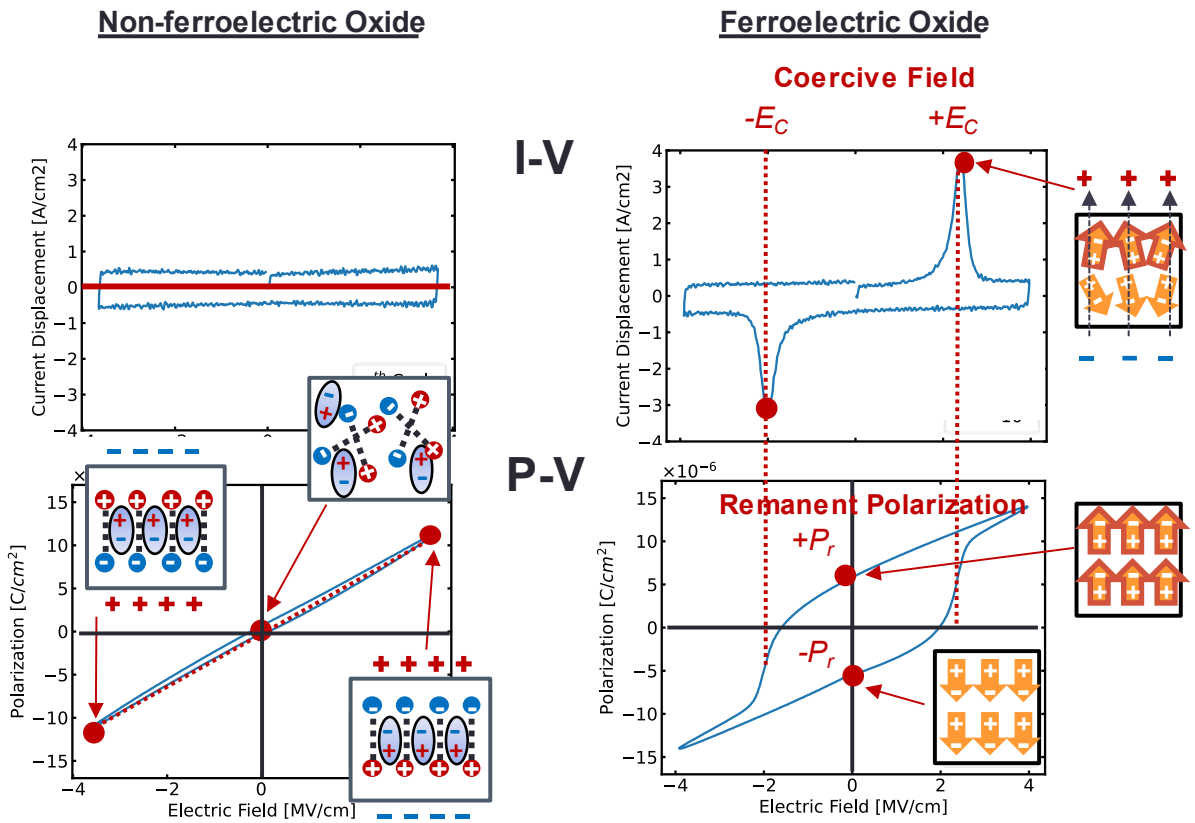


Fig. 1.9 Current displace (I-V) and polarization-voltage (P-V) characteristics of 30 nm thick non-FE and FE-$HfO_2$.

Fig. 1.9 shows the current displacement (I-V) and polarization-voltage field (P-V) characteristics of a non-FE- and an FE-oxide. In a none FE-oxide, the observing current displacement is due to the leakage current across the non-FE oxide. Because the electric and ionic dipole moments do not possess a net polarization in an absence of an electric field, no polarization is observed at E=0. When an electric field is applied, the dipole moments can orientate to compensate for the accumulated charges resulting in the linear increase in the polarization. On the contrary, in an FE-oxide, a net polarization can be observed in an absence of an electric field. The polarization of an FE-oxide in the absence of an electric field is referred to as the **remanent polarization ($P_r$)**. When an electric field is applied, the electric field that causes the polarization to reverse its direction is called the **coercive field ($E_c$)**. This reversal in polarization causes an additional current on top of the leakage current, and the currents can be seen as the maxima and minima in the I-V characteristic.

## 1.3.1 Ferroelectric $HfO_2$

The FE material that we are investigating in this study is FE-$HfO_2$. The reason that we only focus on FE-$HfO_2$ over the conventional FE-perovskite oxides is due to several of its unique properties and advantages both in terms of technology and scientific studies. Before the discovery of ferroelectricity in $HfO_2$ [12], ferroelectric materials were thought to exist only in perovskite-based oxides [13]–[15], such as $SrBi_2Ta_2O_9$ (SBT) and $Pb(Zr_xTi_{1-x})O_3$ (PZT). So far, the origin of the ferroelectricity in $HfO_2$ is now well understood, originating from the **orthorhombic (O) phase**. The detail on the origin of ferroelectricity in $HfO_2$ is described in Section 4.1.1. One of the advantages of FE-$HfO_2$ over the conventional FE-perovskite oxides is its scalability and its compatibility with the current Si-technology. However, one of the remaining issues with FE-$HfO_2$ is the **waking-up effect**. The waking-up effect refers to the increase in the polarization during a device operation when the same magnitude of an electric field was applied. An example of the change in the polarization during an electric field cycling (to simulate a pulse sequence during a typical device operation) is shown in Fig. 1.7. It is known that the waking-up effect in FE-$HfO_2$ is a complex phenomenon involving the interaction of structural and electrical properties. This means that there is an increase in the source of ferroelectricity during the device operation. So far, the origin and the driving force of the waking-up are still not clearly understood and remained to be clarified.

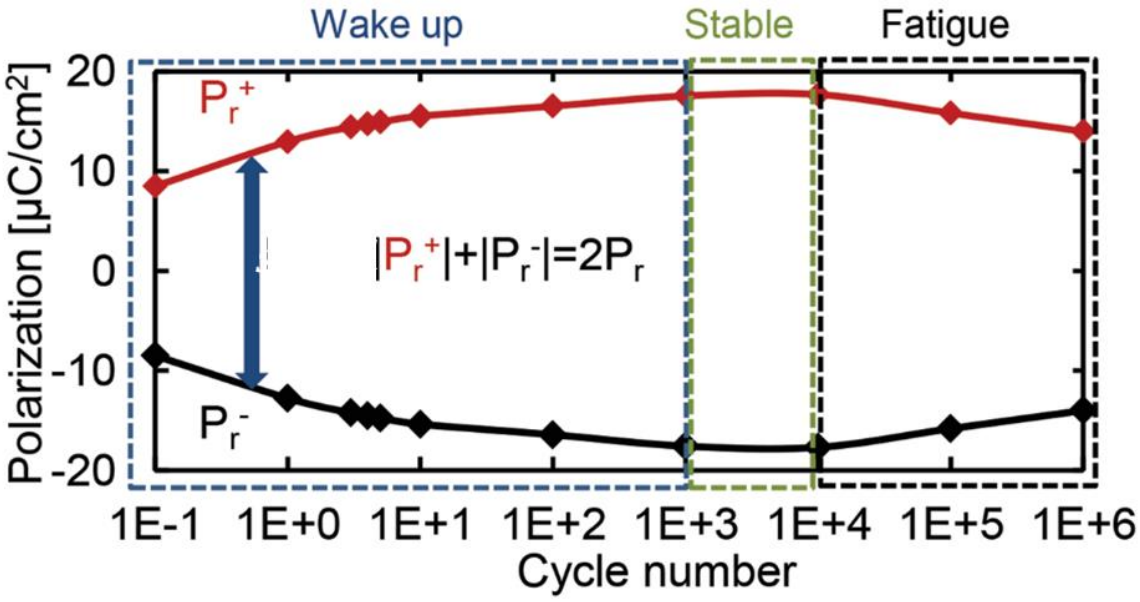


Fig. 1.10 Change in remnant polarization ($P_r$) during electric field cycling (4 V at the frequency of 10 kHz) of 10 nm-thick Sr-doped $HfO_2$ capacitors [16].

One of the possible origins of the waking-up effect is the phase transformation driven by an electric field. The detail on the two possible models of the origins of the waking-up effect, including the phase transformation, are described in 4.1.3. Previous studies have tried to relate the phase transformation driven by an electric field and the waking-up effect, but the two phenomena were not observed on the same scale (*i.e.*, the phase transformation and the waking-u effect were observed on microscopic and macroscopic scales, respectively). In Section 1.1, we emphasized that the macroscopic polarization can only be explained by the collection of microscopic polarization. Hence, the relationship between the two phenomena has not been correctly represented. In this study, Chapters 4-6 are dedicated to the investigation of the waking-up effect in FE-$HfO_2$.

Although we are only focusing on the waking-up effect of FE-$HfO_2$, it is useful to keep in mind the remaining issues in FE-$HfO_2$ that prevent it from being perfect in terms of device performance. Table 1.1 compares several key properties of FE-$HfO_2$ and FE-perovskite oxides. Other than the waking-up effect, FE-$HfO_2$ suffers from the difficulty in fabricating single-crystal $HfO_2$ thin films with high polarization [17]–[19]. Theoretically, the polarization of FE-$HfO_2$ can reach up to 50 $\mu C/cm^2$ [20]. In Table 1.1, the polarization of FE-$HfO_2$ that was experimentally observed can range from 1 to 40 $\mu C/cm^2$. Because only the c-axis of the O-phase is the only polar axis [17], [20] and the $HfO_2$ structure is comprised of mixed phases, it is difficult to fabricate $HfO_2$ films with c-axis perfectly align with the direction of an electric field. For this reason, a wide range of polarization can be observed depending on the fabrication process and the degree of controls in the process.

Another issue with FE-$HfO_2$ that is remained to be solved in the high coercive field ($E_C$). A high coercive field is a double-edged sword for FE-$HfO_2$. The high coercive field does provide a major advantage in the retention of the polarization. This allows FE-$HfO_2$ to be scale down to an ultra-thin film region. So far, FE-$HfO_2$ could be scaled down to 3 nm while maintaining its ferroelectricity [21]. Nevertheless, a high coercive field means that higher voltages are required to switch the polarity of FE-$HfO_2$. This makes FE-$HfO_2$ prone to dielectric breakdown and catastrophic failure of the device during operation. Table 1.1 compares the breakdown field ($E_{BD}$) and the ratio between coercive field and breakdown field ($E_{BD}/E_{BD}$*100) of FE-$HfO_2$ and FE-perovskite oxides.

Table 1.1 The comparison of materials properties between FE-$HfO_2$ and FE-perovskite oxides [22].

| | $SrBi_2Ta_2O_9$ (SBT) | $Pb(Zr_xTi_{1-x})O_3$ (PZT) | FE-$HfO_2$ |
|---|---|---|---|
| Film thickness | >25 nm | >70 nm | 5–30 nm |
| Annealing temp. | >750°C | >600°C | 450°C–1000°C |
| $P_r$ | <10 μC/cm$^2$ | 20–40 μC/cm$^2$ | 1–40 μC/cm$^2$ |
| $E_c$ | 10–100 kV/cm | ~50 kV/cm | 1–2 MV/cm |
| $E_{BD}$ | ~2 MV/cm | 0.5–2 MV/cm | 4–8 MV/cm |
| $E_c/E_{BD}$* 100 | 0.5–5% | 2.5–10% | 12.5–50% |
| Dielectric constant | 150–250 | ~1300 | ~30 |
| ALD capability | limited | limited | mature |
| CMOS compatibility | Bi and $O_2$ diffusion | Pb and $O_2$ diffusion | stable |
| BEOL compatibility | $H_2$ damage | $H_2$ damage | stable |

## 1.4 Importance of Spontaneous Polarization

In terms of technology, spontaneous polarization is a crucial factor because it determines the operating voltage of any field-effect device. The ability to control the spontaneous polarization is important in various aspects of field-effect devices, including the reliability, efficiency, and performance of the device.

Two examples of how the direction of spontaneous polarization at dielectric interfaces and in FE-thin films (Fig. 1.11 (a) and (b), respectively) within a gate dielectric can induce a shift in the operating voltages of a MOS capacitor (MOS-cap) and MOSFET is shown in Fig. 1.12 (a) and (b), respectively. The operating voltages of a MOS-cap and a MOSFET are reflected by the flatband voltage ($V_{fb}$) and the threshold voltage ($V_{th}$), respectively. More details of the meaning of a $V_{fb}$ and $V_{th}$ can be found in ref [23] and ref [24]. Note that the operating voltage of other devices may not be represented by either $V_{fb}$ or $V_{th}$. For instant, in a memory device, the memory window (MW) does not always have to be represented by a shift in neither $V_{fb}$ nor $V_{th}$ but can also be represented by the change in the conductance across the gate dielectric.

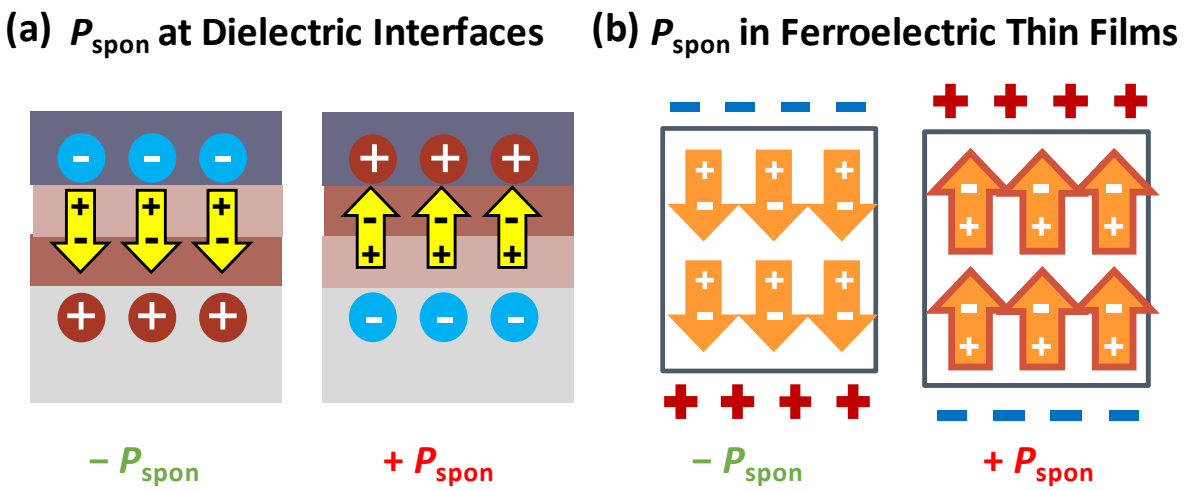


Fig. 1.11 Spontaneous polarization at (a) dielectric interfaces and in (b) ferroelectric thin films in positive and negative polarities.

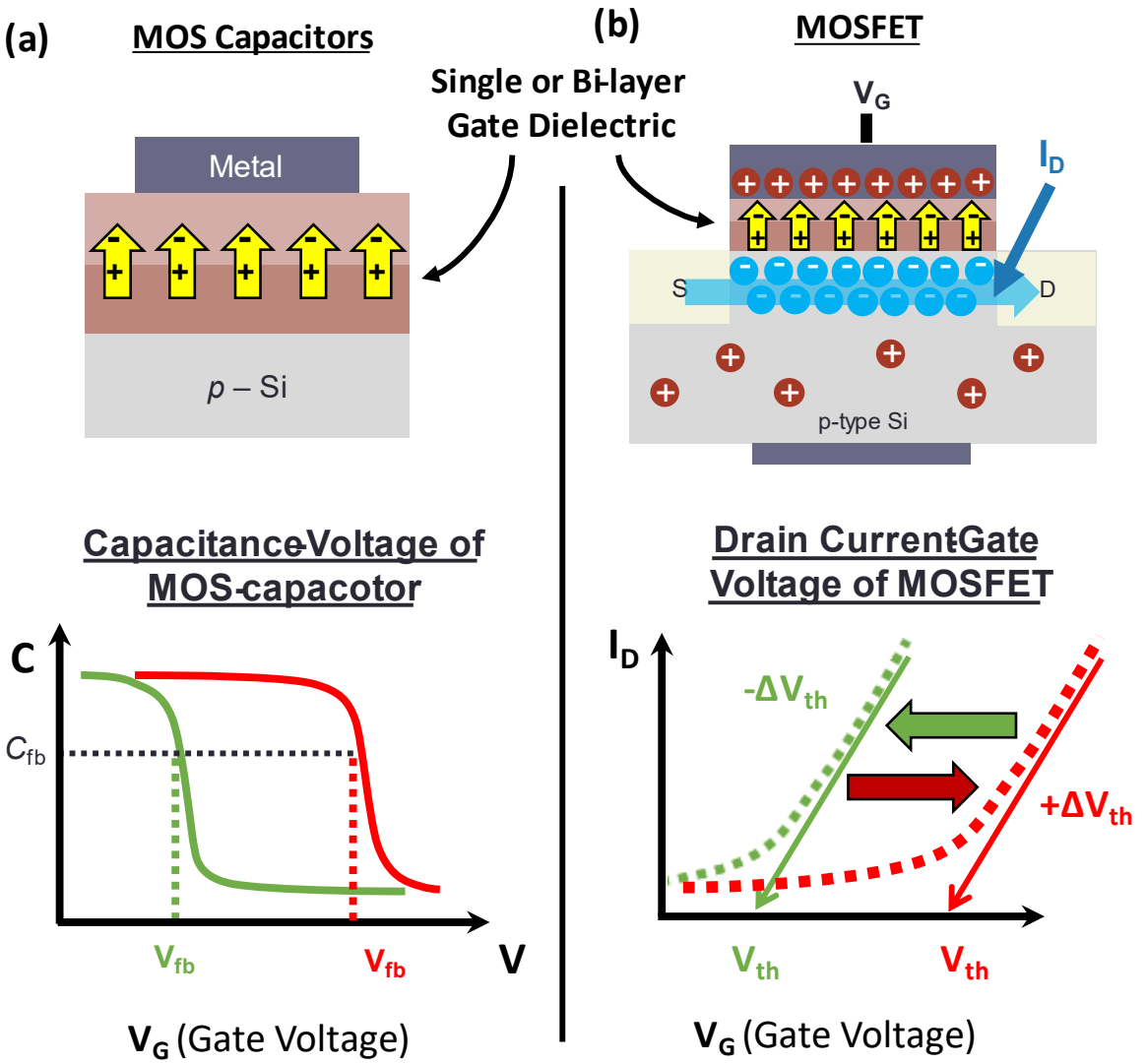


Fig. 1.12 (a) A MOS capacitor and (b) a MOSFET with single layer or bilayer gate dielectric. The shift in the $V_{fb}$ or the $V_{th}$ can be explained by the polarities of either the spontaneous polarization at dielectric interfaces or in ferroelectric thin films shown in Fig. 1.11 (a) and (b), respectively.

### 1.4.1 Importance of Spontaneous Polarization at Dielectric Interfaces and in Ferroelectric Thin Films

In terms of technology, spontaneous polarization at dielectric interfaces and in FE-thin films has become a critical aspect that determines the performance and efficiency of various kinds of devices due to the aggressive miniaturization of CMOS devices [2]. Thus, dielectric interfaces and FE-thin films are essential factors to be considered for the materials design of various devices.

At dielectric interfaces, we are focusing only on the temperature effect on interface dipole layers (spontaneous polarization at dielectric interfaces). For various applications, such as sensor networking and power devices, these devices are expected to operate at a wide range of temperatures. Fig. 1.13 shows an example of power devices in various applications according to their power output capacity and operating frequency. Applications such as electric railways and electric vehicles are the target applications that this study aims for since those applications are expected to operate in various kinds of harsh weather. As emphasized at the beginning of this section (Section 1.4), the magnitude and direction of the spontaneous polarization within a gate dielectric is important in the determination of the operating voltage of devices. Thus, the ability to control the spontaneous polarization at a wide range of temperatures is crucial for the design of high-performance and power-efficient devices.

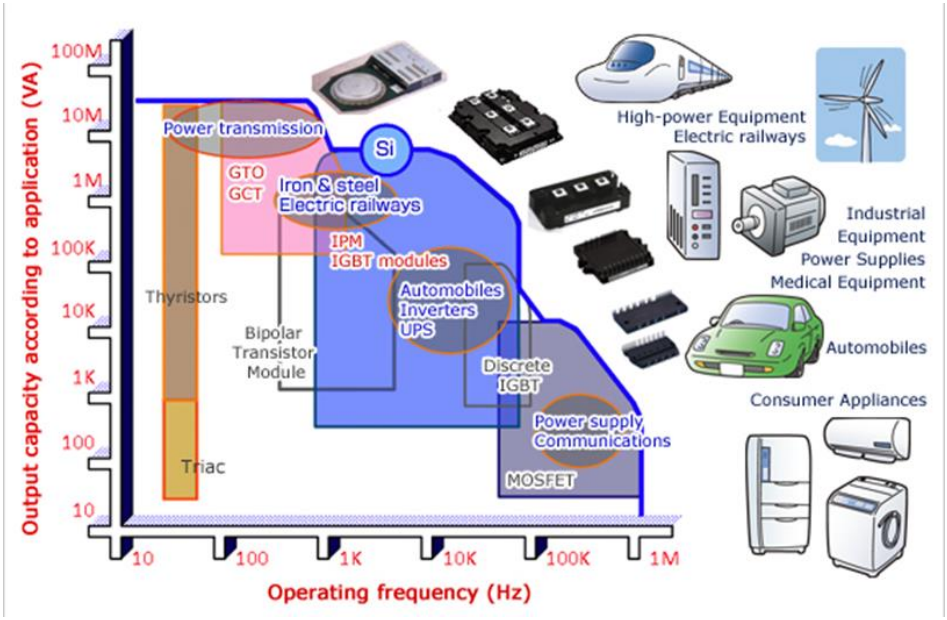


Fig. 1.13 Applications in power devices according to their output power capacity and their operating frequency [25].

FE-$HfO_2$ is unique and special not only in scientific discoveries but also in the semiconductor industries. This is because the non-ferroelectric $HfO_2$ has already been commercialized and is now used as the main material for the gate dielectric in various field-effect devices. Hence, FE-$HfO_2$ is highly compatible with the current Si-technology and has a high potential to be the next material to be mass-produced and commercialized. Several issues with FE-$HfO_2$, including the waking-up effect, are remained to be solved before it can be commercialized.[1] What is important with the waking-up effect is that it directly affects the endurance and reliability of the device and needed to be well controlled before FE-$HfO_2$ can be commercialized. Furthermore, FE-$HfO_2$ also has an impact in a wide range of applications and the development of advanced CMOS and emerging non-volatile memory technologies, such as negative capacitance field-effective transistors (NC-FET), ferroelectric random-access memories (FE-RAMs), ferroelectric tunnel junctions (FTJs), and resistive random-access memories (ReRAMs) for neuromorphic computing. Fig. 1.14 shows several common device structures with FE-$HfO_2$ as a gate dielectric.

In terms of scientific impact, clarifying the temperature effect of interface dipole layers and the waking-up effect of FE-$HfO_2$ means that we have two new methods to control the spontaneous polarization at dielectric interfaces and in FE-thin films.

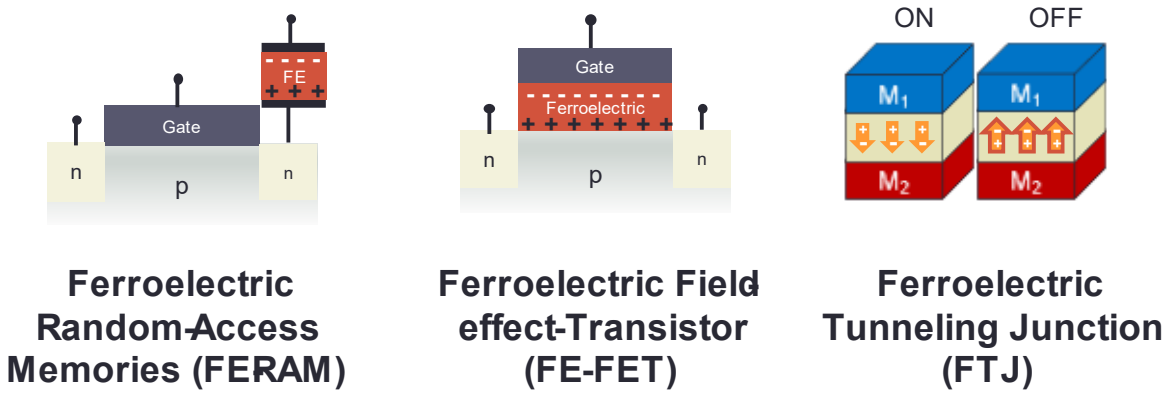


Fig. 1.14 Examples of device structures with FE-$HfO_2$ as a gate dielectric.

[1] The remaining issue with FE-$HfO_2$ are described in Section 1.3.1.

## 1.5 Objectives of this study

Unquestionably, the engineering of spontaneous polarization at dielectric interfaces and in ferroelectric thin films is crucial to the developments of advance complementary metal-oxide-semiconductor (CMOS) and emerging non-volatile memory (NVM) technologies. In this study, we aim to investigate the impact of the change in temperature and structural distortion on the spontaneous polarization at dielectric interfaces and in ferroelectric thin films, respectively. The following are the objectives of this Ph.D. dissertation.

**Chapter 3** – When a dielectric interface was fabricated and annealed, the spontaneous polarization of the dielectric interface was thought to be permanently fixed. In Chapter 3, we first would like to extract the temperature dependence of the spontaneous polarization at several dielectric interfaces. Finally, we would like to postulate a model that can universally explain the temperature dependence that we experimentally extracted.

**Chapter 4** – Previous studies have not yet clearly represented the relationship between the phase transformation driven by an electric field and the waking-up effect because the two phenomena were not observed on the same scale. In Chapter 4, we would like to clarify the origin of the waking-up effect by observing both the phase transformation and the waking-up effect at the same scale. The relationship between different phenomena in our model of the waking-up effect is shown in Fig. 1.15.

**Chapter 5** – In Chapter 4, we clarified that the origin of the waking-up effect is the result of the phase transformation driven by an electric field. In Chapter 5, we would like to clarify the driving force that determines the amount of the phase transformation to be driven by an electric field.

**Chapter 6** –Finally, we would like to clarify the factors the accelerates the phase transformation to the O-phase (clarified to be the origin of the waking-up effect in Chapter 4 ) without thermal annealing.

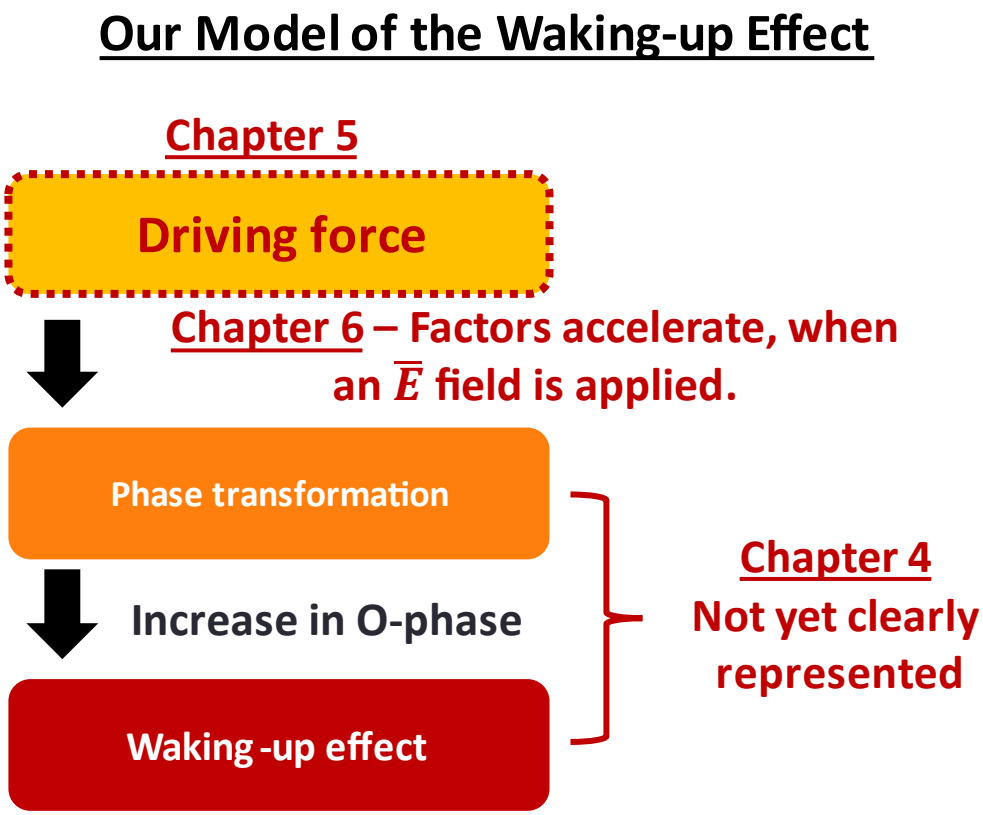


Fig. 1.15 The relationship between different phenomena in our model of the waking-up effect and the outline of how the mechanism of the waking-up effect will be investigated.

# Chapter 2 Experimental method

2.1 Spontaneous Polarization at Dielectric Interfaces

2.2.1 Fabrication Method

2.2.2 Determination of Flatband Voltage

2.2.3 Extraction of the Spontaneous Polarization at Dielectric Interfaces

2.2 Spontaneous Polarization in Ferroelectric Thin Films

2.2.1 Fabrication Method

2.2.2 Structural Analysis by X-ray Diffraction

2.2.3 Electrical Characterization of Ferroelectric Materials

2.2.4 DC-bias Stressing

## 2.1 Spontaneous Polarization at Dielectric Interfaces

### 2.1.1 Fabrication Method

To investigate the spontaneous polarization at high-*k*/$SiO_2$ interfaces, each sample set was fabricated with a sample and a reference. The samples are the MOS capacitor (MOS-cap) with the target high-*k*/$SiO_2$ dielectric layer, where the references are the MOS-cap with a similar structure as the sample but without the top high-*k* layer. The fabrication outlines of the sample MOS-cap with a high-*k*/$SiO_2$ gate dielectric and its reference are shown in Fig. 2.1. First, a modified Radio Corporation (RCA) cleaning solutions were used to clean Si wafers with ~10 nm-thick thermally grown $SiO_2$. The wafers were first clean with isopropyl alcohol (IPA) under ultra-sonication to remove any air-born particle contaminants. After that, the wafers were cleaned with SPM (1 $H_2O_2$: 4 $H_2SO_4$) and HPM (1 DIW: 6 HCl: 1 $H_2O_2$) to eliminate the remaining organic and metallic contaminants. Finally, the wafers were dipped in diluted HF acid (0.1~0.2%) to etch any remaining immovable contaminants. Note that HF cleaning was optional.

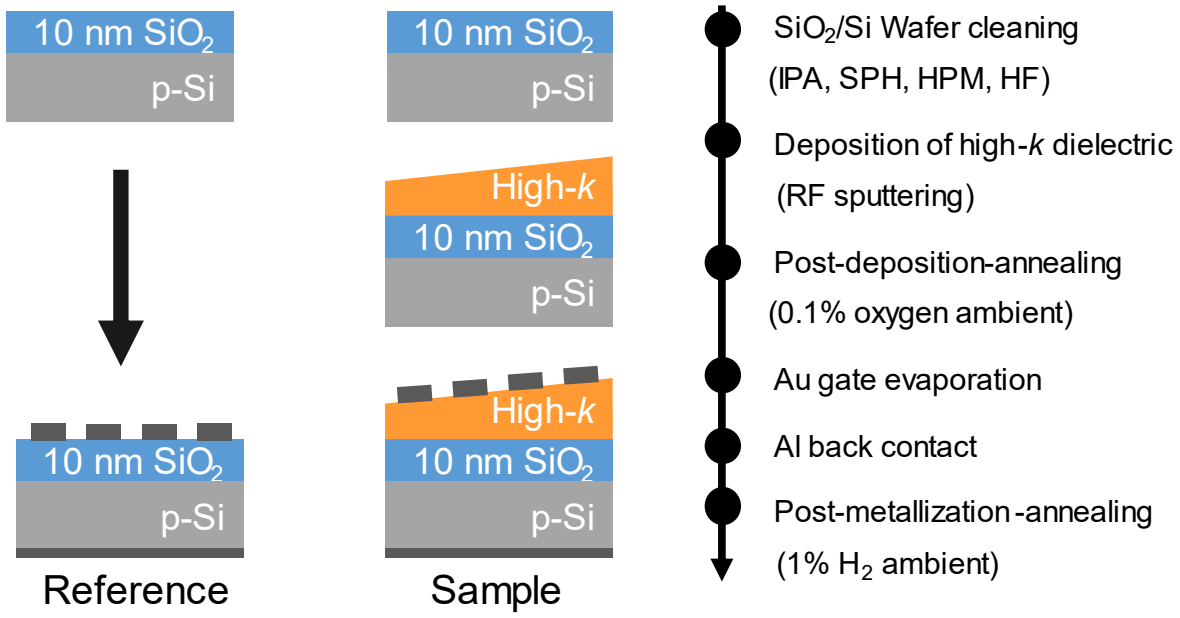


Fig. 2.1 The fabrication process of high-*k*/$SiO_2$ dielectric MOS-cap and their references.

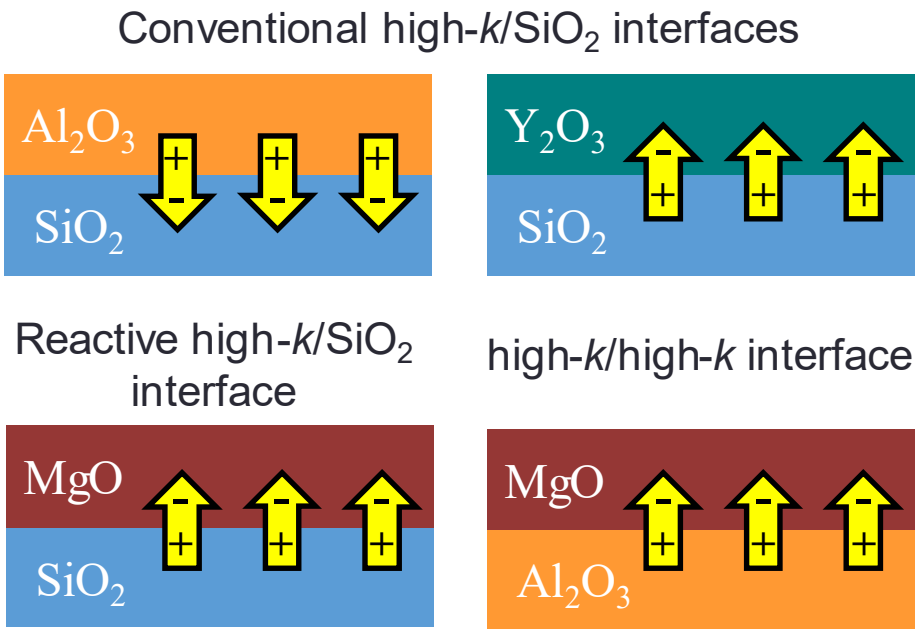


Fig. 2.2 Systematically chosen interfaces for the investigation of temperature effect on the polarization of dielectric interfaces.

Four interfaces were systematically chosen for the investigation of polarization at dielectric interfaces: $Al_2O_3/SiO_2$, $Y_2O_3/SiO_2$, $MgO_2/SiO_2$, and $MgO/Al_2O_3$ interfaces, as shown in Fig. 2.2. $Al_2O_3/SiO_2$ and $Y_2O_3/SiO_2$ interfaces are to represent conventional high-*k*/$SiO_2$ interfaces [8], their direction of the polarization is in the opposite direction. $MgO_2/SiO_2$, and $MgO/Al_2O_3$ are to represent reactive high-*k* [7] oxide and high-*k*/high-*k* [10] interfaces, respectively.[1] All high-*k* oxides were deposited using radio frequency (RF) sputtering. Argon gas was used as the plasma source, and the sputtering rate was controlled by modifying the voltage applied to the sputtering targets. After the deposition of high-*k* dielectrics, post-deposition-annealing (PDA) was performed using rapid thermal annealing (RTA) in 0.1% $O_2$ ambient for 5 min. The temperature that was used to anneal $Al_2O_3$, MgO, and $Y_2O_3$ can be found in Table 2.1. For $MgO/Al_2O_3$ interface, a tri-layer of $MgO/Al_2O_3/SiO_2$ gate dielectric structure has to be used. Then, the Au top electrodes were deposited via metal evaporation. The final MOS capacitor containing the four interfaces is shown in Fig. 2.3. To precisely quantify the polarization of the dielectric interfaces, samples without the top high-*k* oxide were also made as references. Finally, all samples (both the sample and references) were annealed with 1% $H_2$ ambient at 400°C for 5 min; except for samples with $Y_2O_3$, the temperature was set to 300°C.

[1] The literature on the formation mechanism of the selected interface dipole layers can be found in Section 3.1.1

Table 2.1 Post deposited annealing condition of $Al_2O_3$, MgO, and $Y_2O_3$.

| **Post Deposited Annealing ($0.1\%O_2$, 5 min)** | $Al_2O_3$ | MgO | $Y_2O_3$ |
|---|---|---|---|
| **Temperature** | 800°C | 600°C | 400°C |

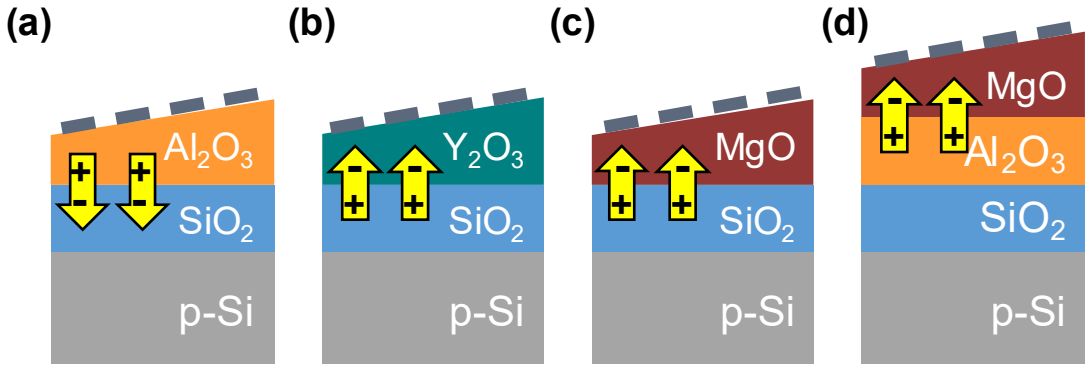


Fig. 2.3 MOS capacitors containing (a) $Al_2O_3/SiO_2$, (b) $Y_2O_3/SiO_2$, (c) $MgO_2/SiO_2$, and (d) $MgO/Al_2O_3$ interface dipole layers.

## 2.1.2 Determination of Flatband Voltage

The spontaneous polarization at dielectric interfaces in this study was determined from the shift in the flatband ($V_{fb}$) of MOS-cap. The $V_{fb}$ of a MOS-cap in this study was determined from the theoretically expected capacitance at the flatband conditions. The equivalent circuit of a MOS-cap at the flatband condition is shown in Fig. 2.4(a). At a flatband condition, the majority and minority carriers are depleted from the oxide/Si interface at the flatband condition, and the depletion depth can be approximated using the Debye length ($L_D$). Thus, the total capacitance at the flatband condition can be calculated as the following equation [23], [24].

$$\frac{1}{C_{total@flatband}} = \frac{1}{C_{ox}} + \frac{1}{C_s} = \frac{1}{C_{ox}} + \frac{L_D}{\varepsilon_{Si}}. \tag{2.1}$$

The Debye length was calculated using $L_D = \sqrt{\varepsilon_s kT/N_A q^2}$, where the doping density $N_A$. The theoretically calculated flatband capacitance was then used to find the $V_{fb}$ from the experimental CV curves, as demonstrated in Fig. 2.4(b**)**. More detail for the determination of $V_{fb}$ can be found in ref [26].

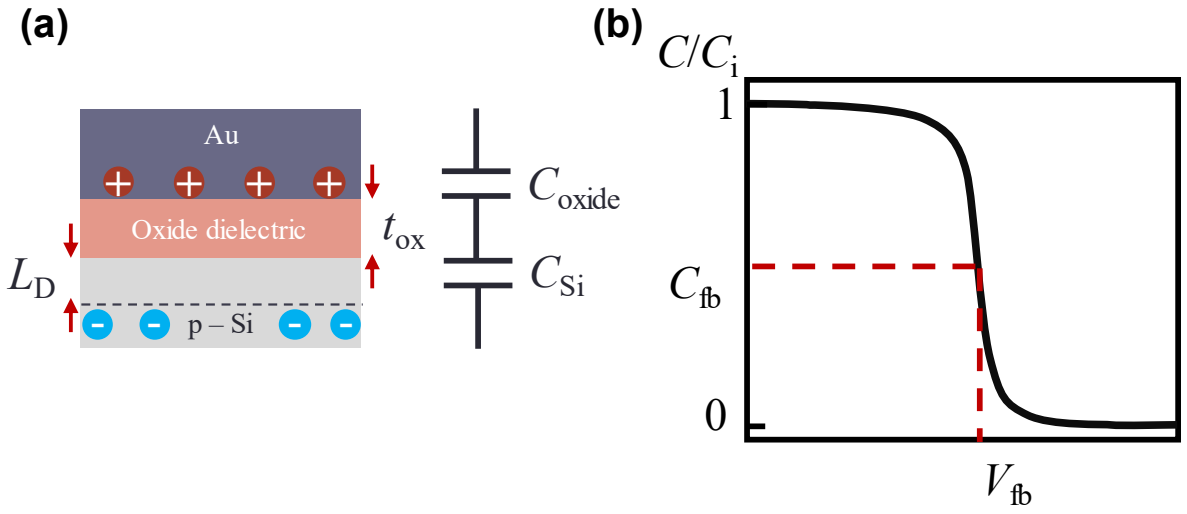


Fig. 2.4 (a) Equivalent circuit of a MOS-cap at the flatband condition. (b) The $V_{fb}$ was determined from the theoretically calculated capacitance at flatband condition $C_{fb}$.

### 2.1.3 Extraction of the Spontaneous Polarization at Dielectric Interfaces

To investigate the polarization at dielectric interfaces, it is important to understand other factors that contribute to the shift in the $V_{fb}$ in MOS capacitors with multiple dielectric layers. The schematic of charges that can affect the $V_{fb}$ of MOS capacitors with high-$k$/$SiO_2$ gate dielectric is shown in Fig. 2.5. To accurately quantify the spontaneous polarization in dielectric interfaces, other factors that can cause a shift in a $V_{fb}$ must be excluded. In general, the $V_{fb}$ of a typical Si MOS-cap with a high-$k$/$SiO_2$ gate dielectric at a constant temperature is described by the following equation:

$$V_{\mathrm{fb}} = \varphi_{\mathrm{ms}} - Q_1 \frac{t_{\mathrm{SiO2}}}{\varepsilon_{\mathrm{SiO2}}} - (Q_1 + Q_2) \frac{t_{\mathrm{high-}k}}{\varepsilon_{\mathrm{high-}k}} \pm \varphi_{\mathrm{dipole}}, \qquad (2.2)$$

where $\varphi_{\mathrm{ms}}$ and $\boldsymbol{\varphi_{\mathrm{dipole}}}$ are the difference of the metal work function and the Si Fermi level, and the **interface dipole layer strength**, respectively. Here, the dipole layer strength is used to quantify the spontaneous polarization at the dielectric interface. $Q_1$ and $Q_2$ are the fixed charge density at $SiO_2$/Si and high-$k$/$SiO_2$ interfaces, respectively. $\varepsilon_{\mathrm{SiO2}}$ and $\varepsilon$high-$k$ are the permittivities of $SiO_2$, and the high-$k$ oxide, respectively. $t_{\mathrm{SiO2}}$ and $t$high-$k$ are the physical thickness of $SiO_2$ and high-$k$, respectively. The direction of a dipole layer strength is defined as positive when the $V_{fb}$ shifts positively, and negative when the $V_{fb}$ shifts negatively.

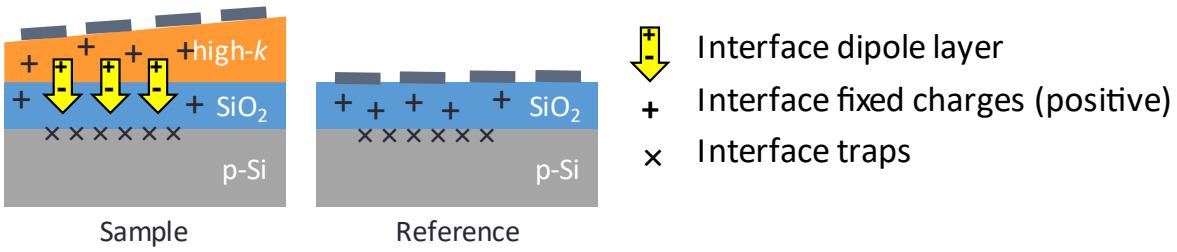


Fig. 2.5 Schematics of different types of charges in MOS-cap with high-$k$/$SiO_2$ and $SiO_2$ dielectric layers.

To accurately extract the dipole layer strength at each temperature, we excluded other factors that have contributed to the $V_{fb}$ shift in two steps – (i) excluding the third term in Eq. (2.2) and (ii) the first and second terms in Eq. (2.2). Fig. 2.6 graphically illustrates how factors described in Eq. (2.2) affect the shift in the $V_{fb}$. The third term was first eliminated by evaluating the thickness dependence of the top high-*k* layer. By extrapolating the thickness of the top high-*k* to zero ($t_{high\text{-}k} \rightarrow 0$), the third term in Eq. (2.2) is removed, and the slope of the linear relationship between the $V_{fb}$ and the thickness corresponds to the total fixed charge density in the stack (*i.e.* $Q_1 + Q_2$). Next, the first two terms in Eq. (2.2) are the factors that describe the $V_{fb}$ of the reference, which is also common in the sample as well. Therefore, by subtracting the $V_{fb}$ of the reference from the imaginary $V_{fb}$ ($V_{fb,img}$) of the sample, the 'intrinsic' component of $\varphi_{ms}$ and the fixed charges at $SiO_2$/Si interface ( the first and second terms in Eq. (2.2)) were eliminated, and the dipole layer strength at the high-*k*/$SiO_2$ interface was finally extracted. The dipole layer strength here is defined by the shift of the $V_{fb}$ value between the sample and its reference caused by the dipole layer. After that, the temperature dependence of the dipole layer ($d\varphi_{dipole}/dT$). at the high-*k*/$SiO_2$ interface was quantified by repeating the extraction process at different temperatures.

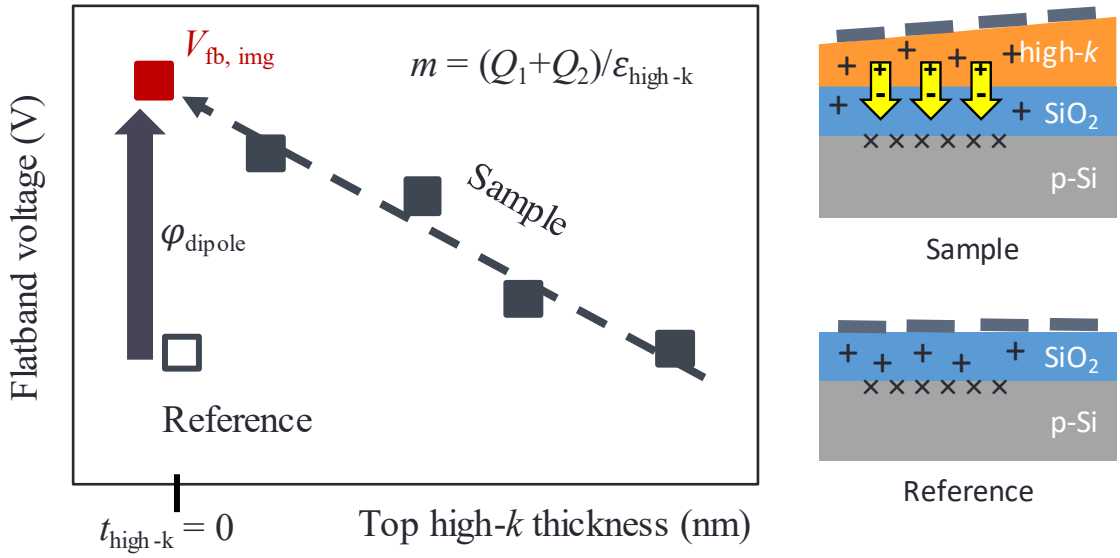


Fig. 2.6 Schematic of how factors described in Eq. (2.2) affect the $V_{fb}$ of a MOS capacitor with a high-*k*/$SiO_2$ gate dielectric.

## 2.2 Spontaneous Polarization in Ferroelectric Thin Films

### 2.2.1 Fabrication Method

In this study, ferroelectric (FE) $HfO_2$ is fabricated on a heavily doped p-Ge substrate ($N_A$= $5\times10^{18}$ $cm^{-3}$). The flow chart of the fabrication is shown in Fig. 2.7. The substrate was clean by isopropyl alcohol (IPA), diluted HCl, and diluted HF. Then, FE-$HfO_2$ was deposited via the co-sputtering of $HfO_2$ and $Y_2O_3$. The amount of Y-doping concentration was controlled by the $Y_2O_3$ sputtering power, normally at 10 W. The sputtering power of $HfO_2$ is fixed at 80 W. Next, the as-deposited $HfO_2$/Ge stacks were annealed at 600°C in $N_2$ ambient for 30 sec before allowing the temperature to drop in free fall during cooling (in the order of 100°C/min), otherwise stated. Finally, Au top electrodes were deposited via a metal evaporator. Note that this fabrication process is a general process for the fabrication of FE-$HfO_2$. A more specific condition of fabrication will be given in detail in each section.

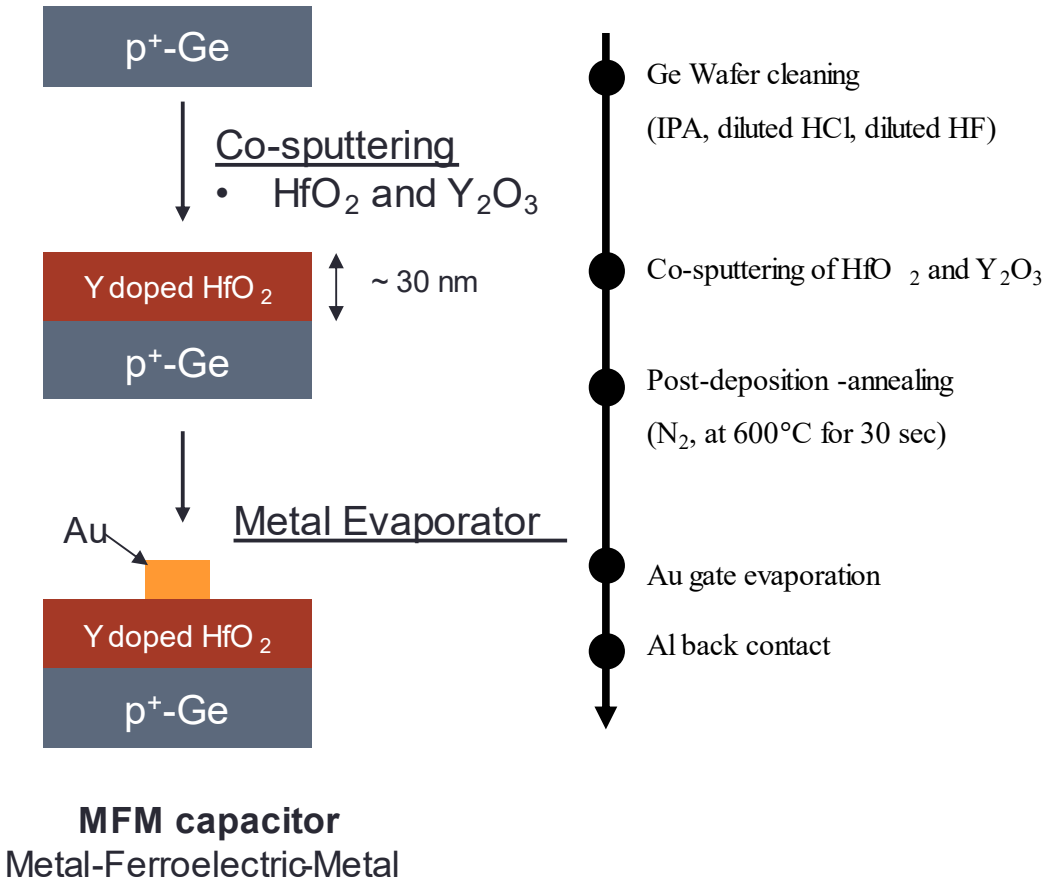


Fig. 2.7 The flow chart of the fabrication process of Au/FE-$HfO_2$/Ge capacitors.

## 2.2.2 Structural Analysis by X-ray Diffraction

The structure of FE-$HfO_2$ in this study was analyzed by various techniques of X-ray diffractions (XRD). In a conventional ($2\theta/\theta$) XRD, the incident angels ($\theta_i$) of the X-ray beam is very high, allowing the incident X-ray beam to penetrate deep into the sample. For this reason, this method is suitable for powder samples or thick films where the interfaces or surfaces do not matter much. However, we are interested in analyzing the surface/interfaces of FE-$HfO_2$ thin films, and the conventional XRD will not be able to differentiate the surface/interface from the rest of the films. The surface/interface can be differentiated by indenting the X-ray at a small angle so that the X-ray is only diffracted near the surface or interface of our FE-$HfO_2$. Fig. 2.8 shows diagrams of diffracted X-ray is incidents at small and large angles.

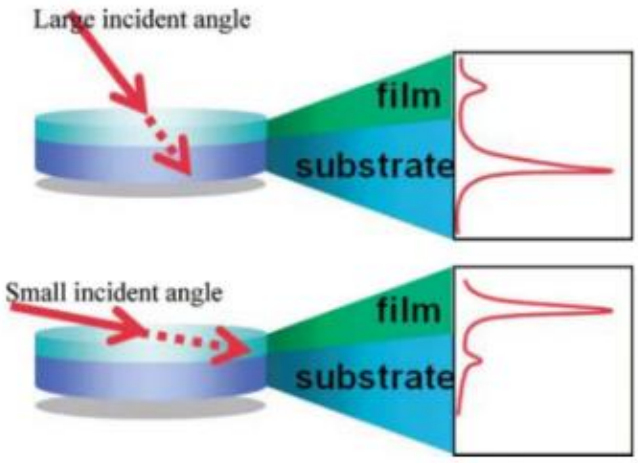


Fig. 2.8 Diagrams of how the diffracted intensities change when the X-ray beam was incident at a smaller and larger angle [27].

The penetration depth ($L$) of the incident X-ray beam can be estimated as a function of the incident angle using the following equation [27]–[29]:

$$L = \begin{cases} \dfrac{\lambda}{2\pi\sqrt{\theta_c^2 - \theta_i^2}} & \text{for } \theta_i < \theta_c \\ \dfrac{\sin\theta_i}{2\mu} & \text{for } \theta_i > \theta_c \end{cases} \tag{2.3}$$

where $\lambda$, $\theta_c$, and $\mu$ are the wavelengths of the X-ray, critical angle, and the X-ray absorption coefficient of the materials. The absorption coefficient of the materials is mainly dependent on the density of the materials. For X-ray wavelengths of 1.54 Å and $HfO_2$ density of 9.68 g/cm$^3$,

we can estimate how deep X-ray penetrates from the surface of $HfO_2$ films as shown in Fig. 2.9.

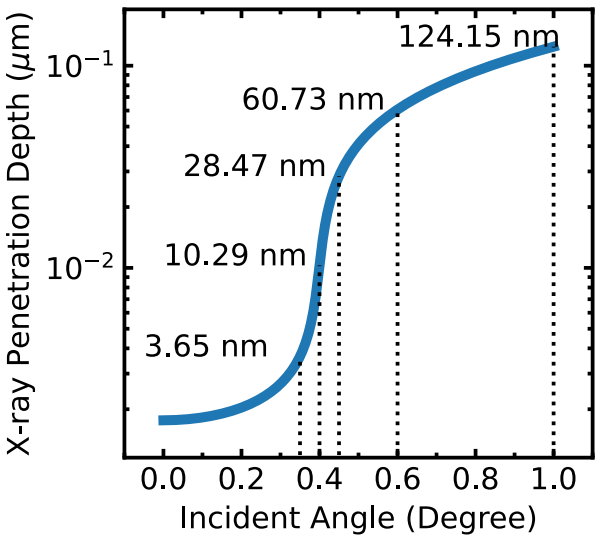


Fig. 2.9 Estimated X-ray penetration depth of $HfO_2$ at the density of 9.68 g/cm$^3$.

There are two kinds of GIXRD measurements we used in this study: asymmetric out-of-plane ($2\theta$scan) XRD and in-plane XRD ($2\theta$ scan). For the sake of convenience, asymmetric out-of-plane XD will be referred to as out-of-plane XRD in this study. In-plane and out-of-plane XRD were used to analyze the crystal planes that are parallel and perpendicular to the surface of $HfO_2$. A diagram showing the difference between in-plane and out-of-plane XRD is shown in Fig. 2.10. Note that there is a difference between the geometry of the diffraction axis scan of the conventional out-of-plane XRD ($2\theta/\theta$) and out-of-plane XRD. The diagram highlighting the difference in the geometry of the scan-axis is shown in Fig. 2.11. In this study, all GIXRD measurements were made at an incident angle of 1.00°, otherwise stated. We intentionally conduct GIXRD measurements at a relatively large incident angle to analyze the properties of the whole films rather than just the interfacial/surface properties.

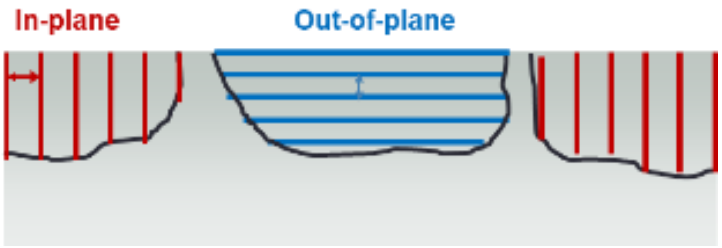


Fig. 2.10 Diagram showing the difference between crystal planes that are parallel and perpendicular to the surface of $HfO_2$. The in-plane and out-of-plane crystal planes can be detected by in-plane and out-of-plane XRD, respectively.

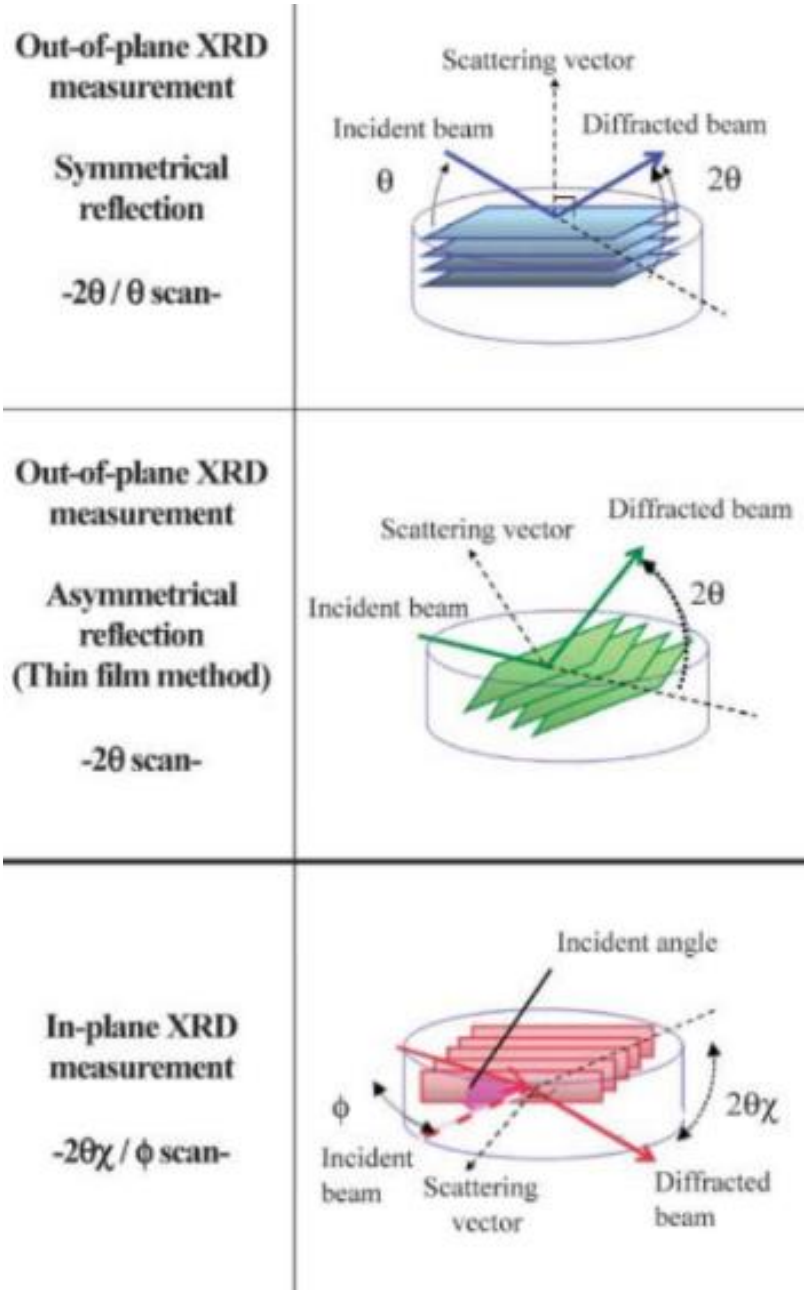


Fig. 2.11 Schematic diagram of geometries different X-ray diffraction scanning axis [27].

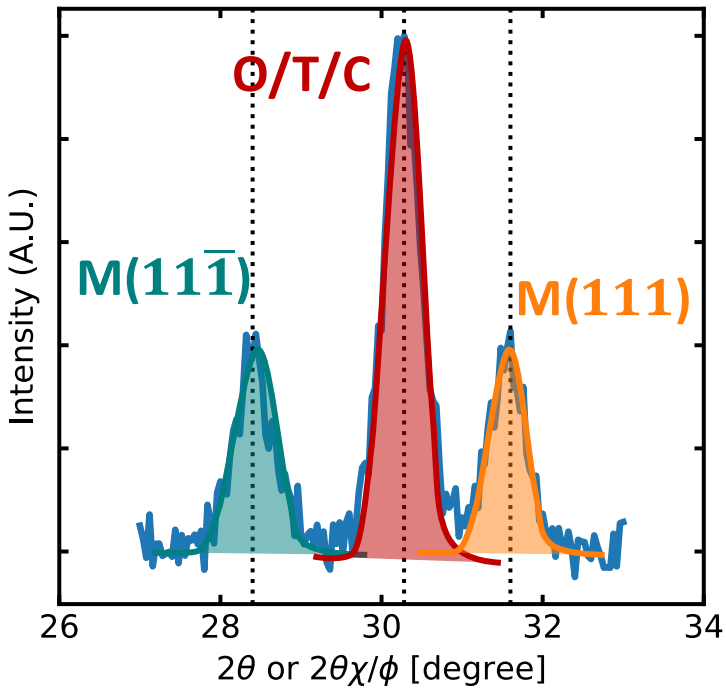


Fig. 2.12 An XRD pattern of $HfO_2$ showing the three characteristics used in this study. The $r_{o,t,c}$ can be estimated from the ratio of the area under the O/T/C peak to the total area.

An example of an XRD pattern (either in-plane or out-of-plane) of $HfO_2$ is shown in Fig. 2.12. The XRD pattern highlights the three characteristic peaks of $HfO_2$ that are used in this study: M(11$\bar{1}$), higher-symmetric (O/T/C), and M(111) peaks. Due to the similarity in the crystal structure of O-, C-, and T-phases and are not distinguished by XRD, they are categorized as the O/T/C phase.

As an indication of the volume ratio of the O/T/C ($r_{o,t,c}$), we estimated $r_{o,t,c}$ from the ratio of the area under the O/T/C peaks to the total area under the three peaks. The $r_{o,t,c}$ was estimated using the following equation:

$$r_{o,t,c} = \frac{A_{O/T/C}}{A_{M(11\bar{1})} + A_{O/T/C} + A_{M(111)}} \tag{2.4}$$

where $A_{M(11\bar{1})}$, $A_{O/T/C}$, and $A_{M(111)}$ are the area under the M(11$\bar{1}$), O/T/C, and M(111) peaks, respectively. To indicate that the phase transformation has taken place after the waking-up, the $r_{o,t,c}$ can be estimated both before and after the waking-up. In the next section (Section 2.2.3), we will describe how FE-$HfO_2$ can wake up – *i.e.*, by electric field cycling.

## 2.2.3 Electrical Characterization of Ferroelectric Materials

The characterization of ferroelectric properties is fundamentally based on Sawyer-Tower Circuit [30]. The system for characterizing the ferroelectric properties is supplied by TOYO Corporation (TOYO FCE-1A). **Electric field cycling** measurement was to simulate electrical pulses during a typical device operation and to characterize the waking-up effect in ferroelectric $HfO_2$. The schematic of a typical pulse sequence is shown in Fig. 2.13. An example of I-V and P-V characteristics during an electric field cycling is shown in Fig. 2.14. An example of the switchable polarization ($P_{sw} = P_r^+ - P_r^-$) during electric field cycling is shown in Fig. 2.15. Note that the measured pulses and the cycling pulses can be set separately. We generally applied $\pm$ 2.67 MV/cm at the frequency of 20 kHz for the cycling pulses (if not stated otherwise) to prevent hard dielectric breakdown. The measured pulses, however, were made at 4 MV/cm (10 kHz) to obtain saturated $P_{sw}$.

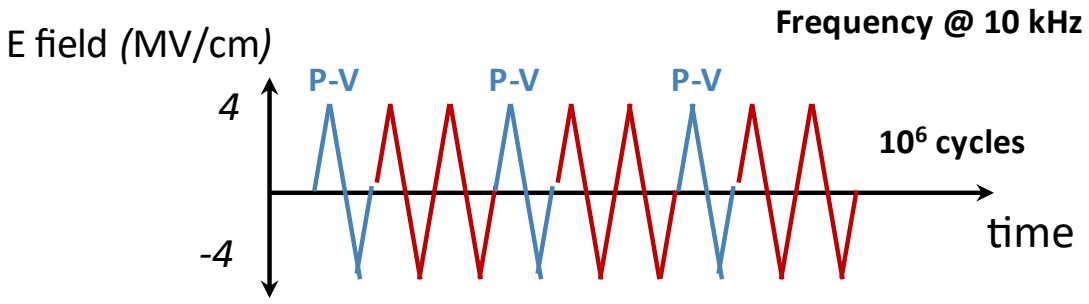


Fig. 2.13 The schematic of the pulse sequence in a typical electric field cycling measurement.

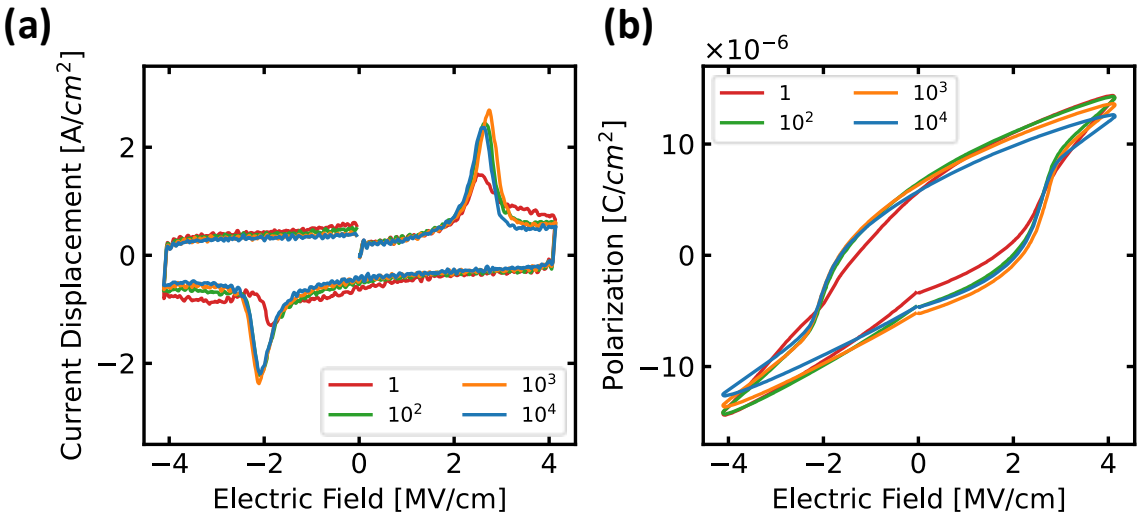


Fig. 2.14 Examples of (a) Current-voltage (I-V) and (b) polarization-voltage (P-V) characteristics of a 30 nm thick FE-$HfO_2$.

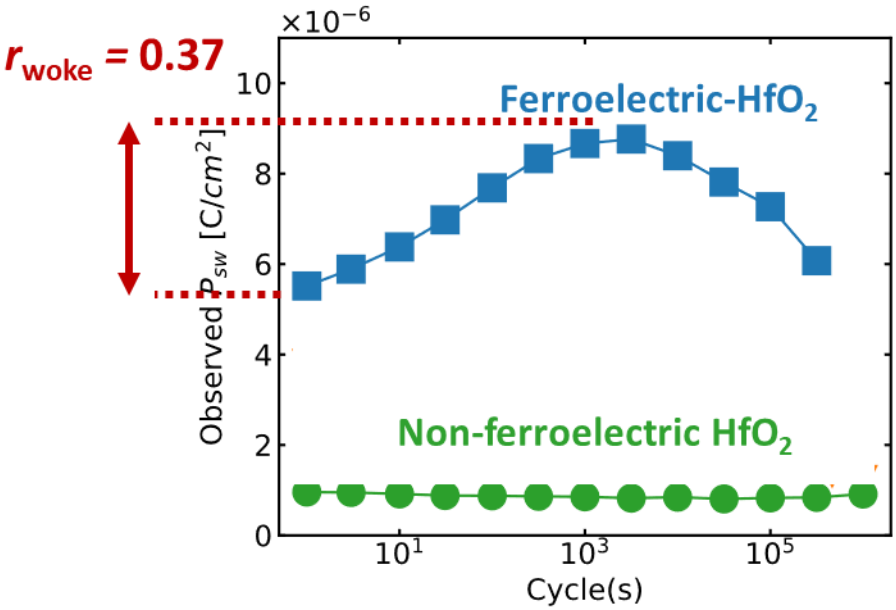


Fig. 2.15 An example of the change in switchable polarization ($P_{sw}$) during electric field cycling.

In this study, we quantify the waking-up of spontaneous polarization using the woke-up ratio ($r_{woke}$),

$$r_{\text{woke}} = \left(P_{\text{max}} - P_{\text{printine}}\right)/P_{\text{max}} \tag{2.5}$$

where $P_{pristine}$ and $P_{max}$ are the $P_{sw}$ at the pristine stage and the maximum $P_{sw}$ during electric field cycling, respectively.

## 2.2.4 DC-Bias stressing

In Chapter 6, we will be investigating the impact of charge injection on the waking-up of the spontaneous polarization in FE-$HfO_2$. DC-bias stressing was used to intentionally inject electrons from either the top or the bottom interfaces. Technically, a DC-bias stress test is simply a modified version of a classical Time-Dependent dielectric breakdown (TDDB) test. During a DC-bias stressing, the amount of the injected charges ($Q_{inj}$) was estimated from the change in current density between the input and the output. Schematics of the pulse sequence and charges that were injected are shown in Fig. 2.16. A constant positive or negative DC bias is applied and held on the capacitor for a certain period before a single pulse of $\pm$3 MV/cm at a frequency of 10 kHz was made to obtain the P-V and I-V characteristics of FE-$HfO_2$. After that, a DC-bias and a single pulse of $\pm$4 MV/cm was alternative until the dielectric break down. During each DC-bias, the period of the biasing was increased by a factor of 10 compared to the previous DC-bias.

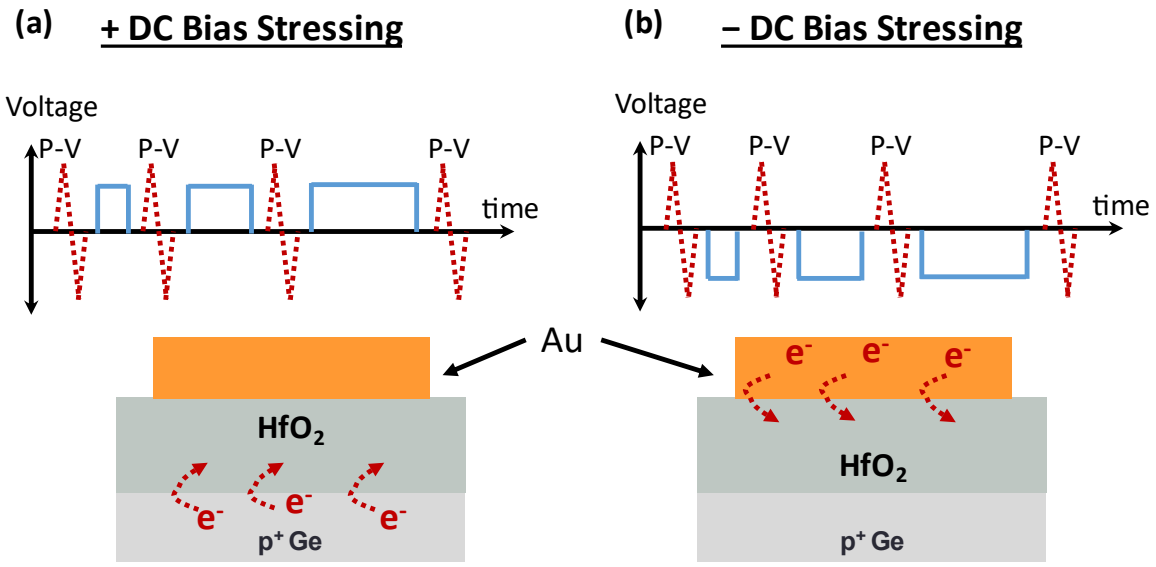


Fig. 2.16 Schematics of the pulse sequence and how charges were injected in an (a) positive and (b) negative DC-bias stressing

# Chapter 3 Temperature Change-Induced the Change in Spontaneous Polarization in Dielectric Interfaces

# 3.1 Introduction

In this chapter, we would like to extract the temperature dependences of the spontaneous polarization at several dielectric interfaces and postulate a model that can explain the extracted temperature dependences. Several models have already been purposed to explain the magnitude and the direction of the spontaneous polarization at several dielectric interfaces (**dipole layer strength,** $\boldsymbol{\varphi_{dipoel}}$) at room temperature [6]–[8], [10], [31], [32]. So far, the formation mechanisms of several interface dipole layers have already been well investigated. We chose four interfaces, **$Al_2O_3/SiO_2$, $Y_2O_3/SiO_2$, MgO/$SiO_2$**, and **MgO/$Al_2O_3$** interfaces, to represent the general dielectric interfaces that are likely to be found in a gate dielectric. We summarize three models that are widely used to explain the formation of interface dipole layers at several dielectric interfaces.

## 3.1.1 Formation Mechanisms of Interface Dipole Layers

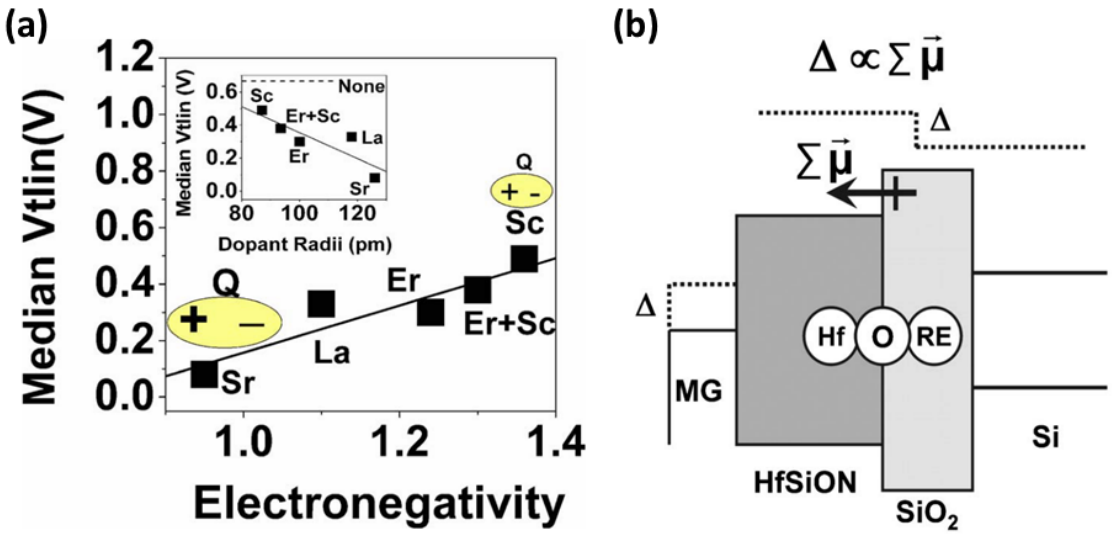


Fig. 3.1 (a) The correlation between the median threshold voltage ($V_{tlin}$) and the electronegativity of the rare earth. The insert shows median $V_{tlin}$ also varies with dopant radii. (b) Energy band diagram showing that the shift the band alignment ($\Delta$) is proportion to the magnitude of the dipole moment ($\vec{\mu}$) due to the formation of Hf-O-RE bonds [32].

**Electronegativity difference model** [6], [32] - The difference in electronegativity of atoms across dielectric interfaces has been examined to explain the magnitude of the spontaneous polarization of several interfaces. A thin layer of rare earth (RE) oxide was used to doped the HfSiON layer in n-type channel field-effect transistors. The study found that the shift in the threshold voltage ($V_{th}$) seems to show a strong correlation with dopants electronegativity (EN) and

ionic radii [32]. Fig. 3.1(a) shows a correlation between the shift in $V_{th}$ and the EN of the RE-oxide. The formation of the dipole layers was explained by the diffusion of RE metal to the HfSiON/$SiO_2$ interface to formed a Hf-O-RE bond at the interface. Because of the difference in the EN, the Hf-O-RE bonds can result in a layer of permanent dipole moments. Fig. 3.1(b) shows that the Hf-O-RE bond forms a permanent dipole moment across the HfSiON/$SiO_2$ interface, and the magnitude of the dipole moment is proportional to the EN of the RE metal. Later, this model was also supported by theoretical simulation for high *k*/$SiO_2$ interfaces [6].

**Oxygen density difference model** [8] – This model considers the relative difference in the areal oxygen density at several high-*k*/$SiO_2$ interfaces. Fig. 3.2 (a) and (b) show the reported shifts in $V_{fb}$ in several high-*k*/$SiO_2$ interface dipole layers and Normalized oxygen density compared to $SiO_2$, respectively. The figures show that the shift in the $V_{fb}$ of several MOS capacitors corresponds to the difference in the areal oxygen density at high-*k*/$SiO_2$ interfaces. The schematic diagram that summarizes the formation of dipoles at high-*k*/$SiO_2$ interfaces due to the difference in areal oxygen density is shown in Fig. 3.3. Due to the difference in the oxygen densities in the interface, there is a tendency for a microscopic displacement of oxygen atoms across the interface. If oxygen atoms are considered to have a partial negative charge, then the displacement of oxygen atoms creates an imbalance of charges at the interface. This imbalance of charges can be visualized as a dipole forming between high-*k* and $SiO_2$ layers. IN this study, the $Al_2O_3$/$SiO_2$ and $Y_2O_3$/$SiO_2$ interfaces were chosen to represent conventional high-*k*/$SiO_2$ interfaces that are formed via the atomic displacement of oxygen atoms at the interface.

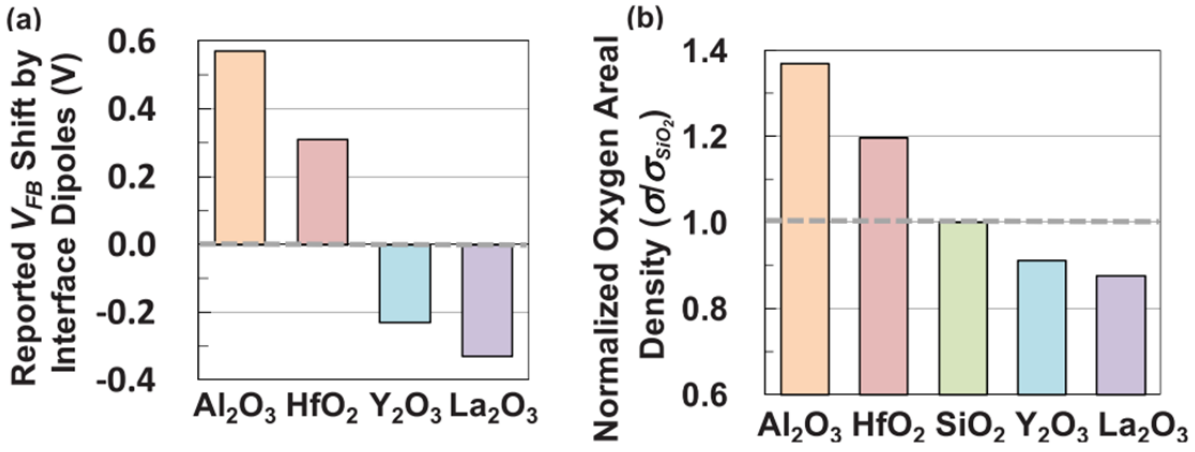


Fig. 3.2 (a) Reported shifts in the $V_{fb}$ of several MOS capacitors with high-*k*/$SiO_2$ interfaces. (b) The normalized areal density of oxygen atoms compared to $SiO_2$ [8].

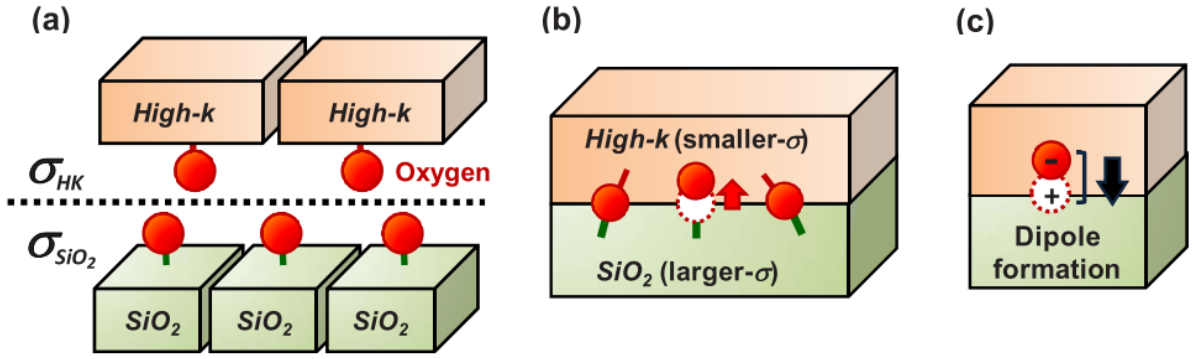


Fig. 3.3 Schematics of the formation of dipoles due to the difference in the areal oxygen density at several high-*k*/$SiO_2$ interfaces. (a) The difference in the areal oxygen density before the high-*k* oxide and $SiO_2$ are in contact. (b) due to the relative difference in the oxygen density at the interface, there is a tendency for oxygen atoms to displace across the interface. (c) If oxygen atoms are assumed to have a partial negative charge, the displacement of oxygen atoms can be visualized as dipole forming at the high-*k*/$SiO_2$ interface [8].

**Cation Migration** [7], [10], [33] – This model considers the difference in cation migration due to the reactivity of interfaces on top of the oxygen density difference model. When an interface is formed (in this case high-*k*/$SiO_2$ interfaces), the total free energy at the interface must be minimized via three approaches: chemical reaction, structural deformation, and electrical potential energy. When a layer of dipoles is formed, the total energy is expected to increase due to the increase in electrical potential. The schematic of this model can be found in Fig. 3.4. For an abrupt interface with high reactivity, the minimization of energy takes place via cation migration to reduce the reactivity of the interface. This migration of cation can then be visualized as a dipole similarly to the oxygen density difference model. For a less reactive interface or an interface that forms a stable silicate interlayer, a fewer number of cations can migrate through the interface and the total energy was minimized through structural relaxation. This model was used to explain the formation of interface dipole layers at MgO/$SiO_2$ and MgO/$Al_2O_3$ interfaces.

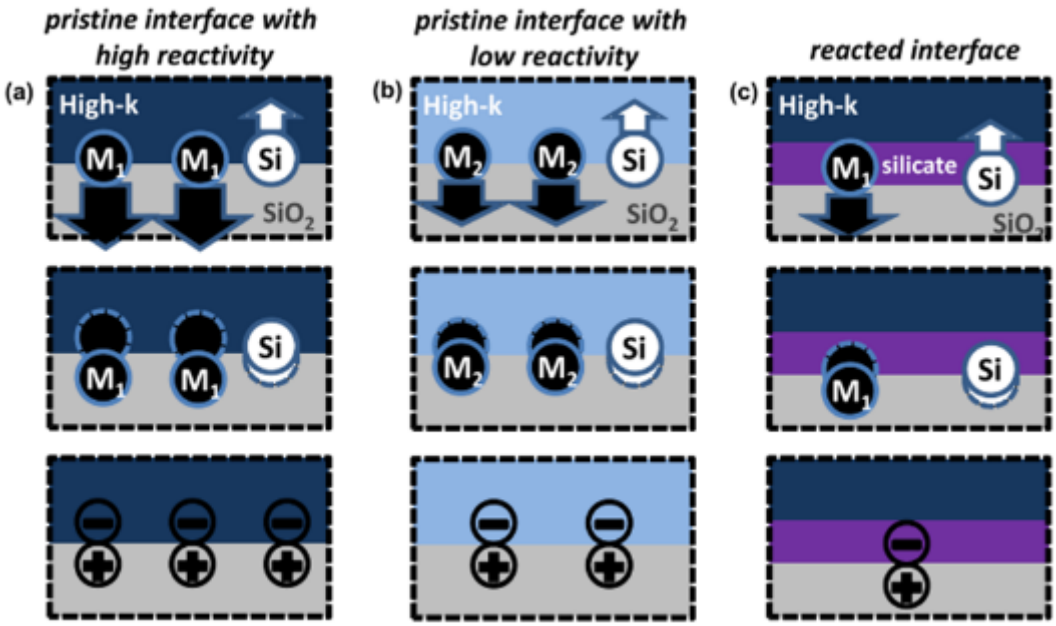


Fig. 3.4 Schematics of cation migration at (a) an abrupt interface with high reactivity, (b) an abrupt interface with low reactivity, and (c) an interface after a chemical reaction forming a layer of dipoles at high-*k*/$SiO_2$ interfaces [10].

## 3.2 Temperature Dependences of the Spontaneous Polarization in Dielectric Interfaces

Four dielectric interfaces were used for the investigation of temperature dependences of the spontaneous polarization in dielectric interfaces: **$Al_2O_3/SiO_2$, $Y_2O_3/SiO_2$, $MgO/SiO_2$**, and **$MgO/Al_2O_3$** interfaces, as shown in Fig. 3.5. $Al_2O_3/SiO_2$ and $Y_2O_3/SiO_2$ interfaces are used to represent conventional high-*k* oxide interfaces [8]. $MgO/SiO_2$ and $MgO/Al_2O_3$ interfaces are used to represent reactive high-*k* oxide [7] and high-*k*/high-*k* [10] interfaces, respectively. The detail of the fabrication process and conditions can be found in Section 2.1.1.

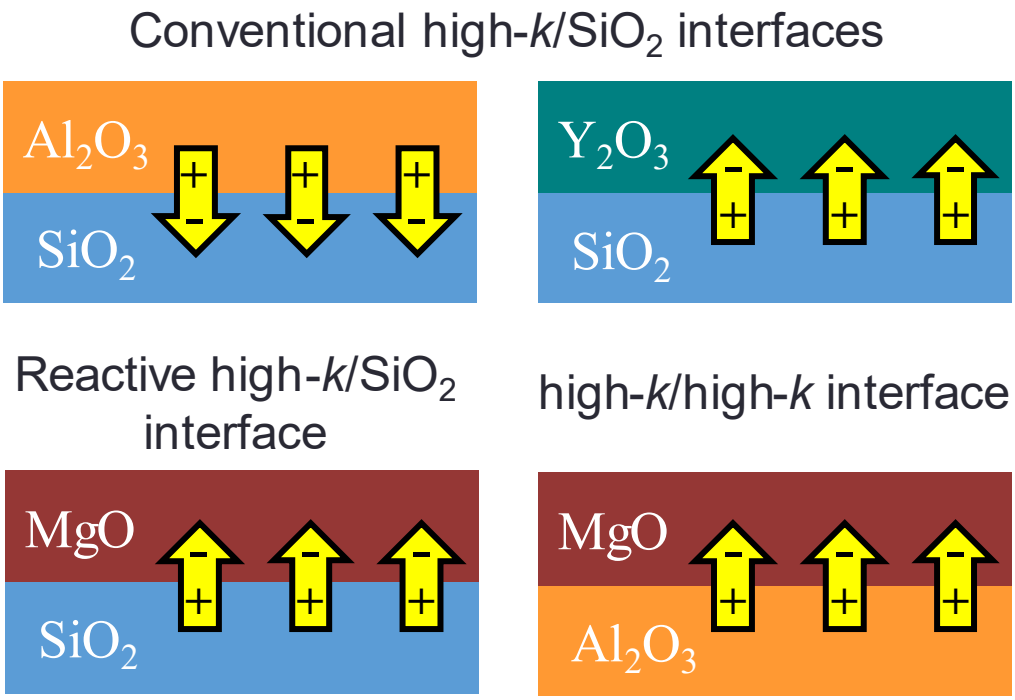


Fig. 3.5 The chosen dielectric interfaces for the investigation of temperature effect on the polarization of dielectric interfaces.

To investigate the temperature dependences of the spontaneous polarization in dielectric interfaces, we first extract the spontaneous polarization of the dielectric interface at different temperatures. For the sake of convenience and to avoid lengthy-phrase like 'spontaneous polarization of the dielectric interface', the phase will be referred to as – **interface dipole layer strength ($\varphi_{dipole}$)**. The general description of the extraction process of the $\varphi_{dipole}$ can also be found in Section 2.1.3.

The $\varphi_{\text{dipole}}$ at each temperature was extracted by comparing the flatband voltage ($V_{\text{fb}}$) of the sample MOS-capacitor (Sample-Cap) with the dielectric interface to a reference MOS-capacitor (Reference-Cap) without the dielectric interface. the extraction process of $\varphi_{\text{dipole}}$ at $Al_2O_3/SiO_2$ is expected to translate to other dielectric interfaces as well. The schematic of Sample-Cap and Reference-Cap are shown in Fig. 3.6. Here, we only discuss the extraction of $\varphi_{\text{dipole}}$ at $Al_2O_3/SiO_2$ interfaces, but a similar discussion can also be translated to other interfaces as well.

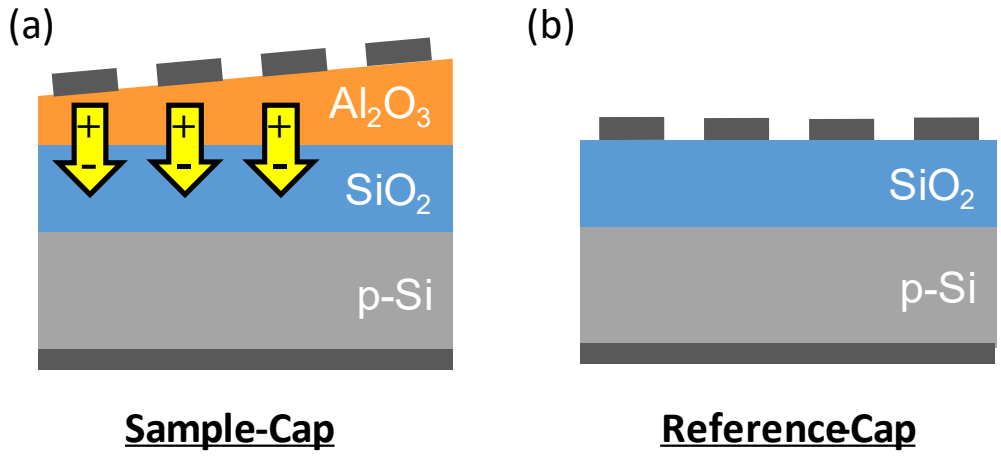


Fig. 3.6 Schematics of (a) a sample MOS capacitor (Sample-Cap) with the dielectric interface and (b) a reference MOS capacitor (Reference-Cap) without the dielectric interface.

From Eq. (2.2), the $V_{\text{fb}}$ of a Sample-Cap as a function of temperature can be explained by the following equation:

$$V_{\text{fb}}(T) = \varphi_{\text{ms}}(T) - Q_1(T)\frac{t_{\text{SiO2}}}{\varepsilon_{\text{SiO2}}} - \big(Q_1(T) + Q_2(T)\big)\frac{t_{\text{Al2O3}}}{\varepsilon_{\text{Al2O3}}} + \varphi_{\text{dipole}}(T). \qquad (3.1)$$

Note that Eq. (3.1) is modified from Eq. (2.2), where the variables are presented as a function of temperature and high-*k* oxide is replace by $Al_2O_3$ for easier comparison.

To extract the $\varphi_{\text{dipole}}$, we must exclude other factors, except $\varphi_{\text{dipole}}$, that contributes to the determination of the $V_{\text{fb}}$ in Sample-Cap. Examples C-V curves of a Sample-Cap and a Reference-Cap measured at several temperatures are shown in Fig. 3.7(a) and (b), respectively. The C-V curves of both Sample-Cap and Reference-Cap shifted positively with the rise in temperatures from 100 K to 400 K. For Reference-Cap, Fig. 3.7(b), the $V_{\text{fb}}$ is described only by the first and second terms in Eq. (2.2), which are $\varphi_{\text{ms}}$ and the effect of fixed charges at $SiO_2/Si$ interfaces. It is reasonable to assume that the fixed charge density at the $SiO_2/Si$

interfaces and the temperature dependence of the Au work function is negligibly small $\varphi_{ms}(T) \cong \varphi_m(T) - \varphi_s(T)$. Then, it can be inferred that the observed temperature-induced $V_{fb}$ shift in Reference-Cap was mainly caused by the change in the Si Fermi level.

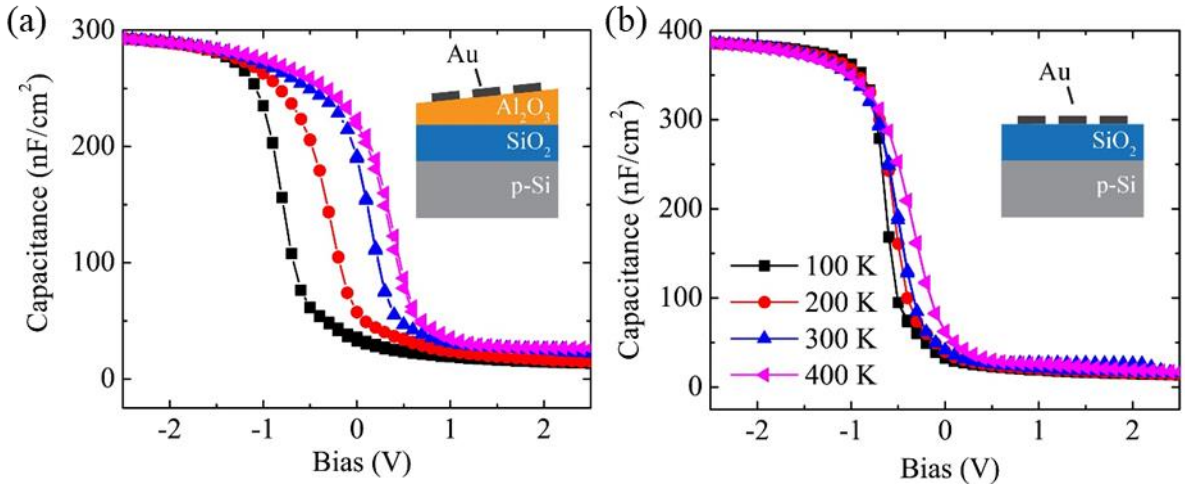


Fig. 3.7 (a) C-V curves of (a) Sample-Cap (with 5 nm-thick $Al_2O_3$) and (b) Reference-Cap measured at 1 Mhz at various temperatures.

On the other hand, the relatively large shift in the $V_{fb}$ in Sample-Cap, Fig. 3.7(a), is comprised of four factors corresponding to the four terms in Eq. (3.1):

- Temperature effect of the Si Fermi level – $\varphi_s$ ($T$),
- Temperature-induced changes in fixed charge densities at the $SiO_2$/Si interface –$Q_1$ ($T$),
- Temperature-induced changes in fixed charge densities at the $Al_2O_3$/$SiO_2$ interface – $Q_2$ ($T$),
- Temperature dependence of the $Al_2O_3$/$SiO_2$ interface dipole layer strength – $\varphi_{dipole}$ ($T$).

The extraction of $\varphi_{dipole}$ was done by excluding other factors except $\varphi_{dipole}$ itself. In the following texts, the third term in Eq. (3.1) is first eliminated, and later the first and second terms in Eq. (3.1) are eliminated.

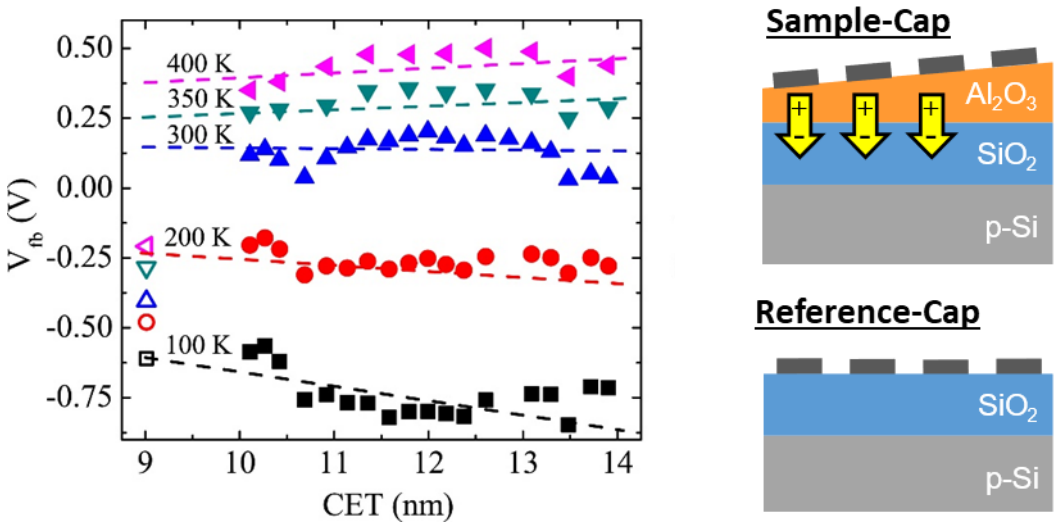


Fig. 3.8 $V_{fb}$ cs capacitance equivalent thickness (CET) of the Sample-Cap with different $Al_2O_3$ film thickness and its Reference-Cap, indicated by the solid and open symbols respectively. CET is an equivalent thickness of $SiO_2$ that would result in the same capacitance under an accumulation of charges at Si surfaces.

Series of $V_{fb}$ in Fig. 3.8 was obtained from various $Al_2O_3$ thicknesses in the Sample-Cap and its Reference-Cap at several temperatures indicated by the solid and open symbols, respectively. The thickness of the top $Al_2O_3$ was extrapolated to zero ($t_{Al2O3} \rightarrow 0$), eliminating the third term in Eq. (3.1). The linear relationship between the $V_{fb}$ and *CET* of sample (A) indicates that bulk fixed charges have an insignificant contribution to the $V_{fb}$ shift. The densities of total interface fixed charges (*i.e.* $Q_1$ +$Q_2$) from 100 K to 400 K can be estimated from the slope of the fitting lines in Fig. 3.8. Note that the majority of the total interface fixed charge is expected to originate from the $Al_2O_3/SiO_2$ interface. In this temperature range, the areal density of fixed charges was estimated to be in the order of $10^{11}$ $cm^{-2}$, which is too small to explain the observed temperature dependence of $V_{fb}$.

Fig. 3.9(a) shows the imaginary $V_{fb}$ $V_{fb,img}$ of Sample-Cap after the removal of the third term in Eq. (3.1), together with the $V_{fb}$ of it Reference-Cap at different temperatures. By subtracting the $V_{fb}$ of Reference-Cap from the $V_{fb,img}$ of Sample-Cap and, the 'intrinsic' component of $\varphi_{ms}$, and the fixed charges at the $SiO_2$/Si interface (the first and second terms in Eq. (3.1)), were eliminated, and $\varphi_{dipole}$ at $Al_2O_3/SiO_2$ interfaces can be finally quantified. By repeating the process at various the temperature dependence of the $\varphi_{dipole}$of the dielectric interface (in this case – $Al_2O_3/SiO_2$ interfaces) can be obtained, as shown in Fig. 3.9(b).

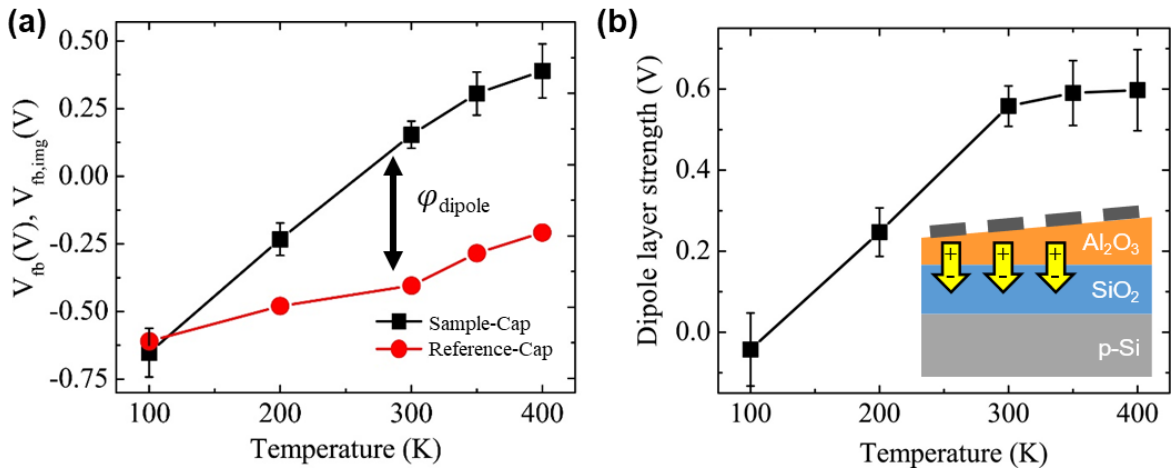


Fig. 3.9 (a) The $V_{fb,img}$ of Sample-Cap and its Reference-Cap at different temperatures. (b) Temperature dependence of the extracted dipole layer strength at $Al_2O_3/SiO_2$ interfaces. The error bars in both (a) and (b) are from the ambiguity of the fitting lines in Fig. 3.8.

The relationship between $V_{fb}$ and CET for Sample-Cap with $Al_2O_3/SiO_2$, $Y_2O_3/SiO_2$, $MgO/SiO_2$, and $MgO/Al_2O_3$ interfaces and their Reference-Cap is shown in Fig. 3.10. More detail on the extraction process of the temperature dependence of $\varphi_{dipole}$ at dielectric interfaces , and the detailed analysis of temperature effect on $Al_2O_3/SiO_2$ and $Y_2O_3/SiO_2$ interfaces can also be found in Ref. [34]. The more detail of temperature dependence of $\varphi$ at $MgO/SiO_2$ and $MgO/Al_2O_3$ interfaces can also be found in Ref. [35].

Fig. 3.11(a) summarized the temperature dependences of $\varphi_{dipole}$ at $Al_2O_3/SiO_2$, $Y_2O_3/SiO_2$, $MgO/SiO_2$, and $MgO/Al_2O_3$ interfaces. In $Al_2O_3/SiO_2$ and $Y_2O_3/SiO_2$ interfaces, almost no dipole layers were observed at 100 K. With the increase in temperature, the $\varphi_{dipole}$ of $Al_2O_3/SiO_2$ and $Y_2O_3/SiO_2$ interfaces increased approximately at the rate of +2.2 $mV{\cdot}K^{-1}$ and -0.7 $mV{\cdot}K^{-1}$, respectively, from 100 K to 400 K. On the other hand, clear negative dipoles were observed in $MgO/SiO_2$ and $MgO/Al_2O_3$ interfaces at 150 K. The $\varphi_{dipole}$ of MgO/SiO2 interfaces decrease approximately at the rate of +1.5 $mV{\cdot}K^{-1}$ with the rise in temperature from 150 K to 300 K. In contrast to $Al_2O_3/SiO_2$, $Y_2O_3/SiO_2$, and $MgO/SiO_2$ interfaces, the $\varphi_{dipole}$of $MgO/Al_2O_3$ remains fairly stable with the temperature change. The relative stable temperature dependence of $MgO/Al_2O_3$ compared to other high-*k*/$SiO_2$ interfaces could suggest the difference in the mechanism that determines the temperature dependence of $\varphi_{dipole}$ or even formation of high-*k*/high-*k* interfaces. The average temperature dependences of $\varphi_{dipole}$ at $Al_2O_3/SiO_2$, $Y_2O_3/SiO_2$, $MgO/SiO_2$, and $MgO/Al_2O_3$ interfaces are summarized in Fig. 3.11(b).

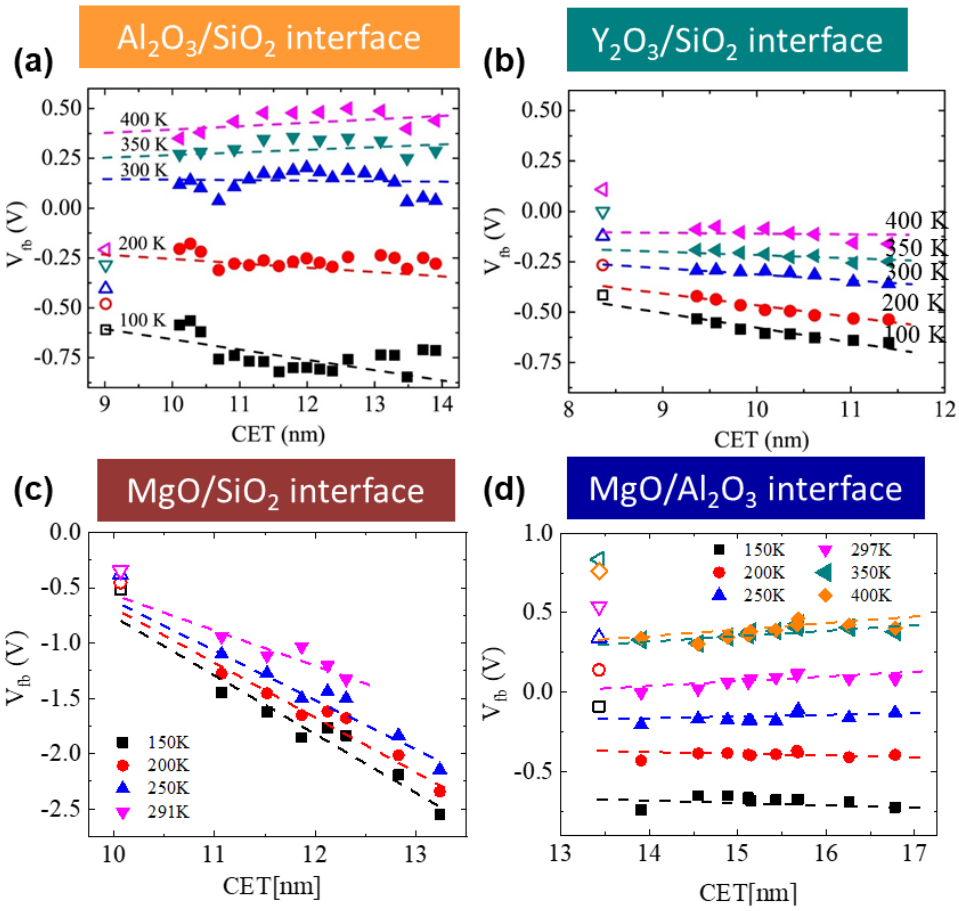


Fig. 3.10 $V_{fb}$ vs CET of Sample-Cap(s) with (a) $Al_2O_3/SiO_2$, (b) $Y_2O_3/SiO_2$, (c) $MgO/SiO_2$, and (d) $MgO/Al_2O_3$ interfaces and their Reference-Cap(s).

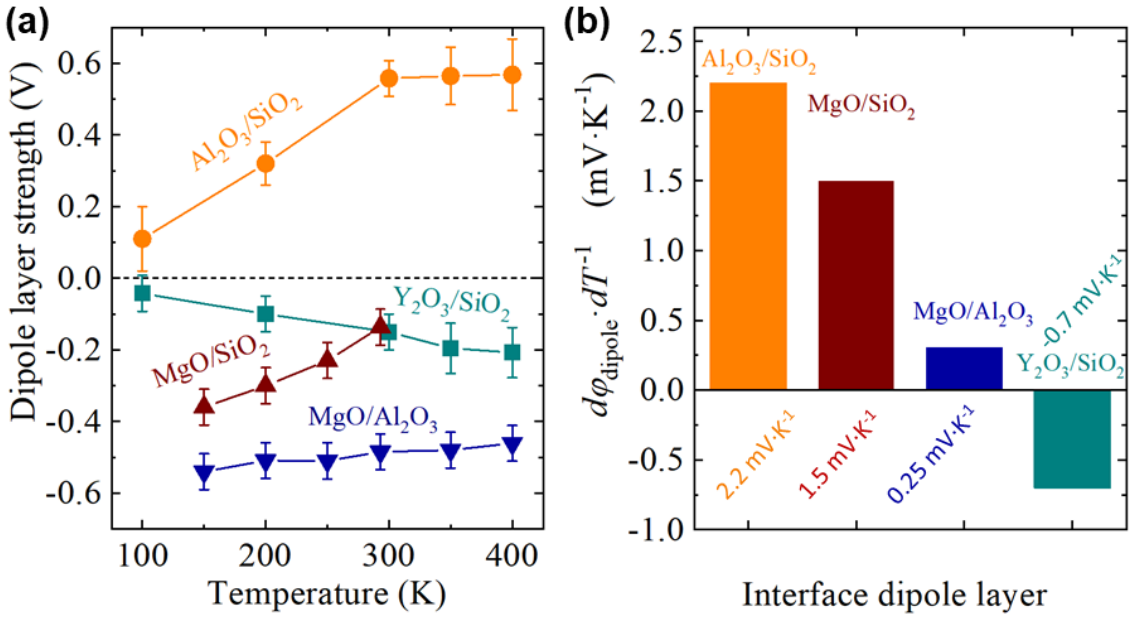


Fig. 3.11 (a) The temperature dependences of $\varphi_{dipole}$ at $Al_2O_3/SiO_2$, $Y_2O_3/SiO_2$, $MgO/SiO_2$, and $MgO/Al_2O_3$ interfaces. (b) The average temperature dependence of the $\varphi_{dipole}$ calculated from (a).

Generally, a dipole layer strength is proportional to the dipole length (*i.e.*, the length of the charge separation) and the number of the dipole moments,

$$\varphi_{\mathrm{dipole}} \cong \frac{qN_{dipole}d_{\mathrm{eff}}}{\varepsilon_{int}}, \tag{3.2}$$

where $q$, $N_{\mathrm{dipole}}$, $\boldsymbol{d_{\mathrm{eff}}}$, and $\varepsilon_{\mathrm{int}}$ are the elementary charge, the areal dipole density, the **effective dipole length**, and the permittivity of the interface, respectively. Note that $\varepsilon_{\mathrm{int}}$ can be approximated to be the geometric mean of bulk $\varepsilon_{\mathrm{high\text{-}}k}$ and $\varepsilon_{\mathrm{SiO2}}$., and $d_{\mathrm{eff}}$ does not necessarily equal to the physical length of the dipole moment, as it will be discussed later in Section 3.3. If the $q$ and $N_{\mathrm{dipole}}$ was assumed to be constant with temperature, then the change in $d_{\mathrm{eff}}$ can directly result in the change in the $\varphi_{\mathrm{dipole}}$.

We first considered that the atom-to-atom distance of a dipole moment can be physically lengthened due to the thermal expansion of the two oxides layers at the interface. The schematic on how the lengthening of the physical distance of dipole moments could increase the $\varphi_{\mathrm{dipole}}$.is shown in Fig. 3.12. If we assume that the thermal expansion could have a direct effect on the physical distance of a dipole moment, then the thermal expansion coefficient of the oxides in the order of $10^{-7}$ to $10^{-5}$ $K^{-1}$, as shown in Table 3.1, can only cause a change in the $\varphi_{\mathrm{dipole}}$ by ~5.0 $\mu V \cdot K^{-1}$, at maximum. By comparing to the experimentally observed temperature dependence in Fig. 3.11(b), which is in the range of 0.25 – 2.2 $mV \cdot K^{-}$, it is clear that the thermal expansion is to small to explained our experimental data. For this reason, we discarded the assumption that the $d_{\mathrm{eff}}$ can be physically lengthed by the thermal expansion of the oxides and consider that the $d_{\mathrm{eff}}$ is not just only limited by the physical distance of a dipole moment. In the next section, we will further investigate and discuss that the temperature dependence that we had observed in Fig. 3.11 can be explained by the screening ability of oxides layers near the interface region.

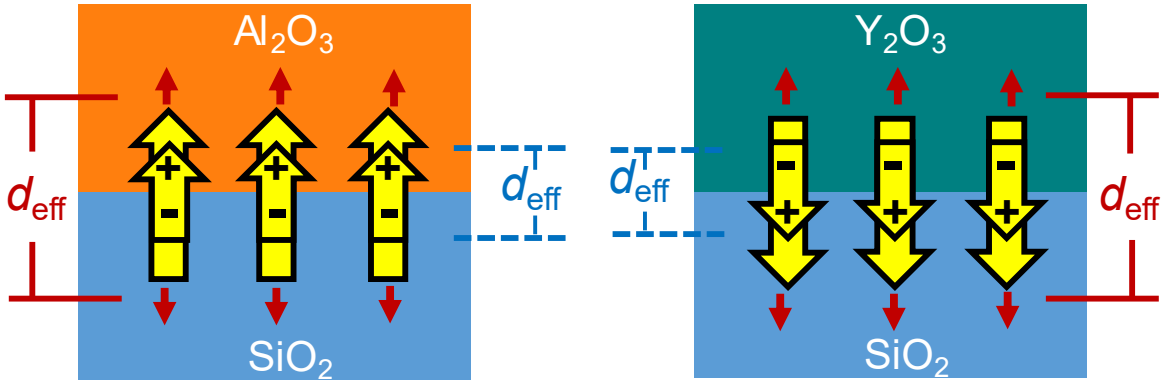


Fig. 3.12 The schematic of the increase in the effective dipole length ($d_{eff}$) by the thermal expansion of the two oxide layers at the interface. Solid-red and dashed-blue lines are $d_{eff}$ at high and low temperatures, respectively.

Table 3.1 The thermal expansion coefficient of $Al_2O_3$, $Y_2O_3$, MgO, and $SiO_2$ found in the literature [36]–[38].

| | $Al_2O_3$ | $Y_2O_3$ | MgO | $SiO_2$ |
|---|---|---|---|---|
| Therm. Exp. Coeff. [$K^{-1}$] | $10^{-6}$ | $10^{-6}$ | $10^{-5}$ | $10^{-7}$ |

## 3.3 Screening Length of Interface Dipole Layers

To explain the remarkable temperature dependence of $\varphi_{\text{dipole}}$ we had observed in Fig. 3.11, we consider that the $d_{\text{eff}}$ is not limited only by the physical distance of a dipole moment but the $d_{\text{eff}}$ could also be proportional to the **screening length ($L_s$)** of an interface dipole layer; where the $L_s$ length is a function of temperature.

Due to the relatively low density of charges in dielectric layers compared to a meal, charges are less electrostatically screened, and the $L_s$ of a dipole layer can extend much longer than the actual physical dipole length. For a given mobile charge density near the interface region ($\rho_{\text{int}}$), the $L_s$ of a charge can be generally approximated by the **Debye length ($L_D$)** [23]:

$$L_s \cong L_{\text{D}} = \sqrt{\frac{\varepsilon_{\text{int}} kT}{\rho_{\text{int}} q^2}} \tag{3.3}$$

where $\varepsilon_{\text{int}}$, $k$, and $T$ are the permittivity near the interface region, the Boltzmann constant, and the temperature, respectively. Although we can to precisely estimate the $L_s$ of an interface dipole layer without knowledge of the mobile $\rho_{\text{int}}$, we can assume that the mobile $\rho_{\text{int}}$ is in an order of fixed charges. In that range, the $L_s$ can range to sever tenths of nm. Conceptually, the $d_{\text{eff}}$ in Eq. (3.2) can be treated as proportional to $L_{\text{D}}$ in Eq. (3.3). The schematic of the $d_{\text{eff}}$ that is determined by the $L_s$ of interface dipole layers is shown in Fig. 3.13.

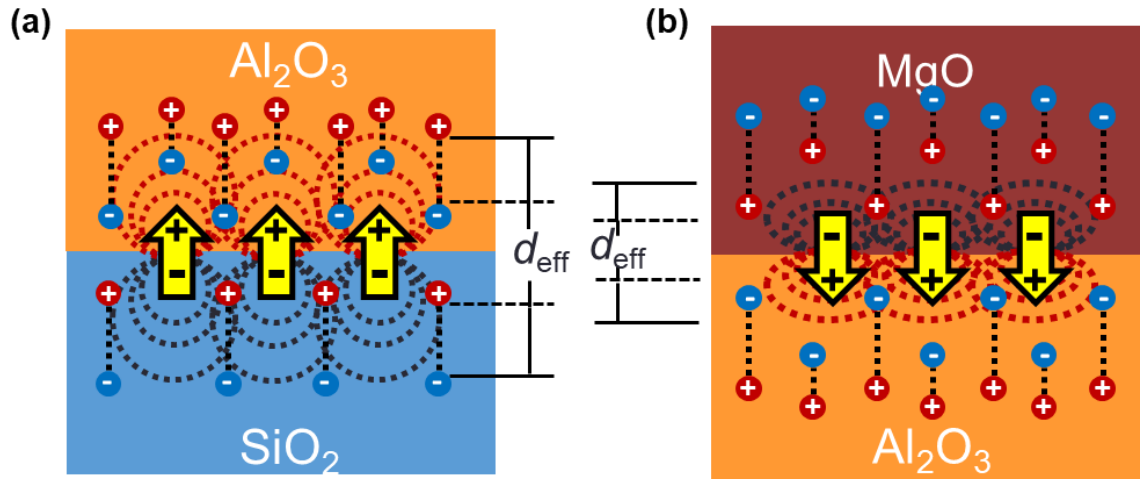


Fig. 3.13 Schematic of (a) high-$k$/$SiO_2$ and (b) high-$k$/high-$k$ interface dipole layers that are screen by the upper and lower oxide layers. At a constant temperature, the $L_s$ of an interface dipole lay could be a function of either mobile $\rho_{\text{int}}$ or $\varepsilon_{\text{int}}$. The two examples here show the screening of the interface dipole layers only by the ionic polarization of the oxides, since the mobile $\rho_{\text{int}}$ in an oxides is small and could be neglected.

By combining the two equations, we obtain an equation that can explain the temperature dependence of $\varphi_{\mathrm{dipole}}$ (that we had experimentally obtained in Fig. 3.11) as a function of temperature,

$$\begin{array}{ccccccc} y & = & & m & x & + & b \\ \downarrow & & & \downarrow & \downarrow & & \downarrow \\ \varphi_{\mathrm{dipole}} & \cong & N_{\mathrm{dipole}} & \sqrt{\frac{k}{\rho_{\mathrm{int}}}\frac{1}{\sqrt{\varepsilon_{\mathrm{int}}}}} \cdot \sqrt{T} & + & \mathrm{offset} & \end{array} \tag{3.4}$$

where 'offset' is the $\varphi_{\mathrm{dipole}}$ with $T$ = 0 K. The temperature dependence of the $\varphi_{\mathrm{dipole}}$ (Fig. 3.11) plotted as a function of $\sqrt{T}$ is shown in Fig. 3.14, and the slope of the temperature dependence corresponds to the **temperature coefficient of the $\varphi_{\mathrm{dipole}}$**.

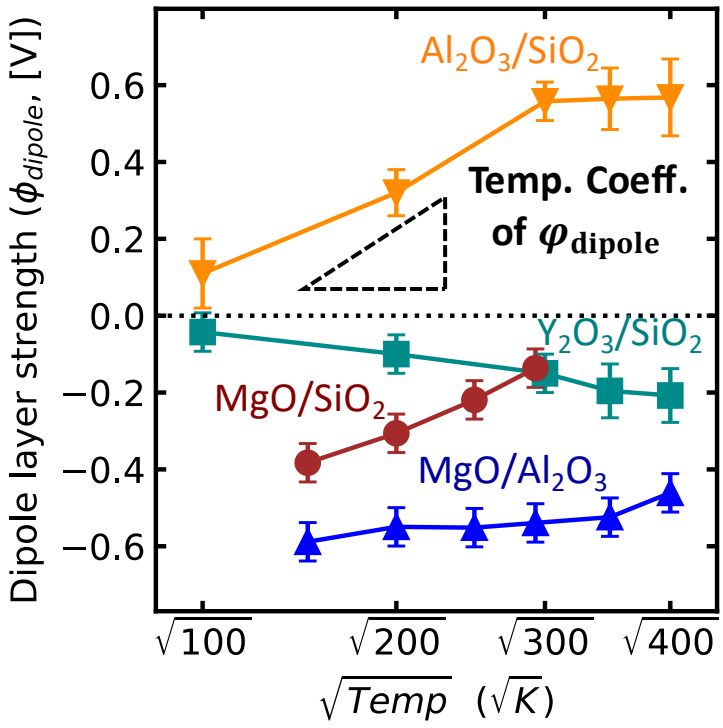


Fig. 3.14 The temperature dependences of $\varphi_{\mathrm{dipole}}$ at $Al_2O_3/SiO_2$, $Y_2O_3/SiO_2$, $MgO/SiO_2$, and $MgO/Al_2O_3$ interfaces from Fig. 3.11 plotted as a function of $\sqrt{\mathrm{temperature}}$.

We can estimate the permittivity near the interface region by taking the geometric mean of the two dielectric constants ($\varepsilon_{\mathrm{int}} = \sqrt{\varepsilon_1 \varepsilon_2}$), since the screening ability of the upper and lower oxide layers is expected to be independent of each other. The dielectric constants of the oxides used in this study are shown in Table 3.2. If we assume that the $N_{\mathrm{dipole}}$ and mobile $\rho_{\mathrm{int}}$ in each interface are in the same order, then the magnitude of the temperature coefficient of $\varphi_{\mathrm{dipole}}$

can be explained by the screening of the $d_{\text{eff}}$ by the $\varepsilon_{\text{int}}$. The magnitude of the experimentally observed temperature coefficient of $\varphi_{\text{dipole}}$ plotted as a function of $1/\sqrt{\varepsilon_{\text{int}}}$ is shown in Fig. 3.15. From the figure, it is clear that the temperature coefficient of $\varphi_{\text{dipole}}$ can be universally explained by the screening ability of the upper and the lower oxide layers. It is important to note that our model on the screening length can only explain the magnitude of the temperature coefficient of $\varphi_{\text{dipole}}$ and does not cover the swith in the polarity of an interface dipole layer with the temperature change. However, we do know that an offset, as shown in Eq. (3.4), suggesting there is a new phenomenon to be further investigated.

Table 3.2 Dielectric constants report in the literature [2].

| | $SiO_2$ | $Al_2O_3$ | MgO | $Y_2O_3$ |
|---|---|---|---|---|
| Dielectric constant ($\varepsilon$) | 4 | 8-9 | 9-10 | 15 |

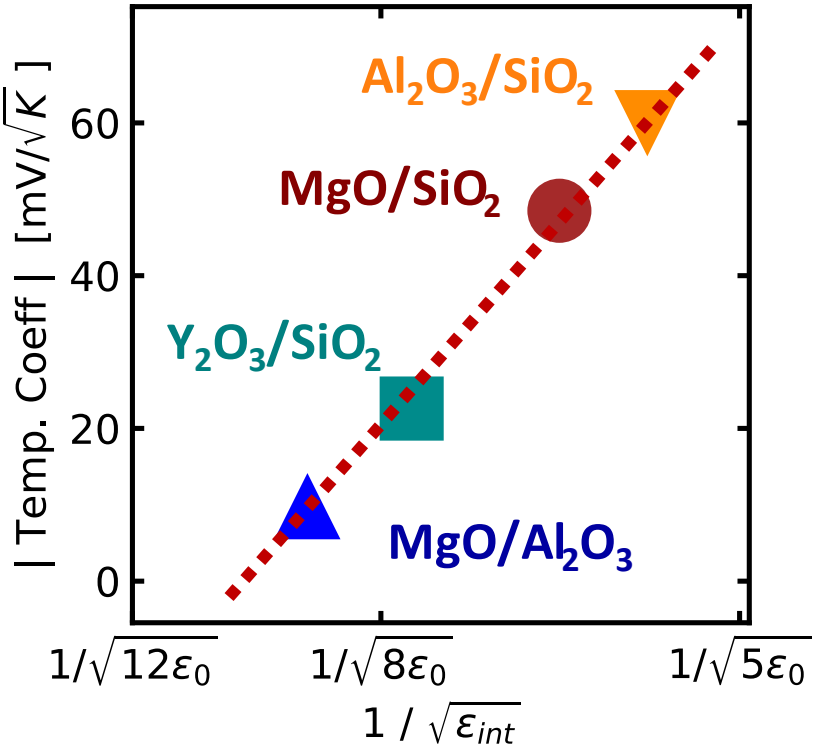


Fig. 3.15 The relationship between the temperature coefficient of $\varphi_{\text{dipole}}$ extrected from Fig. 3.14 and the $\varepsilon_{\text{int}}$ estimated from the geometric mean of the dielectric constant of the upper and lower oxide layers.$\varepsilon_0$ is the permittivity of vacuum.

## 3.4 Summary

We investigated the temperature dependence of $\varphi_{\mathrm{dipole}}$ at several dielectric interfaces in order to postulate a model that can universally explain the temperature dependence of $\varphi_{\mathrm{dipole}}$.The temperature dependence of the spontaneous polarization at $Al_2O_3/SiO_2$, $Y_2O_3/SiO_2$, $MgO/SiO_2$, and $MgO/Al_2O_3$ interfaces were investigated from 100 K to 400 K. The spontaneous polarization at dielectric interfaces was extracted from the shift in the flatband voltage ($V_{\mathrm{fb}}$) of metal-oxide-semiconductor (MOS) capacitors with the mentioned interfaces in a multilayer-gate dielectric. The spontaneous polarization of a dielectric interface was quantified using interface dipole layer strength ($\varphi_{\mathrm{dipole}}$) by excluding the factors that contribute to the shift in the $V_{\mathrm{fb}}$ other from the $\varphi_{\mathrm{dipole}}$. By repeating the process at several temperatures, we can finally extract the temperature dependences of $\varphi_{\mathrm{dipole}}$ at several dielectric interfaces as shown in Fig. 3.11.

We found that the change in temperature significantly affects the $\varphi_{\mathrm{dipole}}$.of high-*k*/$SiO_2$ interfaces. In contrast, the $\varphi_{\mathrm{dipole}}$ of the high-*k*/high-*k* interface remain fairly constant with the temperature change. We first considered that the effective dipole length ($d_{\mathrm{eff}}$) of an interface dipole layer could be explained by the thermal expansion of the oxide layers at the interface. However, the thermal expansion of the oxide layers was too small to explain the temperature dependences of $\varphi_{\mathrm{dipole}}$ Hence, a new concept is needed to explain the temperature dependences of $\varphi_{\mathrm{dipole}}$ that were experimentally observed.

We further investigated and considered that the $d_{\mathrm{eff}}$ could be approximated by the screening length ($L_{\mathrm{s}}$) of an interface dipole layer, where $L_{\mathrm{s}}$ is a function of temperature. We quantified the magnitude of the temperature dependence using the temperature coefficient of $\varphi_{\mathrm{dipole}}$. We then estimated the permittivity near the interface region from the geometric mean of the two oxide layer's dielectric constant. Finally, we were able to postulate a model of $L_{\mathrm{s}}$ that can universally explain the experimentally observed temperature coefficient of $\varphi_{\mathrm{dipole}}$, as shown in Fig. 3.15.

# Chapter 4 Origin of the Waking-up in the Spontaneous Polarization of Ferroelectric $HfO_2$

# 4.1 Introduction

In this chapter, we would like to clarify the origin of the waking-up effect by observing both phase transformation and waking-up effect at the same scale. Currently, the possible mechanisms of the waking-up effect are known. What is unknown is which one is the dominant mechanism. To investigate the origin of the waking-up effect, it is important to understand the origin of the ferroelectricity in $HfO_2$ (*i.e.*, O-phase) and how it can be induced and stabilized with certain experimental parameters. We also summarize the current consideration on the mechanisms of the waking-up effect. Origin of Ferroelectricity in $HfO_2$

## 4.1.1 Origin of Ferroelectricity in $HfO_2$

Before the discovery of ferroelectricity in $HfO_2$, ferroelectricity was thought to exist only on perovskite oxides. So far, the source of ferroelectricity in $HfO_2$ is well understood, which is originating from the metastable orthorhombic (O) phase. [12], [39]–[42]. Although we only focus on the waking-up effect, it is important to understand the mechanism to induce and crystallize the O-phase because we expect that the factors that stabilize the O-phase will also affect the waking-up effect as well. Furthermore, in our experiments, the fabrication conditions were designed accordingly to what is already known to stabilize the O-phase.

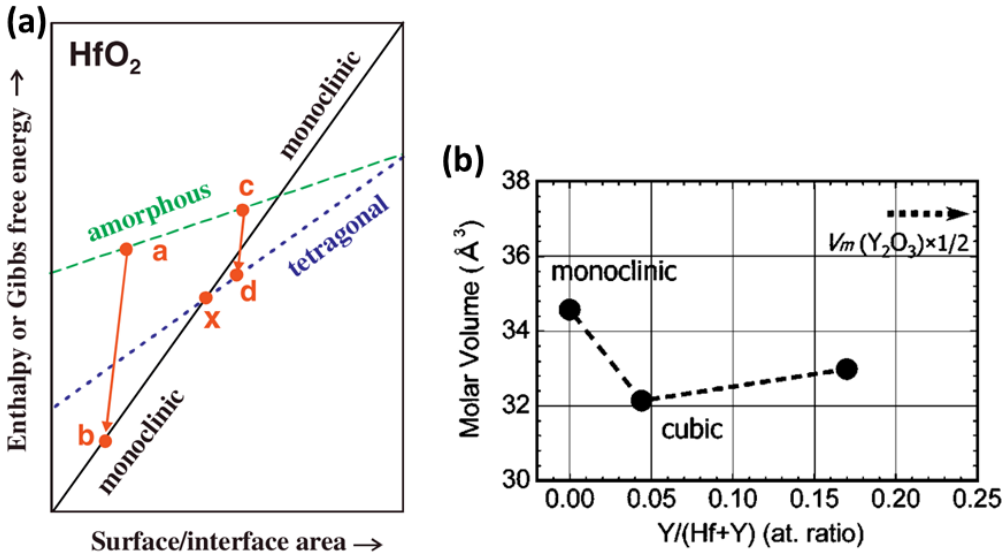


Fig. 4.1 (a) Energy profile of $HfO_2$. Path a→b corresponds to the crystallization of amorphous bulk $HfO_2$ into the M-phase. Path c→d corresponds to the crystallization of amorphous $HfO_2$ with the high surface area into the T-phase. Point x is the region where M- and T-phases can co-exist [43]. (b) Change in molar volume of $HfO_2$ by Y-doping concentration in Y-doped $HfO_2$ films [44].

In a non-ferroelectric/paraelectric bulk $HfO_2$, the structure of crystallized $HfO_2$ is a polymorph of three phases: monoclinic (M), cubic (C), and tetragonal (T) phases. At room temperature, M-phase is the most thermodynamically stable phase [45]. Whereas C- and T-phases can be found at high temperature and high pressure, respectively. It was then later found that at room temperature T-phase can also be stabilized in a thin film due to the introduction of surface energy [43], [46], [47], and the C-phase can also be stabilized by the introduction of dopants [44]. Fig. 4.1 (a) and (b) illustrate how T- and C-phase can be stabilized owing to surface energy and dopant, respectively. However, all M-, T-, and C-phases are non-polar phases; thus, they do not exhibit any ferroelectricity.

It was not until 2011, that ferroelectricity in $HfO_2$ was first discovered [12]. Evidence has pointed that the ferroelectric phase in $HfO_2$ originating from the O-phase, which was crystallized during the phase transformation from T- to M-phase [12], [39]–[42]. In other words, O-phase is a metastable phase that can be crystallized by a non-equilibrium or an incomplete phase transformation from either T- or C-phase to M-phase. The schematic of the energy profile and the different configurations in $HfO_2$ is shown in Fig. 4.2. Note that the factors, such as surface energy [48]–[50] and doping concentration [44], that induced and stabilized the crystallization of the T- or C- phase can also be translated to O-phase as well. In the next section, we briefly summarize the experimental factors that are to stabilize the formation of the O-phase.

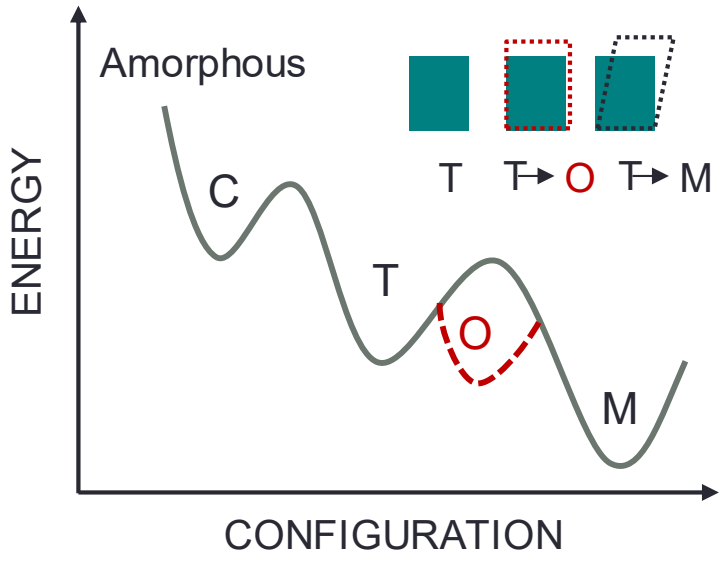


Fig. 4.2 (a) Schematic of the energy profile of different phases in $HfO_2$. The stabilization and formation of the metastable O-phase can be done through the suppression of crystallization into the thermodynamic stable M-phase.

## 4.1.2 Factors that Stabilize the Formation of O-phase

Although the factors that stabilize the formation of the O-phase are already known, the factors that determine the amount of the waking-up effect are still unknown and remain to be clarified. We expect that the experimental factors that stabilize the O-phase can also impact the waking-up effect as well. The factors the stabilize the O-phase can be categorized into two categories: the factors that stabilize the O-phase from (i) the fabrication conditions and (ii) when an electric field is applied.

Three fabrication conditions that we are focusing on in this study are (i) doping concentration, (ii) cooling time ($\downarrow \tau$), and (iii) annealing time ($\tau_{\mathrm{PDA}}$). In this chapter (Chapter 4), we only investigate the impact of doping concentration and $\downarrow \tau$. Later in Chapter 5, we will systemically the impact of the three fabrication conditions on the waking-up effect in FE-$HfO_2$. Even though the impact of these fabrication conditions on the waking-up effect has not been schematically investigated, the impact on the amount of polarization is already known. We will briefly summarize the impact of these fabrication conditions on the amount of polarization.

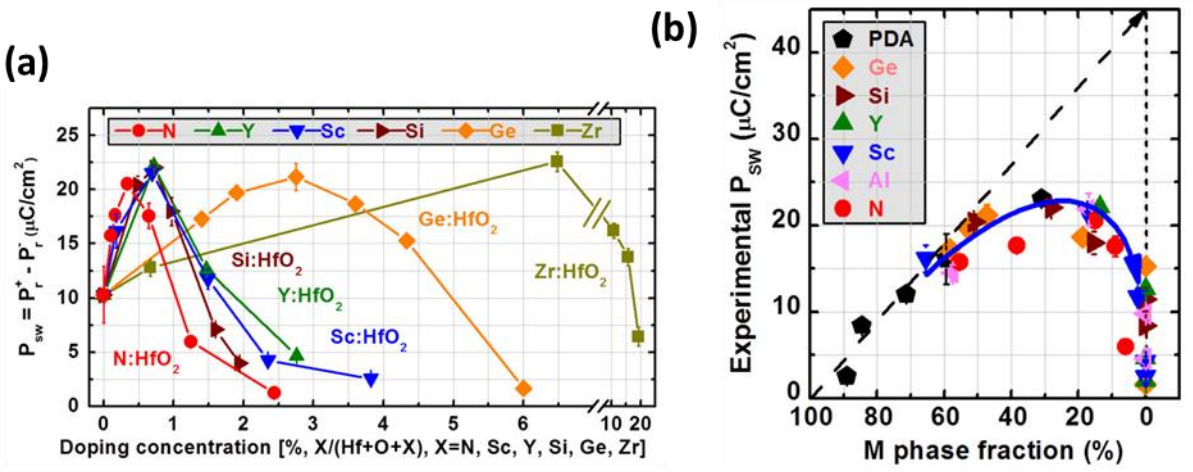


Fig. 4.3 (a) The switchable polarization ($P_{\mathrm{sw}}$) of different doped-$HfO_2$ as a function of its doping concentration. (b) The relationship between the observed $P_{\mathrm{sw}}$ and M-phase fraction [51].

In Section 4.1.1, we have already shown that the introduction of dopants can inhibit the crystallization of the M-phase to favor the formation of the T- or C-phase. Similarly, dopants can induce the formation of the O-phase by hindering the phase transformation between T-/C-phase to M-phase. Various kinds of dopants have been widely reported to have a similar effect on the polarization in FE-$HfO_2$ [51], [52]. Fig. 4.3(a) shows the switchable polarization of FE-$HfO_2$ as a function of several dopant species concentrations. Despite that the doping

concentration in different dopant species has different effects on the polarization, each dopant has its sweet spot that can maximize the polarization. Fig. 4.3(b) shows the observed polarization of various doped $HfO_2$ and undoped-$HfO_2$ with their M-phase fraction. Because in principle the amount of O-phase is related to the amount of polarization, the common trajectory in Fig. 4.3(b) strongly suggests that the pathways to induce phase transformation in several FE-$HfO_2$ films are common and universal, regardless of doped or undoped $HfO_2$ films.

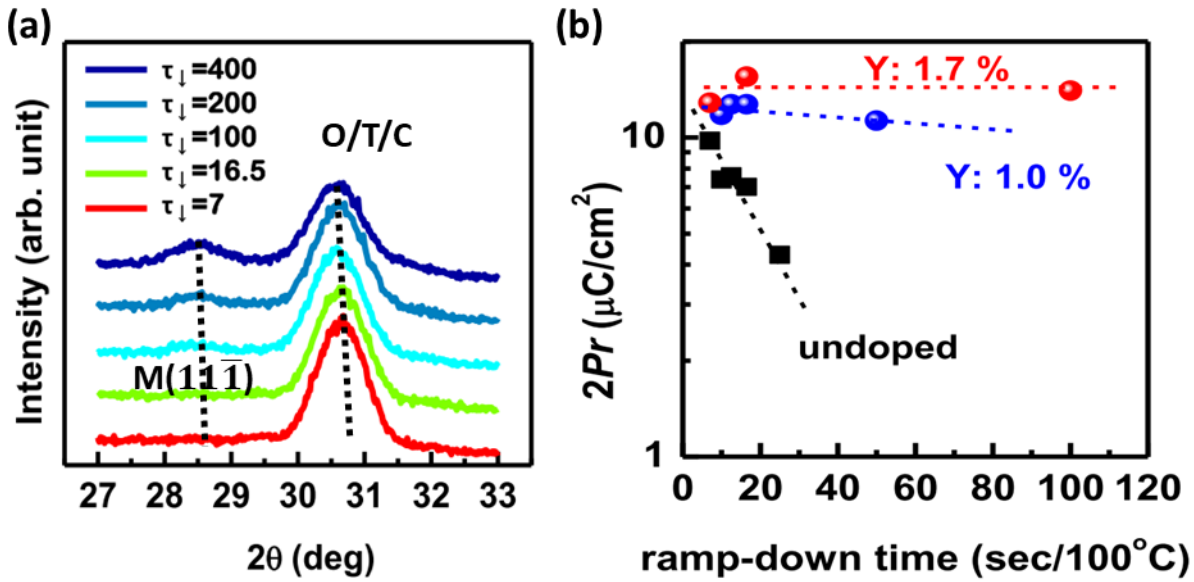


Fig. 4.4 (a) XRD patterns of Y:1.7% doped $HfO_2$ (b)The amount of polarization in undoped $HfO_2$, 1.0% Y-doped $HfO_2$, and 1.7% Y-doped $HfO_2$ as a function of their cooling time [53].

Another important factor that significantly affects the crystallization of O-, T-, and C-phase, as well as the polarization, is the thermal annealing profile (*i.e.*, $\downarrow \tau$ and $\tau_{PDA}$). It is already known that in non-FE $HfO_2$, the T- and C-phase can be induced through a non-equilibrium annealing profile (in other words – rapid annealing and cooling) [54]. Generally, rapid annealing is required to cap the phase transformation between T/C-phase and M-phase. A longer cooling time would allow more T/C-phase to transform into M-phase; thus, reducing the amount of O-phase and polarization. Fig. 4.4(a) shows XRD patterns of 1.7% Y-doped $HfO_2$ at different $\downarrow \tau$. With the increase in the $\downarrow \tau$, larger peak intensity of the M(11$\bar{1}$) was observed. This means that a longer $\downarrow \tau$ allows more T/C- phase to transformation into M-phase. Fig. 4.4(b) shows the effect of $\downarrow \tau$ on the amount of polarization in an undoped $HfO_2$, 1.7% and 1.0% Y-doped $HfO_2$. In an undoped $HfO_2$, the amount of the polarization was significantly affected by the $\downarrow \tau$. In contrast, Y-doped $HfO_2$ was not affected by the $\downarrow \tau$.

$\tau_{PDA}$ is an experimental factor that we speculate has a significant effect on the waking-up effect. Unfortunately, no studies have been found to already investigate the impact of $\tau_{PDA}$ on the amount of the polarization.

Other than the fabrication conditions that can stabilize the O-phase, the O-phase can be stabilized when an electric field is applied as well. The stabilization of the O-phase when an electric field is applied is more specific to the waking-up effect since thermal annealing is not involved. It is known that positive charges can lower the energy and induce the generation of the O-phase [55], without a need for thermal annealing. It is also well known that oxygen vacancies ($V_O$) are intrinsic defects in $HfO_2$ and can act as trapping sites for electrons to trap or de-trapped [56]–[58]. It is important to note that $V_O$ is not always presented in a charged state. Unless electrons are available, neutral $V_O$ tends to be more stable than the charged species [57]. Furthermore, it is important to note that the ferroelectricity in $HfO_2$ is not originating from the movement of oxygen vacancies, but the lattice ionic displacement in the polar O-phase [59].

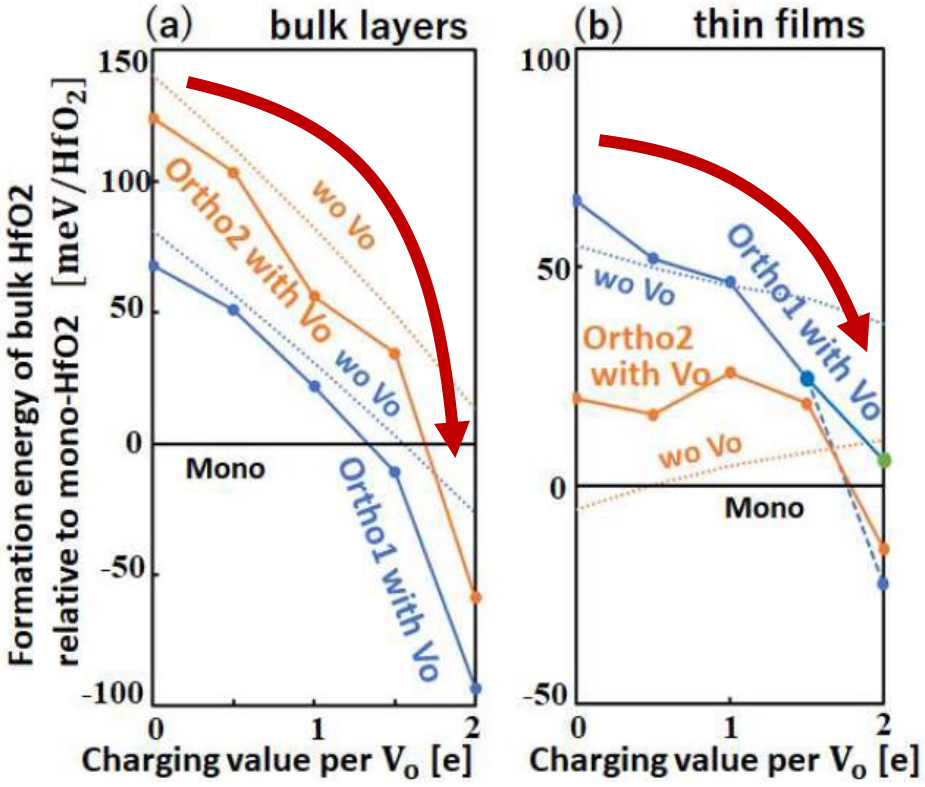


Fig. 4.5 Formation energy of O-phase as a function of the charged state of $V_O$ relative to M-phase (Mono) in (a) bulk layers and (b) thin films.Ortho1 and Ortho2 are O-phase with $Pca2_1$ and $Pnm2_1$ space groups, respectively [55].

### 4.1.3 Possible Mechanisms for the Waking-up Effect

To investigate the origin and the driving force of the waking-up effect in FE-$HfO_2$,[1] it is important to understand the current considerations on the origin of the waking-up effect. It has been highlighted that the waking-up of spontaneous polarization in FE-$HfO_2$ is a complex phenomenon that involves the interaction between electrical and structural properties of FE-$HfO_2$ [16]. It is widely accepted that the origin of the waking-up effect can be concentrated into two models : (i) the depinning of FE-domains (also known as the removal of internal built-in bias) [16], [60]–[66], and/or (ii) the phase transformation driven by an electric field cycling [16], [67]–[73].

In the depinning of the FE-domains model, the increase in the polarization is the result of the de-pinning of the pre-existing O-phase from the pristine charged defects [62], [63]. In other words, the increase in the active FE-domains leads to the waking-up of polarization. Therefore, if this model is to be the dominant model, no phase transformation is expected to have taken place. The depinning of FE-domains can be observed by the merge of two or more distinct maxima in the current displacement (I-V) curves after the pristine stage. An example of the merge of two distinct maxima in I-V curves is shown in Fig. 4.6

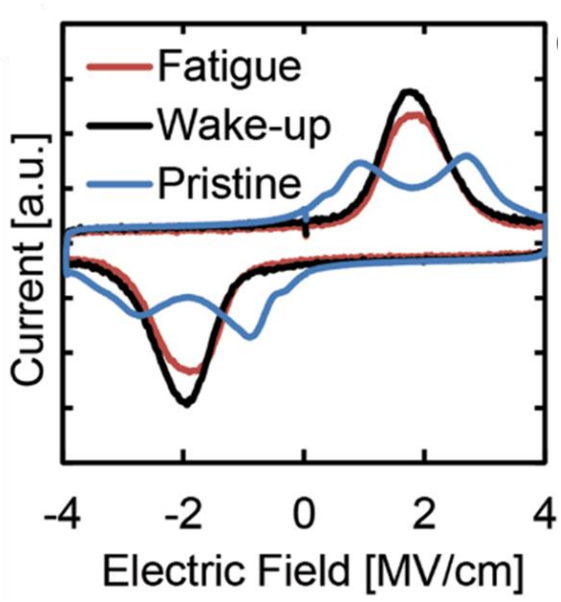


Fig. 4.6 I-V curves of an FE-$HfO_2$ at pristine, wake-up, and fatigue stages [16].

[1] The literature review on the impact of dopant on the polarization of FE-$HfO_2$, as well as the crystallization of the O-, T-, and C-phases can be found on Section 4.1.1 and 4.1.2.

In contrast to the depinning of the FE-domains model, the polarization is directly related to the amount of O-phase in the phase transformation model. It is important to emphasize that the phase transformation as a result of thermal annealing [44], [51], [72], [74] is different from the phase transformation during the waking-up effect. That is during a waking-up effect, the phase transformation is to be driven solely by an electric field cycling. Park *et al*. suggested a tetragonal (T)→O phase transformation from the decrease in the *k*-value.[72] However, Grimley *et al*. found that the bulk section undergoes a monoclinic (M)→O phase transformation by observing the change in the local lattice structure using a transmission electron microscope, showing in Fig. 4.7, which should have increased the *k*-value instead [70]. Recently, the phase transformation was also observed using a synchrotron XRD on a microscopically small area under the electrode by Fields *et al.* [68] and Shimizu *et al.* [67]. However, the waking-up effect can also be observed even on a macroscopic scale.

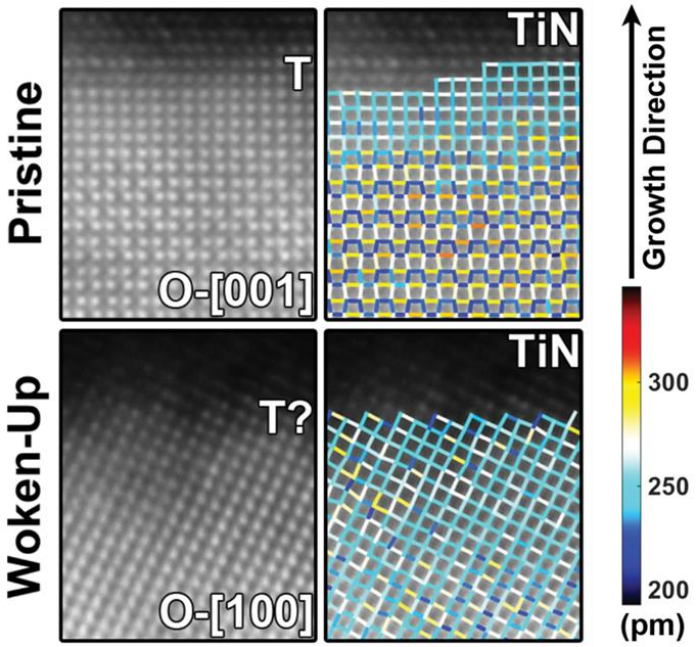


Fig. 4.7 HAADF-STEM images of Gd-doped $HfO_2$ at the pristine and woken-up stage. The structure of near interfacial and bulk regions had gone through a complex structural change after electric field cycling [70].

Despite these efforts, the relationship between the waking-up effect and the phase transformation was not been correctly represented, since both phenomena were not observed on the same scale. As emphasized in Section 1.1 a macroscopic polarization can only be explained by the collection of microscopic polarization and not by an individual microscopic polarization. Hence, to correctly represent the relationship between the two phenomena, both the electrical (waking-up effect) and structural characteristics (phase transformation) have to

be observed on the same scale. *i.e.*, both the waking-up effect and the phase transformation driven by an electric field have to be observed on a macroscopic scale.

It is already known that there are two possible mechanisms of the waking-up effect (*i.e.*, depinning of the FE-domains and the phase transformation driven by an electric field). What is unknown is which mechanism is the dominant mechanism of the waking-up effect in FE-$HfO_2$.

## 4.2 Effect of Y-doping Concentration

To investigate the impact of doping concentration on the waking-up effect,[1] we fabricated three types of $HfO_2$ films to represent different ranges of ferroelectricity in $HfO_2$. **Undoped $HfO_2$**, ~1.5-2.0 cat% Y-doped $HfO_2$ (**Y-$HfO_2$**), and >15 cat% Y-doped **(High Y-$HfO_2$)**. The Y-doping concentrations were estimated from X-ray photoelectron spectroscopy. Fig. 4.8 shows the P-V and I-V characteristics of Undoped-$HfO_2$, Y-$HfO_2$, and High Y-$HfO_2$ during electric field cycling. In Fig. 4.8 (c.1 and c.2), no ferroelectric displacement current was observed in High Y-$HfO_2$; therefore, High Y-$HfO_2$ is considered none-ferroelectric. The change in switchable polarization ($P_{\mathrm{sw}} = P_r^+ - P_r^-$) during electric field cycling of the three samples is summarized in Fig. 4.9(a). The observed $P_{\mathrm{sw}}$ in High Y-$HfO_2$ is the result of the passive charge trapping that can produce a ferroelectric-like hysteresis [75].

To quantify the amount of the waking-up effect, we used the **woke-up ratio ($r_{\mathrm{woke}}$),**

$$r_{\mathrm{woke}} = \left(P_{\mathrm{max}} - P_{\mathrm{pristine}}\right)/P_{\mathrm{max}} \tag{4.1}$$

where $P_{\mathrm{pristine}}$ and $P_{\mathrm{max}}$ are the $P_{\mathrm{sw}}$ at the pristine stage and the maximum switchable polarization ($P_{\mathrm{sw}}$) during electric field cycling, respectively. The $r_{\mathrm{woke}}$ of Y-$HfO_2$ and Undoped-$HfO_2$ were calculated as indicated in Fig. 4.9(a), and the impact of Y-doping concentration on the $r_{\mathrm{woke}}$ is summarized in Fig. 4.9(b). From the figure, it is clear that Y-doping concentration not only affects the total amount of polarization induced in FE-$HfO_2$ but also significantly affects the $r_{\mathrm{woke}}$ similarly to the way it induced the amount of polarization.

Fig. 4.10(a-c) shows the in-plane XRD patterns of Y-$HfO_2$, Undoped-$HfO_2$, and High Y-$HfO_2$, respectively. Due to the similarity in the structure of O-, T-, and C-phases, they are categorized as the O/T/C phase. Because it is well known that doping $HfO_2$ with high Y-concentration will induce the formation of C-phase, the O- phase is not assigned to the XRD peak of High Y-$HfO_2$. The $r_{\mathrm{o,t,c}}$ of Y-$HfO_2$ and Undoped-$HfO_2$ were estimated as indicated in Fig. 4.10(a-c), and the impact of Y-doping concentration on the $r_{\mathrm{o,t,c}}$ is summarized in Fig. 4.10(d). It is clear that by slightly doped $HfO_2$ with yttrium, higher $r_{\mathrm{o,t,c}}$ as well as the $r_{\mathrm{woke}}$, shown in Fig. 4.9(b), can be induced. In section 4.4, we will provide evidence that the waking-

[1] The literature review on the effect of doping concentration on the observed polarization and the crystallization of the O/T/C phase can be found in Section 4.1.2

up of spontaneous polarization in Y-$HfO_2$ is the result of the increase in the $r_{o,t,c}$ after electric field cycling. The difference between the $r_{woke}$ of Y-$HfO_2$ and Undoped-$HfO_2$ could then be explained by the difference in the amount of phase transformation that was driven by electric field cycling.

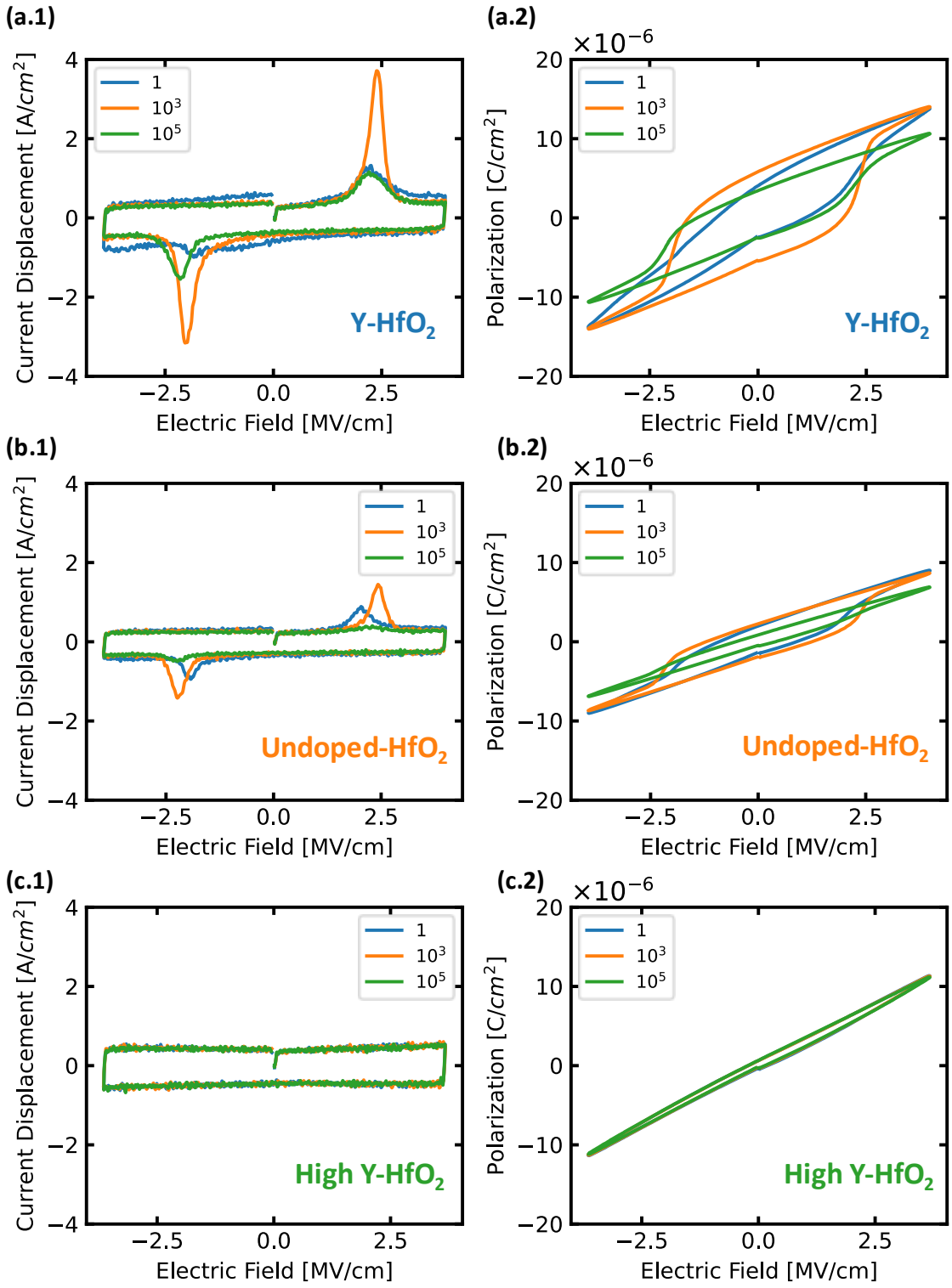


Fig. 4.8 P-V and I-V characteristics of (a) Y-$HfO_2$, (b) Undoped-$HfO_2$, and (c) High Y-$HfO_2$.

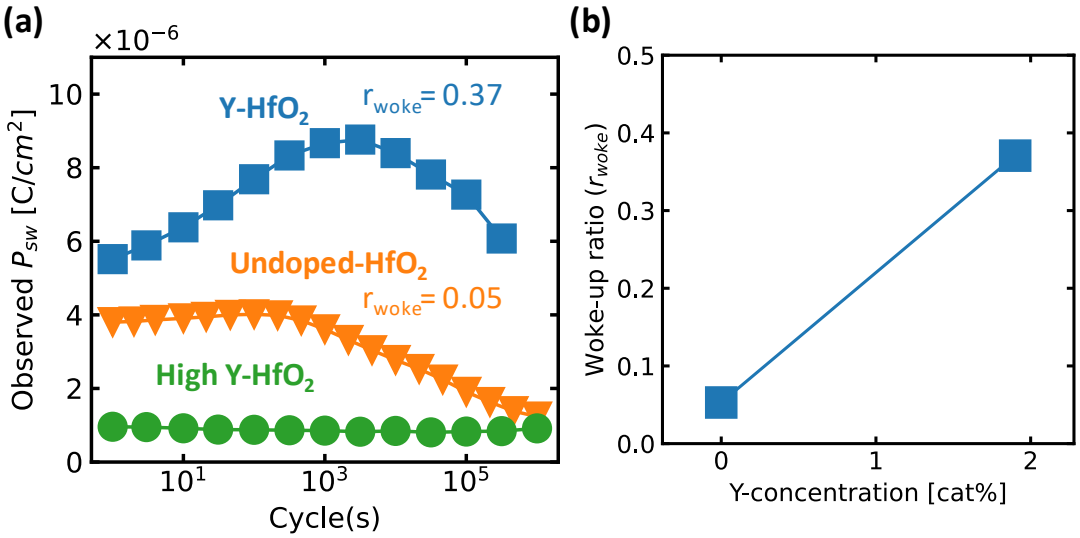


Fig. 4.9 (a) The change in the switchable polarization ($P_{sw}$) during electric field cycling of Y-$HfO_2$, Undoped-$HfO_2$, and High Y-$HfO_2$. High Y-$HfO_2$ is non-ferroelectric; thus, no $r_{woke}$ was calculated. (b) Impact of Y-doping concentration on $r_{woke}$.

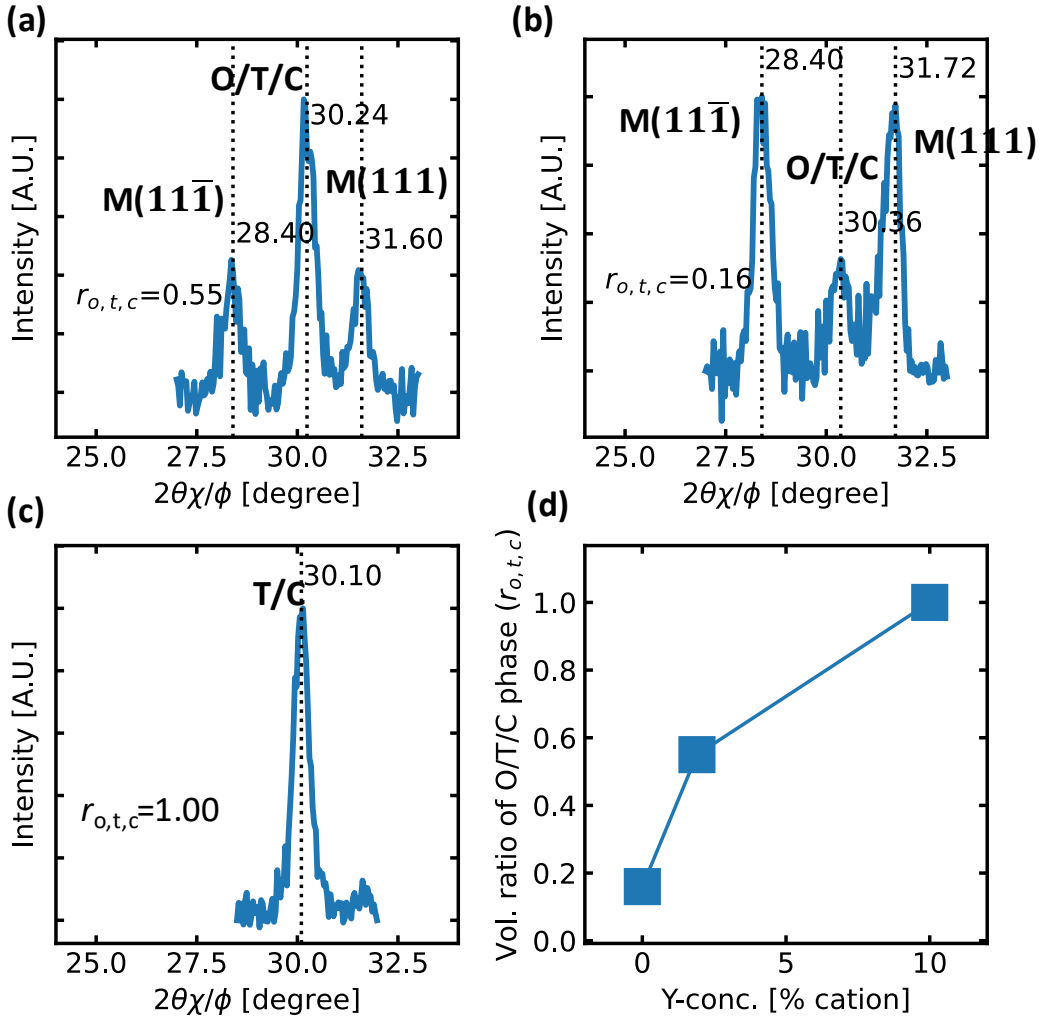


Fig. 4.10 In-plane XRD patterns of (a) Y-$HfO_2$, (b) Undoped-$HfO_2$, and (c) High Y-$HfO_2$ ($\theta_i$=1.00°). (d) Impact of Y-concentration on $r_{o,t,c}$.

## 4.3 Effect of Cooling Time

To investigate the effect of cooling rate on the waking-up of polarization,[1] we fabricated three Y-doped $HfO_2$ (Y-concentration is fixed at ~1.5% cat) where after annealing at 600°C for 30 s, the cooling time ($\downarrow \tau$) to 200°C was controlled: $\downarrow \boldsymbol{\tau}$ **= 0,** $\downarrow \boldsymbol{\tau}$**=45 min**, and $\downarrow \boldsymbol{\tau}$**=200 min**. $\downarrow \tau = 0$ means that after annealing the temperature was dropped freely (in the order of 100°C/min). The schematic of the temperature profile during annealing and cooling is shown in Fig. 4.11. Note that we did not investigate the effect of cooling rate on Undoped-$HfO_2$ because, in Section 4.2, we observed that the $r_{woke}$ of Undoped $HfO_2$ was very low.

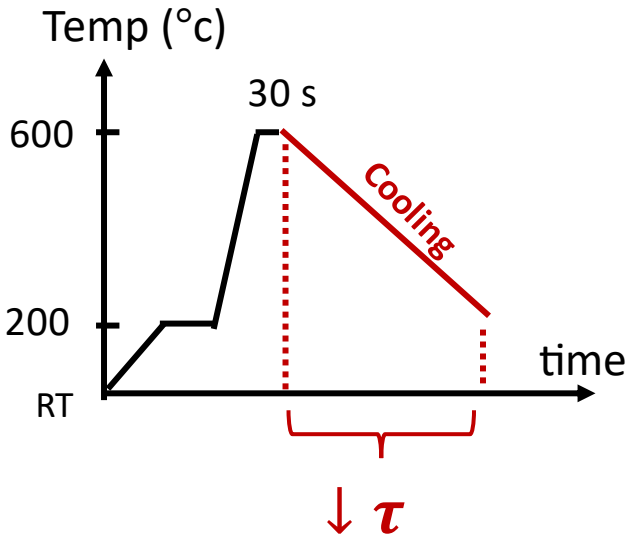


Fig. 4.11 The schematic of the temperature profile during annealing and cooling.

The changes in the $P_{sw}$ during electric field cycling of $\downarrow \tau = 0$, $\downarrow \tau$=45 min, and $\downarrow \tau$=200 min are shown in Fig. 4.12 (a-c), respectively. The effect of the $\downarrow \tau$ on $r_{woke}$ is summarized in Fig. 4.12(d). From the figure, it is clear that $\downarrow \tau$ not only has an impact amount of polarization [53] but also reduces $r_{woke}$ of FE-$HfO_2$ as well the waking-up of the polarization in Y-$HfO_2$.

[1] The literature review on the effect of cooling rate on the observed polarization and the crystallization of the O/T/C phase can be found in Section 4.1.2

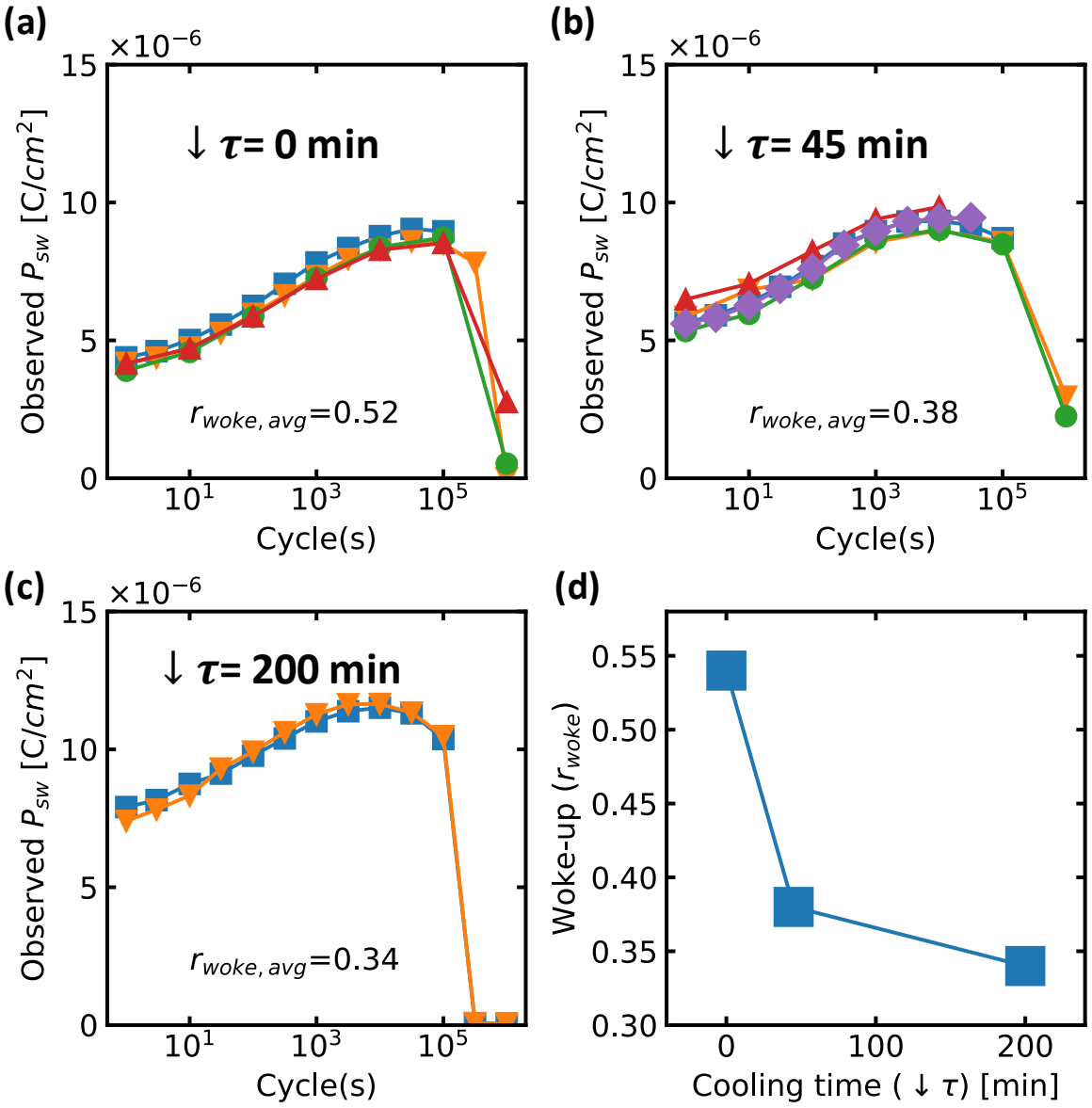


Fig. 4.12 The change in switchable polarization ($P_{sw}$) during electric field cycling for Y-$HfO_2$ with (a) ↓ $\tau$ = 0, (b) ↓ $\tau$=45 min, and (c) ↓ $\tau$=200 min. (d) The effect of cooling time on the $r_{woke}$ of Y-$HfO_2$.

The in-plane XRD patterns of ↓ $\tau$ = 0, ↓ $\tau$=45 min, and ↓ $\tau$=200 min are shown in Fig. 4.13(a). The $r_{o,t,c}$ of ↓ $\tau$ = 0, ↓ $\tau$=45 min, and ↓ $\tau$=200 min are also indicated in Fig. 4.13(a). The impact of cooling time on the $r_{o,t,c}$ in Fig. 4.13(b). Longer ↓ $\tau$ results in the decrease of the $r_{o,t,c}$. This indicates that a longer ↓ $\tau$ not only lowers the $r_{woke}$, as shown in Fig. 4.12(d) but also lowering the $r_{o,t,c}$. The reduction of $r_{o,t,c}$ with a longer ↓ $\tau$ can suggest that more T/C-phase were transformed into M-phase during the cooling process, since the O/T/C can be easier stabilized with rapid annealing and cooling [54].

In next section (Section 4.4), we will demonstrate that by increase the cooling time, the reduction in the $r_{woke}$ of a slow-doing Y-$HfO_2$ could be explained by a minor increase in the $r_{o,t,c}$ after electric field cycling.

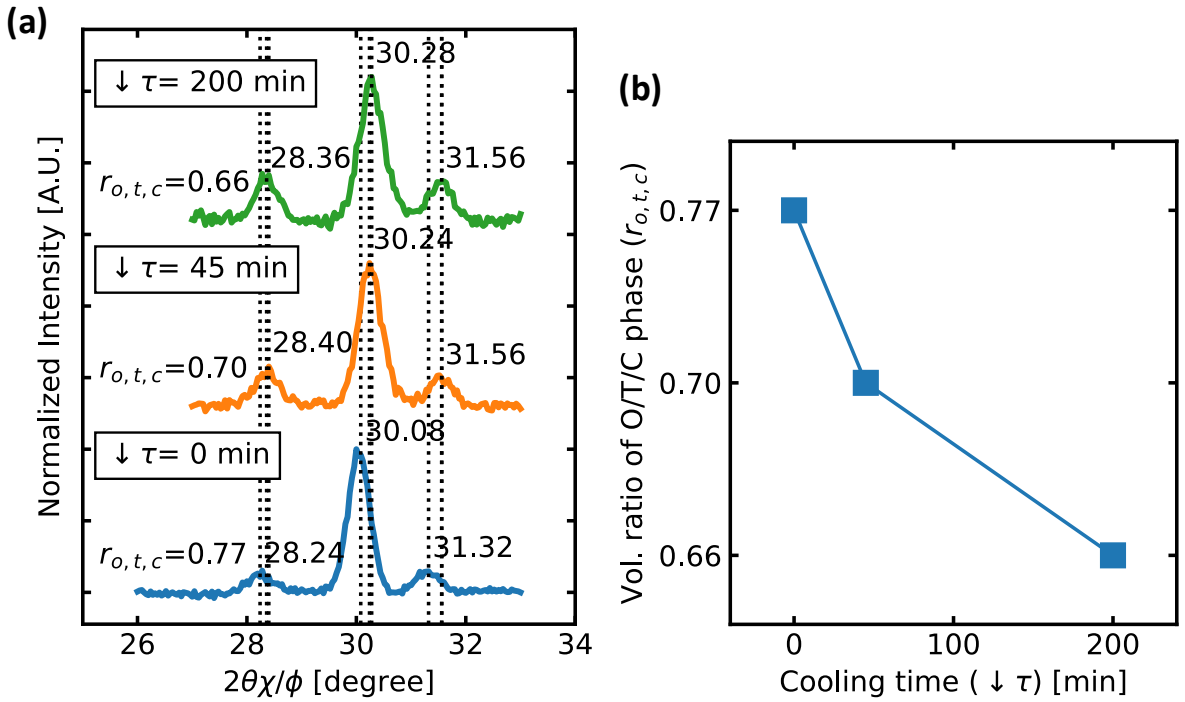


Fig. 4.13 (a) In-plane XRD patterns of Y-$HfO_2$ where after annealing at 600°C for 30 s, the cooling time (↓ $\tau$) to 200°C was varied. (b) The reduction of $r_{o,t,c}$ with the increase in the cooling time.

## 4.4 Evidence of Phase Transformation driven by Electric Field Cycling

In this section, we would like to clarify the origin of the waking-up effect by observing both phase transformation and waking-up effect on a macroscopic scale. It is important to note that we are not the first to purpose a relationship between the waking-up effect (quantified as $r_{woke}$ in this study) and the phase transformation (quantified as the change in $r_{o,t,c}$ in this study) [70]. What previous studies fail to do is to consider the scale that the two phenomena were observed.[1] In Section 1.1, we emphasized that macroscopic polarization can only be explained by the collection of microscopic polarization. To relate the relationship between the waking-up effect and the phase transformation (quantified as $r_{woke}$ and the change in the $r_{o,t,c}$, respectively), both the $r_{woke}$ and the $r_{o,t,c}$ have to be observed on the same scale (*i.e.*, macroscopic scale). Only then the waking-up effect can be described by the phase transformation driven by an electric field, where the phase transformation observed on a macroscopic scale can be explained by the collection of phase transformation observed microscopic scale (*i.e.*, by TEM or a synchrotron XRD)

To vary the $r_{woke}$, three types of FE-$HfO_2$ samples were fabricated : (i) **Undoped $HfO_2$**, (ii) **Y-$HfO_2$**, and **slow-cooling Y-$HfO_2$ ($\downarrow \tau$ Y-$HfO_2$)**.[2&3] All samples were deposited on Ge-substrate with a thickness of 30 nm. After annealing in $N_2$ ambient at 600 °C for 30 sec, the temperature was dropped (~ at the rate of100°C/min). Except for $\downarrow \tau$ Y-$HfO_2$, the temperature was controlled to cool at the rate of 2 °C/min. In addition, relatively thick films were intentionally used in this study to focus on the bulk properties of FE-$HfO_2$ rather than just its interfacial properties on the waking-up phenomenon.

In general, the size of the top electrode is relatively small making it difficult for a conventional XRD to differentiate and detect the signal of woke-up $HfO_2$ structure from the surrounding. Hence, to observe the phase transformation on a macroscopic scale, the signal of

[1] The literature review of the model on the waking-up effect as the result of phase transformation driven by electric field cycling is descried in 4.1.3.

[2] The fabrication condition can be found in Section 2.2.1.

[3] The experiment result on the impact of Y-doping concentration and cooling time on the waking-up effect can be found on Sections 4.2 &4.3, respectively.

the woke-up $HfO_2$ has to be amplified. Hence, an array of 144 top Au electrodes with the size of ~$380 \times 380$ $\mu$m was patterned and deposited within $5 \times 5$ mm $HfO_2$/Ge stacks using photolithography. The schematic diagram for an array of 144 top Au electrodes is shown in Fig. 4.14. An outline of the fabrication process on an array of 144 Au/FE-$HfO_2$/Ge capacitors is shown in Fig. 4.15. Then, the array of 144 Au/FE-$HfO_2$/Ge capacitors were individually woke up by a $1000^{th}$ cycle of $\pm$ 2.67 MV/cm at the frequency of 20 kHz before the Au top electrodes were removed for structural analysis. An example of P-V and I-V characteristics during electric field cycling for Undoped-$HfO_2$, Y-$HfO_2$, and $\downarrow \tau$ Y-$HfO_2$ are shown in Fig. 4.17. The measured pulses were made at 4 MV/cm (10 kHz) to obtain saturated $P_{sw}$. The change in switchable polarization ($P_{sw}$) during electric field cycling of the three samples is shown in Fig. 4.16. The average $r_{woke}$ of Undoped-$HfO_2$, Y-$HfO_2$, and $\downarrow \tau$ Y-$HfO_2$ were calculated to be 0.14, 0.25, and 0.02, respectively, as indicated in Fig. 4.16. The variation of $P_{sw}$ of each sample was due to the variation in the area of the top electrodes.

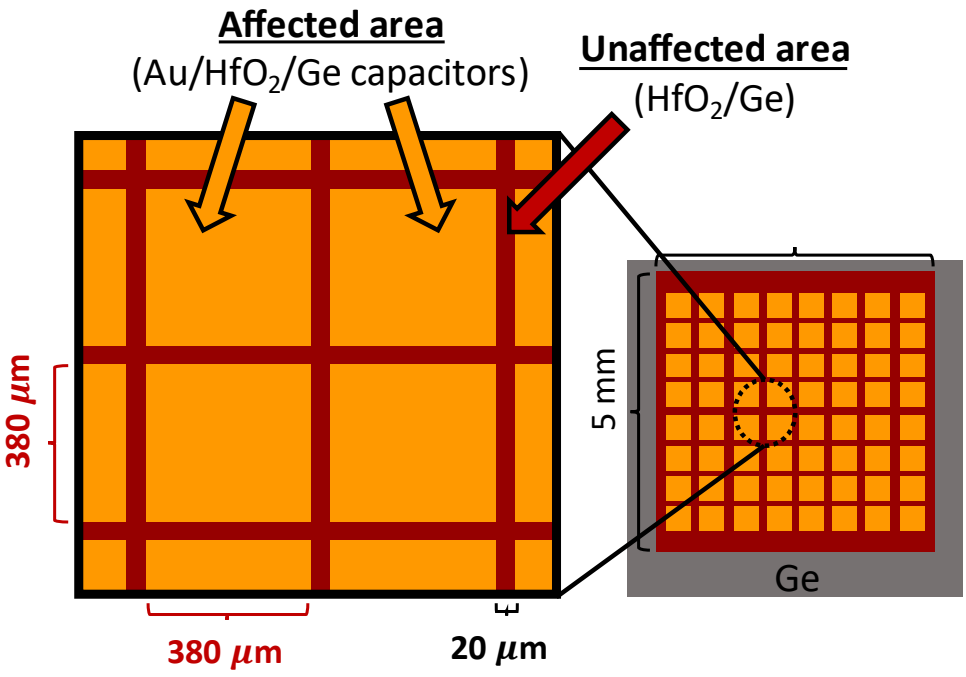


Fig. 4.14 Schematic diagram for an array of 144, 400×400 μm, Au/FE-$HfO_2$/Ge capacitors. The unaffected area is the area that has not been woke-up (*i.e.*, the area was not covered by the top electrodes).

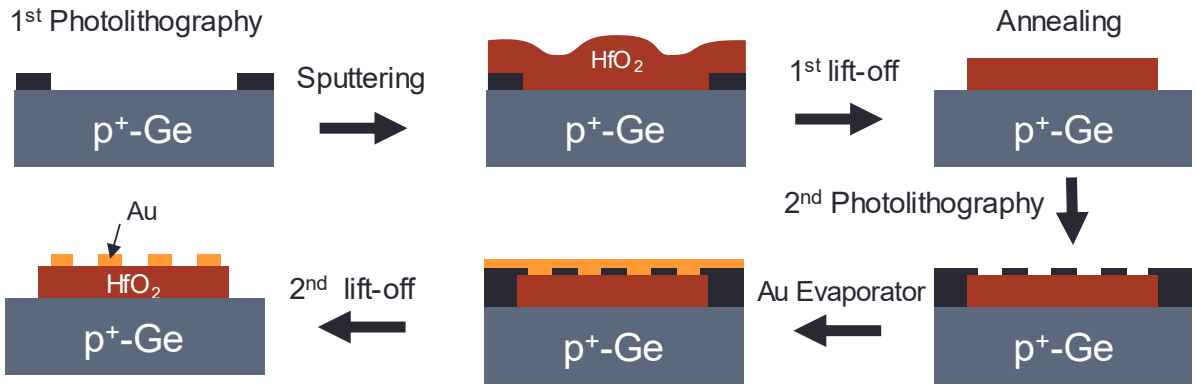


Fig. 4.15 An outline of the fabrication process for an array of 144 Au/FE-$HfO_2$/Ge capacitors as shown in Fig. 4.14.

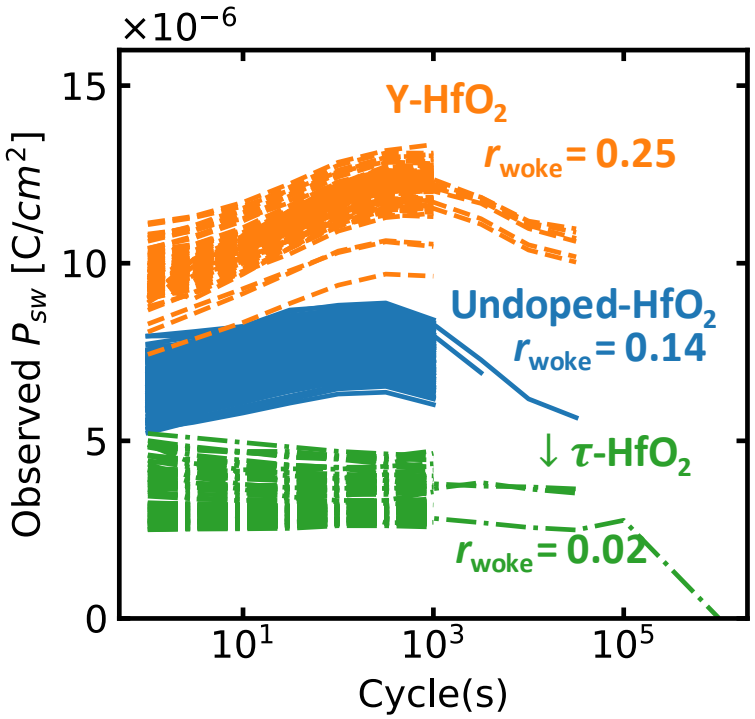


Fig. 4.16 The change in the switchable polarization ($P_{sw}$) of the 144 Au/FE-$HfO_2$/Ge capacitors during electric field cycling.

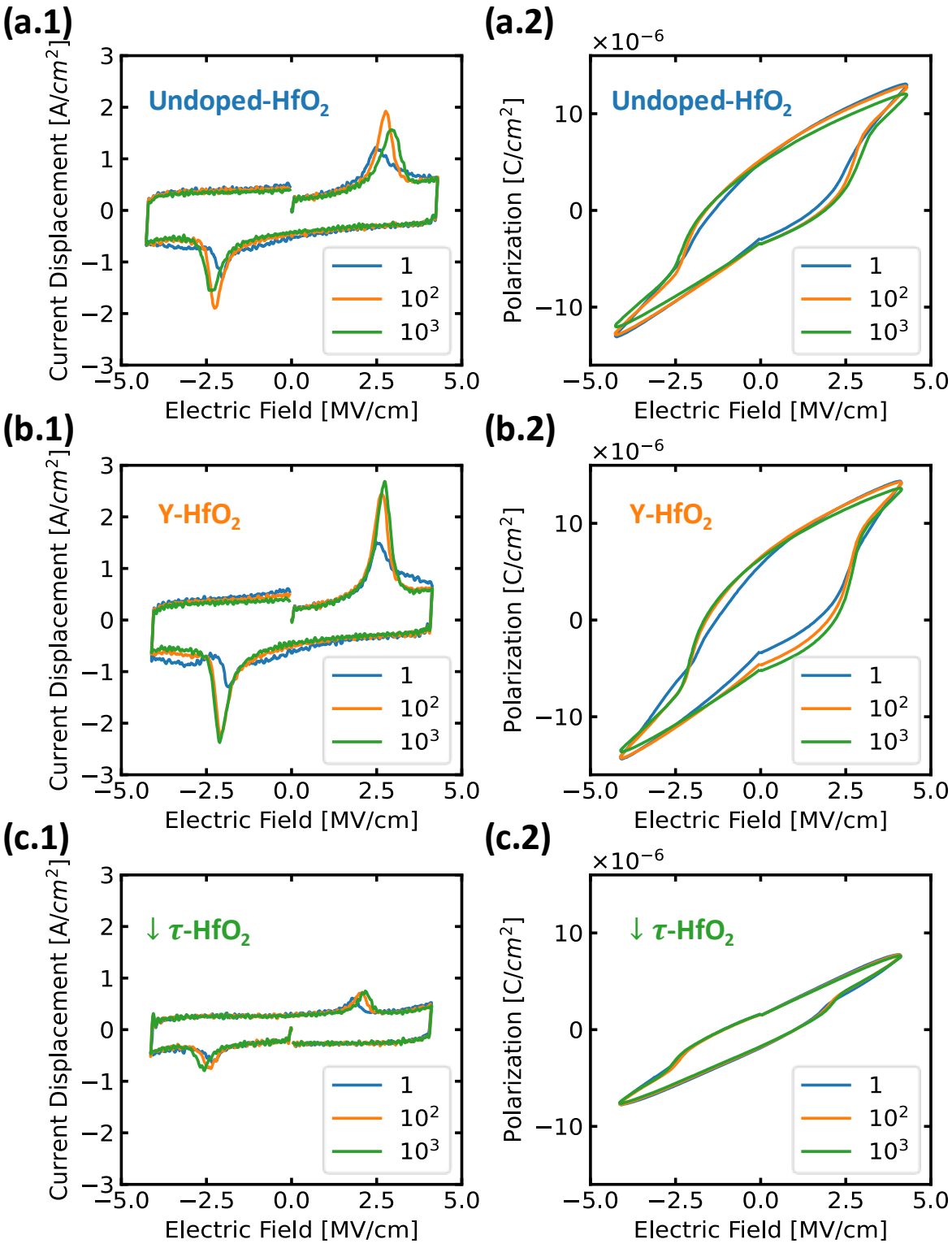


Fig. 4.17 The I-V and P-V characteristics during electric field cycling of (a) Undoped-$HfO_2$, (b) Y-$HfO_2$, and (c)↓ τ Y-$HfO_2$.

To indicate that if a phase transformation has occurred, we measured the change in the $r_{o,t,c}$ before and after a 1000$^{th}$ cycle of electric field cycling. The in-plane XRD patterns and the experimentally estimated $r_{o,t,c}$ of Undoped-$HfO_2$, Y-$HfO_2$, and ↓ $\tau$ Y-$HfO_2$, before and after a 1000$^{th}$ cycle of electric field cycling are shown in Fig. 4.18. To take the unaffected woke-up area into account, as indicated in Fig. 4.14, a correction on the experimentally observed $r_{o,t,c}$ has to be made using the following equation:

$$r_{o,t,c}^{after"} = r_{o,t,c}^{before}(1 - S_{wk}) + r_{o,t,c}^{after}(S_{wk}), \tag{4.2}$$

where $r_{o,t,c}^{before}$ and $r_{o,t,c}^{after"}$ are the experimentally observed $r_{o,t,c}$ before and after the waking-up, respectively. $r_{o,t,c}^{after}$ and $S_{wk}$ are the corrected $r_{o,t,c}$ after the waking-up process and the ratio of the affected woke-up area ($A_{eff}$) to the total area ($A_{total}$), where $S_{wk} = A_{eff}/A_{total}$.

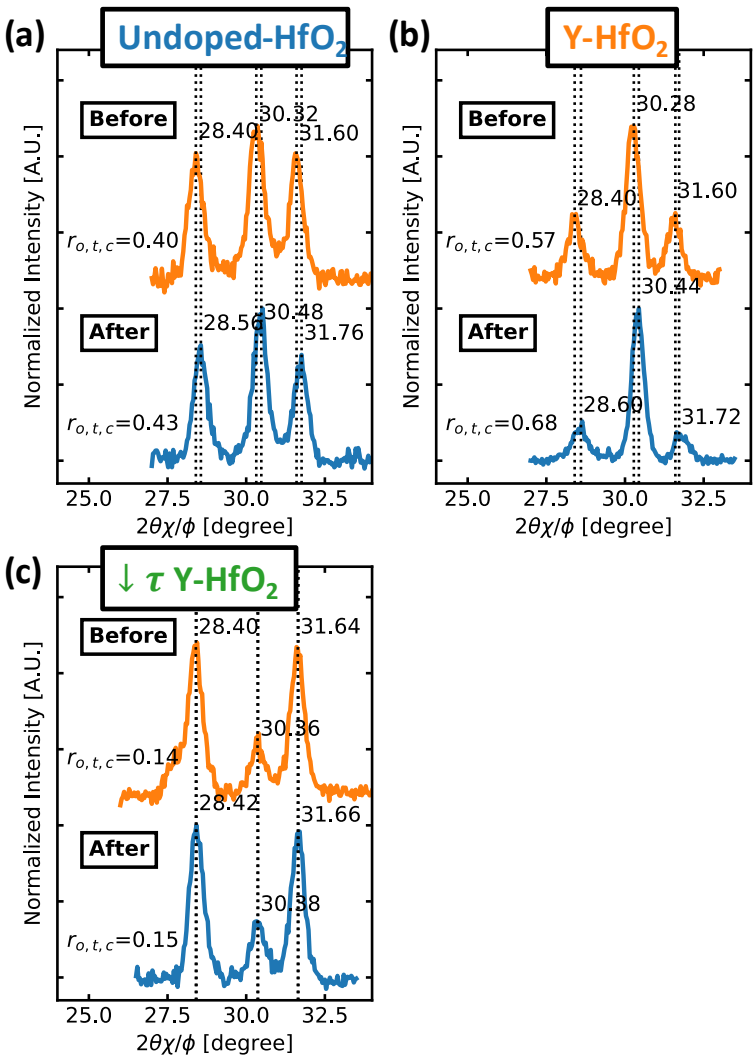


Fig. 4.18 In-plane XRD patterns of (a) Undoped-$HfO_2$ (b) Y-$HfO_2$ (c) ↓ $\tau$ Y-$HfO_2$ before and after a 1000th cycle of electric field cycling ($\theta_i$=1.00°).

The change in the $r_{o,t,c}$ after corrections of the three samples before and after the waking-up is shown in Fig. 4.19. We found that there is a significant increase in the $r_{o/t/c}$ after the waking-up on Y-$HfO_2$ and Undoped-$HfO_2$ where the $r_{woke}$ are relatively high compared to the $r_{woke}$ of ↓ $\tau$ Y-$HfO_2$. The increase in the $r_{o,t,c}$ indicates two things. It means that (i) the phase transformation has taken place and (ii) the electric field cycling drove the phase transformation. Thanks to the implication of a conventional XRD, we now have successfully observed both the waking-up effect and the phase transformation driven by an electric field on a macroscopic scale.

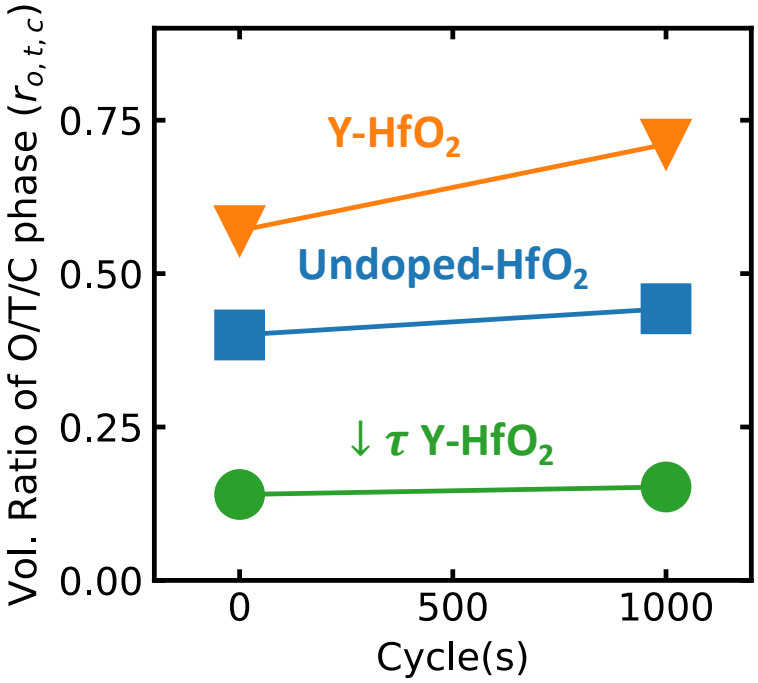


Fig. 4.19 The change in the $r_{o,t,c}$ of Undoped-$HfO_2$, Y-$HfO_2$, and ↓ $\tau$ Y-$HfO_2$ before and after electric field cycling.

We also found that the increase in the $r_{o,t,c}$ ($r_{o,t,c}^{after}/r_{o,t,c}^{before}$) is proportional to the $r_{woke}$ of the three samples, as shown in Fig. 4.20. Considering the two possible models of the waking-up effect as described in Section 4.1.3: Model I – De-pinning of FE-domains and Model II – phase transformation model. If Model I is to be the dominant mechanism, then the waking-up effect is totally to be the result of the de-pining of the pre-existing O-phase. Therefore, no phase transformation should have taken place (*i.e,* $r_{o,t,c}^{after}/r_{o,t,c}^{before}$=1, shows a the black dotted line in Fig. 4.20 ). However, our experimental data shows that there is an increase in the $r_{o,t,c}$ after electric field cycling; and thus, we discard the contribution of the de-pinning of FE-domains to the waking-up effect in our FE-$HfO_2$ system.

Conversely to the de-pinning of FE-domains, the waking-up effect has a direct relationship with the phase transformation to the volume ratio of the O-phase ($r_o$). In other words, $r_{o,t,c}^{after}/r_{o,t,c}^{before}>1$, and the slope of the relationship between $r_{woke}$ and $r_o^{after}/r_o^{before}=1$. Since it is known that ferroelectricity in $HfO_2$ is originating from the O-phase, we assume that the increase in the $r_{o,t,c}$ that we experimentally observed to be the result of the increase in the $r_o$ – *i.e.*, $r_{o,t,c}^{after}/r_{o,t,c}^{before} \rightarrow r_o^{after}/r_o^{before}$. Then, the proportionality between the $r_{woke}$ and $r_{o,t,c}^{after}/r_{o,t,c}^{before}$ that we observed in Fig. 4.20 would indicate that the waking-up effect in our FE-$HfO_2$ system is dominated by the phase transformation driven by electric field cycling. More detail of the evidence of the phase transformation driven by electric field cycling can be found in Ref [76].

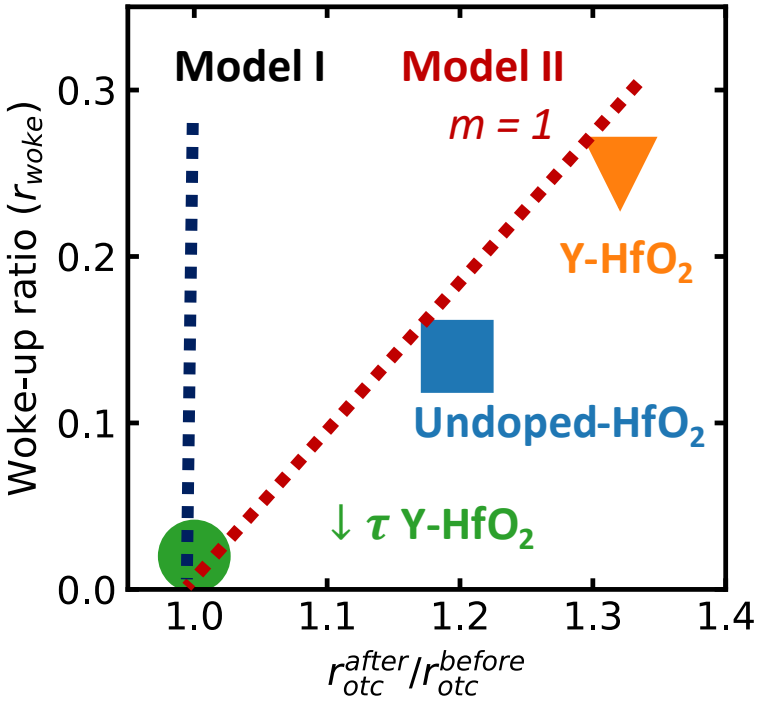


Fig. 4.20 The relationship between the $r_{woke}$ and the amount of the phase transformation ($r_{o,t,c}^{after}/r_{o,t,c}^{before}$) in our FE-$HfO_2$ samples. The dotted lines are speculations of the experimental data if either Model I – De-pinning of FE-domains or Model II – phase transformation to be the dominant mechanism.

## 4.5 Pathways of the Phase Transformation driven by Electric Field Cycling

Although our result can only indicate that the phase transformation has occurred as shown in Fig. 4.19, it is still important to discuss the possible pathways of the phase transformation that we observed.

If we assume that there was no change in the crystallinity after the thermal annealing, then the increase in the $r_{o/t/c}$ could only mean that there was a reduction in the amount of the M-phase. Although M-phase is known as the thermodynamically stable phase in a bulk $HfO_2$ [45], [47], the M→O phase transformation was already observed by a TEM in the bulk region of FE-$HfO_2$ films [16], [70], [71]. This phase transformation was also supported by a first principle study that positive charges can lower the energy of the O-phase to become the most stable phase [55]. The schematic diagram showing the energy profile of each phase in bulk $HfO_2$ and $HfO_2$ thin films is shown in Fig. 4.21. Later, Our result in Section 5.3 also suggesting that the M→O phase transformation has taken place. Another possibility that we can not neglect is the T→O phase transformation, which has also been experimentally observed by a TEM [69], [70], and a synchrotron XRD [68]. Unfortunately, our experimental setup and results could not indicate that the T→O phase transformation has taken place.

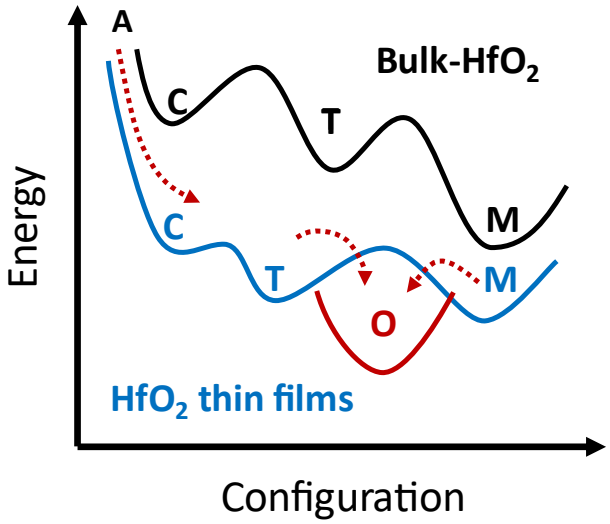


Fig. 4.21 Schematic diagram on the energy profile of each phase in a bulk $HfO_2$ and a $HfO_2$ thin film. Note – A=amorphous, C=cubic, T=tetragonal, O=orthorhombic, and M=monoclinic

Another possibility is the crystallization of the remaining amorphous (A) to one of the O/T/C phases. Although the phase transformation is commonly reported in FE-$HfO_2$, it is still considered unconventional for a phase transformation to take place without thermal annealing. For this reason, we speculate that this unconventional phase transformation is most likely governed by a unique phenomenon that has not yet been discussed, and this unique phenomenon may allow the remaining A-phase to crystallize into one of the O/T/C phases during an electric field cycling.[1] Note that the crystallization of the remaining A-phase is not to be confused with the crystallization in a phase-change random access memory (PC-RAM) [77], since crystallization in a PC-RAM is a result of pulse-heating rather than purely by an electric field.

In summary, there are three possible pathways of the phase transformation to be driven by an electric field cycling: T→O, M→O, and A→O/T/C phase transformations. Between T→O and M→O phase transformations, where both have already been experimentally observed, the T→O phase transformation is the most favorable in terms of energy. Nonetheless, we only observed an increase in the $r_{o,t,c}$ (as shown Fig. 4.19), and this does not indicate that a T→O phase transformation has taken place. Hence, we consider the crystallization of the remaining A-phase during the electric field cycling. Unfortunately, we are unable to support this consideration with experimental data due to the difficulty in calibrating the XRD peak intensity with the crystallinity.

[1] This unique phenomenon will be introduced in Section Anomalous Structural Distortion4.6 and discussed in Chapter 5.

## 4.6 Anomalous Structural Distortion

Although the phase transformation is driven by an electric field is commonly reported in FE-$HfO_2$, it is still unconventional for a phase transformation to be driven solely by an electric field. Hence, we speculate that another phenomenon that has not yet been discussed is governing this unconventional phase transformation. Continue from the previous section (Section 4.4), during the structural characterization by XRD, we consistently observed an anomalous difference in the XRD peak positions between the in-plane and the out-of-plane diffractions [78]. The in-plane and out-of-plane XRD patterns of Undoped-$HfO_2$, Y-$HfO_2$, and $\downarrow \tau$ Y-$HfO_2$ are shown in Fig. 4.22(a-c), respectively. The difference in the XRD peak positions between the in-plane and the out-of-plane diffractions indicates that there is a difference in the **interplanar spacing ($d_{spacing}$)** that is parallel (out-of-plane) and perpendicular (in-plane) to the surface of $HfO_2$ films. We attribute this anomalous difference in the XRD peal positions to the structural distortion that was induced during the crystallization of FE-$HfO_2$ thin films.

In the next chapter, we will continue our discussion on what is the driving force that determines the amount of the phase transformation to be driven by an electric field cycling. We will also discuss the relationship between this anomalous structural distortion and the waking-up effect in our FE-$HfO_2$ system.

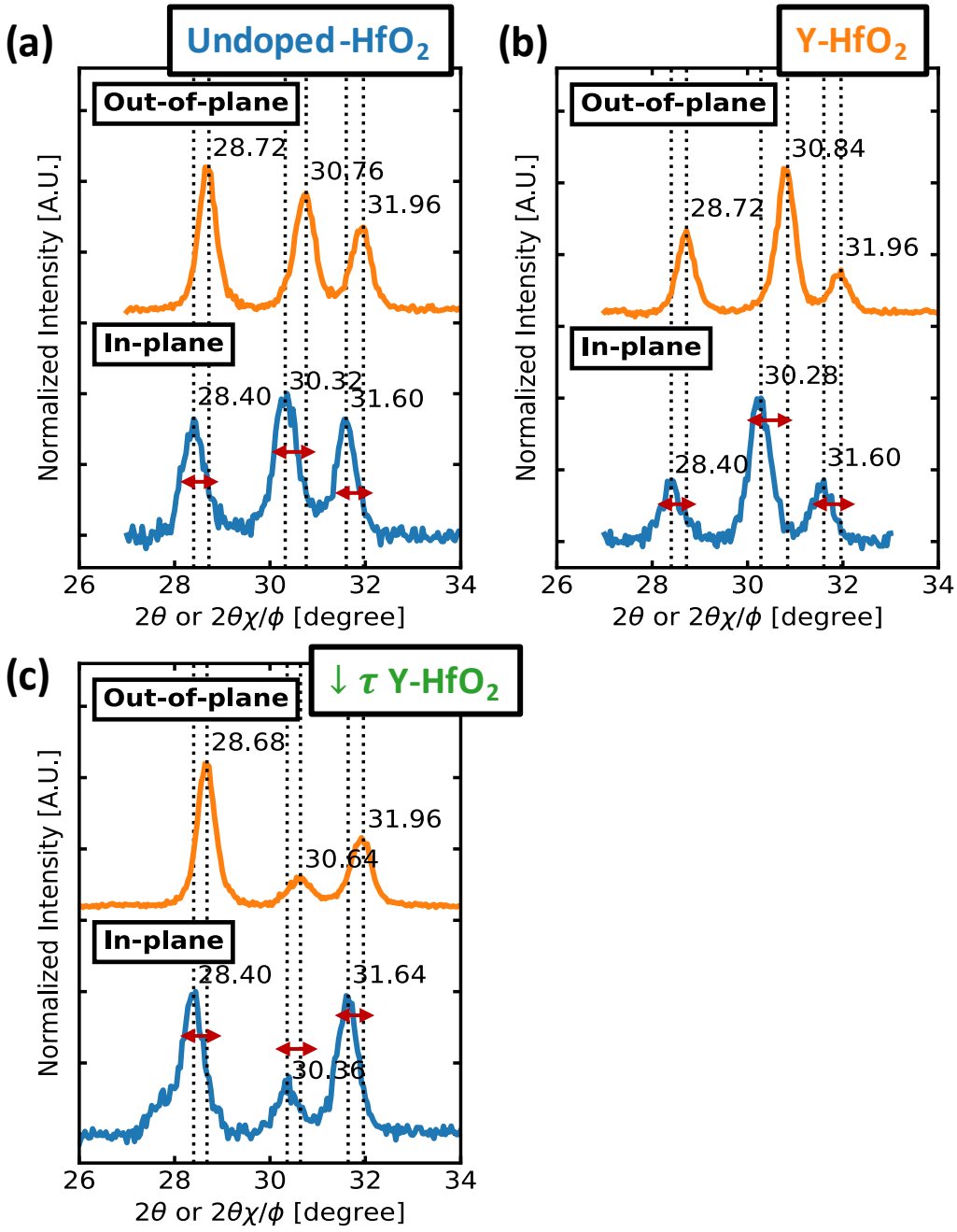


Fig. 4.22 In-plane and out-of-plane XRD patterns of (a) Undoped $HfO_2$, (b) Y-$HfO_2$, and ↓ $\tau$ Y-$HfO_2$ before electric field cycling.

## 4.7 Summary

We investigated the origin of the waking-up effect by observing both the phase transformation and the waking-up effect at the same scale. We first investigated the impact of Y-doping concentration and the $\downarrow \tau$ on the amount of the waking-up effect. We use the woke-up ratio ($r_{woke}$) to quantify the amount of the waking-up effect. We found that both Y-doping concentration and $\downarrow \tau$ affect the $r_{woke}$ similarly to the way they affect ratio of the higher symmetric phase ($r_{o,t,c}$). We found that an undoped $HfO_2$ and/or long $\downarrow \tau$ are the condition to minimize the $r_{woke}$ of an FE-$HfO_2$ thin film, as shown in Fig. 4.9(b) and Fig. 4.12(d).

To clarify the origin of the waking-up effect, we conducted another set of experiments where we can observe both the waking-up effect and the phase transformation on a macroscopic scale. We found that there was an increase in the $r_{o,t,c}$ after the waking-up, as shown in Fig. 4.19. This indicates that the phase transformation has taken place and the electric field cycling drove the phase transformation. We also found that the increase in the $r_{o,t,c}$ is proportional to the $r_{woke}$, as shown in Fig. 4.20. If we assume that the increase in the $r_{o,t,c}$ is the result of the phase transformation to increase the amount of O-phase, it indicates that electric field-driven phase transformation is the dominant mechanism of the waking-up effect in our FE-$HfO_2$ system.

Because it is unconventional for a phase transformation to take place without thermal annealing, we speculate that this unconventional phase transformation is governed by a phenomenon that has not yet been discussed. During our structural characterization, we found an anomalous difference in the XRD peak positions between the in-plane and the out-of-plane diffractions, where we attribute the anomalous difference to the structural distortion that was induced during the crystallization of FE-$HfO_2$ films. We hypothesize that this structural distortion is what governs the waking-up effect. In the next chapter, we will discuss how this anomalous structural distortion is related to the waking-up of FE-$HfO_2$.

# Chapter 5 Structural Distortion-induced the Waking-up of Spontaneous Polarization in Ferroelectric $HfO_2$ and Its Origin

# 5.1 Introduction

In Chapter 4, we have clarified the origin of the waking-up effect is due to the phase transformation is driven by electric field cycling. Although the mechanisms of the waking-up effect and the factors that induce the crystallization of the polar O-phase have already been investigated, the driving force that determines the amount of the phase transformation to be driven by electric field cycling (*i.e.*, waking-up effect) is still unknown and remains to be clarified. In this chapter, we would like to clarify the driving force that determines the amount of the phase transformation to be driven by electric field cycling.

In the previous chapter, we found an anomalous structural distortion. We hypothesize that this structural distortion is what determines the amount of the phase transformation to be driven by electric field cycling. We summarize the importance of unidirectional stress and distortion in FE-$HfO_2$. We also summarize the impact of the capping layer, a common technique to fabricate FE-$HfO_2$, on the crystallization of the O/T/C phase.

## 5.1.1 Importance of Unidirectional Stress and Distortion

Several studies have already indicated that stress [79]–[81] and structural distortion [82] as well as the distortion near the interphase boundaries [83] play an important role in determining the total energy and the phase stabilization in FE-$HfO_2$.

Shiraishi *et al*. suggested that an in-plane tensile strain is an important parameter to enhance the ferroelectricity in FE-$HfO_2$ [79]. Fig. 5.1(a) shows P-V of 17 nm thick-$(Hf_{0.5}Zr_{0.5})O_2$ on Si, $SiO_2$, and $CaF_2$ substrates. From the figure, $SiO_2$ substrate was able to induce the largest polarization; whereas, no ferroelectricity was observed on $(Hf_{0.5}Zr_{0.5})O_2$ that was deposited on $CaF_2$ substrate. By comparing the interplanar spacing of $M(11\bar{1})$ and a stress-free M-phase, the study found that polarization increase with the amount of tensile stress exerts in an in-plane direction. as shown in Fig. 5.1(b). On the contrary, the polarization of $(Hf_{0.5}Zr_{0.5})O_2$ deposited on $CaF_2$ was nearly zero while the film was under out-of-plane compressive stress.

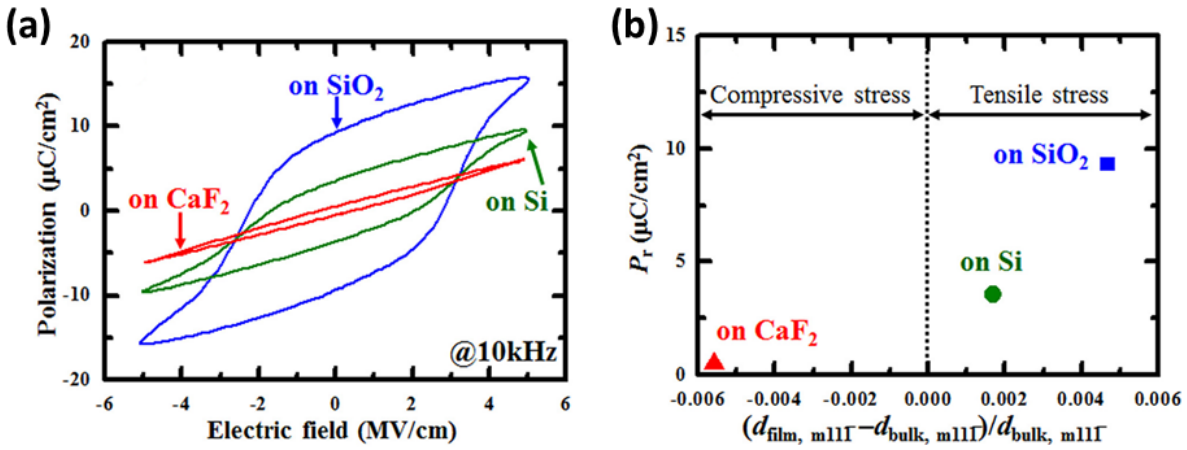


Fig. 5.1 (a) P-V characteristics of 17 nm thick-$(Hf_{0.5}Zr_{0.5})O_2$ on Si, $SiO_2$, and $CaF_2$ substrates. (b) The relationship between remanent polarization and strain in an in-plane induced on $(Hf_{0.5}Zr_{0.5})O_2$ films. The induced strain was estimated from the shift in the interplanar spacing of the observed M$(11\bar{1})$ to a stress-free monoclinic [79].

A theoretical study has also found that the polar O-phase can arise from the distortion of its parent non-polar T-phase [82]. Fig. 5.2 shows that a distortion of the non-polar T-phase in the [110] direction could minimize the total energy of the system and stabilize the polar O-phase. This was later found that the interphase boundaries between O- and M-phases can impose strain/distortion conditions. This distortion near the interphase boundaries may allow the FE-domain wall motion when an electric field is applied.

These findings indicate that stress and structural distortion has already played critical roles in the determination of the total energy and the phase stabilization in FE-$HfO_2$. What is still missing is the impact of stress and/or distortion on the waking-up of spontaneous polarization in FE-$HfO_2$.

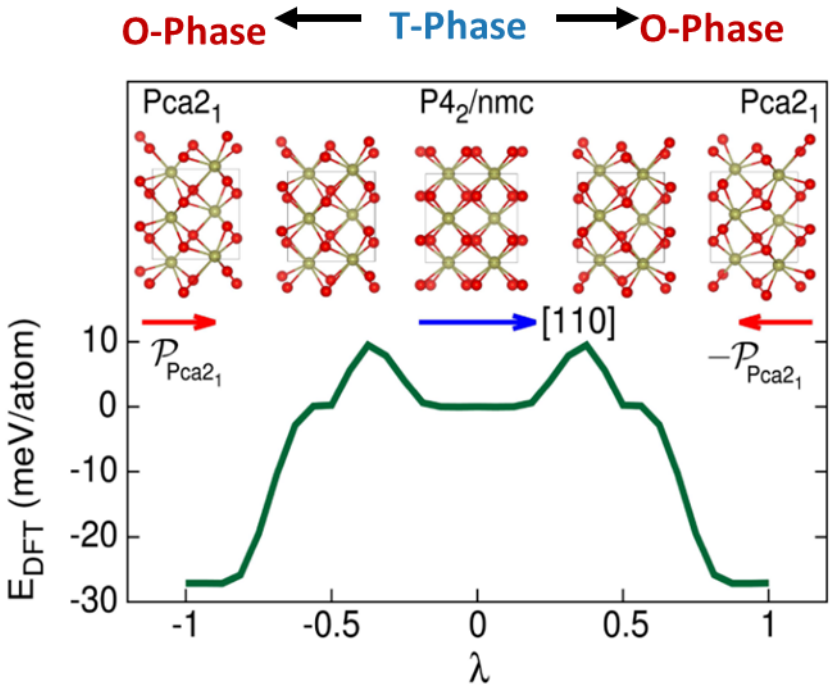


Fig. 5.2 Minimum energy pathways (calculated from a density functional theory) of the polar O-phase in 'up' ($\lambda = 1$) and 'down' ($\lambda = -1$) states, and non-polar T-phase [82].

## 5.1.2 Capping Effect

It is a common method to mechanically encapsulated $HfO_2$ films with either a dielectric or a metallic layer before thermal annealing to induce the formation of T- or C-phase in non-FE-$HfO_2$ [54], and O-phase in FE-$HfO_2$ [12], [84]–[86] This is known as the capping effect. The capping layers (CL) provides another factor that suppresses the phase transformation into the thermodynamic stable M-phase and allowing the phase transformation to stop at the metastable O-phase. Examples of XRD patterns of $HfO_2$ with Si-capping and without a capping layer at different cooling rates after annealing are shown in Fig. 5.3(a) and (b), respectively. Without a doubt that Si-caped $HfO_2$ was able to induce much more T-/C-phase than $HfO_2$ without a capping layer regardless of the cooling rate. For $HfO_2$ without a capping layer to indue stabilize the formation of T-/C-phase, it needed to be quenched to prevent the phase transformation into M-phase.

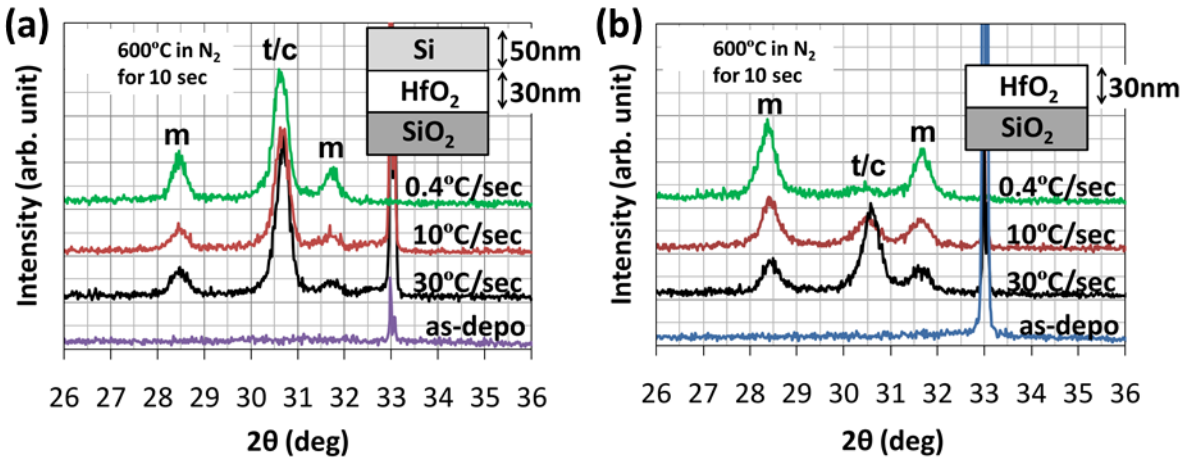


Fig. 5.3 XRD pattern of $HfO_2$ (a) with a Si-capping layer and (b) without a capping layer at different cooling rates after annealing at 600°C for 10 sec [54].

## 5.2 Relationship between Structural Distortion and the Waking-up of Spontaneous Polarization

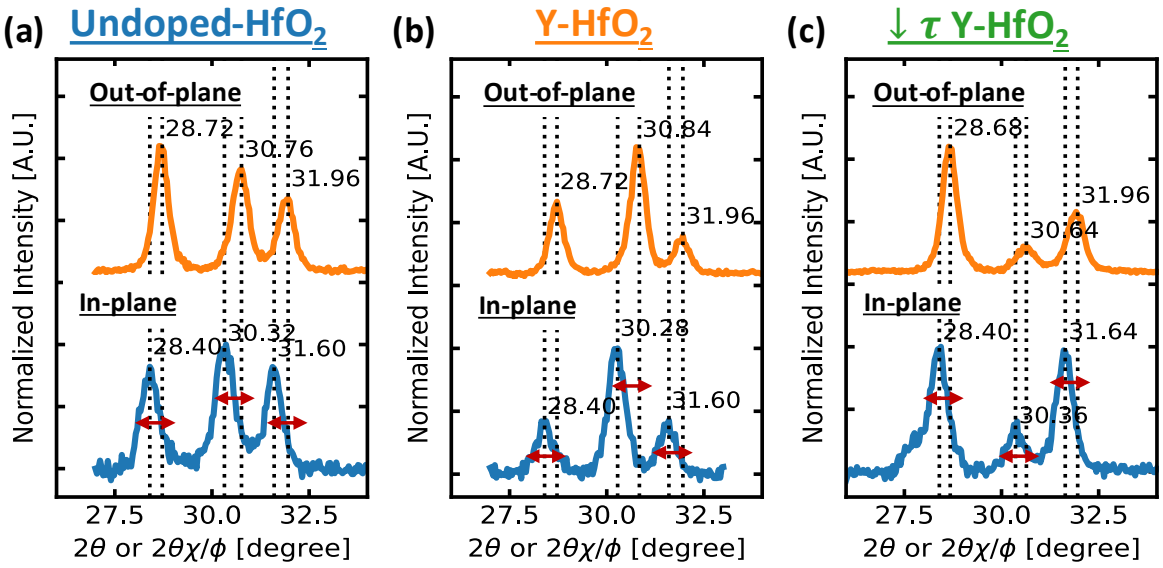


Fig. 5.4 In-plane and out-of-plane XRD patterns of (a) Undoped $HfO_2$, (b) Y-$HfO_2$, and ↓ $\tau$ Y-$HfO_2$ before electric field cycling. The same data as in Fig. 4.22.

Continue from Section 4.6,[1] we consistently observed an anomalous difference in the XRD peak positions difference between the in-plane and the out-of-plane diffractions, as shown in Fig. 5.4. This indicates that there is a difference between the **interplanar spacing** ($d_{spacing}$) that are parallel (out-of-plane) and perpendicular (in-plane) to the surface of $HfO_2$ thin films [78]. The schematic diagram showing the difference between an in-plane and an out-of-plane crystal plane is shown in Fig. 5.5. By comparing the observed peak positions with the M(111) and M($11\bar{1}$) of a bulk $HfO_2$ (as shown in Fig. 5.6) and a calculated stress-free O-phase of $HfO_2$ [87], we found that the out-of-plane $d_{spacing}$ are compressed. Even though it was reported that a strong preferred orientation in O-phase could be observed in some polycrystalline $HfO_2$ thin films [88], such a large difference in $d_{spacing}$ cannot be explained by the preferred orientation in O-phase. Besides it still could not explain the shrinkage of the M-phase's out-of-plane $d_{spacing}$.

[1] Same sample set discussed in Sections 4.4 & 4.6 is continued to be discussed in this section. However, the point of discussion is focusing on the anomalous structural distortion that was introduce in Section 4.6.

Hence, we attribute this anomalous difference between the in-plane and the out-of-plane $d_{\text{spacing}}$ to structural distortion that was induced during the annealing and cooling-down processes. We quantify the amount of structural distortion ($\Delta d_{\text{in-out}}$) to be the difference between the in-plane and out-of-plane $d_{\text{spacing}}$: $d_{\text{spacing}}^{\text{in-plane}}$ and $d_{\text{spacing}}^{\text{out-of-plane}}$, respectively:

$$\Delta d_{\text{in-out}} = d_{\text{spacing}}^{\text{in-plane}} - d_{\text{spacing}}^{\text{out-of-plane}}. \quad (5.1)$$

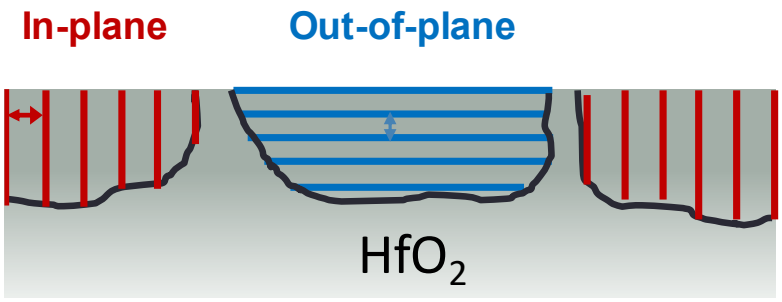


Fig. 5.5 (a) Schematic of in-plane and out-of-plane interplanar spacing that are perpendicular and parallel to the surface of $HfO_2$.(b) XRD pattern of a powder $HfO_2$.

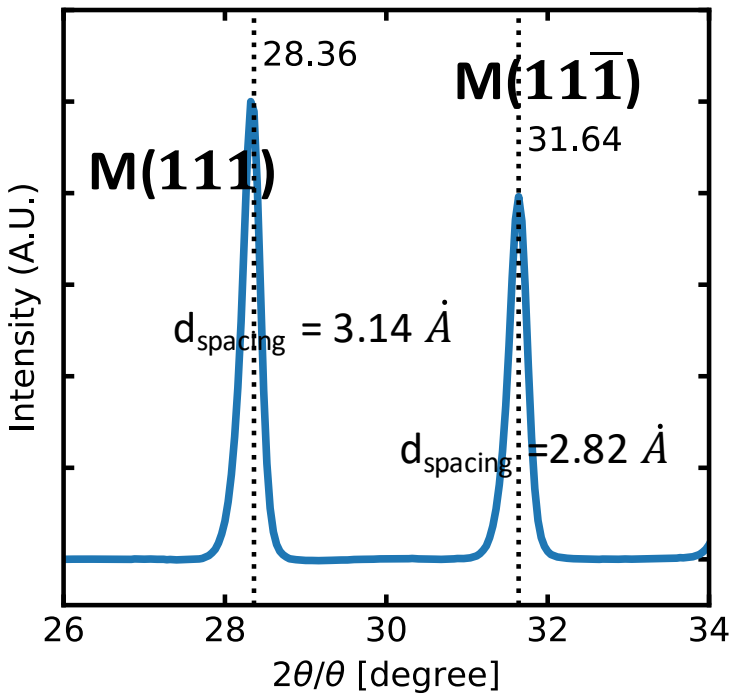


Fig. 5.6 XRD pattern of an experimentally observed bulk $HfO_2$, scanned using a conventional diffraction scan-axis (*i.e.*, $2\theta/\theta$ scan)

We introduced in Sections 4.5 and 4.6 that it is unconventional for a phase transformation to take place without thermal annealing, even though phase transformations driven by an electric field are commonly reported in FE-$HfO_2$. Note that it is a material property of FE-oxides that the structure of the polar phase re-orientates itself in response to the direction of the applied electric field, but not the phase transformation to the polar phase. We speculate that this unconventional phase transformation is governed by another phenomenon that is unique to $HfO_2$ thin films and has not yet been discussed. Because it is known that unidirectional stress [79]–[81] and structural distortion [82], as well as the distortion near the interphase boundaries [83], are critical factors in the determination of phase stabilization in FE-$HfO_2$, we speculate that $\Delta d_{\mathrm{in-out}}$ is one of the crucial factors that govern the unconventional phase transformation.

We found that there is a relationship between the initial $\Delta d_{\mathrm{in-out}}$ and the amount of phase transformation ($r_{\mathrm{o,t,c}}^{\mathrm{after}}/r_{\mathrm{o,t,c}}^{\mathrm{before}}$), as shown in Fig. 5.7. In turn, there is also a relationship between the initial $\Delta d_{\mathrm{in-out}}$ and the $r_{\mathrm{woke}}$, as shown in Fig. 5.8(a), since in Chapter 4 we already clarified that the origin of the waking-up effect. We hypothesize that $\Delta d_{\mathrm{in-out}}$ is one of the driving forces that determine the $r_{\mathrm{woke}}$ of FE-$HfO_2$ via the unconventional phase transformation to be driven by an electric field. Our model of the waking-up effect in FE-$HfO_2$ is summarized in Fig. 5.8(b). Detail of the discussion on the $\Delta d_{\mathrm{in-out}}$ as a driving force that determine the $r_{\mathrm{woke}}$ of FE-$HfO_2$ can be found in Ref [89].

In the current set of experiments, the $\downarrow \tau$ Y-$HfO_2$ was intentionally prepared to demonstrate that the initial $\Delta d_{\mathrm{in-out}}$ can be reduced, as well as its $r_{\mathrm{woke}}$. Nevertheless, an offset of approximately 2 pm is still observed, as shown in Fig. 5.8(a). This suggests that cooling time is not the main factor that determines the $\Delta d_{\mathrm{in-out}}$, where we speculate that this anomalous structural distortion, quantified as $\Delta d_{\mathrm{in-out}}$, is a crystallization property of $HfO_2$ thin films.

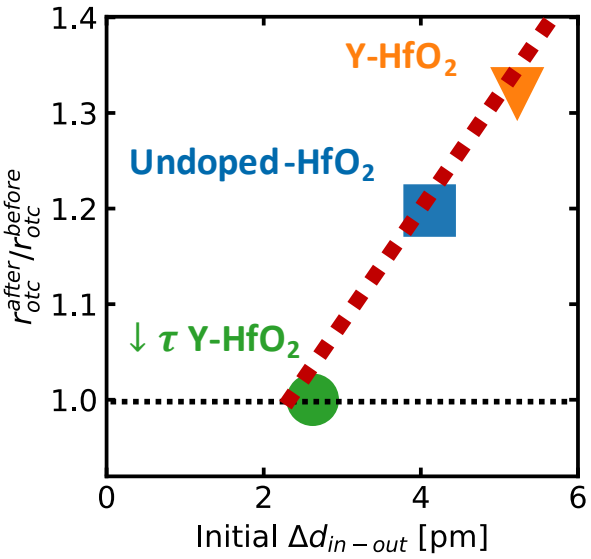


Fig. 5.7 The relationship between the initial $\Delta d_{\mathrm{in-out}}$ and the amount of the phase transformation that was driven by the electric field cycling ($r_{\mathrm{o,t,c}}^{\mathrm{after}}/r_{\mathrm{o,t,c}}^{\mathrm{before}}$).[1] The initial $\Delta d_{\mathrm{in-out}}$ is the $\Delta d_{\mathrm{in-out}}$ of the O/T/C peak before the electric field cycling.

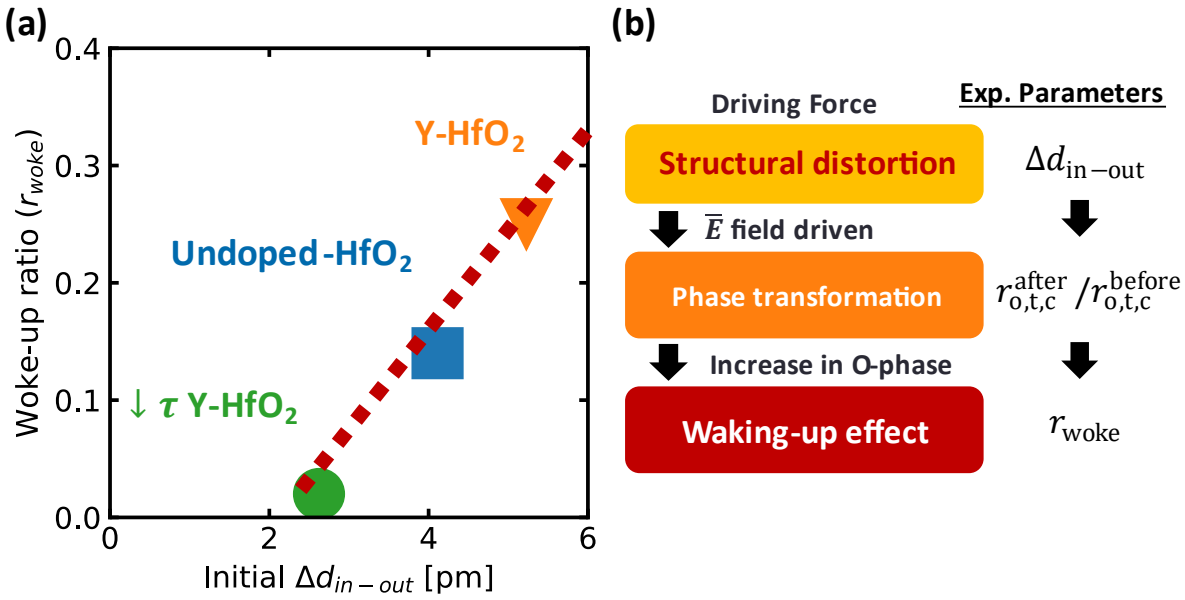


Fig. 5.8 (a) The relationship between the woke-up ratio ($r_{\mathrm{woke}}$)[2] and the initial amount of structural distortion ($\Delta d_{\mathrm{in-out}}$) of the O/T/C peak. The initial $\Delta d_{\mathrm{in-out}}$ is the $\Delta d_{\mathrm{in-out}}$ before electric field cycling. (b) The relationship between different phenomena in our model of the waking-up effect and how the experimental parameters are related to one another. The relationships between the $r_{\mathrm{woke}}$ and the $r_{\mathrm{o,t,c}}$; and between the $r_{\mathrm{o,t,c}}$ and the $\Delta d_{\mathrm{in-out}}$ were clarified in Fig. 4.20 and Fig. 5.7, respectively.

[1] The amount of the phase transformation that was driven by the electric field cycling ($r_{\mathrm{o,t,c}}^{\mathrm{after}}/r_{\mathrm{o,t,c}}^{\mathrm{before}}$) were obtained from Fig. 4.19.

[2] The woke-up ratio was previously quantified in Section 4.4.

## 5.3 Origin of the Structural Distortion

In the previous section, we found that there is a relationship between the initial $\Delta d_{\mathrm{in-out}}$ and the $r_{\mathrm{woke}}$ in our FE-$HfO_2$. To support our hypothesize that the $\Delta d_{\mathrm{in-out}}$ is one of the driving forces that determine the $r_{\mathrm{woke}}$ of FE-$HfO_2$, we have to clarify the origin of the anomalous structural distortion that we have experimentally observed.

We further investigate this anomalous structural distortion by analyzing the change in the in-plane and the out-of-plane $d_{\mathrm{spacing}}$, before and after the waking-up. Fig. 5.9(a-c) show the change in the in-plane and out-of-plane $d_{\mathrm{spacing}}$ before and after the waking-up for the O/T/C, M($11\bar{1}$), and M(111) peaks, respectively. From the figure, we found that the out-of-plane $d_{\mathrm{spacing}}$ remains constant after the waking-up in all three samples. Conversely, there is a large reduction in the in-plane $d_{\mathrm{spacing}}$ after the waking-up on Y-$HfO_2$ and Undoped-$HfO_2$, where the $r_{\mathrm{woek}}$ is relatively high.

The reduction in the in-plane $d_{\mathrm{spacing}}$ could suggest that an M→O phase transformation has taken place. Because the lattice constant of the O-phase is similar to T-/C- phase, O-phase is expected to have a smaller lattice constant than M-phase [90]. Therefore, an M→O phase transformation can result in shrinkage in the volume of $HfO_2$ and cause a reduction in the $d_{\mathrm{spacing}}$. This reduction in the $d_{\mathrm{spacing}}$ as a result of the M→O phase transformation is consistent with the increase $r_{\mathrm{o,t,c}}$ observed in Fig. 4.19 in Section 4.4. What could not explain is why there was no reduction in the out-of-plane $d_{\mathrm{spacing}}$, since the shrinkage in the volume of $HfO_2$ is not expected to be anisotropic. Thus, another factor must be involved in the determination of the $\Delta d_{\mathrm{in-out}}$ either before or after the waking-up.

A recap from the previous section, we found that the out-of-plane $d_{\mathrm{spacing}}$ of our FE-$HfO_2$ thin films are compressed. To explain the compressed out-of-plane $d_{\mathrm{spacing}}$ and the origin of the anomalous structural distortion, we consider that during the crystallization, the volume of $HfO_2$ underdoes a rapid shrinkage while the underlying substrate pins the in-plane $d_{\mathrm{spacing}}$. The diagram showing our consideration of the reduction in the volume of $HfO_2$ films during crystallization is illustrated in Fig. 5.10. It was also demonstrated that substrates can exert a force in an in-plane direction that can affect the polarization of FE-$HfO_2$ [79], [81]. Due to the large difference between the density of an amorphous $HfO_2$ and a crystalline $HfO_2$ [90], [91], a significant reduction in the volume is expected to have taken place, when the as-deposited $HfO_2$ films crystallized. The volume per formula of different phases in $HfO_2$ is shown in Table

5.1. Then, the decrease in the in-plane $d_{spacing}$, in Fig. 5.9, after electric field cycling could be explained by the release of the strain exerted by the substrate. We also found that the $\Delta d_{in-out}$ is related to the $r_{o,t,c}$ as shown in Fig. 5.11, where the lower $\Delta d_{in-out}$ observed on $\downarrow \tau$ Y-$HfO_2$ could also be explained by the re-expansion of the structure because Y-$HfO_2$ has lower $r_{o,t,c,}$ and M-phase has a larger volume than O/T/C-phase [90]. Next, we will verify the $\Delta d_{in-out}$ can be universally explained by the crystallinzation of the O/T/C phase.

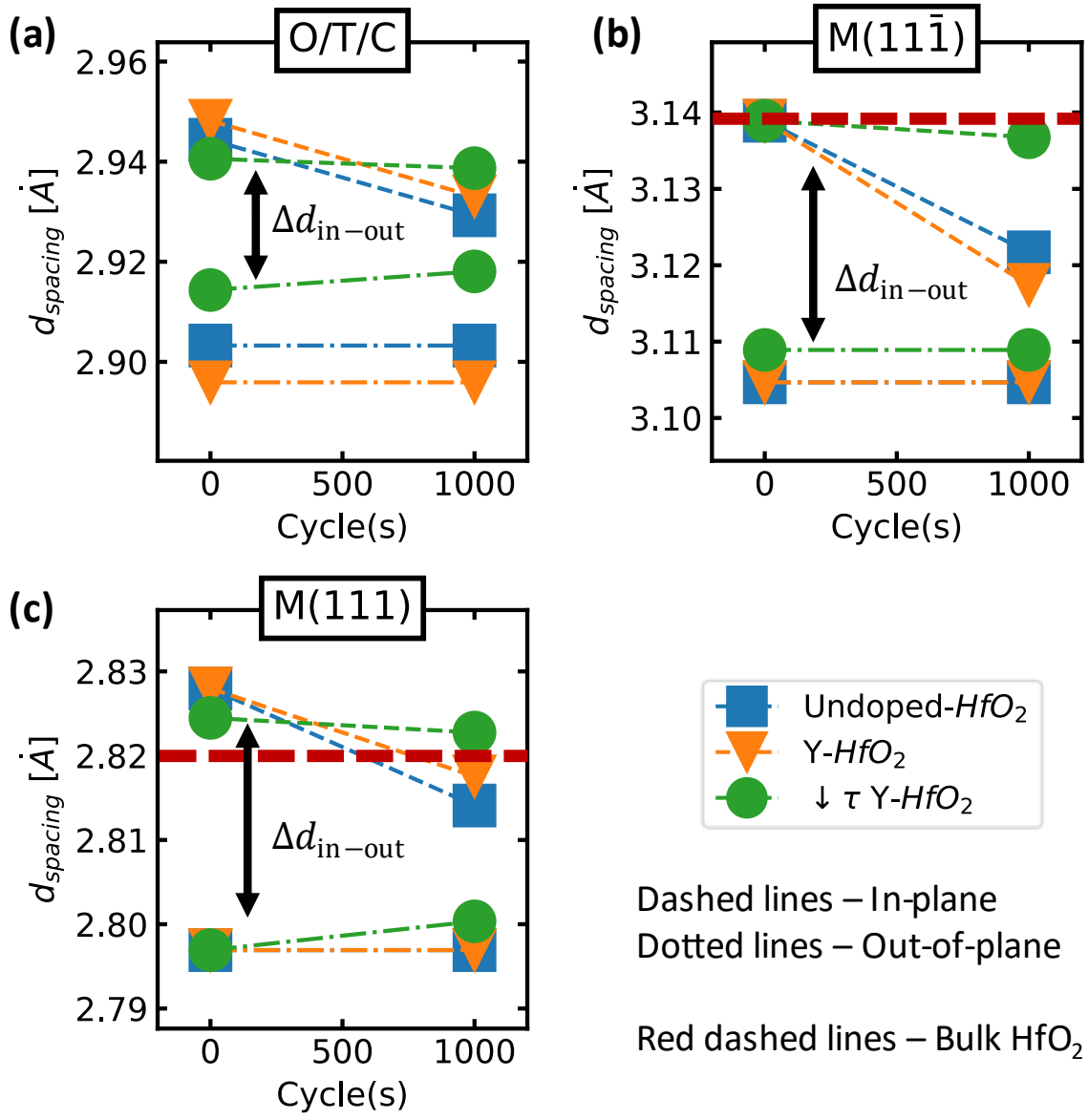


Fig. 5.9The change in in-plane and out-of-plane interplanar spacing ($d_{spacing}$) before and after the waking-up for (a) the O/T/C(111), (b) M(11$\bar{1}$), and (b) M(111) peaks. Red dashed lines are the $d_{spacing}$ of bulk $HfO_2$ in Fig. 5.6.

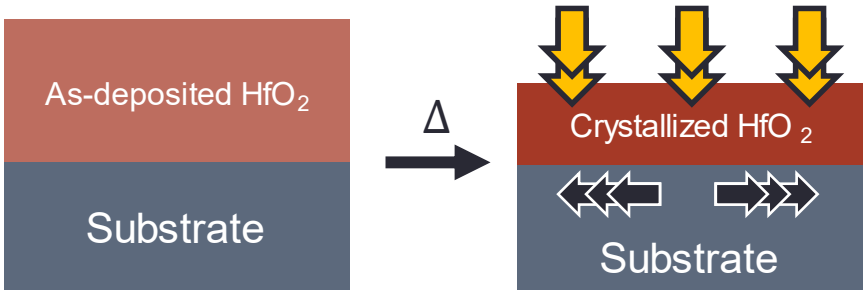


Fig. 5.10 A diagram on our consideration of the shrinkage in the volume of $HfO_2$ during crystallization while the underlying substrate pins the in-plane $d_{spacing}$.

Table 5.1 Volume per unit formula ($Å^3$) of different phases in $HfO_2$ [90], [91].

| Volume. per formular ($Å^3$) | C | T | M | Amorp. |
|---|---|---|---|---|
| | 31.9 | 32.8 | 34.4 | 37.2 |

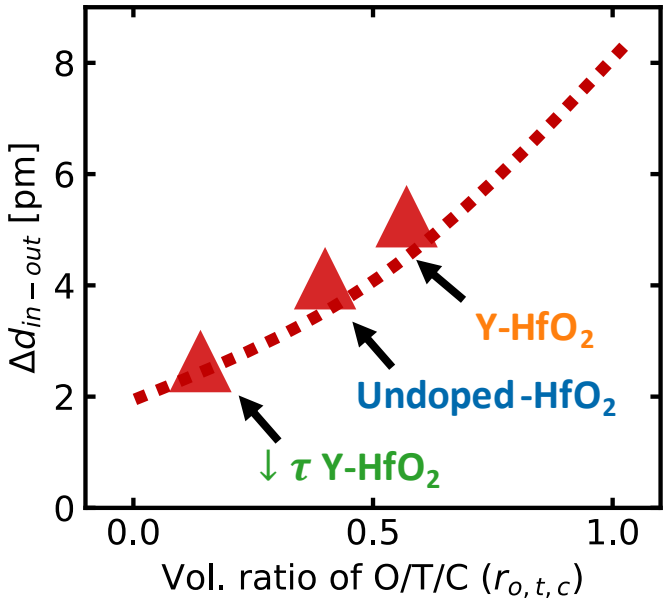


Fig. 5.11 The relationship between the initial $\Delta d_{\mathrm{in-out}}$ and the $r_{\mathrm{o,t,c.}}$ The data showing here was obtained from the same set of the experiment described in Sections 4.4 and 5.2.

## 5.3.1 Verification of our Hypothesis

To validate our model and hypothesis that

- the $\Delta d_{\mathrm{in-out}}$ is a driving force that determines the $r_{\mathrm{woke}}$ in FE-$HfO_2$ thin films, as shown in Fig. 5.8, and
- the origin of the anomalous structural distortion, as shown in Fig. 5.11,

we conducted three series of experiments to fabricate various FE-$HfO_2$ samples with different $r_{\mathrm{woke}}$, $\Delta d_{\mathrm{in-out}}$, and $r_{\mathrm{o,t,c}}$ by various fabrication conditions. The three fabrication conditions of interest are: Y-doping concentration, cooling time ($\downarrow \tau$), and annealing time ($\tau_{\mathrm{PDA}}$). In each set of experiments, other parameters were fixed, while the parameter of interest was varied to fabricate FE-$HfO_2$ with various $r_{\mathrm{woke}}$, $\Delta d_{\mathrm{in-out}}$, and $r_{\mathrm{woke}}$. Fig. 5.12 summarizes the experimental methods of each set of the experiments. The same analyses method that was described in Section 5.2 was conducted in the three sets of experiments. Sub-sections 5.3.1.1 - 5.3.1.3 provide the raw data and a detailed explanation for the three sets of experiments, but the main contents are summarizing here.

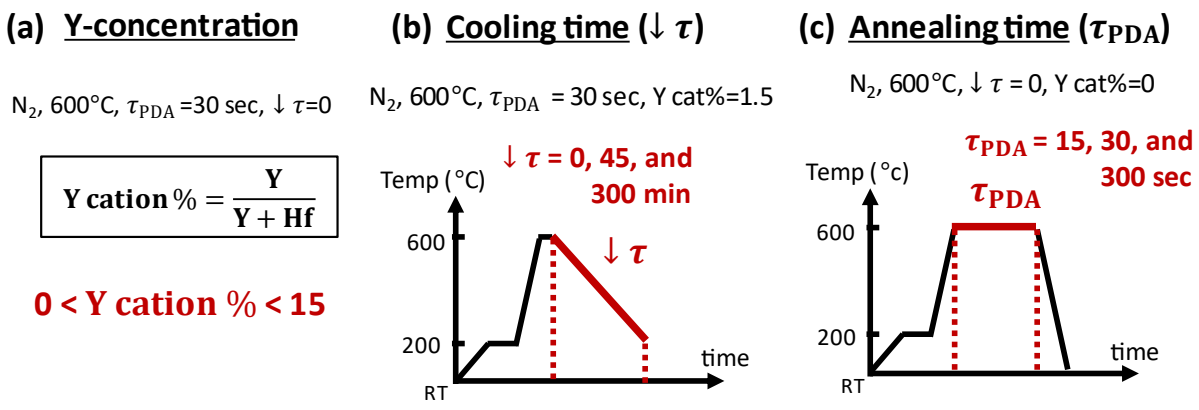


Fig. 5.12 The summaries of experimental methods for the three additional series of experiments focusing on the impact of (a) Y-doping concentration, (b) cooling time, and (c) annealing time on the $r_{\mathrm{woke}}$, $\Delta d_{\mathrm{in-out}}$, and $r_{\mathrm{o,t,c.}}$ In each series, other parameters were fixed; except for the parameter of interests.

After repeating the same analysis on the three series of experiments, we found that the $\Delta d_{\mathrm{in-out}}$ can be universally explained by the crystallization of the O/T/C phase, as shown in Fig. 5.13. This indicates that the anomalous structural distortion is originating from the shrinkage in the volume of $HfO_2$ films during the crystallization while the in-plane $d_{\mathrm{spacing}}$ was pinned by the underlying substrate. Where, the magnitude of the structural distortion, quantified as $\Delta d_{\mathrm{in-out}}$, can be explained by the amount of the denser crystalline phase (predominantly C-phase) during the crystallization. Unfortunately, we were not able to differentiate the phases among the O/T/C phase. Nevertheless, as $r_{\mathrm{o,t,c}}$ approaches unity, the samples are non-ferroelectric, and either C- or T-phase is expected to be the predominant crystal phase in the samples.

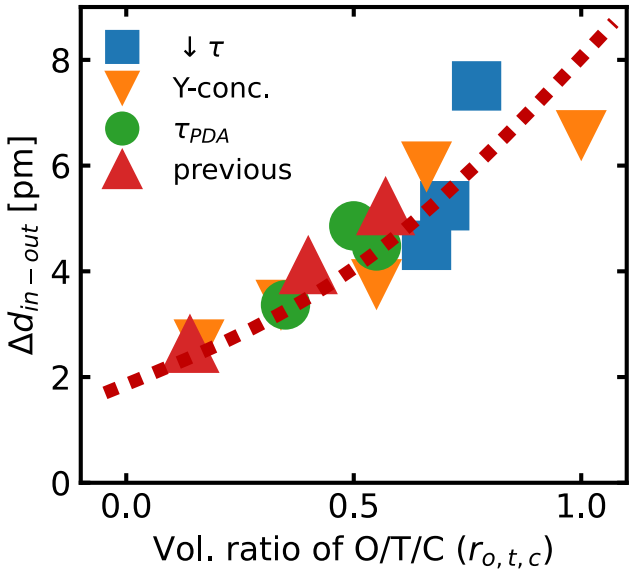


Fig. 5.13 The relationship between the initial $\Delta d_{\mathrm{in-out}}$ and the $r_{\mathrm{o,t,c.}}$ The data showing here is comprised of four different series of experiments with various FE-$HfO_2$ samples fabricated from various conditions. “previous” is the data set from at the beginning of Section 5.3. “Y-conc.”, “$\downarrow \tau$”,and “$\tau_{\mathrm{PDA}}$” are the data set from Section 5.3.1.1 -5.3.1.3, respectively.

We also found that the $r_{\mathrm{woke}}$ in various FE-$HfO_2$ samples fabricated with various conditions can also be universally explained by the initial $\Delta d_{\mathrm{in-out}}$, as shown in Fig. 5.14. This means that the structural distortion is not specific to a particular fabrication condition and is general to FE-$HfO_2$ in our system. This also indicates that the $\Delta d_{\mathrm{in-out}}$ is a factor, to our knowledge so far, that determines the $r_{\mathrm{woke}}$ of an FE-$HfO_2$ via the unconventional phase transformation.

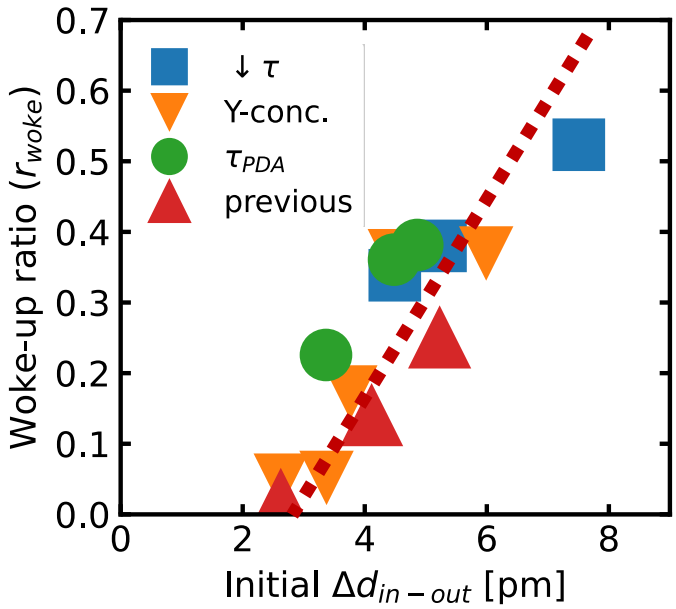


Fig. 5.14 The relationship between the $r_{\mathrm{woke}}$ and the initial $\Delta d_{\mathrm{in-out}}$ of the O/T/C peak. "previous" is the data set from at the beginning of Section 5.3. "Y-conc.", "↓ $\tau$",and "$\tau_{\mathrm{PDA}}$" are the data set from Section 5.3.1.1 -5.3.1.3, respectively.

### 5.3.1.1 Y-Doping Concentration

Several FE-$HfO_2$ and non-FE $HfO_2$ were fabricated on a heavily doped Ge substrate with different Y-doping concentrations. All $HfO_2$ samples can be categorized into three categories according to their Y-doping concentration range: **Undoped-$HfO_2$**, **Y-$HfO_2$** (~1.5 cat%), and **High Y-$HfO_2$** (>10 cat%).[1] All samples were annealed in $N_2$ ambient at 600 °C for 30 sec before letting the temperature drop freely. The change in the switchable polarization of several FE-$HfO_2$ and non-FE $HfO_2$ during electric field cycling is shown in Fig. 5.15. The differences between in-plane and out-of-plane XRD patterns of several $HfO_2$ films are shown in Fig. 5.16.

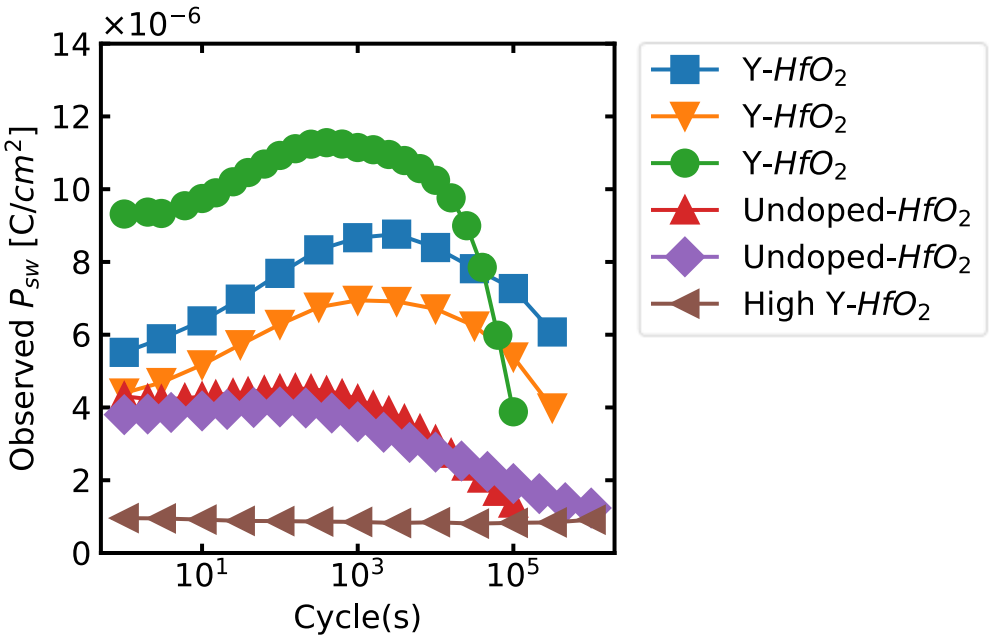


Fig. 5.15 The change in the observed switchable polarization ($P_{sw}$) of several FE-$HfO_2$ and non-FE $HfO_2$ during electric field cycling in Section 5.3.1.1. The observed $P_{sw}$ in High Y-$HfO_2$ is the result of the passive charge trapping that can produce a ferroelectric-like hysteresis [75].

[1] Some of the samples were carried out from Section 4.2.

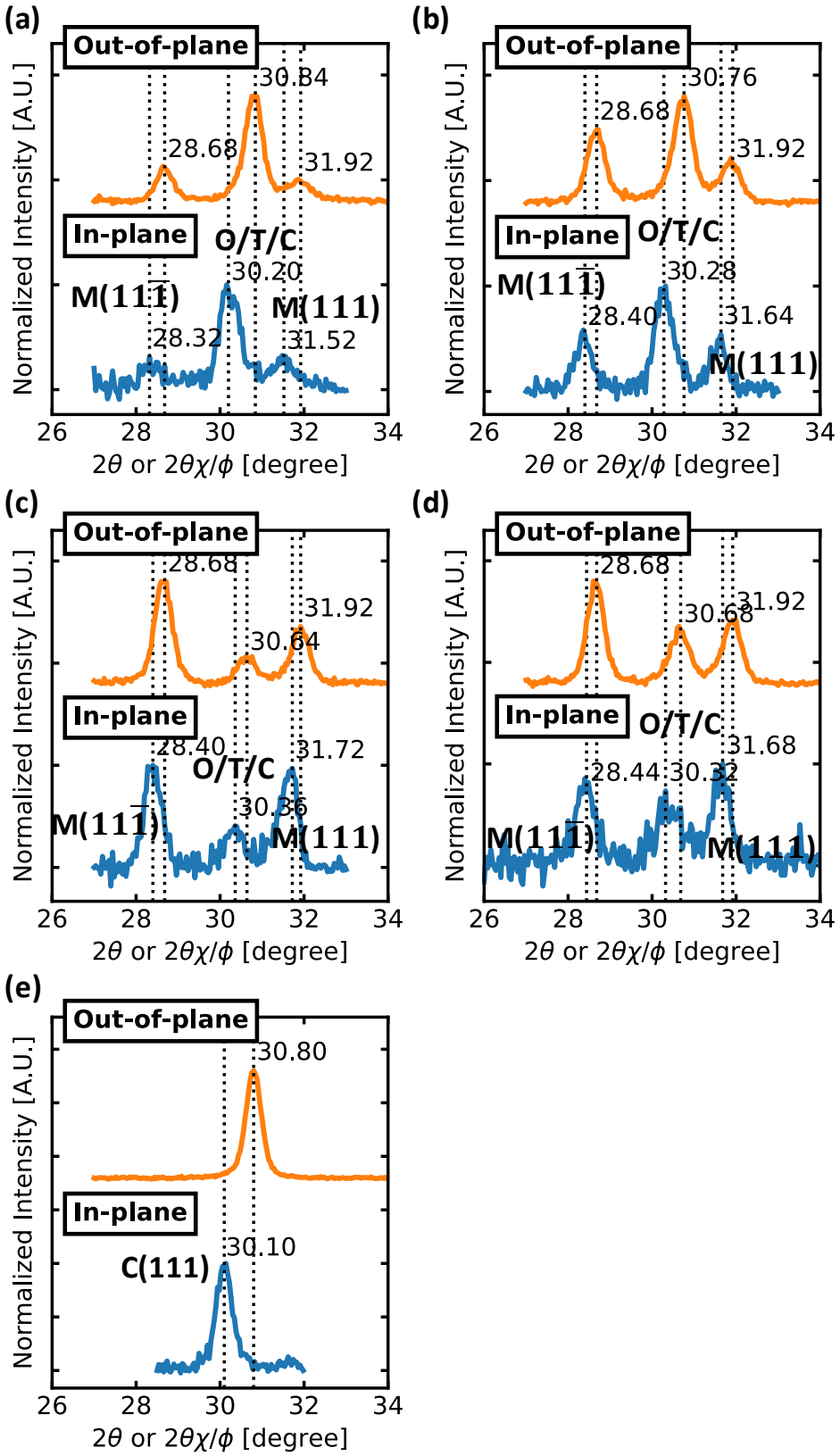


Fig. 5.16 In-plane and out-of-plane GIXRD patterns for (a,b) Y-$HfO_2$, (c, d) Undoped-$HfO_2$, and (e) High Y-$HfO_2$. All XRD patterns were made at an incident angle of 1.00°.

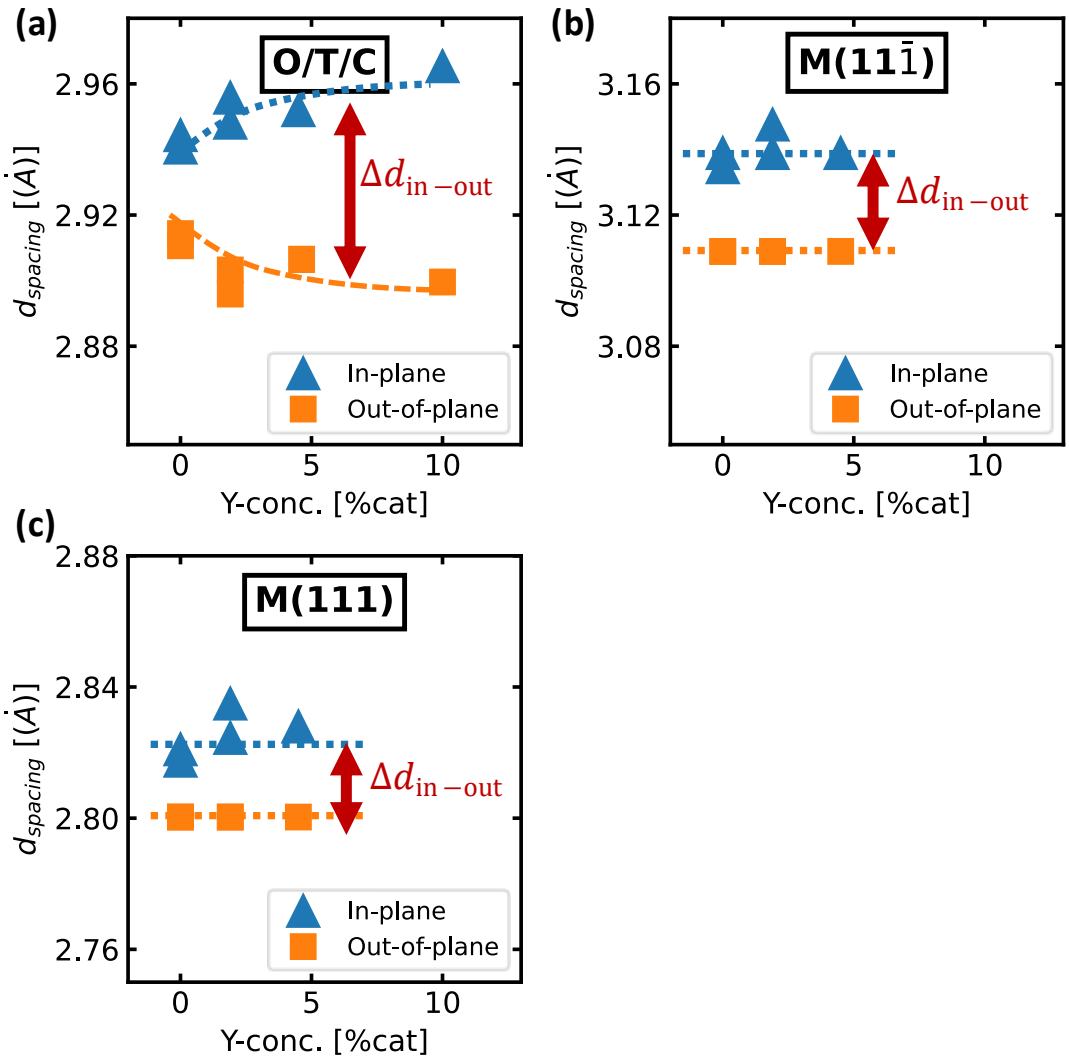


Fig. 5.17 The effect of Y-doping concentration on in-plane and out-of-plane $d_{\text{spacing}}$ on (a) O/T/C, (b) M(11$\bar{1}$), and (c) M(111) crystal plane. The $d_{\text{spacing}}$ was calculated from the peak position measured at $\theta_{\text{i}}$ = 1.00°.

Fig. 5.17(a-c) show the effect of Y-doping concentration on the $d_{\text{spacing}}$ of O/T/C, M(11$\bar{1}$), and M(111) crystal planes, respectively. From the figure, both the in-plane and out-of-plane $d_{\text{spacing}}$ of the O/T/C phase were significantly affected by the amount of Y-doping concentration. In contrast to the thermodynamically stable M-phase, both the out-of-plane interplanar spacing were not affected by the Y-doping concentration. This indicates that the $\Delta d_{\text{in}-\text{out}}$ induced by Y-doping concentration is a local phenomenon specific to the O/T/C phase. Fig. 5.18 shows the relationship between the $\Delta d_{\text{in}-\text{out}}$ and $r_{\text{o,t,c}}$, where other parameters were fixed except the Y-doping concentration. It is known that high Y-doping in $HfO_2$ can induce the formation of the C-phase [44], which has the highest density among the crystal phases in $HfO_2$ [90]. Then, the large $\Delta d_{\text{in}-\text{out}}$ in High Y-$HfO_2$ could be explained by the crystallization of C-phase, where larger shrinkage in the volume is expected to have taken place.

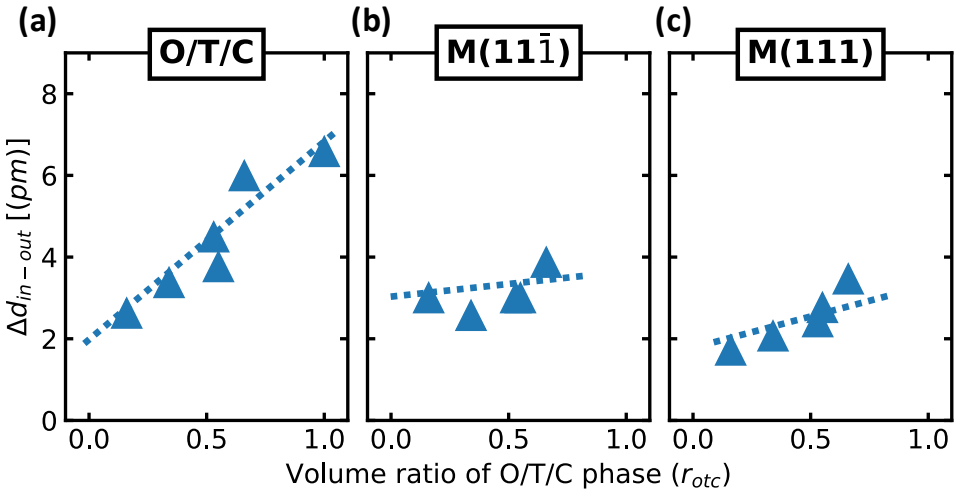


Fig. 5.18 The relationship between the $r_{o,t,c}$ and the $\Delta d_{\mathrm{in-out}}$ in (a) O/T/C, (b) M(11$\bar{1}$), and (c) m(111) crystal planes.

The relationship between the $\Delta d_{\mathrm{in-out}}$ and the $r_{o,t,c}$ of the current data set and the previous data set is shown in Fig. 5.19(a). The relationships obtained from the current and previous data set match with each other. This reinforces the validity of our hypothesis that the anomalous structural distortion is originating from the rapid shrinkage in the volume of $HfO_2$ during the crystallization while the in-plane $d_{\mathrm{spacing}}$ was pinned by the substrate. Fig. 5.19(b) shows the relationship between the $r_{\mathrm{woke}}$ and the initial $\Delta d_{\mathrm{in-out}}$ of two data sets. The $r_{\mathrm{woke}}$ of several FE-$HfO_2$ in both current and the previous data sets can be explained by the initial $\Delta d_{\mathrm{in-out}}$. This strengthen our model on the waking-up in FE-$HfO_2$ that the $\Delta d_{\mathrm{in-out}}$ is a driving force that determines the $r_{\mathrm{woke}}$ via the unconventional phase transformation.

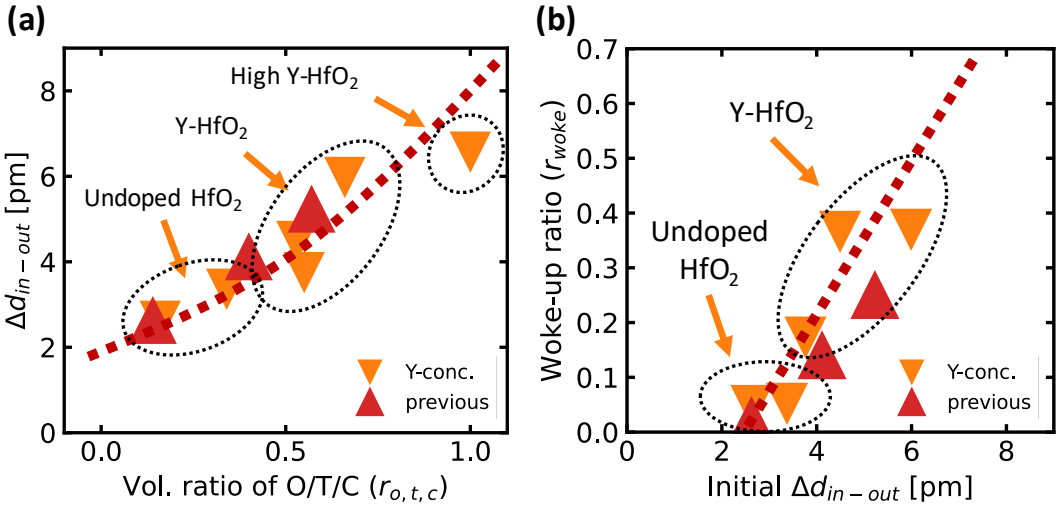


Fig. 5.19 (a) The relationship between the $\Delta d_{\mathrm{in-out}}$ and $r_{o,t,c}$ of both FE-$HfO_2$ and non-FE $HfO_2$ with different Y-doping concentrations. "Y-conc." is the current data set where other parameters were fixed except the Y-doping concentration. "previous" is the data set from at the beginning of Section 5.3. (b) The relationship between the $r_{\mathrm{woke}}$ and the initial $\Delta d_{\mathrm{in-out}}$ (*i.e.*, no electric field cycling was applied) of FE-$HfO_2$ with various Y-doping concentrations.

### 5.3.1.2 Cooling Time

Three FE-$HfO_2$ with approximately 1.5 Y-doped cation% were fabricated on p-type heavily doped Ge-substrates. All samples were annealed in $N_2$ ambient at 600 °C for 30 sec. After annealing, the cooling time ($\downarrow \tau$) from 600 °C to 200 °C was controlled to cool in **200 min**, **45 min**, and **0 min**. [1] $\downarrow \tau$ = 0 min means that after annealing the temperature was dropped. The same set of samples in Section 4.3 were carried out in this section. The change in the switchable polarization during electric field cycling of this sample set can be found in Fig. 4.9(a-c)), and the relationship between the $r_{woke}$ and $\downarrow \tau$ can be found in Fig. 4.12(d).

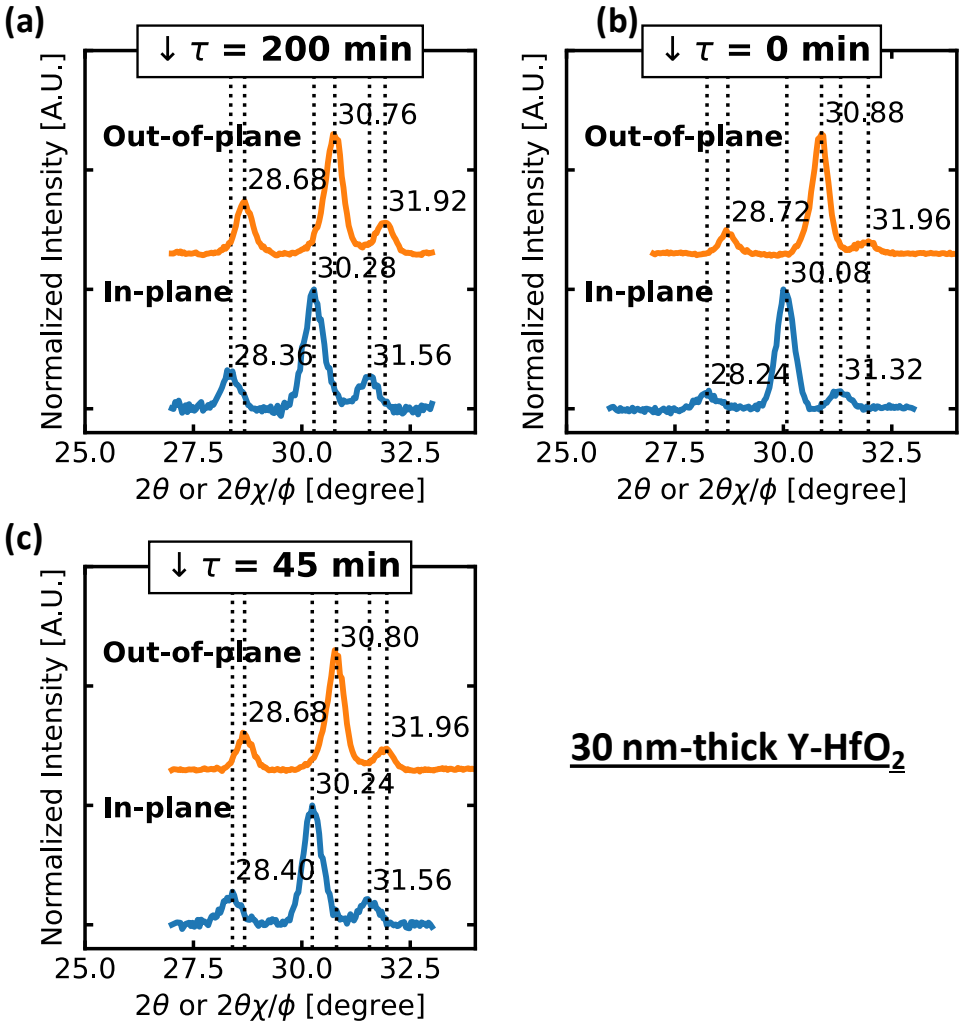


[1] These samples are the same samples described in Section 4.3, but here we are focusing on the impact of cooling time on the $\Delta d_{\mathrm{in-out}}$.

Fig. 5.20 In-plane and out-of-plane XRD patterns of 30 nm-thickY-$HfO_2$ at different cooling times after annealing at 600°C ($\theta_i$=1.00°).

Fig. 5.20 shows the in-plane and out-of-plane XRD patterns of Y-$HfO_2$ with different $\downarrow \tau$ after annealing at 600°C. The reduction in the $\Delta d_{\mathrm{in-out}}$ of the O/T/C, M($11\bar{1}$), and M(111) crystal planes with the increase the cooling time ($\downarrow \tau$) is shown in Fig. 5.21 (a-c), respectively. At $\downarrow \tau$=0, large $\Delta d_{\mathrm{in-out}}$ were observed in all crystal planes. With the increase in the $\downarrow \tau$ to 45 min, the $\Delta d_{\mathrm{in-out}}$ in all crystal planes was significantly reduced. A further increase in the $\downarrow \tau$ to 200 min, there was an extra minor reduction in the $\Delta d_{\mathrm{in-out}}$ in the O/T/C crystal plane. Whereas, in the two M-phase crystal planes, no further reduction in the $\Delta d_{\mathrm{in-out}}$ was observed and remains constant at ~ 3 pm. The reduction in the $\Delta d_{\mathrm{in-out}}$ with the increase in the $\downarrow \tau$ can be explained by the phase transformation to generate more M-phase, where there is less tendency for the volume of $HfO_2$ to shrink.[1] Fig. 5.22 also shows the relationship between the $\Delta d_{\mathrm{in-out}}$ and $r_{o,t,c}$ of Y-$HfO_2$ with different $\downarrow \tau$.

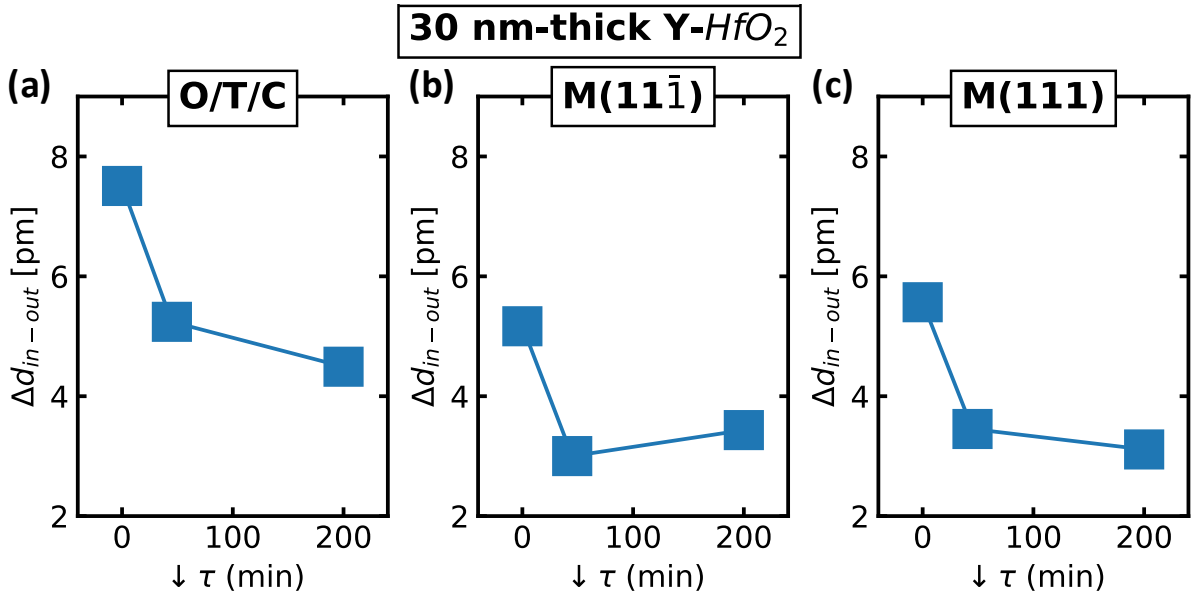


Fig. 5.21 The effect of cooling time ($\downarrow \tau$) on $\Delta d_{\mathrm{in-out}}$ of (a) O/T/C, (b) M($11\bar{1}$), and (c) M(111) crystal planes. The samples here are 1.5% Y-cation with a thickness of 30 nm.

[1] The impact of cooling time on the $r_{o,t,c}$ can be found on Fig. 4.13.

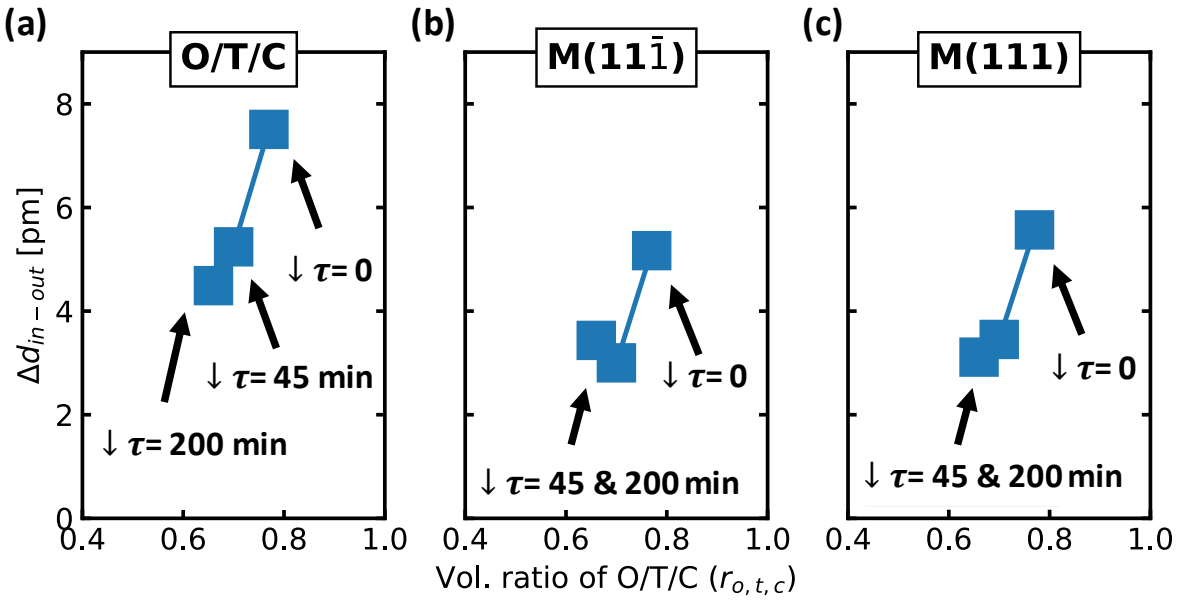


Fig. 5.22 The relationship between the $r_{o,t,c}$ and the $\Delta d_{\mathrm{in-out}}$ in (a) O/T/C, (b) M(11$\bar{1}$), and (c) M(111) crystal planes. The samples here are 1.5% Y-cation with a thickness of 30 nm at different cooling times (↓ $\tau$).

The relationship between the $\Delta d_{\mathrm{in-out}}$ and the $r_{o,t,c}$ of the current data set and the two previous data set is shown in Fig. 5.23(a). The relationship obtained from the current matches with the relationship obtained from the previous section (Section 5.3.1.1) and the beginning of Section 5.3. This reinforces the validity of our hypothesis that the anomalous structural distortion is originating from the rapid shrinkage in the volume of $HfO_2$ during the crystallization while the in-plane $d_{spacing}$ was pinned by the substrate. Fig. 5.23 (b) shows the relationship between the $r_{woke}$ and the initial $\Delta d_{\mathrm{in-out}}$ of the current data set and the two previous data sets. The $r_{woke}$ of several FE-$HfO_2$ fabricated at different Y-doping concentrations and ↓ $\tau$ can be explained by the initial $\Delta d_{\mathrm{in-out}}$. This strengthen our model on the waking-up in FE-$HfO_2$ that the $\Delta d_{\mathrm{in-out}}$ is a driving force that determines the $r_{woke}$ via the unconventional phase transformation.

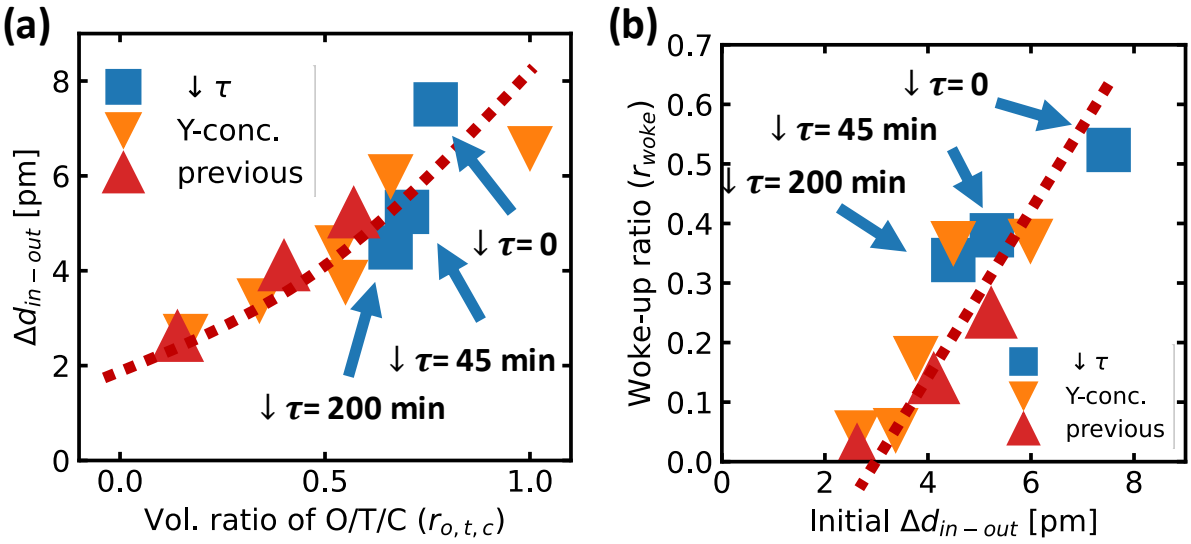


Fig. 5.23 (a) The relationship between the $\Delta d_{\mathrm{in-out}}$ and $r_{\mathrm{o,t,c}}$ of both FE-$HfO_2$ and non-FE $HfO_2$ with different cooling time ($\downarrow \tau$) and Y-doping concentrations. "$\downarrow \tau$" is the current data set where other parameters were fixed except the $\downarrow \tau$. "Y-conc." and "previous" are the two prevous data set obtained in Section 5.3.1.1 and the beginning of Section 5.3, respectively. (b) The relationship between the $r_{\mathrm{woke}}$ and the initial $\Delta d_{\mathrm{in-out}}$ (*i.e.*, no electric field cycling was applied) of FE-$HfO_2$ with various $\downarrow \tau$ and Y-doping concentrations.

.

### 5.3.1.3 Annealing Time

Three undoped FE-$HfO_2$ were fabricated on p-type heavily doped Ge-substrates. The three samples were annealed in $N_2$ ambient at 600 °C for **15 sec**, **30 sec,** and **300 sec**. After annealing, the temperature was dropped freely. The I-V and P-V characteristics of undoped $HfO_2$ at different annealing times ($\tau_{PDA}$) are shown in Fig. 5.24. The change in $P_{sw}$ during electric field cycling of undoped FE-$HfO_2$ with different $\tau_{PDA}$ are shown in Fig. 5.25(a), and the impact of $\tau_{PDA}$ on the $r_{woke}$ is summarized in Fig. 5.25(b).

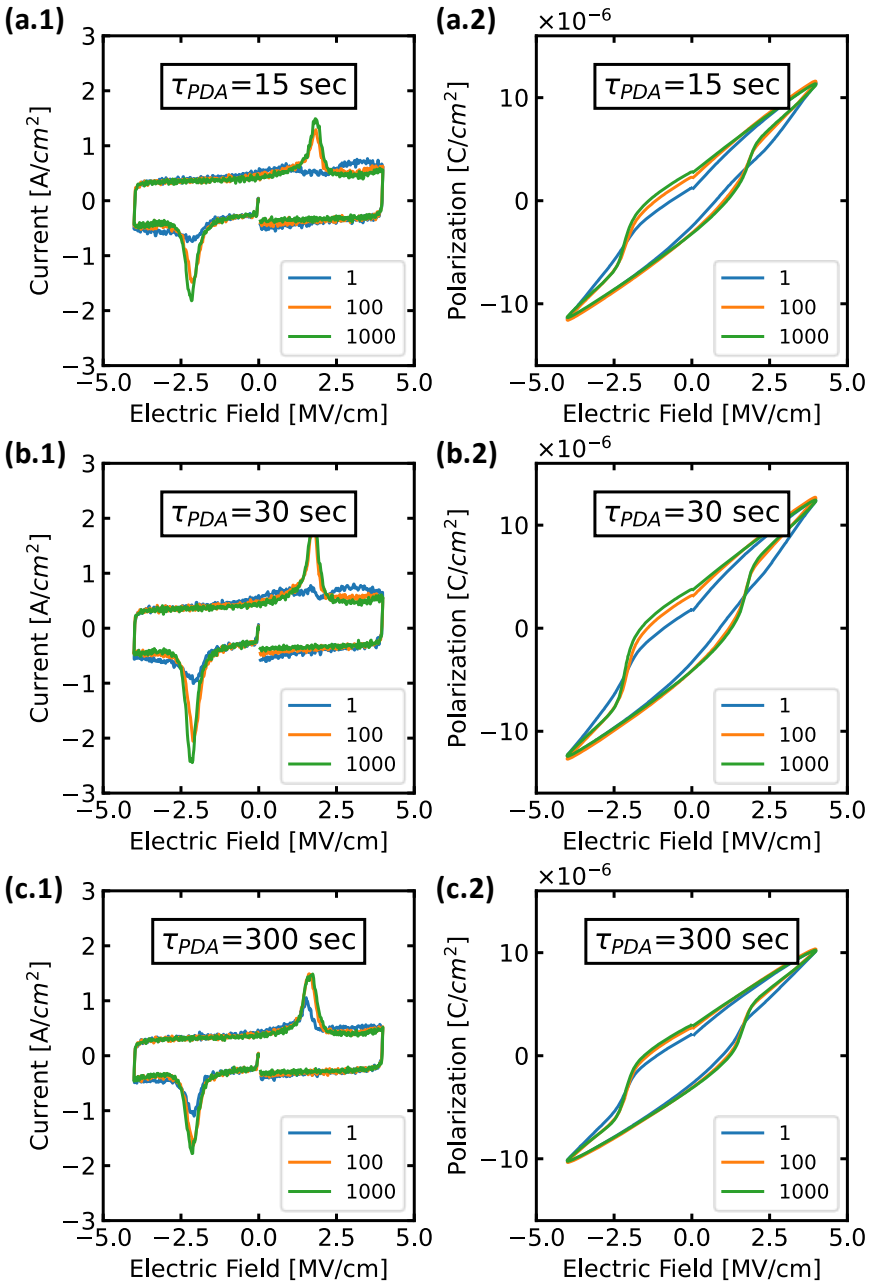


Fig. 5.24 The I-V and P-V characteristics during electric field cycling of several undoped $HfO_2$ annealed for (a) 15 sec, (b) 30 sec, (c) 300 sec.

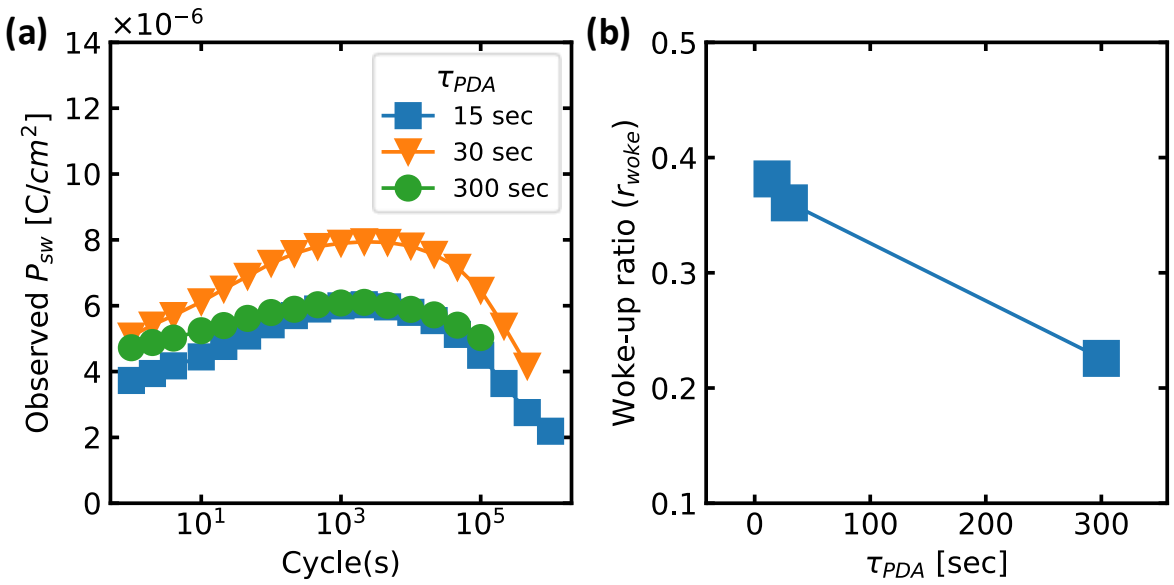


Fig. 5.25 (a) (a) The change in the switchable polarization ($P_{sw}$) during electric field cycling of several undoped $HfO_2$ annealed for 15 sec, 30 sec, and 300 sec. (b) The impact of annealing time ($\tau_{PDA}$) on the $r_{woke}$ calculated from (a).

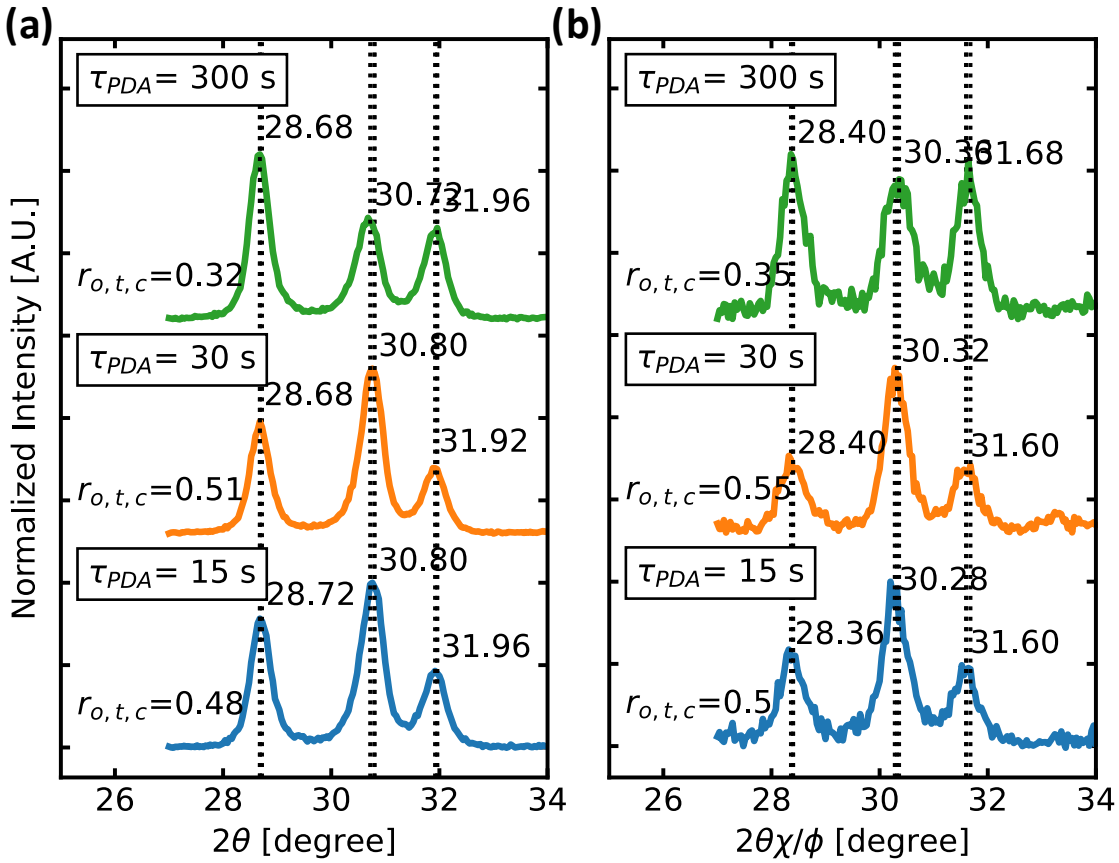


Fig. 5.26 (a) Out-of-plane and in-plane XRD patterns of 30 nm-thick undoped $HfO_2$ at different annealing time ($\tau_{PDA}$) ($\theta_i$=1.00°).

Fig. 5.26 (a) and (b) show the out-of-plane and in-plane XRD patterns undoped-$HfO_2$ at different $\tau_{\mathrm{PDA}}$. The reduction in the $\Delta d_{\mathrm{in-out}}$ of the O/T/C, M($11\bar{1}$), and M(111) crystal planes with the increase in the $\tau_{\mathrm{PDA}}$ is shown in Fig. 5.27 (a-c), respectively. With longer $\tau_{\mathrm{PDA}}$, less $\Delta d_{\mathrm{in-out}}$ in the O/T/C crytal plane is observed. Nonetheless, the $\Delta d_{\mathrm{in-out}}$ on the two M-phase crystal planes do not seem to be significantly affected by the $\tau_{\mathrm{PDA}}$. Longer $\tau_{\mathrm{PDA}}$ can allow the M-phase to be crystallized, since M-phase is in the thermodynamically stable phase in $HfO_2$. Then, the lower $\Delta d_{\mathrm{in-out}}$ when undoped $HfO_2$ was annealed for 300 sec can be explained by the re-expansion in the volume of $HfO_2$, since M-phase is the least dense crystalline phase in $HfO_2$. The relationship between the $\Delta d_{\mathrm{in-out}}$ and the $r_{\mathrm{o,t,c}}$ of several undoped $HfO_2$ annealed at the difference $\tau_{\mathrm{PDA}}$ is shown in Fig. 5.28. From the figure, it is clear that longer $\tau_{\mathrm{PDA}}$ allows more M-phase to be generated; thus, lower $\Delta d_{\mathrm{in-out}}$ and lower $r_{\mathrm{o,t,c}}$ were observed when a undoped $HfO_2$ was annealed at a longer $\tau_{\mathrm{PDA}}$.

The relationship between the $\Delta d_{\mathrm{in-out}}$ and the $r_{\mathrm{o,t,c}}$ of the current data set and the three previous data set is shown in Fig. 5.29(a). The relationship obtained from the current matches with the relationship obtained from the two previous sections (Section 5.3.1.1 & 5.3.1.2) and the beginning of Section 5.3. This again reinforces the validity of our hypothesis that the anomalous structural distortion is originating from the rapid shrinkage in the volume of $HfO_2$ during the crystallization while the in-plane $d_{\mathrm{spacing}}$ was pinned by the substrate. Fig. 5.29(b). shows the relationship between the $r_{\mathrm{woke}}$ and the initial $\Delta d_{\mathrm{in-out}}$ of the current data set and the other three data sets. The $r_{\mathrm{woke}}$ of several FE-$HfO_2$ fabricated at different Y-doping concentrations, $\downarrow \tau$, and $\tau_{\mathrm{PDA}}$ can all be explained by the initial $\Delta d_{\mathrm{in-out}}$. This validate our model on the waking-up in FE-$HfO_2$ that the $\Delta d_{\mathrm{in-out}}$ is a driving force that determines the $r_{\mathrm{woke}}$ via the unconventional phase transformation.

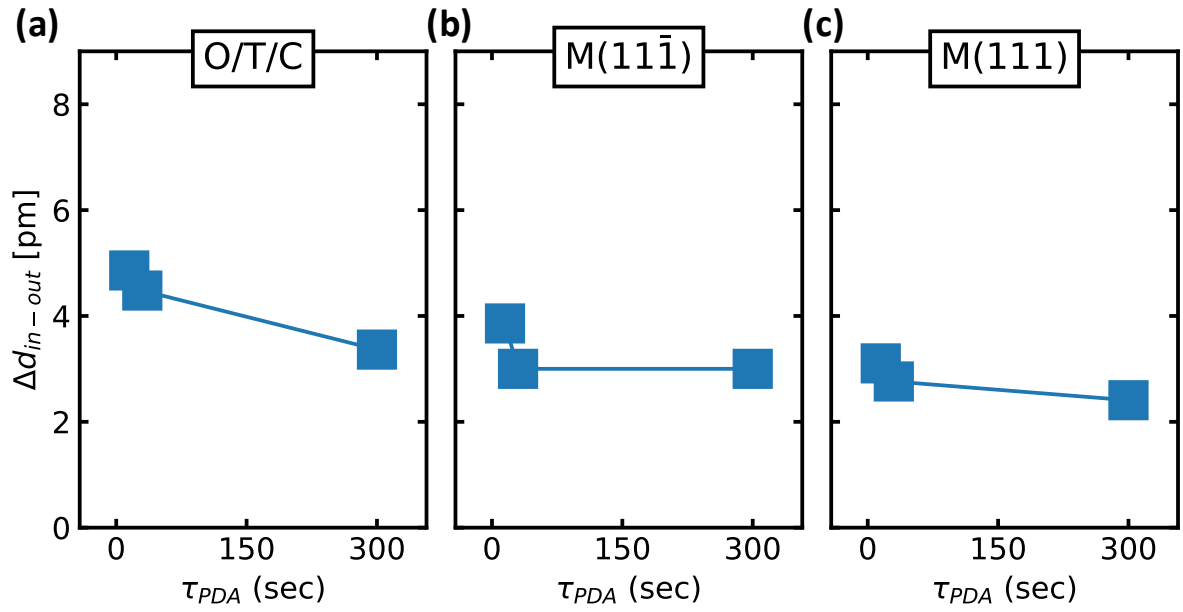


Fig. 5.27 The effect of annealing time ($\tau_{\mathrm{PDA}}$) on $\Delta d_{\mathrm{in-out}}$ of (a) O/T/C, (b) M(11$\bar{1}$), and (c) M(111) crystal planes. The samples here are undoped $HfO_2$ with a thickness of 30 nm.

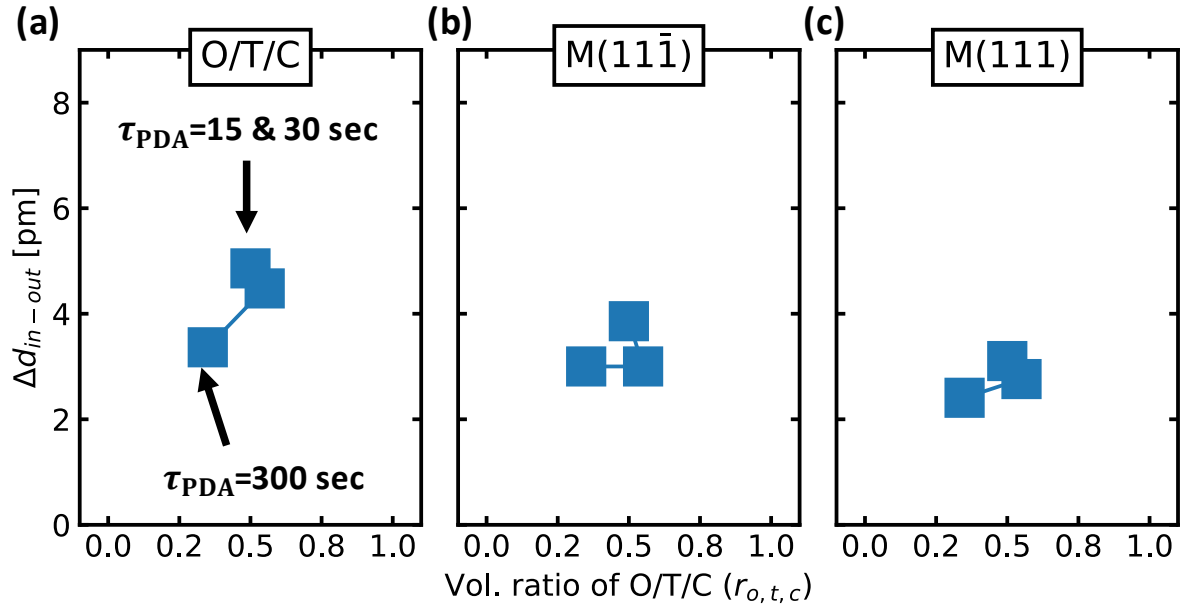


Fig. 5.28 The relationship between the $\Delta d_{\mathrm{in-out}}$ and the $r_{\mathrm{o,t,c}}$ of (a) O/T/C, (b) M(11$\bar{1}$), and (c) M(111) crystal planes. The samples here are undoped $HfO_2$ with a thickness of 30 nm annealed at different annealing times ($\tau_{\mathrm{PDA}}$).

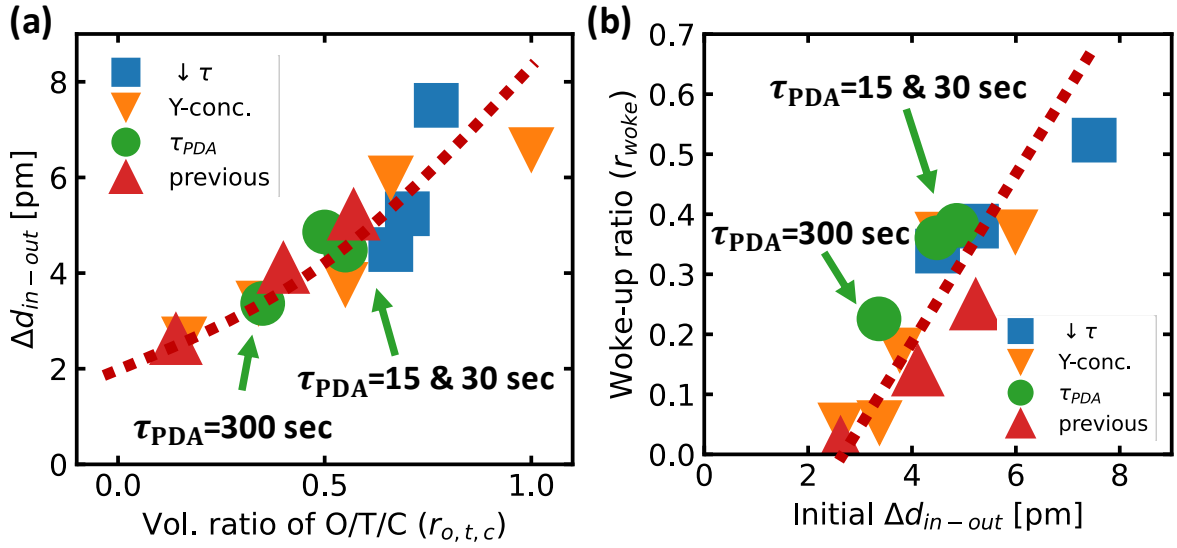


Fig. 5.29 (a) The relationship between the $\Delta d_{\mathrm{in-out}}$ and $r_{\mathrm{o,t,c}}$ of both FE-$HfO_2$ and non-FE $HfO_2$ with different annealing times ($\tau_{\mathrm{PDA}}$),cooling time ($\downarrow \tau$) and Y-doping concentrations. "$\tau_{\mathrm{PDA}}$" is the current data set where other parameters were fixed except the $\tau_{\mathrm{PDA}}$. "$\downarrow \tau$", "Y-conc." and "previous" are the three prevous data set obtained in Section 5.3.1.2, Section 5.3.1.1, and the beginning of Section 5.3, respectively. (b) The relationship between the $r_{\mathrm{woke}}$ and the initial $\Delta d_{\mathrm{in-out}}$ (*i.e.*, no electric field cycling was applied) of FE-$HfO_2$ with various $\tau_{\mathrm{PDA}}$, $\downarrow \tau$ and Y-doping concentrations. The data shown in (a) and (b) is the same datas that is shown in Fig. 5.13 and Fig. 5.14, respectively.

## 5.4 Structural Distortion in Other Ferroelectric and Non-Ferroelectric Systems

In the previous section,

- we had validated our model of the waking-up effect in FE-$HfO_2$ that the $\Delta d_{\mathrm{in-out}}$ is the driving force that determines the amount of phase transformation to be driven by an electric field.
- We also clarified that the structural distortion is originating from the rapid shrinkage in the volume of $HfO_2$ during the crystallization, while the underlying substrate pins the in-plane $d_{\mathrm{spacing}}$.

Despite our effort, our conclusion only extends to our FE-$HfO_2$ and non-FE $HfO_2$ system. That is, approximately 30 nm-thick $HfO_2$ films on Ge substrates, annealed in $N_2$ ambient without a capping layer Hence, we would like to extend our original finding to other ferroelectric and non-ferroelectric systems as well. Although we are not able to reach a conclusive conclusion, there are several questions that we would like to answer to reinforce the originality of our study, as shown below:

- Is there a depth dependence of the $\Delta d_{\mathrm{in-out}}$ both in our FE and non-FE $HfO_2$? How does the depth dependence affect the waking-up effect?
- How does a capping layer, which is a common technique to include higher polarization, affects the waking-up effect?
- How does surface energy, as a result of either the increase or decrease in the thickness, impact the $\Delta d_{\mathrm{in-out}}$? Does the $\Delta d_{\mathrm{in-out}}$ has a thickness dependence?
- Since all FE-$HfO_2$ samples in this study so far were annealed in $N_2$ ambient, is it possible that oxygen vacancies are that caused the structural distortion? Is the structural distortion unique to FE-$HfO_2$ films?
- Is the structural distortion unique only to $HfO_2$ films?

In the following sub-sections, we intend to answer those questions to get a bigger picture of the novel phenomenon that we observed. Answering these questions provides useful preliminary information and a starting point for any future studies.

## 5.4.1 Depth Dependence

In this section, we analyze the depth dependence of anomalous structural distortion. Although depth dependence of the $\Delta d_{\mathrm{in-out}}$ is covered by our current FE-$HfO_2$ system, it is important to understand the depth dependence of the $\Delta d_{\mathrm{in-out}}$ in the current system before analyzing the impact of the capping layer in the next section. The samples in this section were obtained from Section 5.3.1.1. **Undoped-$HfO_2$**, **Y-$HfO_2$**, and **High Y-$HfO_2$** were selected to represent an undoped $HfO_2$, a Y-doped $HfO_2$, and a high Y-doped $HfO_2$. To analyze the depth dependence of the $\Delta d_{\mathrm{in-out}}$, multiple XRD measurements were made on the sample but at various incident angles ($\theta_{\mathrm{i}}$).

Examples of a Y-$HfO_2$ out-of-plane and in-plane XRD patterns measured at several $\theta_{\mathrm{i}}$ are shown in Fig. 5.30(a) and (b), respectively. From the figure, there is a shift in the out-of-plane XRD peak positions to a higher diffraction angle at a lower $\theta_{\mathrm{i}}$; whereas the shift in the in-plane XRD peak positions was observed. A higher $\theta_{\mathrm{i}}$ means that the incident X-ray can penetrate deeper into $HfO_2$ films. The shift in the out-of-plane XRD peak positions to a higher diffraction angle at a lower $\theta_{\mathrm{i}}$ indicates that the surface of $HfO_2$ has a smaller out-of-plane $d_{\mathrm{spacing}}$ than the rest of the film. The X-ray penetration depth of $HfO_2$ can be found in Fig. 2.9.

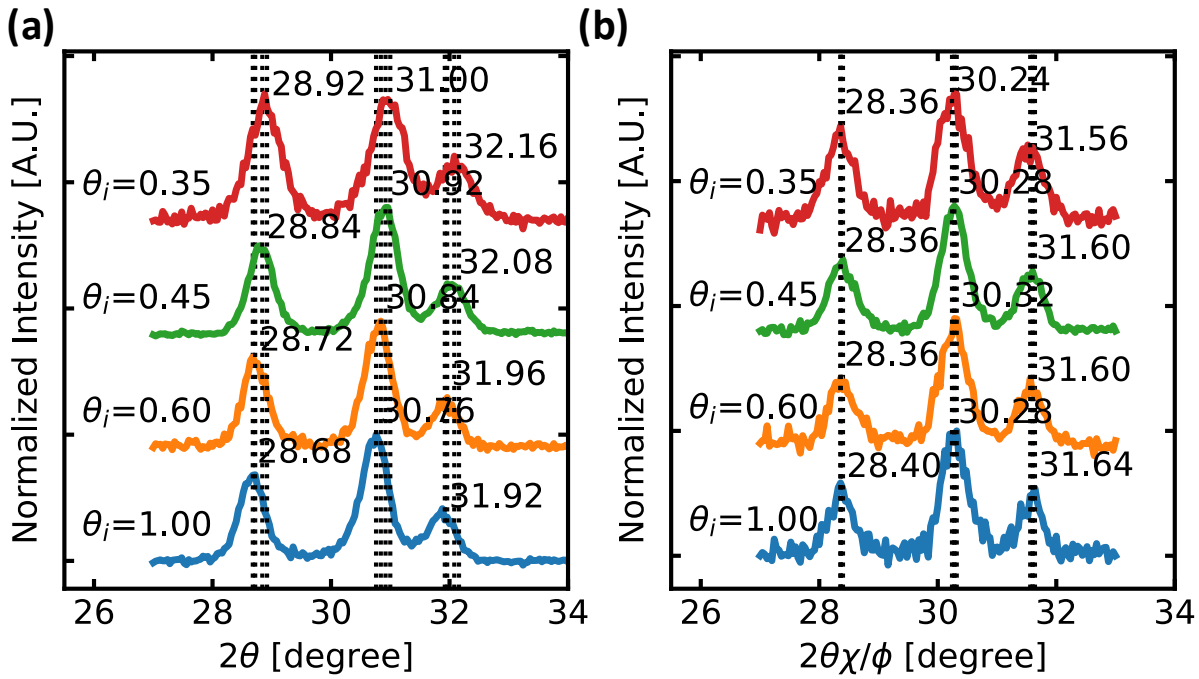


Fig. 5.30 (a) Out-of-plane and (b) in-plane XRD patterns of Y-$HfO_2$ measured at various incident angles ($\theta_i$)

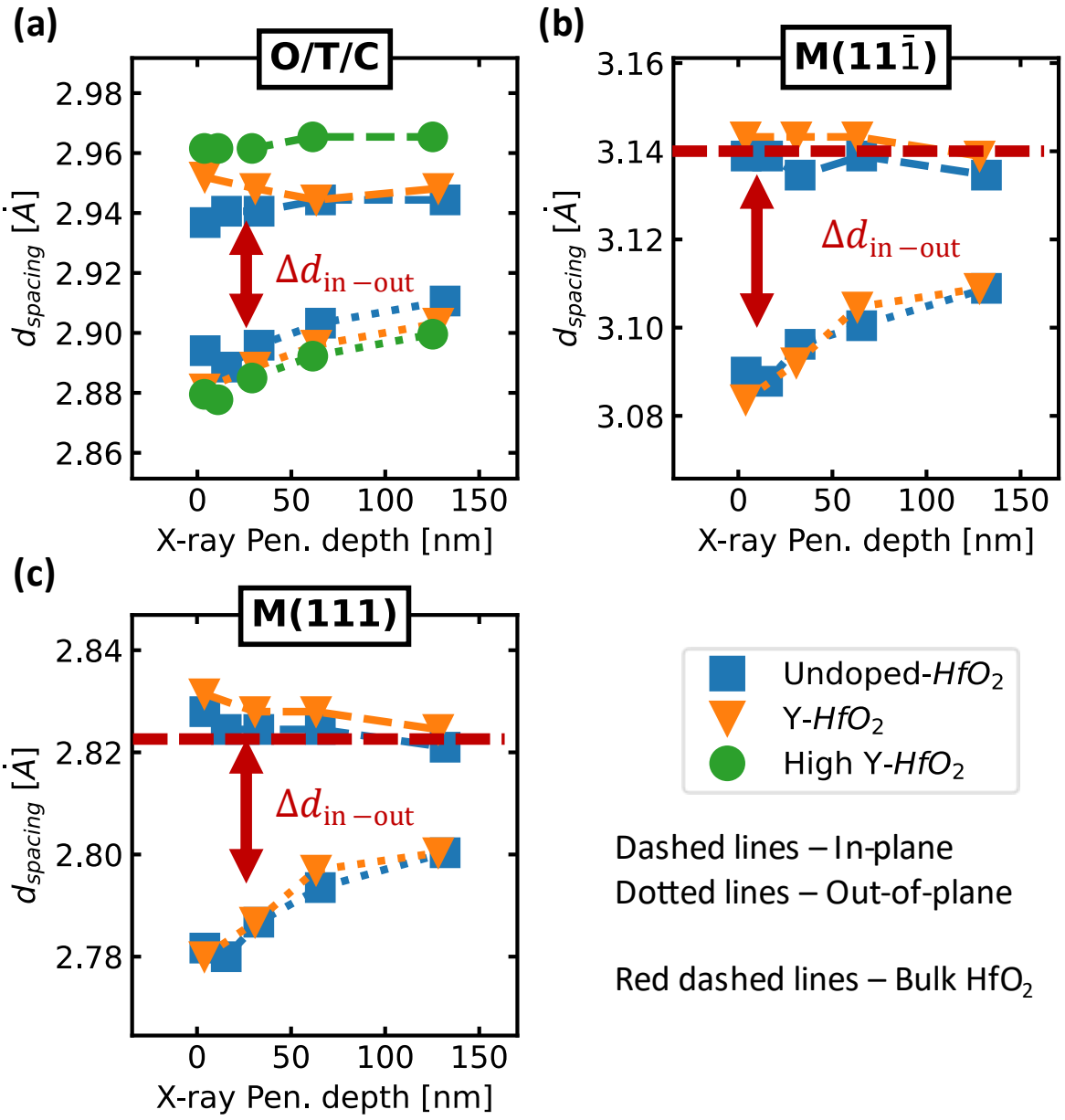


Fig. 5.31 Depth dependence of in-plane and out-of-plane $d_{spacing}$ of several $HfO_2$ films. Red dashed lines are the $d_{spacing}$ of bulk $HfO_2$ in Fig. 5.6.

The depth dependence of several $HfO_2$'s in-plane and out-of-plane $d_{spacing}$ is shown in Fig. 5.31. It can be seen from the figure that the in-plane $d_{spacing}$ is constant with the depth from the surface. Whereas the out-of-plane $d_{spacing}$ near the surface of $HfO_2$ is significantly compressed than the rest of the film. The depth dependence of $\Delta d_{\text{in}-\text{out}}$ of O/T/C, M(11$\bar{1}$), and M(111) crystal planes are summarized in Fig. 5.32. Although some variation in the depth dependence is expected between $HfO_2$ films fabricated with different conditions, it is clear that near the surface of both FE and non-FE $HfO_2$ films is more distorted than the rest of the films.

Moreover, it is also important to understand the depth dependence of the $r_{o,t,c}$ as well, since the amount of O/T/C phase being crystallized determines the $\Delta d_{in-out}$ which in turn determines the $r_{woke}$.[1] Fig. 5.33 shows the depth dependence of the $r_{o,t,c}$ of Y-$HfO_2$ and Undoped-$HfO_2$. From the figure, less amount of O/T/C phase can be observed near the top surface than the rest of the film; however, we already found that the top surface is also more distorted in Fig. 5.32. Although in Section 5.3 we conclude that the $\Delta d_{in-out}$ can be explained by the crystallization of the denser O/T/C phase, the contrast here suggests that the generation of the O/T/C phase and the shrinkage in the volume may have happened separately but not independently. Unfortunately, we do not have data to conclude the consideration of this experiment. We speculate that the crystallization took place from the $HfO_2$/Ge interface since the interface can provide nucleation sites for $HfO_2$ to crystallize. In the next sub-section, we will look that how the introduction of a capping layer may affect the depth dependence of the $\Delta d_{in-out}$ and $r_{o,t,c}$. In Chapter 6, we will also investigate how depth dependence of $\Delta d_{in-out}$ can play a role in the waking-up effect in our FE-$HfO_2$ system.

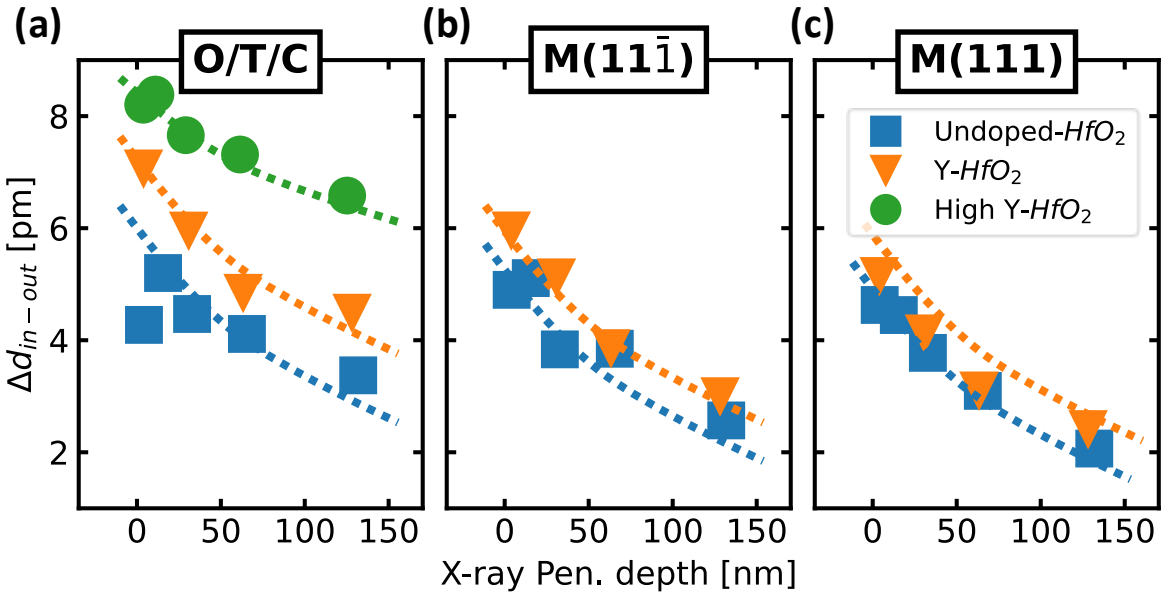


Fig. 5.32 Depth dependence of the $\Delta d_{in-out}$ in (a) the O/T/C, (b) M(11$\bar{1}$), and (c) M(111) crystal planes.

[1]The discussion on our model of the waking-up effect and the origin of the structural distortion can be found in Sections 5.2 &5.3, respectively.

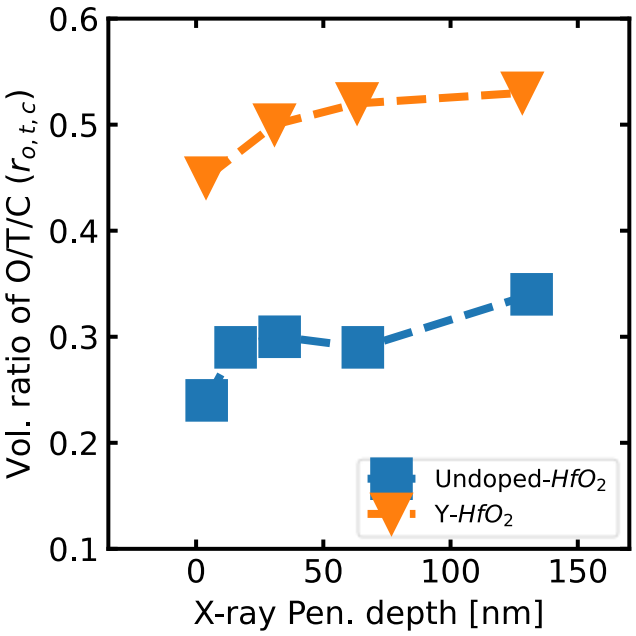


Fig. 5.33 Depth dependence of the $r_{o,t,c}$ in Undoped-$HfO_2$ and Y-$HfO_2$. The depth dependence of the $r_{o,t,c}$ in High Y-$HfO_2$ was not shown because the $r_{o,t,c}$ of High Y-$HfO_2$ equal to 1.00 regardless of the X-ray penetration depth.

## 5.4.2 Capping Effect

It is a typical fabrication condition to mechanically encapsulated $HfO_2$ films by a deposition of a capping layer, either a heat resistant metal or an oxide layer, before the annealing process, also known as the capping effect, to induce the formation of the O/T/C phase [12], [54], [84]–[86]. In this section, we investigated the impact of the capping effect on depth dependences of the $\Delta d_{\mathrm{in-out}}$ and the $r_{\mathrm{o,t,c}}$ by introducing an **$Al_2O_2$-capping layer (CL)** and an **$Al_2O_3$-interfacial layer (IL)** in $HfO_2$/Ge stacks. Undoped-$HfO_2$ layers were used in this section since we would like to exclude the contribution of dopant on the $\Delta d_{\mathrm{in-out}}$. The flowchart of the fabrication process is shown in Fig. 5.34.

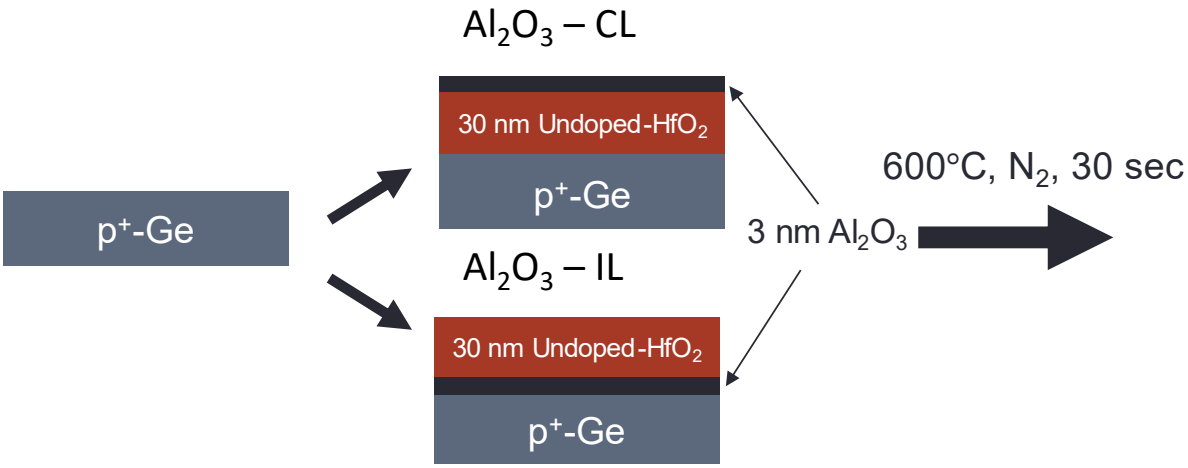


Fig. 5.34 The flowchart of the fabrication process of $Al_2O_3/HfO_2$/Ge ($Al_2O_3$ – Cap) and $HfO_2/Al_2O_3$/Ge ($Al_2O_3$ – IL) stacks.

In-plane and out-of-plane XRD patterns of the $Al_2O_3/HfO_2$/Ge and $HfO_2/Al_2O_3$/Ge stacks measured at various incident angles are shown Fig. 5.35. From the figure, no depth dependences were observed on the in-plane XRD peak positions of both stacks. The depth dependences of out-of-plane XRD peak positions were observed on both stacks, similar to the ones we observed in Section 5.4.1.

The depth dependences of the $r_{\mathrm{o,t,c}}$ in $Al_2O_3/HfO_2$/Ge, $HfO_2/Al_2O_3$/Ge, and the reference $HfO_2$/Ge stacks are shown Fig. 5.36. Both the insertion of $Al_2O_3$-CL and $Al_2O_3$-IL caused depth dependences of $r_{\mathrm{o,t,c}}$ to shift upward compared to the $HfO_2$/Ge stack. Despite the fact, a depth dependence of $r_{\mathrm{o,t,c}}$ is only observed in the $HfO_2/Al_2O_3$/Ge stack. Whereas, the $r_{\mathrm{o,t,c}}$ of the $Al_2O_3/HfO_2$/Ge stack remains constant regardless of the depth. It is known that surface energy [43], [47] and the mechanical encapsulation [12], [54], [84]–[86] of the CL can suppress the formation of the M-phase and favor the formation of the O/T/C phase. For this reason, the

upward shift in the depth dependence of $r_{o,t,c}$ due to the introduction of $Al_2O_3$ either a CL or an IL can be explained by the increase in the surface energy in the system which then suppresses the formation of the M-phase. The uniformed depth of $r_{o,t,c}$ in the $Al_2O_3/HfO_2/Ge$ stack can then be further explained by the nucleation of the O/T/C phase that took place from both $Al_2O_3/HfO_2$ and $HfO_2/Ge$ interfaces. We also speculate that the depth dependence of the $r_{o,t,c}$ would be more uniformed in a thinner $HfO_2$ film than a thicker $HfO_2$ film (both without a CL).

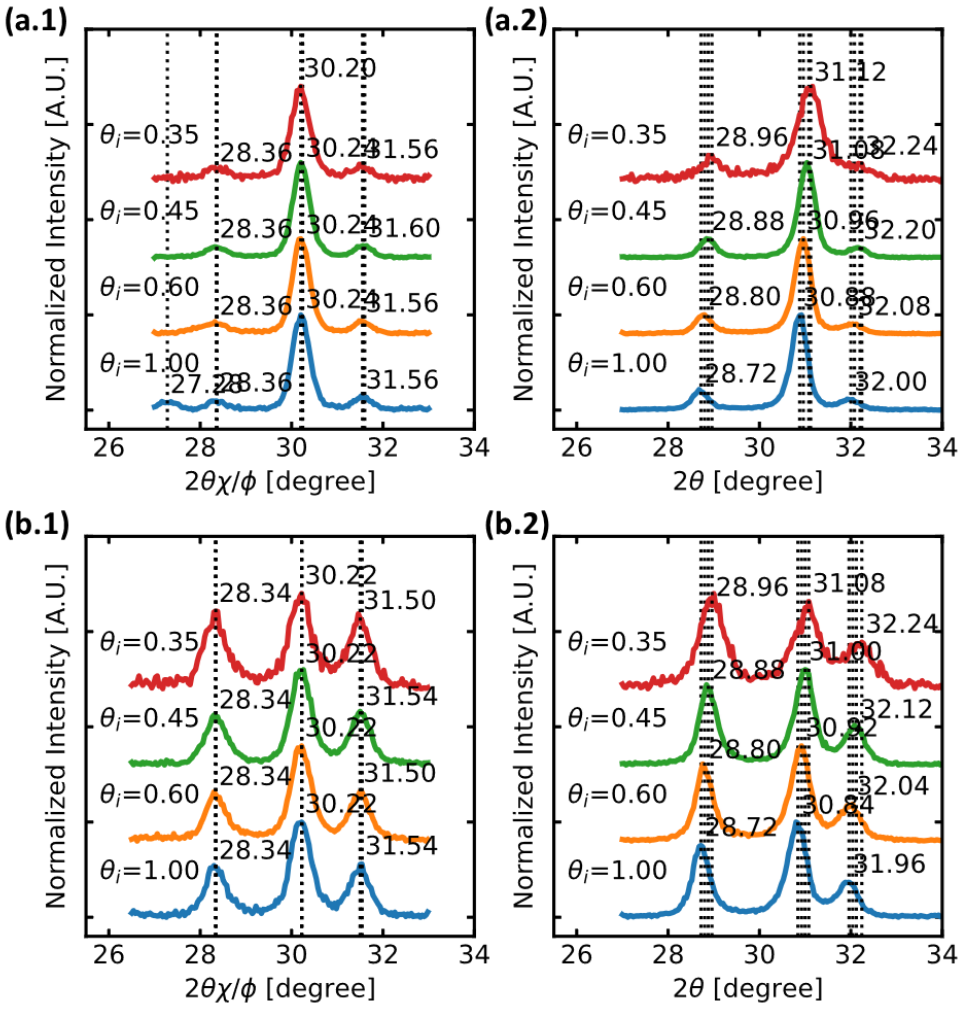


Fig. 5.35 In-plane (a.1 & b1) and out-of-plane (a.2 & b2) XRD patterns of (a) $Al_2O_3/HfO_2/Ge$ and (b) $HfO_2/Al_2O_3/Ge$ stacks.

Likewise to the increase in the $r_{o,t,c}$ with the insertion of either $Al_2O_3$-CL and $Al_2O_3$-IL, the insertion also increases the depth dependences of the $\Delta d_{\mathrm{in-out}}$. The depth dependences of $\Delta d_{\mathrm{in-out}}$ in the $Al_2O_3/HfO_2/Ge$, $HfO_2/Al_2O_3/Ge$, and the reference $HfO_2/Ge$ stacks are shown in Fig. 5.37. With the introduction of $Al_2O_3$ either as a CL or an IL, there was an increase in the depth dependences of $\Delta d_{\mathrm{in-out}}$ in the O/T/C and the two M-crystal planes compared to the reference $HfO_2/Ge$ stack. However, between the depth dependences of $\Delta d_{\mathrm{in-out}}$ induced by

an $Al_2O_3$-CL or an $Al_2O_3$-IL, there was almost no difference in the depth dependences of $\Delta d_{\mathrm{in-out}}$. Despite that we observed that there was more increase in the $r_{\mathrm{o,t,c}}$ (Fig. 5.36) when $Al_2O_3$ was inserted as a CL, the insertion of $Al_2O_3$-CL does not further shift the depth dependence of $\Delta d_{\mathrm{in-out}}$ upward.

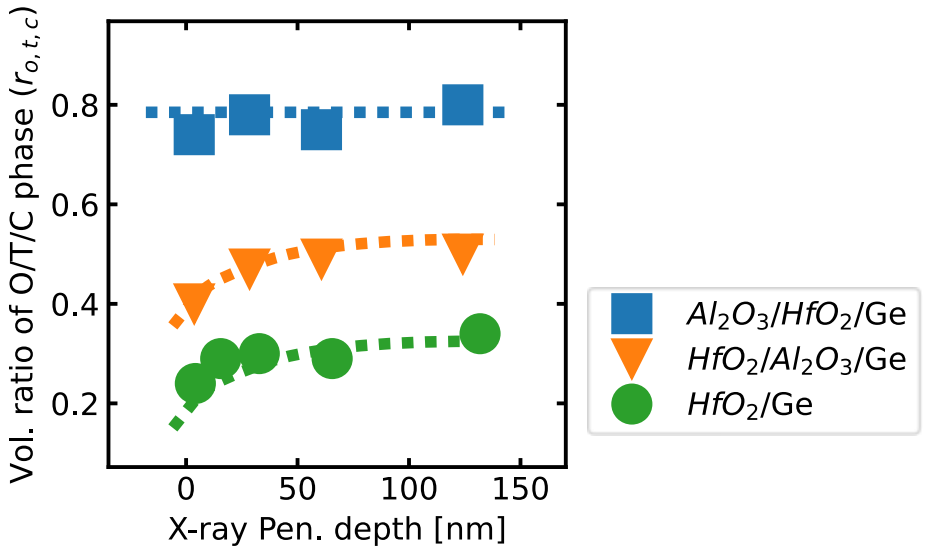


Fig. 5.36 Depth dependence of $r_{\mathrm{o,t,c}}$ of $Al_2O_3/HfO_2$/Ge, $HfO_2/Al_2O_3$/Ge, and the reference $HfO_2$/Ge stacks.

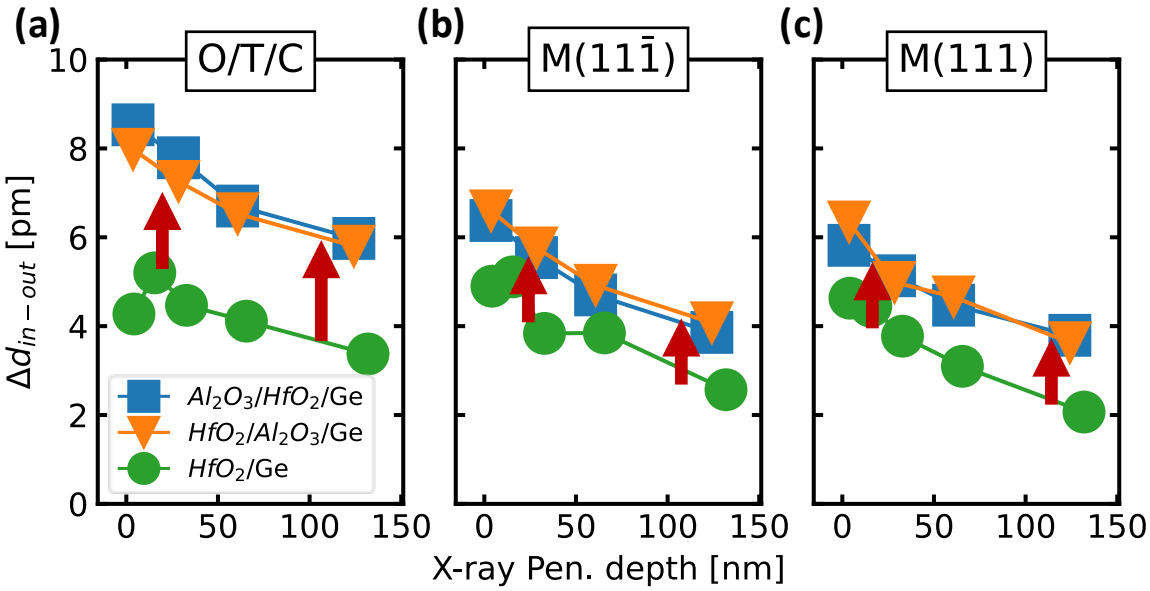


Fig. 5.37 The impact of the insertion of $Al_2O_3$ either as a capping layer or an interlayer on the depth dependences of $\Delta d_{\mathrm{in-out}}$ in (a) O/T/C, (b) M(11$\bar{1}$), and M(111) crystal planes.

We further analyzed the impact of $Al_2O_3$ insertion (either as a CL or IL) on the in-plane and the out-of-plane $d_{\mathrm{spacing}}$. Fig. 5.38 shows the depth dependences of $d_{\mathrm{spacing}}$ in the $Al_2O_3/HfO_2$/Ge, $HfO_2/Al_2O_3$/Ge, and the reference $HfO_2$/Ge stacks. Comparing the $d_{\mathrm{spacing}}$ of the reference $HfO_2$/Ge stack with the $d_{\mathrm{spacing}}$ of the two stacks with $Al_2O_3$ insertion, the insertion

of $Al_2O_3$ (either as a CL or an IL) causes the in-plane and out-of-plane $d_{spacing}$ to be more expanded and compressed, respectively. The expanded and compressed $d_{spacing}$ are more pronounced on the O/T/C crystal plane than the two M-phase crystal planes. We think that the insertion of $Al_2O_3$-CL can provide an additional layer to pin the in-plane $d_{spacing}$ apart from the underlying substrate. Consequently, the $Al_2O_3$-CL can act as an additional layer for nucleation to take place. As a result, more amorphous $HfO_2$ can be crystallized and caused the out-of-plane $d_{spacing}$ to be more compressed. Unfortunately, it is unclear why there is no significant difference in the depth dependencies of $d_{spaicng}$ between $Al_2O_3/HfO_2/Ge$ and $HfO_2/Al_2O_3/Ge$ stacks. We speculate that the nucleation and crystal growth took place predominantly from $Al_2O_3/HfO_2$ interfaces; thus, there is no significant difference in the depth dependencies of $d_{spaicng}$ with $Al_2O_3$ was inserted either as a CL or an IL.

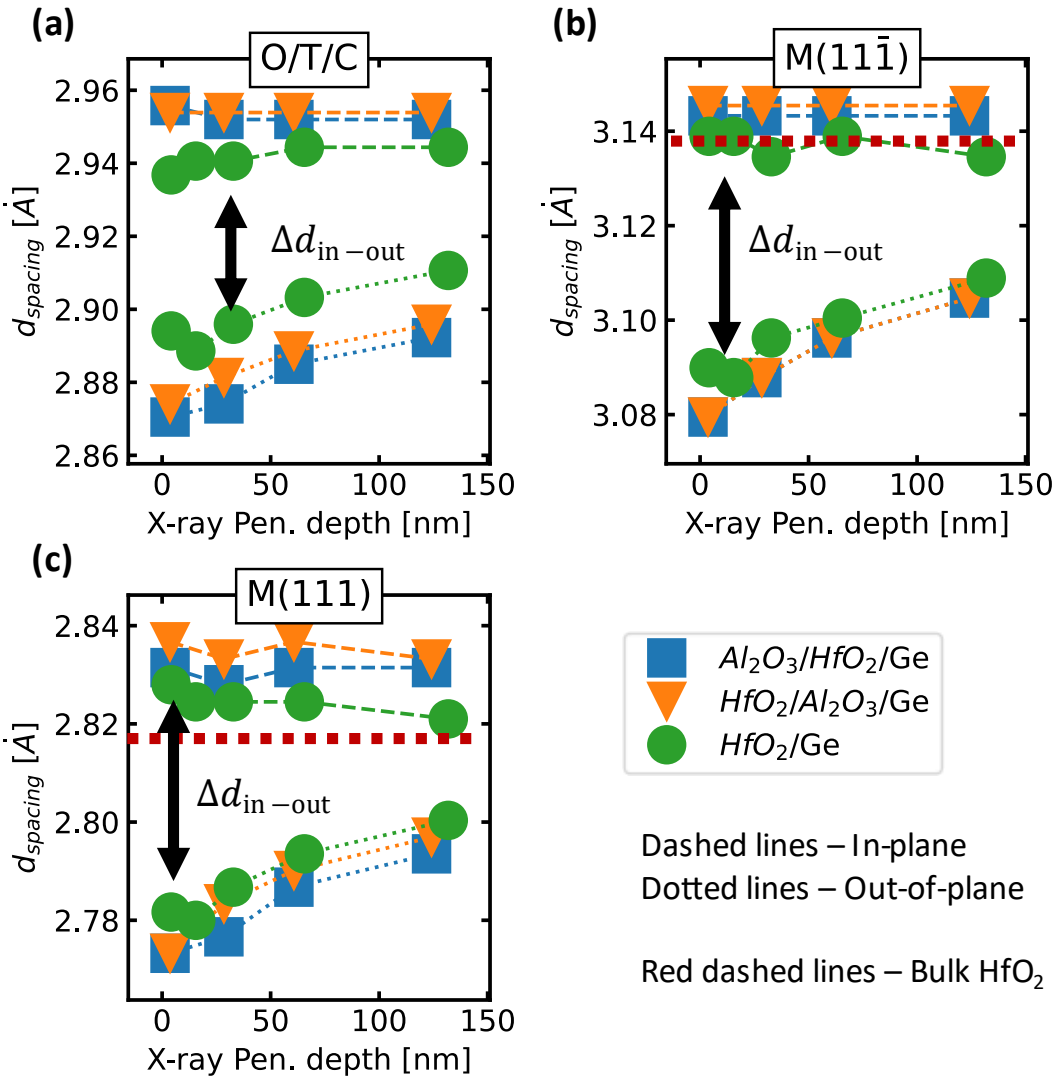


Fig. 5.38 The impact of the insertion of $Al_2O_3$ either as a capping layer or an interlayer on the depth dependences of $d_{spacing}$ in (a) O/T/C, (b) M(11$\bar{1}$), and M(111) crystal planes.

## 5.4.3 Surface Energy

To investigate the effect of surface energy on the $\Delta d_{\mathrm{in-out}}$, we fabricated several 200 nm-thick 1.5 % cations Y-doped and undoped $HfO_2$ on Ge substrate: **200 nm Y-$HfO_2$** and **200 Undoped-$HfO_2$**, respectively. To vary the $r_{o,t,c}$ and $\Delta d_{\mathrm{in-out}}$, after annealing both 200 nm Y-$HfO_2$ and Undoped-$HfO_2$ were cooled at three different cooling times ($\downarrow \tau$): *i.e.*, $\downarrow \tau$= 0, ., $\downarrow \tau$=45 min, ., $\downarrow \tau$ = 200 min.[1] In other words, there are two series of samples (200 nm Y-$HfO_2$ and Undoped-$HfO_2$), and each series has three samples with different $\downarrow \tau$ ($\downarrow \tau$= 0, ., $\downarrow \tau$=45 min, ., $\downarrow \tau$ = 200 min). In total, there are six individual samples. **30 nm-thick Y-$HfO_2$** samples with different $\downarrow \tau$ from Sections 4.3 and 5.3.1.2 are also used as references for 30 nm-thick $HfO_2$ films.

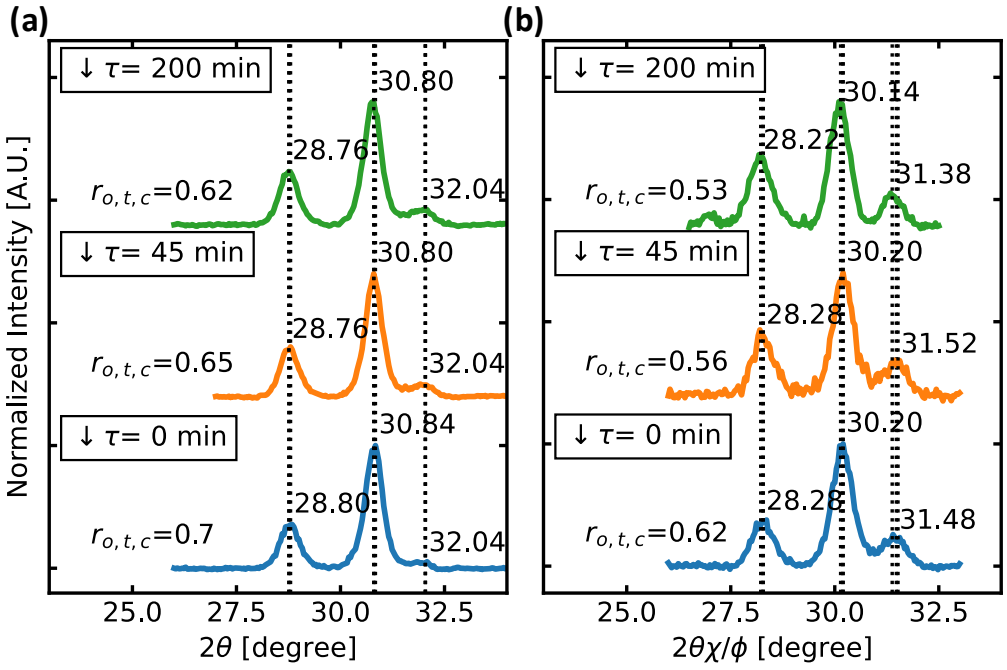


Fig. 5.39 (a) Out-of-plane and (b) in-plane XRD patterns of 200 nm-thickY-$HfO_2$ at different cooling times ($\downarrow \tau$) after annealing at 600°C ($\theta_i$=1.00°).

[1] The thermal annealing and cooling profiles are the same as the ones described in Sections 4.3 & 5.3.1.2.

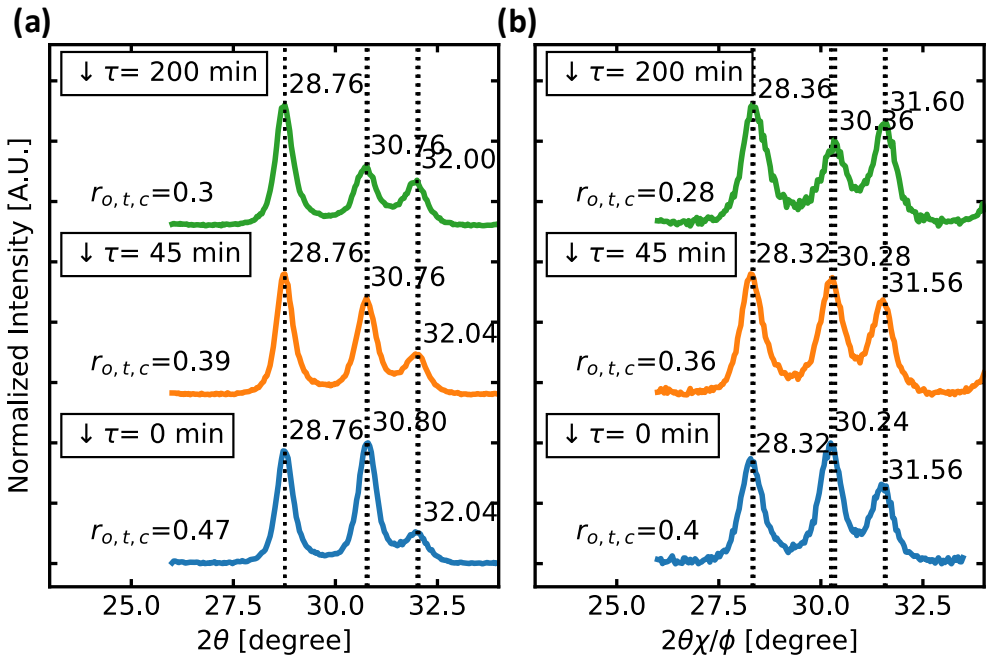


Fig. 5.40 (a) Out-of-plane and (b) in-plane XRD patterns of 200 nm-thick Undoped-$HfO_2$ at different cooling times (↓ $\tau$) after annealing at 600°C ($\theta_i$=1.00°).

The XRD patterns of 200 nm Y-$HfO_2$ and 200 nm Undoped-$HfO_2$ at different ↓ $\tau$ are shown in Fig. 5.39 and Fig. 5.40, respectively. The impact of ↓ $\tau$ on the $r_{o,t,c}$ of 200 nm-thick Y-$HfO_2$ and Undoped-$HfO_2$ is shown in Fig. 5.41; the impact of ↓ $\tau$ on the $r_{o,t,c}$ of 30 nm-thick Y-$HfO_2$ from Section 4.3 (Fig. 4.13) is also shown as a reference. Since it is known that the formation of the O/T/C phase is related to the increase in the surface energy [43], [46], [47], [50], the upward shift in the $r_{o,t,c}$ then the thickness was reduced to 30 nm can be explained by the increase in the surface energy. Between the 200 nm-thick Y-$HfO_2$ and Undoped-$HfO_2$, the upward shift in the $r_{o,t,c}$ of Y-$HfO_2$ can be explained by the introduction of Y-dopant to stabilize the O/T/C phase [44]. The decrease in the $r_{o,t,c}$ with the increase in ↓ $\tau$ of 30 nm-thick Y-$HfO_2$, 200 nm Y-$HfO_2$, and 200 nm Undoped-$HfO_2$ can be explained by the generation of M-phase when the films were cooled at longer ↓ $\tau$ [54]. The similarity in the trend between 200 nm-thick and 30 nm-thick $HfO_2$ films in Fig. 5.41 indicates that the crystallization of the O/T/C phase took place via the same mechanism.

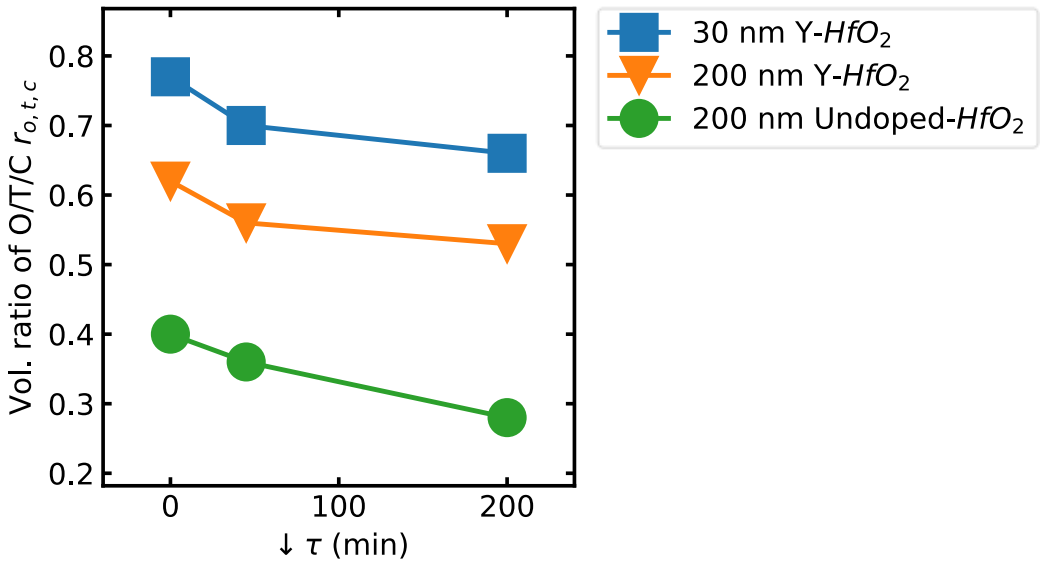


Fig. 5.41 The impact of cooling time (↓) on the $r_{o,t,c}$ in 200 nm and 30 nm-thick $HfO_2$ films.

The impact of ↓ $\tau$ on the $\Delta d_{in-out}$ in 200 nm and 30 nm-thick $HfO_2$ films is shown in Fig. 5.42. From the figure, the $\Delta d_{in-out}$ of both 200 nm Y-$HfO_2$ and Undoped-$HfO_2$ are not so sensitive to the ↓ $\tau$. Whereas in 30 nm Y-$HfO_2$, longer ↓ $\tau$ can significantly lower $\Delta d_{in-out}$ in the film. The difference in the impact of ↓ $\tau$ on the $\Delta d_{in-out}$ in 200 nm and 30 nm-thick $HfO_2$ films could suggest that the structural distortion in 200 nm and 30 nm-thick $HfO_2$ originate from different roots, or there is another factor involved that we have considered. We think that the latter is most likely, where surface energy might be the missing factor.

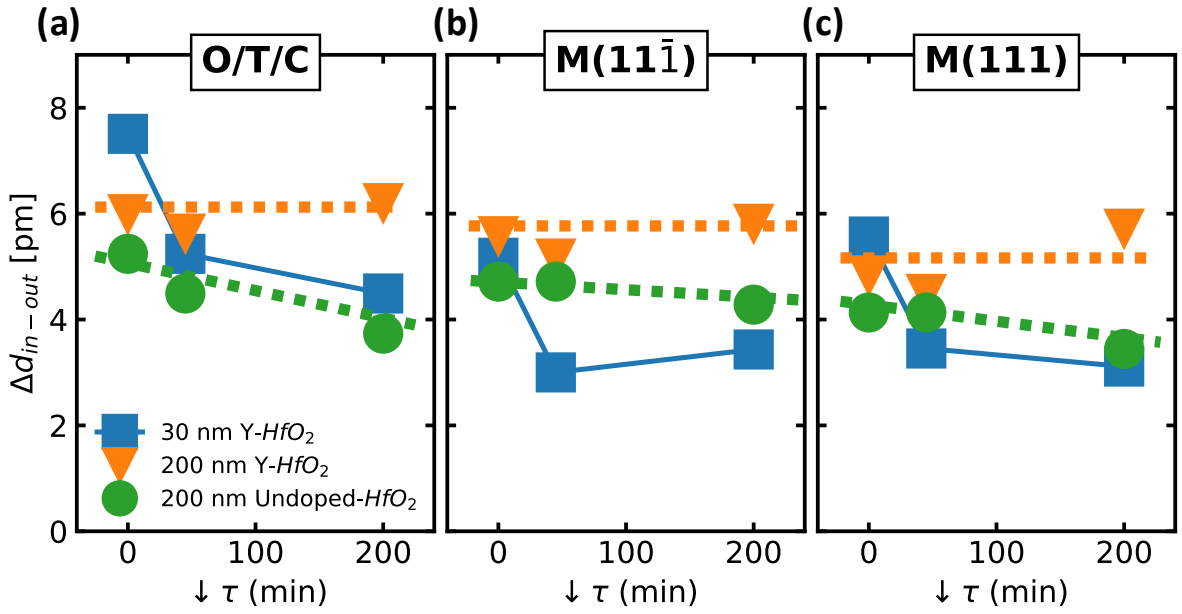


Fig. 5.42 The effect of cooling time (↓ $\tau$) on $\Delta d_{in-out}$ of (a) O/T/C, (b) M(11$\bar{1}$), and (c) M(111) crystal planes in 200 nm and 30 nm-thick $HfO_2$ films.

Fig. 5.43 shows the relationship between the $\Delta d_{\mathrm{in-out}}$ and the $r_{\mathrm{o,t,c}}$ of several 200 nm and 30 nm thick-$HfO_2$ films fabricated with various fabrication conditions. There is a similarity in the relationship between 200 nm and 30 nm-thick $HfO_2$ films; however, the relationship between the $\Delta d_{\mathrm{in-out}}$ and the $r_{\mathrm{o,t,c}}$ of 200 nm thick $HfO_2$ films shift upward compared to 30 nm thick $HfO_2$ films. Unfortunately, we do not have a conclusive answer to explain why there is a shift in the relationship between $\Delta d_{\mathrm{in-out}}$ and the $r_{\mathrm{o,t,c}}$ of 200 nm and 30 nm thick-$HfO_2$ films. We speculate that the formation of the O/T/C phase and the shrinkage in the volume may have happened separately but not independently, as we already introduced in 5.4.1. Because the 200 nm-thick $HfO_2$ films are much thicker, the larger depth dependence of $r_{\mathrm{o,t,c}}$ is expected and may likely affect the shrinkage in the volume of $HfO_2$ films.

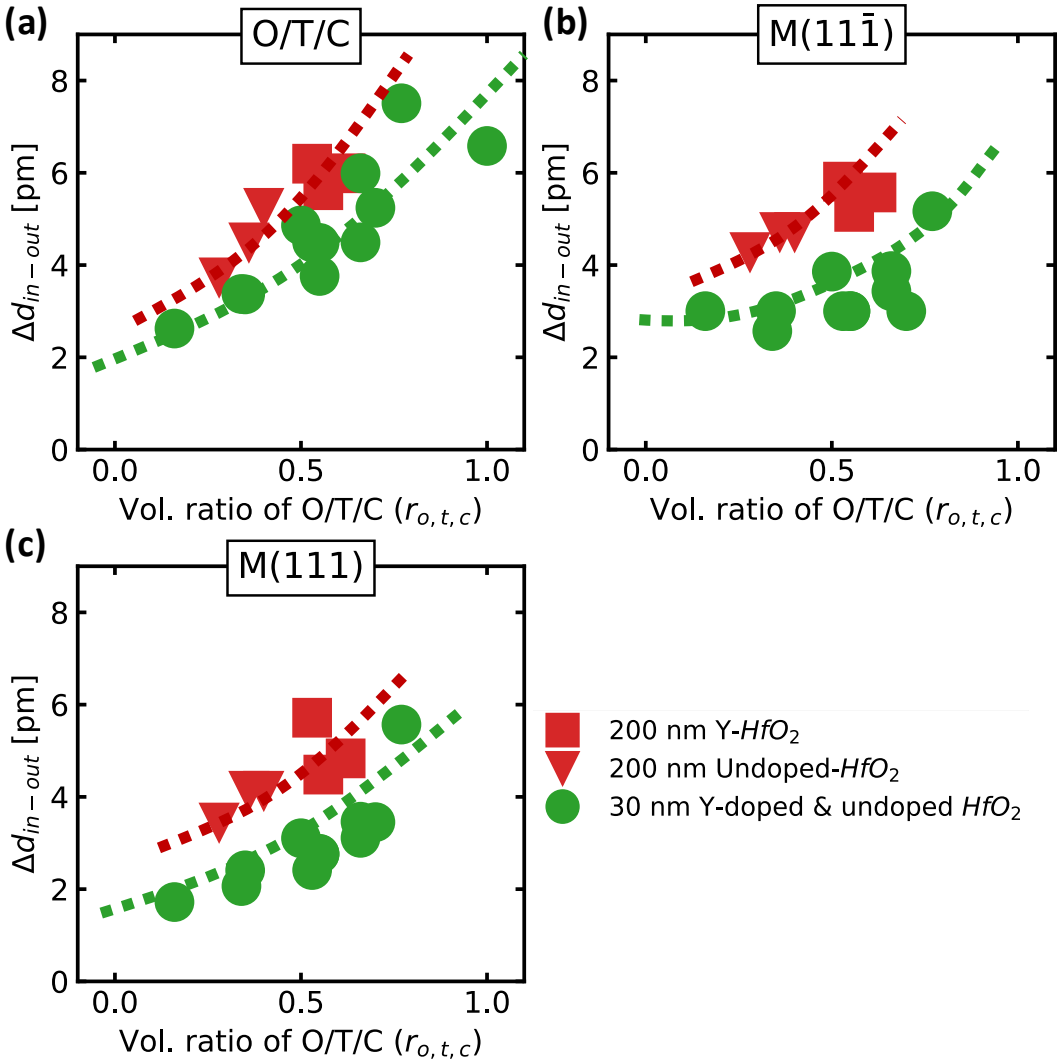


Fig. 5.43 The relationship between the $\Delta d_{\mathrm{in-out}}$ and $r_{\mathrm{o,t,c}}$ of several 200 nm and 30 nm-thick $HfO_2$ films fabricated at various fabrication conditions. The data from 30 nm-thick $HfO_2$ films were obtained from Fig. 5.13.

## 5.4.4 Non-Ferroelectric $HfO_2$

Our $HfO_2$ samples so far were all annealed in $N_2$ ambient. Hence, one might wonder if oxygen vacancies are what cause the structural distortion and if the structural distortion is specific only to FE-$HfO_2$. To discard that the structural distortion that we have observed is not the result of oxygen vacancies, we annealed several $HfO_2$ films in concentrated $O_2$ ambient at high temperature to ensure that the annealed $HfO_2$ films are not oxygen-deficient in any way. To anneal $HfO_2$ in concentrated $O_2$ ambient at high temperature, 10 nm-$SiO_2$/*p*-Si substrates were used instead of $p^+$-Ge substrate. After ~30 nm-thick undoped $HfO_2$ was deposited on $SiO_2$/*p*-Si substrates, the stacks were annealed in 100% $O_2$ ambient at 800 °C to ensure that the annealed $HfO_2$ films are not oxygen-deficient, and the thermodynamic stable M-phase is crystallized. The layout of the non-FE $HfO_2$ stacks is shown in Fig. 5.44. We also took a step further by annealing $HfO_2$ films at different annealing times ($\tau_{PDA}$) to capture the crystallization profile of $HfO_2$ under 100% $O_2$ ambient: $\boldsymbol{\tau_{PDA}}$**= 0 sec**, $\boldsymbol{\tau_{PDA}}$**=60 sec**, and $\boldsymbol{\tau_{PDA}}$**=300 sec**.

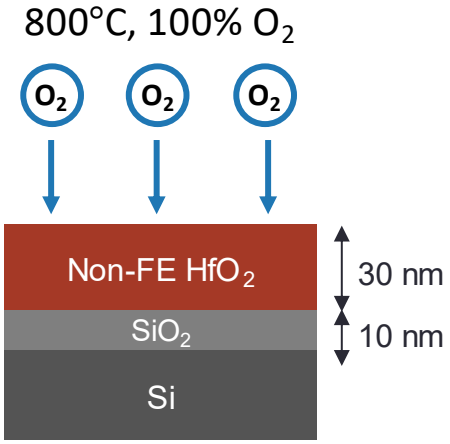


Fig. 5.44 (a) Schematics layout of non-FE $HfO_2$/$SiO_2$/Si stacks used in the section.

To confirm that the deposited $HfO_2$ films are non-ferroelectric, we also measured the I-V characteristic of several Au/non-FE-$HfO_2$/$SiO_2$/Si capacitors. An example of the I-V characteristic of an Au/non-FE-$HfO_2$/$SiO_2$/Si capacitor is shown in Fig. 5.45. When a positive bias is applied on Au top-electrode, negative charges were depleted from the surface of p-Si. For this reason, no displacement current was observed during the positive bias. When the bias is switched to negative, however, positively charged accumulates at the surface of p-Si, allowing electrons to tunnel through the layer. In both positive and negative bias regions, no ferroelectric displacement was observed; thus, the $HfO_2$ films are non-ferroelectric.

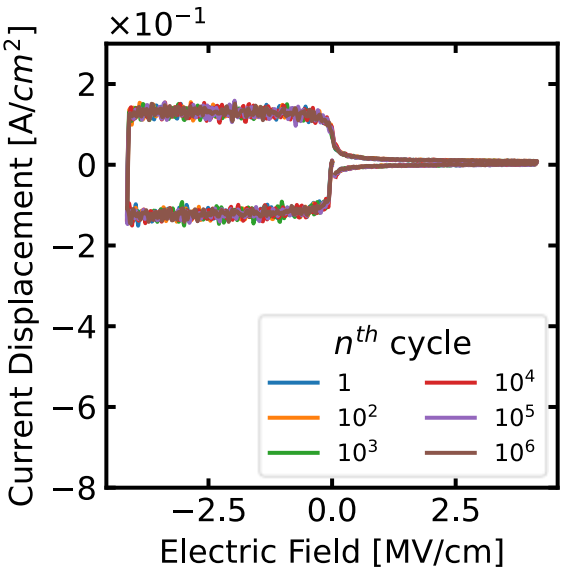


Fig. 5.45 I-V characteristic of Au/non-FE-$HfO_2$/$SiO_2$/Si ($\tau_{PDA}$=300 sec) during electric field cycling.

Fig. 5.46(a) and (b) show the in-plane and out-of-plane XRD patterns of undoped $HfO_2$ annealed in 100% $O_2$ ambient at different $\tau_{PDA}$, respectively. Both in-plane and out-of-plane XRD patterns show high and sharp peaks of the two M-crystal planes, and no O/T/C peak can be detected from either in-plane or out-of-plane XRD patterns. This also indicates that all the $HfO_2$ films here are non-FE. No shift in the peak position was observed even when the $HfO_2$ films were annealed at different $\tau_{PDA}$. The $\tau_{PDA}$ dependence of $\Delta d_{in-out}$ in M$(11\bar{1})$ and M$(111)$ crystal planes are shown in Fig. 5.47(a) and (b), respectively. From the figure, a constant of $\Delta d_{in-out}$ is still observed on both M$(11\bar{1})$ and M$(111)$ crystal planes regardless of $\tau_{PDA}$. This indicates that the structural distiortion is not unique only to FE-$HfO_2$ and oxygen vacancies are not what caused the structural distortion. This implies that structural distortion is a crystallization property of $HfO_2$ thin films, and the structural distortion takes place at the early stage of the crystallization since the structural distortion can be observed even at $\tau_{PDA}$ = 5 sec.

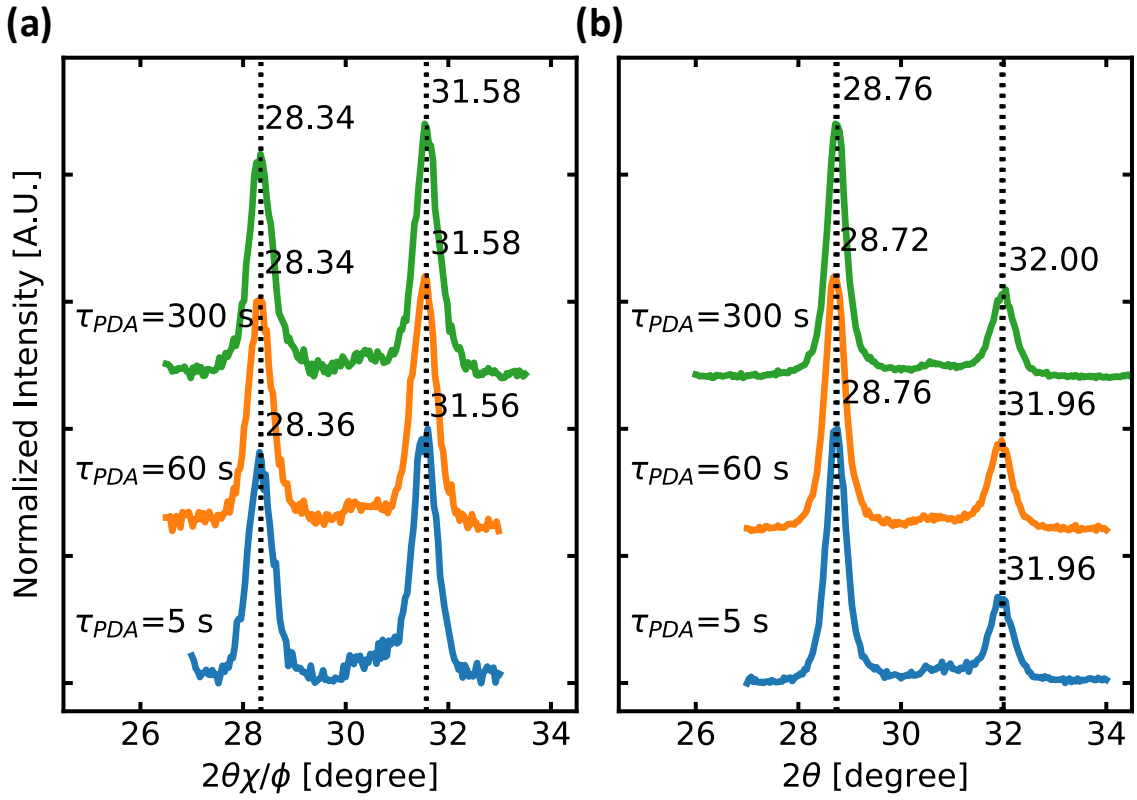


Fig. 5.46 (a) In-lane and (b) out-of-plane XDR patterns of non-FE-$HfO_2$/$SiO_2$/Si stacks at different post-deposited-annealing time intervals ($\tau_{PDA}$) at $\theta_i$ = 1.00°.

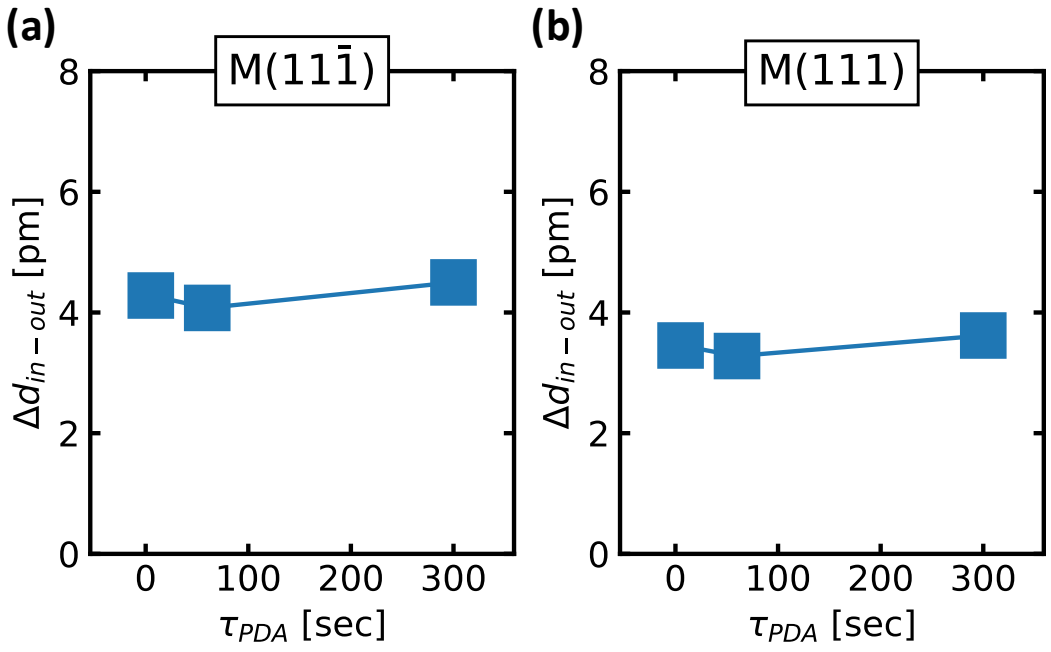


Fig. 5.47 Post-deposited-annealing times ( $\tau_{PDA}$ ) dependence on $\Delta d_{in-out}$ of non-FE-$HfO_2$/$SiO_2$/Si stacks in (a) M(11$\bar{1}$) and (b) M(111) crystal planes.

## 5.4.5 Yttrium-Hafnium System

One might wonder if the structural distortion that we observed is unique only to $HfO_2$ films or it is general to other oxide films as well. Hence, we investigate the structural distortion that was induced by Y-dopants and in $Y_2O_3$ thin films as well. From the phase diagram of the $HfO_2$-$Y_2O_3$ system [45], slight doping of $Y_2O_3$ in $HfO_2$ can induce the formation of the T-/C- phase. With a higher doping concentration can induce the formation of C-phase [44], [45], [47], [54], [92]. $Y_2O_3$ structure itself is a C-type rare-earth oxide that can be thought of as a modified fluorite-type C-structure with oxygen vacancies [47]. Thus, we decided to investigate the impact of Y-doping concentration on the $\Delta d_{\mathrm{in-out}}$ similar to Section 5.3.1.1 but at a wider range of Y-doping concentration.

In this section, ~30 nm-thick $HfO_2$, Y-doped $HfO_2$ at various concentrations, and $Y_2O_3$ films were deposited on $p^+$-Ge substrates. All films were annealed at 600 °C in $N_2$ ambient for 30 sec to keep the comparison fair. After annealing, the temperature was dropped with any temperature control.

The in-plane and out-of-plane XRD patterns of several $HfO_2$ and $Y_2O_3$ films are shown in Fig. 5.48(a-d). With slight doping of yttrium, Fig. 5.48(b), O-phase along with C-/T- phase can be easily induced compared to an undoped $HfO_2$ Fig. 5.48(a). At a higher Y-doping concentration, Fig. 5.48(c), only the C- or T-phases can be crystallized. Finally, only the C-phase is stabilized in $Y_2O_3$ films. The difference in the in-plane and out-of-plane XRD peak positions of the C-phase in $Y_2O_3$ also confirms that the structural distortion is not unique only to $HfO_2$ films.

Fig. 5.49 shows the diagram of the $\Delta d_{\mathrm{in-out}}$ in crystalline $Y_2O_3$-$HfO_2$ films on Ge substrate. Approximate 2.5 pm of the $\Delta d_{\mathrm{in-out}}$ in a FE-undoped $HfO_2$. The $\Delta d_{\mathrm{in-out}}$ then rapidly raise with slight doping of Y-dopant, where the Y-doped $HfO_2$ film still remains ferroelectric. The rise in the $\Delta d_{\mathrm{in-out}}$ can be explained by the $r_{\mathrm{o,t,c}}$, as discussed in Section 5.3. The $\Delta d_{\mathrm{in-out}}$ then peaks at ~ 7 pm, which at this point $HfO_2$ films no longer remain ferroelectric. The peak in the $\Delta d_{\mathrm{in-out}}$ can be explained by the crystallization of the densest phase in a $HfO_2$ – C-phase. Further increase in the Y-concentration results in a large reduction in the $\Delta d_{\mathrm{in-out}}$ to ~ 2.5 pm, where the $\Delta d_{\mathrm{in-out}}$ remains steady until the films became $Y_2O_3$ films. Beyond 25 Y-cation%, the crystal structure of $Y_2O_3$-$HfO_2$ films is expected to be predominated by the C-phase of $Y_2O_3$. Because the molar volume ($V_m$) of C-$Y_2O_3$ is packed more loosely therefore larger than

the $V_m$ of C-phase of $HfO_2$, there is a lesser tendency for the C-phase of $Y_2O_3$ to shrink. Thus, smaller $\Delta d_{\mathrm{in-out}}$ is observed on crystalline $Y_2O_3$-$HfO_2$ films where the C-phase of $Y_2O_3$ is the dominant structure. Furthermore, another interesting point to be pointed out is that the $\Delta d_{\mathrm{in-out}}$ in crystalline $Y_2O_3$-$HfO_2$ films on Ge substrate system seems to have a baseline of 2.5 pm. This might suggest the contribution of the underlying Ge substrate on the $\Delta d_{\mathrm{in-out}}$ is common in 30 nm thick crystalline $Y_2O_3$-$HfO_2$ films.

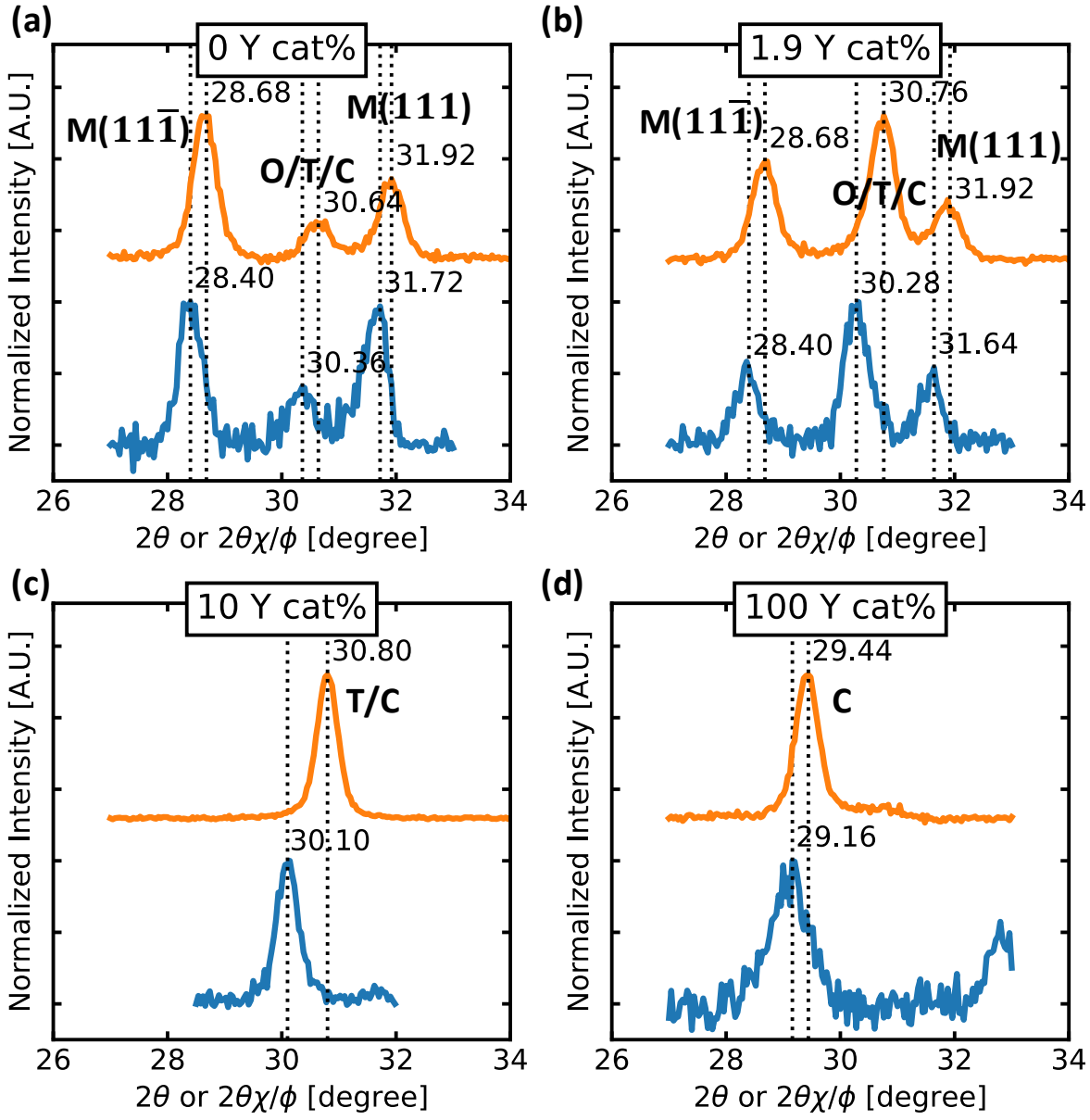


Fig. 5.48 In-plane and out-of-plane XRD patterns of 30 nm-thick (a) an undoped $HfO_2$, (b) a Y-doped $HfO_2$, (c) a high Y-doped $HfO_2$, and (d) $Y_2O_3$ films ($\theta_i$=1.00°).

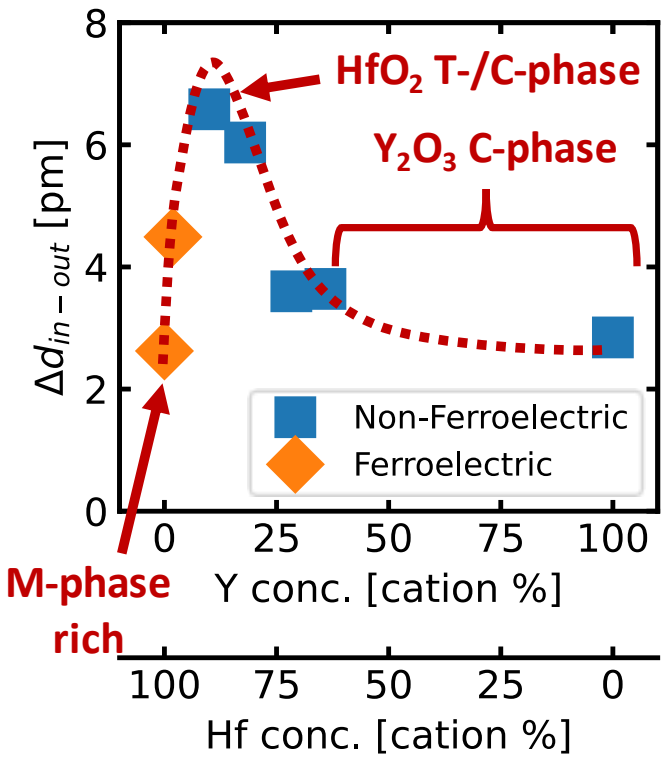


Fig. 5.49 In-plane and out-of-plane XRD patterns of $Y_2O_3$/Ge annealed in (a) $N_2$ and (b) $O_2$ ambientes ($\theta_i$=1.00°).

## 5.5 Summary

We investigate the driving force that determines the amount of the phase transformation[1] to be driven by an electric field cycling. During the clarification of the origin of the waking-up effect in Chapter 4, we found an anomalous difference in the XRD peak positions between the in-plane and the out-of-plane diffractions. We attribute and quantify this as the amount of structural distortion ($\Delta d_{\mathrm{in-out}}$) that is defined as the difference between the in-plane and out-of-plane interplanar spacing ($d_{\mathrm{spacing}}$).

Comparing to a bulk $HfO_2$, we found that the out-of-plane $d_{\mathrm{spacing}}$ is compressed. We also found that there is a relationship between the initial $\Delta d_{\mathrm{in-out}}$ (before electric field cycling) and the amount of phase transformation, as shown in Fig. 5.7. In turn, there is also a relationship between the initial $\Delta d_{\mathrm{in-out}}$ and the woke-up ratio ($r_{\mathrm{woke}}$), as shown in Fig. 5.8. We speculate that the $\Delta d_{\mathrm{in-out}}$ is a driving force that determine the amount of the phase transformation to be driven by an electric field. After electric field cycling, we also found that a reduction in the in-plane $d_{\mathrm{spacing}}$; whereas, the out-of-plane $d_{\mathrm{spacing}}$ remains constant. We hypothesize that the $\Delta d_{\mathrm{in-out}}$ is originating from the rapid shrinkage in the volume of crystalline $HfO_2$ films during the crystallization, while the underlying substrate pins the in-plane $d_{\mathrm{spacing}}$; where we found there is a relationship between the $\Delta d_{\mathrm{in-out}}$ and the $r_{\mathrm{o,t,c}}$, shown in Fig. 5.11.

To validate our hypothesize that (i) the origin of the structural distortion and (ii) the $\Delta d_{\mathrm{in-out}}$ is a driving force that determines the amount of phase transformation, we fabricated multiple FE-$HfO_2$ and non-FE $HfO_2$ with various fabrication conditions to vary the $r_{\mathrm{woke}}$, $r_{\mathrm{o,t,c}}$, and $\Delta d_{\mathrm{in-out}}$. We clarified that (i) the $\Delta d_{\mathrm{in-out}}$ can be universally explained by the $r_{\mathrm{o,t,c}}$ crystallized in $HfO_2$ thin films, as shown in Fig. 5.13. We also found that (ii) the $r_{\mathrm{woke}}$ can be universally explained by the initial $\Delta d_{\mathrm{in-out}}$, regardless of the fabrication conditions, as shown in Fig. 5.14. These two findings mean that it does not matter which fabrication condition was used to fabricate FE-$HfO_2$; the only thing that determines the $r_{\mathrm{woke}}$ of FE-HfO is the $\Delta d_{\mathrm{in-out}}$ induced during the crystallization.

[1] The origin of the waking-up effect in our FE-$HfO_2$ system was clarified to be due to the phase transformation driven by an electric field cycling in Chapter 4.

# Chapter 6 Investigation of Electric Field-driven Phase Transformation in Ferroelectric $HfO_2$

# 6.1 Introduction

Although the thermodynamic stable phase in $HfO_2$ is normally referring to M-phase [43], [46], [47], under certain circumstances (*i.e.*, distorted $HfO_2$ films in this case) the energy profile of $HfO_2$ may be altered allowing O-phase to be the most stable phase. The diagram illustrating how a distorted $HfO_2$ film can alter the energy profile to allow O-phase to become the stable phase is shown in Fig. 6.1. However, even O-phase becomes the thermodynamically stable phase in distorted $HfO_2$ films; kinetically, the phase transformation to O-phase is not expected without thermal annealing. Thus, a factor or factors must have altered the kinetics of the phase transformation to O-phase when an electric field was applied.

In Chapter 4, we clarified that the origin of the waking-up effect is due to the phase transformation that is driven by electric field cycling. In Chapter 5, we clarified that the $\Delta d_{\mathrm{in-out}}$ is what determines the amount of the phase transformation to be driven by an electric field. What missing and remains to be clarified are the factors that alter the kinetics of the phase transformation to O-phase and accelerate the generation of O-phase without a need for thermal annealing.

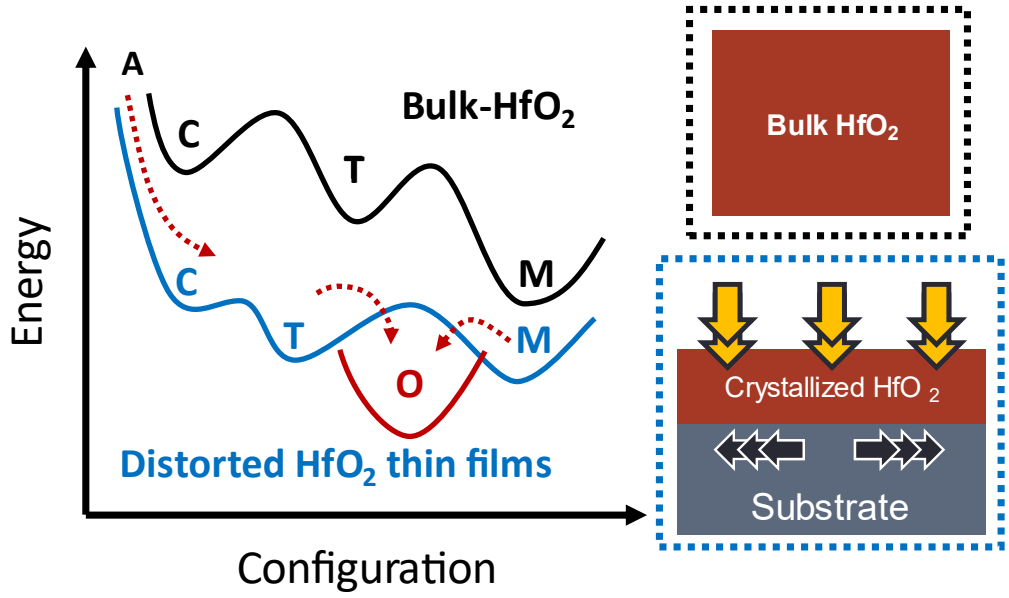


Fig. 6.1 A diagram showing how a distorted $HfO_2$ film can alter the energy profile, making O-phase become the thermodynamically stable phase. In a bulk $HfO_2$, M-phase is the thermodynamically stable phase.

In Section 4.1.2, we introduced that positive charges can lower the total energy of the O-phase making it become the most stable phase [55]. We also speculate that during an electric

field cycling, positive charges might be injected into $HfO_2$ and accelerate the phase transformation into O-phase. Another finding that we found in Section 5.4.1 is that the top surface of $HfO_2$ films is more distorted than the bottom surface, referring to Fig. 5.32. According to our model in Fig. 5.8(b), more $\Delta d_{\mathrm{in-out}}$ means more phase transformation to be driven by an electric field; thus, more waking-up effect. We hypothesize that the $r_{\mathrm{woke}}$ during electric field cycling that we have observed so far is the result of the phase transformation into O-phase that took place near the top surface of FE-$HfO_2$ films. Fig. 6.2 illustrates our hypothesize on the phase transformation that took place near the top surface because the region near the top surface is more distorted.

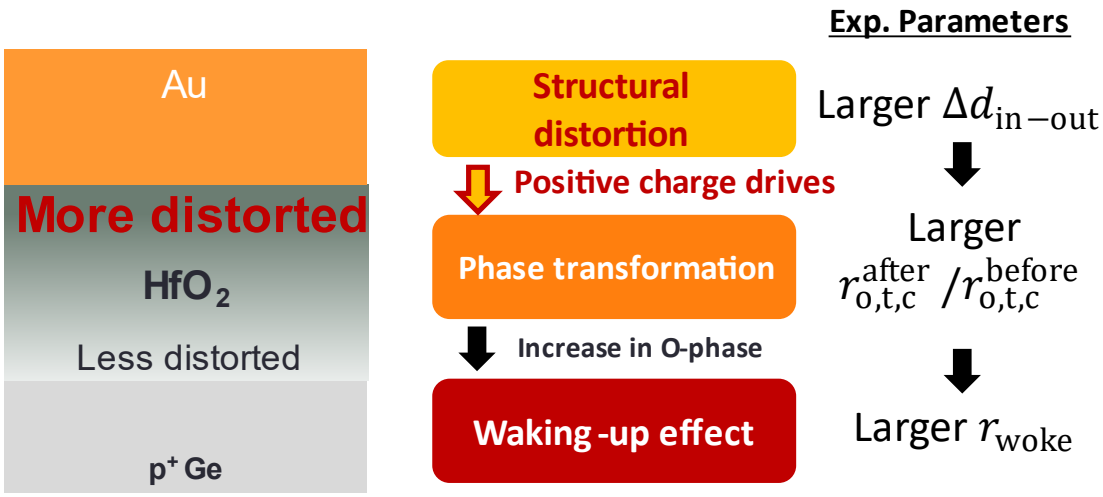


Fig. 6.2 Our hypothesis that the waking-up effect in our FE-$HfO_2$ is due to the phase transformation that took place near the top surface since we observed in Fig. 5.32 that the region near the top surface is more distorted.

The issue is that during an electric field cycling,[1] it is difficult to distinguish which surface that charges were injected. Therefore, a new method is required to distinguish the impact of charge injection from either the top or bottom surface on the waking-up effect in FE-$HfO_2$ – *i.e.*, DC-bias stressing.[2] With DC-bias stressing, we can intentionally inject electrons from either the top (Au side) or the bottom ($p^+$ Ge side) surfaces.

[1] The schematic of the pulse sequence in a typical electric field cycling measurement is shown in Fig. 2.13.

[2] The detailed description of DC-bias stressing can be found in Section 2.2.4.

## 6.2 Factors that Accelerate the Phase Transformation to the O-phase

Because it is not feasible in terms of kinetics for a phase transformation to take place without thermal annealing, the phase transformation to the O-phase must have been accelerated during electric field cycling. It is known that positive charges can lower the energy and stabilize the O-phase [55]. However, it is difficult to distinguish which interfaces that charges were injected. To differentiate the surface at which charges were injected, we performed DC-bias stressing to intentionally inject electrons from either the top (Au side) or the bottom ($p^+$ Ge side) interfaces. Positive and negative DC-bias stressing were used to inject electrons from the bottom and the top surface, respectively.[1]

Approximately 30 nm-thick Y-doped $HfO_2$ films were used in this section. All samples were annealed in $N_2$ ambient at 600 °C for 30 sec, before letting the temperature drops. Three voltages were applied during the DC-bias stressing to evaluate the impact of the magnitude of an electric field on the waking-up effect:: $\pm$9 V, $\pm$12 V, and $\pm$15 V corresponding to $\pm$3, $\pm$4, and $\pm$5 MVcm$^{-1}$, respectively.

The change with the normalized $P_{sw}$ with the amount of injected charges ($Q_{inj}$) during a positive and negative DC-bias stressing is shown in Fig. 6.3(a) and (b), respectively. The $P_{sw}$ was normalized to the pristine stage for easier comparison. A similar waking-up of $P_{sw}$ compared to the one observed from an electric field cycling is observed when positive DC-bias stressing was applied. In contrast, no waking-up in the $P_{sw}$ when negative DC-bias stressing was applied. The difference between positive and negative DC-bias stressing indicates the polarity and surface that an electric field is applied is an important parameter to accelerates the phase transformation to O-phase.

[1] The pulse sequences of positive and negative DC-bias stressing can be found in Fig. 2.16.

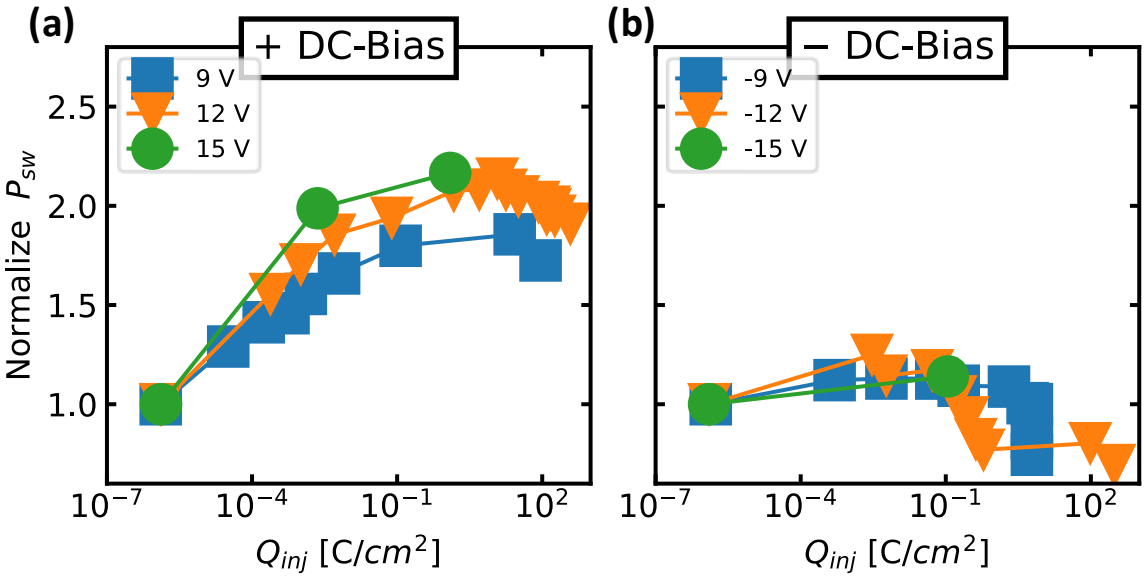


Fig. 6.3 The change in the switchable polarization ($P_{sw}$) during an (a) positive and (b) negative DC-bias stressing. The $P_{sw}$ is normalized to the $P_{sw}$ at a pristine stage for easier comparison.

During a positive DC-bias stressing, electrons were injected from the bottom interface, and electrons were extracted from the top interface leaving positive charges behind. Fig. 6.4 shows how electrons are injected and extracted during a positive DC-bias stressing. We also know that the region near the top interface is more distorted. According to our model, the $\Delta d_{\text{in-out}}$ is the driving force that determines the amount of phase transformation to be driven by an electric field. Thus, we consider those electrons extracted near the top surface can leave behind positive charges and accelerate the phase transformation to the O-phase in our FE-$HfO_2$.

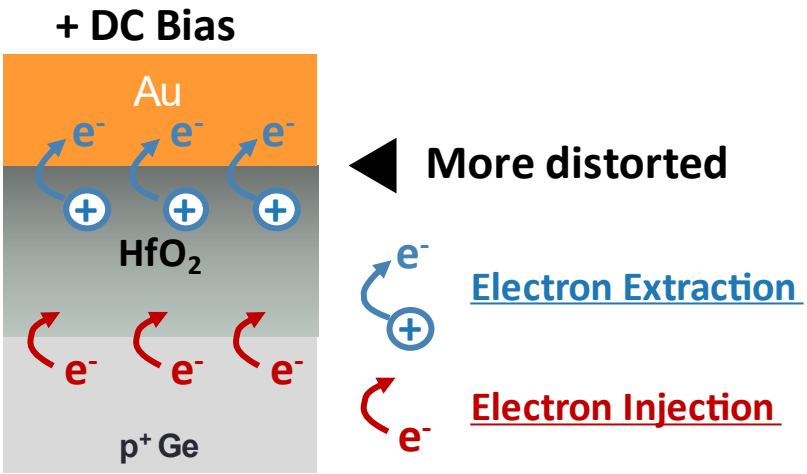


Fig. 6.4 A diagram showing the electron injection and extraction when positive DC-bias stress was applied on our FE-$HfO_2$ films.

The thing that is unclear in Fig. 6.3(a) is that the $Q_{inj}$ does not seem to be the factor that accelerates the phase transformation to O-phase. Larger $P_{sw}$ was being woke up when a higher positive voltage DC-bias was applied even the same $Q_{inj}$ was injected. If we plotted the data in Fig. 6.3 but as a function of the time that the electric field was applied, as shown in Fig. 6.5, we found that positive charge at the top interface, the magnitude of the electric field, and the time that it was applied seem to be the important factors accelerate the phase transformation to O-phase. Nonetheless, with the current experimental setup, we are unable to distinguish the impact of $Q_{inj}$ and an electric field on the waking-up effect, since the $Q_{inj}$ was accelerated into $HfO_2$ under the different magnitude of an electric field.

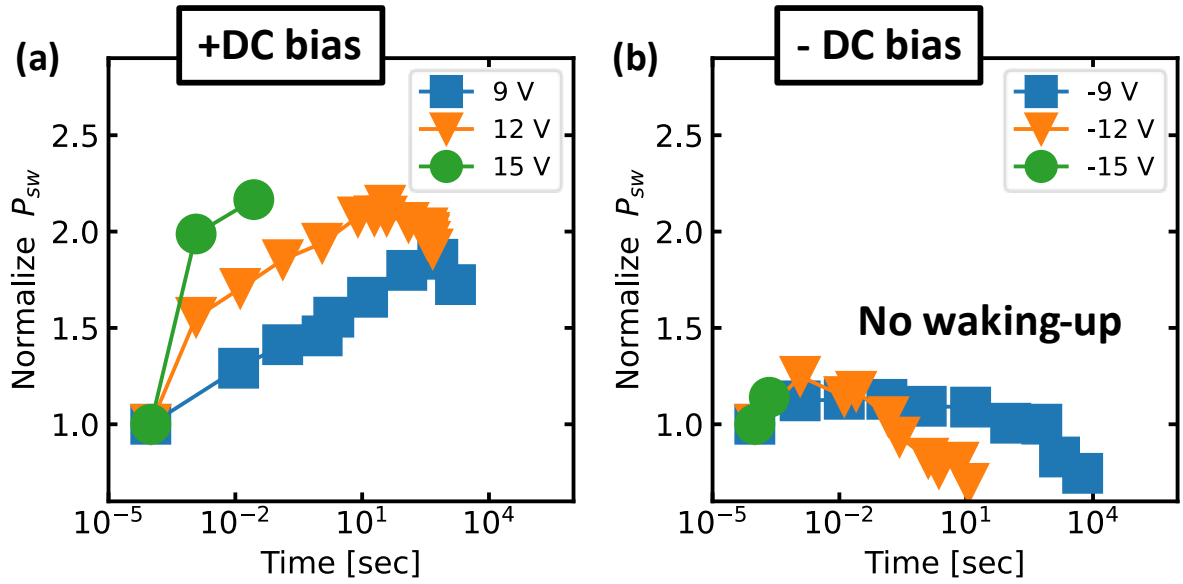


Fig. 6.5 The change in the switchable polarization ($P_{sw}$) during an (a) positive and (b) negative DC-bias stressing. This figure plots similar data as the one in Fig. 6.3 but as a function of the time that an electric field was applied.

To differentiate the impact of $Q_{inj}$ and the magnitude of an electric field on the waking-up effect, DC-bias stressing was assisted with photo-irradiation to photoexcite electrons and inject into $HfO_2$, instead of just by an applied electric field. In this way, more electrons can be injected independently from the magnitude of the applied electric field. The schematic diagram on how electrons are photo-excited and injected into $HfO_2$ during a positive DC-bias stressing is shown in Fig. 6.6. To photoexcite electrons at the interface ($HfO_2$/Ge interface), semitransparent Au electrodes are needed to allow photons to reach the bottom interface. The thickness of semi-transparent Au top electrodes is ~15 nm. Because it is expected that the barrier height between Ge's valence band to $HfO_2$'s conduction is approximately 3.0 eV [93]–[95], all capacitors were irradiated with 3.5 eV ($\lambda$=350 nm) of photons to ensre that all electrons are photoexcited above

the barrier height. Only two voltages, +8 and +9 V, were used in this to prevent excessive leakage current at higher voltages.

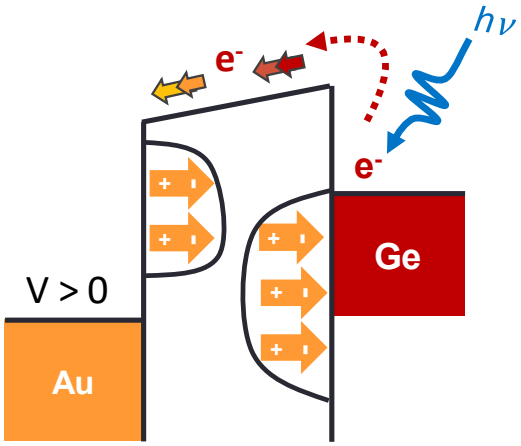


Fig. 6.6 Schematic diagram of a positive DC-bias stressing assisted by a photoirradiation.

The difference in the current density between positive DC-bias stressing with and without photo-assisting is shown in Fig. 6.7. With photo-assisting, the current level increase by the order of two; this means that the rate the charges were injected also increases by the order of two: $10^{-2}$ C/s·cm$^2$ and $10^{-4}$ C/s·cm$^2$ for positive DC bias stressing with and without photo-assisting, respectively.

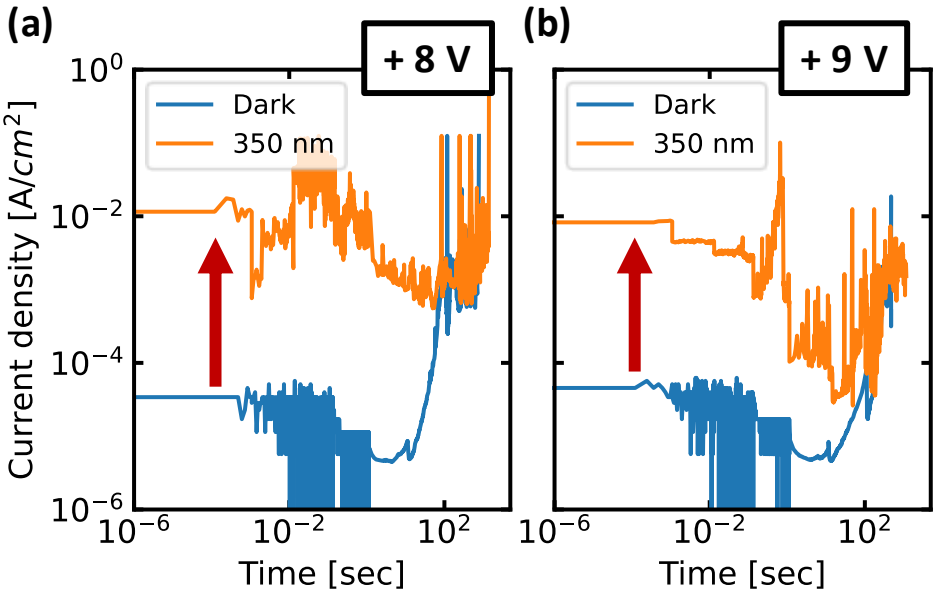


Fig. 6.7 Current density of (a) +8 V and (b) + 9 V DC-bias stressing with and without photo-assisting. ‘Dark’ is DC-bias stressing without photo-assisting. ‘350 nm’ is the wavelength of the irradiated photos.

Fig. 6.8 shows the change in $P_{sw}$ during positive DC-bias stressing with and without photo-assisting. A similar waking-up effect was observed regardless of positive DC-bias stressing with or without photo-assisting. Nevertheless, there is a parallel shift in the positive direction when a positive DC-bias stressing was assisted with a photo-irradiation. This suggests that the amount of injected charges ($Q_{inj}$) is not important in the acceleration of the phase transformation to the O-phase. Rather than, the time and the magnitude of an electric field that was applied is important.

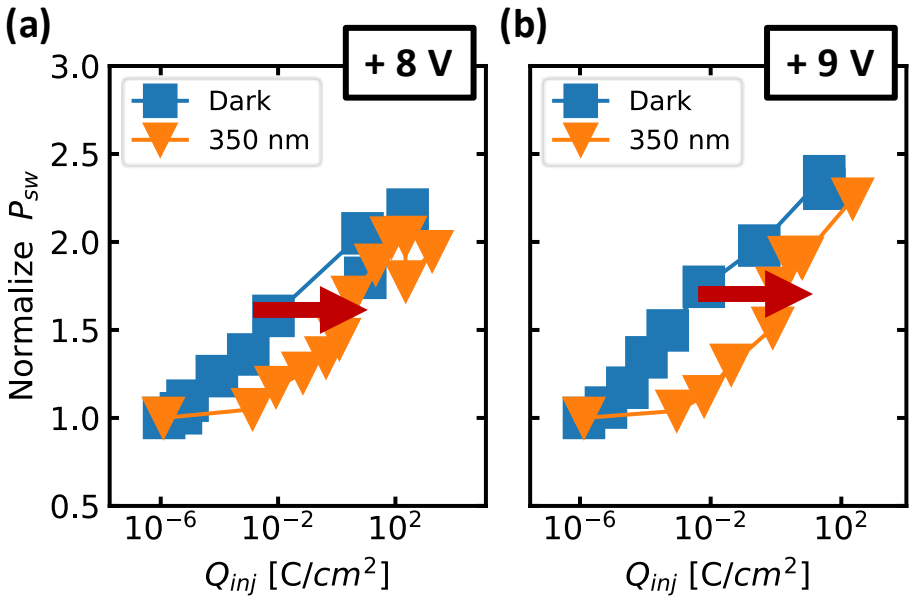


Fig. 6.8 Change in switchable polarization ($P_{sw}$) during (a) + 8V and (b) + 9 V DC-bias stressing with and without photo-assisting. 'Dark' is DC-bias stressing without photo-assisting. '350 nm' is the wavelength of the irradiated photos.

If we plotted the data Fig. 6.8 but as a function of time that the electric field was applied as shown in Fig. 6.9, we found that there is no difference in the change of $P_{sw}$ between positive DC-bias stressing with or without the photo-assisting. This indicates that the amount of injected charges is not important but positive charges are important in the acceleration of the phase transformation to the O-phase. In summary, we now know that (i) positive charges near the top surface (where the $\Delta d_{\text{in}-\text{out}}$ is high), (ii) magnitude, and (iii) the time that the electric field was applied

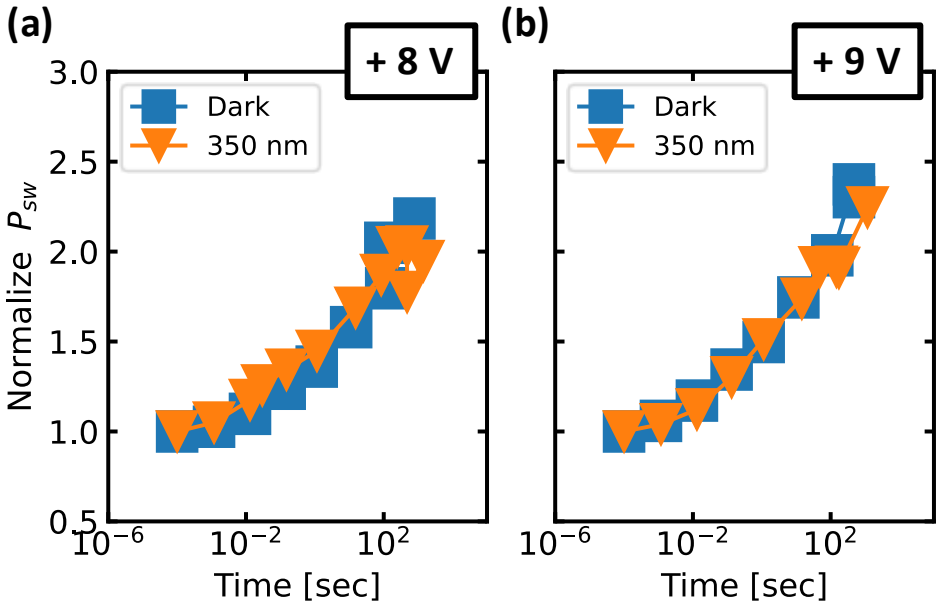


Fig. 6.9 Change in switchable polarization ($P_{sw}$) during (a) + 8V and (b) + 9 V DC-bias stressing with and without photo-assisting similar to the one in Fig. 6.8 but as a function of time. 'Dark' is DC-bias stressing without photo-assisting. '350 nm' is the wavelength of the irradiated photos.

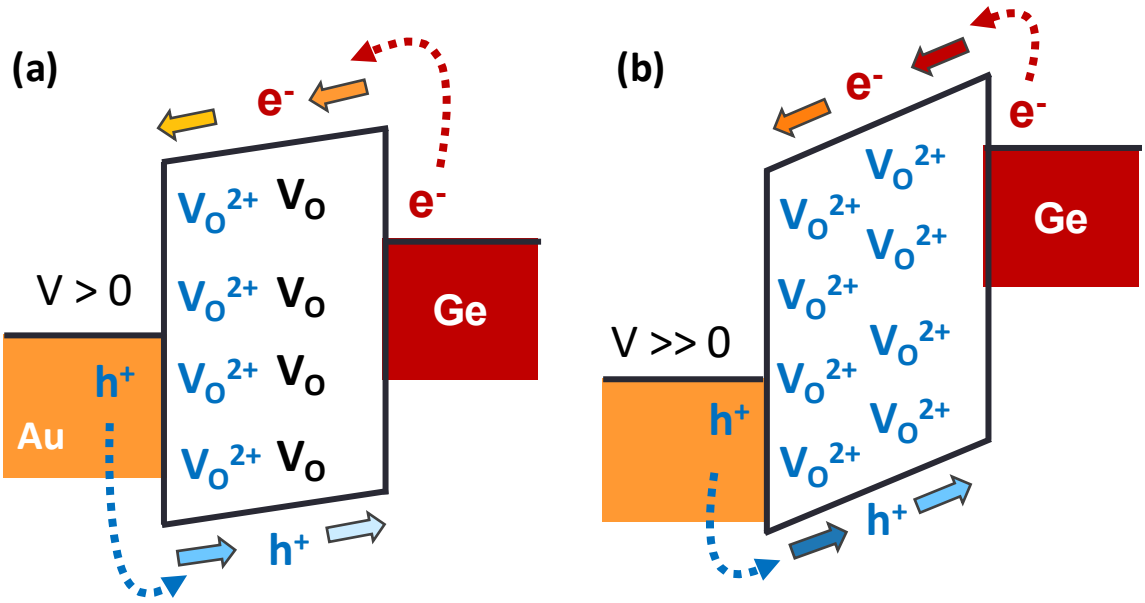


Fig. 6.10 Diagrams of the charged stages in oxygen vacancies ($V_O$) when (a) low positive and (b) high positive bias was applied.

To further explain the smaller waking-up effect when a low positive DC-bias was applied, we consider the charge state of the pre-existing defects in $HfO_2$. It has been reported that oxygen vacancies ($V_O$) are commonly found in many transition metal oxides, such as $HfO_2$ and $ZrO_2$ [56]–[58], [96], [97], and especially ones that have not been annealed in $O_2$ ambient. In

our case, all $HfO_2$ films were annealed in $N_2$ ambient. Therefore, we could expect our $HfO_2$ films to contain a certain amount of $V_O$. It is important to note that $V_O$ does not always present in a charge state. When electrons are extracted from the top interface (or injection of positive charges at the top interface), we speculate that it could induce a positively charged state, which in turn will lower the energy of the O-phase and accelerate the phase transformation to the O-phase. Fig. 6.10 shows schematic diagrams on the stabilization of the positively charged state in $V_O$. When a low positive DC-bias stress was applied (Fig. 6.10(a)), the extraction of electrons only takes place in the region near the top interface. Whereas, the extraction of electrons can take place deeper into the film when a high positive DC bias was applied (Fig. 6.10(b)). Thus, more volume in an FE-$HfO_2$ film can undergo the phase transformation to the O-phase. Furthermore, one might consider that mobile positive charges are what accelerate the phase transformation rather than the charged stated of $V_O$. Because we observed that the amount of the injected charges is not important as the magnitude and time that the electric field was applied, we do not consider that the acceleration of the phase transformation is caused by the mobile positive charges. Unfortunately, we do not have evidence that will rule out the contribution of the mobile positive charges on the acceleration of the phase transformation.

One might also argue that the injection of positive charges is the driving force of the waking-up effect, rather than the $\Delta d_{\mathrm{in-out}}$. Although positive changes are needed to induce the phase transformation to the O-phase, positive charges and the $\Delta d_{\mathrm{in-out}}$ are equally important as the waking-up effect will not be observed without both factors. Unfortunately, we do not have evidence that claims which one is more important and another. We speculate that the structural distortion affects the thermodynamic of $HfO_2$ films, and positive charges affect the kinetics of the phase transformation to the O-phase. Because it is known that surface energy can alter the phase stability in $HfO_2$ [43], [46], [47], we think that the structural distortion can alter the energy profile of FE-$HfO_2$ films and predetermine the pathway of the phase transformation. Whereas, positive charges affect the kinetics of the phase transformation to O-phase and accelerate the phase transformation to occur without thermal annealing.

## 6.3 Summary

We investigated the factors that accelerate the phase transformation to the O-phase without thermal annealing. In Section 5.4.1, we found that the region near the top interface is more distorted than the rest of the films. According to our model, more structural distortion means more phase transformation to be driven to the O-phase.[1] It is also known that positive charges can induce the formation of the O-phase. However, it is difficult to distinguish which interfaces that charges were injected during an electric field cycling. Hence, DC-bias stressing was used to intentionally injected electrons from either the top or the bottom interfaces.

By comparing the waking-up effect between positive and negative DC-bias stressing, we found that positive charges at the top surface are necessary to accelerate the phase transformation to the O-phase in our FE-$HfO_2$ system. However, a DC-bias stressing can not differentiate the impact of the amount of injected charges and the electric field on the waking-up effect. Hence, photo-assisted DC-bias stressing was used to inject electrons independently from the magnitude of the electric field. Comparing the DC-bias with and without photo-assisting, we clarified that only the magnitude and the time that the electric field was applied are also important. In summary, we know know that (i) positive charges near the top interface, (ii) the magnitude, and (iii) the time that the electric field was applied are important to the acceleration of the phase transformation to the O-phase without thermal annealing.

[1] Our model of the waking-up effect can be found in Fig. 5.8(b).

# Chapter 7 Conclusion and Future Prospects

## 7.1 Conclusions

We were able to provide two new methods to control the $P_s$ at dielectric interfaces and in FE-thin films, this is by the change in temperature and the amount of the structural distortion ($\Delta d_{\mathrm{in-out}}$), respectively.

The $P_s$ of dielectric interfaces were always thought to be fixed with the choice of materials and the thermal annealing process. In other words, once a dielectric interface was fabricated and annealed, the $P_s$ of the dielectric interfaces were thought to be fixed permanently. In this study, the $P_s$ of a dielectric interface is quantified as the interface dipole layer strength ($\varphi_{\mathrm{dipole}}$). We extracted the temperature dependences of $\varphi_{\mathrm{dipole}}$ in several dielectric interfaces. We found that the $\varphi_{\mathrm{dipole}}$ of an interface can be changed by the change in temperature and is not fixed by the choice of materials selection. We come up with a model that can universally explain the observed magnitude of the temperature dependence of $\varphi_{\mathrm{dipole}}$ using the concept of screening ability near the interface region.

One of the remaining issues of FE-$HfO_2$ is the waking-up of $P_s$ (*i.e.*, waking-up effect). Up to this point, the mechanism and the origin of the waking-up effect have been established but not well discussed. Studies suggest that the origin of the waking-up effect is due to the phase transformation that by driven by electric field cycling; however, the waking-up effect and the phase transformation were not provided at the same scale. Thus, the relationship between the two phenomena is not correctly represented. We clarified the origin of the waking-up effect by observing both the waking-up effect and the phase transformation on the same scale. We quantified the amount of the waking-up effect using the woke-up ratio ($r_{\mathrm{woke}}$) in this study. We found that the phase transformation driven by electric field cycling is the origin of the waking-up effect in our FE-$HfO_2$ system (*i.e.*, ~30 nm-thick FE-$HfO_2$ annealed in $N_2$ ambient without a capping layer).

Because it is unconventional to consider that a phase transformation occurs without thermal annealing, we consider that the phase transformation is governed by a phenomenon that has not yet been discussed. We clarified that the $\Delta d_{\mathrm{in-out}}$ is a driving force that determines the

amount of phase transformation to the O-phase to be driven by an electric field. In this study, we quantify the $\Delta d_{\mathrm{in-out}}$ to be the difference between the interplanar spacing ($d_{\mathrm{spacing}}$) that is parallel (out-of-plane) and perpendicular (in-plane) to the surface of $HfO_2$ films. We also clarified that the structural distortion is originating from the rapid shrinkage in the volume of $HfO_2$ during the crystallization of the denser higher symmetric (O/T/C) phase[1] while the in-plane $d_{\mathrm{spacing}}$ was pinned by the underlying substrate. To validate our claim on the driving force of the waking-up effect and the origin of the structural distortion, we fabricate multiple $HfO_2$ films with various fabrication conditions to vary the $r_{\mathrm{woke}}$ , the volume ratio of the O/T/C phase ($r_{\mathrm{o,t,c}}$), and the $\Delta d_{\mathrm{in-out}}$. We found that the $r_{\mathrm{woke}}$ can be universally explained by the $\Delta d_{\mathrm{in-out}}$ and the $\Delta d_{\mathrm{in-out}}$ can be universally explained by the $r_{\mathrm{o,t,c}}$ as well.

Although O-phase can become the stable phase in $HfO_2$ in some circumstances (distorted $HfO_2$ films in this case), the kinetics of the phase transformation to the O-phase without thermal annealing is most likely not feasible. Hence, additional factors must have accelerated the phase transformation to the O-phase during an electric field cycling. We found that positive charges, the magnitude, and the time that the electric field are the important factors in the acceleration. Because oxygen vacancies ($V_O$) are common defects in $HfO_2$, we speculate that when an electric field was applied, it induces a positively charged state on the pre-existing $V_O$. This then accelerates the phase transformation to the O-phase resulting in the waking-up effect of FE-$HfO_2$.

[1] The O/T/C phase includes orthrohumbic (O), cubic (C), and tetragonal (T) phase.

## 7.2 Future Prospects

At dielectric interfaces, we clarified that the magnitude of the temperature dependence of the $P_s$ can be universally explained by using the concept of screening length. Although we did not experimentally observe a switch in the polarity of $P_s$ at dielectric interfaces, we also know that a switch in the polarity could exist outside the temperature range of our experiment. Despite that our model of the screening length can not explain the switch in the polarity, mathematically, our model still allows an offset in the temperature dependence of $P_s$. This means that there is a new phenomenon to be explored here. Thus, it is worth it to further investigate if it is possible for the polarity of the $P_s$ at dielectric interfaces can switch.

In FE-thin films, we first clarified that the origin of the waking-up effect is due to the phase transformation that was driven by electric field cycling. What is missing and remains to be clarified is the pathway or pathways of the phase transformation to the O-phase that was driven by electric field cycling. We know that there are three possible pathways of the phase transformation – *i.e.,* T→O, M→O, and A→ O/T/C phase.[1] Unfortunately, we do not have evidence to pinpoint which pathway or pathways was or were taken. From a scientific phenomenal point, it is very meaningful to clarify which pathway(s) was taken as the phase transformation to occur without thermal annealing is not common.

We also clarified that the $\Delta d_{\mathrm{in-out}}$ is the driving force that determines the amount of the phase transformation to be driven an electric field, and the structural distortion is originating from the rapid shrinkage in the volume of $HfO_2$ during the crystallization of the O/T/C phase while the underlying substrate pins the in-plane $d_{\mathrm{spacing}}$. Although we clarified the origin of the structural distortion in our $HfO_2$ system (*i.e.,* 30 nm-thick annealed without a capping layer) and expect that the phenomenon to translate to other $HfO_2$ systems (thinner or thicker films with a capping layer) as well, our preliminary studies in Section 5.4 shows that other factors, such as surface energy, may be involved. It is worthwhile to further investigate the $\Delta d_{\mathrm{in-out}}$ in other systems as well in order to get a bigger picture of the phenomenon. We also want to emphasize that an investigation on thinner $HfO_2$ films with a capping layer will be very

[1] "A" stands for amorphous phase.

meaningful in terms of device technology since thinner $HfO_2$ films with a capping layer are most likely the system that will be used in an actual device.

Lastly, we clarified positive charges, the magnitude, and time that the electric field was applied are important in the acceleration of the phase transformation to the O-phase without thermal annealing. Nevertheless, we also clarified that the $\Delta d_{\mathrm{in-out}}$ is the driving force that determines the amount of the phase transformation to be driven by an electric field. One might argue that the positive charge is the driving force of the phase transformation rather than the $\Delta d_{\mathrm{in-out}}$ instead. We think that both positive charges and the $\Delta d_{\mathrm{in-out}}$ are crucial for the phase transformation to the O-phase, since the phase transformation would not occur without both factors. We speculate that structural distortion plays a role in the thermodynamic of the $HfO_2$ film and predetermines the pathway of the phase transformation to the O-phase. Whereas, positive charges affect the kinetics of the phase transformation and accelerate the phase transformation to occur without thermal annealing. It will be very meaningful in terms of science to distinguish and clarify the roles of structural distortion and positive charges in the mechanism of the waking-up effect in FE-$HfO_2$.

# References


[1] C. Kittel and M. Paul, *Introduction to Solid State Physics*, 8th ed. John Wiley & Sons, Inc.

[2] J. Robertson and R. M. Wallace, "High-*k* materials and metal gates for CMOS applications," *Mater. Sci. Eng. R Reports*, vol. 88, pp. 1–41, Feb. 2015, doi: 10.1016/J.MSER.2014.11.001.

[3] M. T. Bohr, R. S. Chau, T. Ghani, and K. Mistry, "The high-*k* solution," *IEEE Spectr.*, vol. 44, no. 10, pp. 29–35, Oct. 2007, doi: 10.1109/MSPEC.2007.4337663.

[4] Y. Yamamoto, K. Kita, K. Kyuno, and A. Toriumi, "Study of La-Induced Flat Band Voltage Shift in Metal/HfLaOx/$SiO_2$/Si Capacitors," *Jpn. J. Appl. Phys.*, vol. 46, no. 11, pp. 7251–7255, Nov. 2007, doi: 10.1143/JJAP.46.7251.

[5] K. Iwamoto *et al.*, "Experimental evidence for the flatband voltage shift of high-k metal-oxide-semiconductor devices due to the dipole formation at the high-*k*/$SiO_2$ interface," *Appl. Phys. Lett.*, vol. 92, no. 13, p. 132907, Mar. 2008, doi: 10.1063/1.2904650.

[6] L. Lin and J. Robertson, "Atomic mechanism of electric dipole formed at high-*k*: $SiO_2$ interface," *J. Appl. Phys.*, vol. 109, no. 9, p. 094502, May 2011, doi: 10.1063/1.3583655.

[7] J. Fei and K. Kita, "Opportunity of dipole layer formation at non-$SiO_2$ dielectric interfaces in two cases: Multi-cation systems and multi-anion systems," *Microelectron. Eng.*, vol. 178, pp. 225–229, Jun. 2017, doi: 10.1016/J.MEE.2017.05.035.

[8] K. Kita and A. Toriumi, "Origin of electric dipoles formed at high-*k*/$SiO_2$ interface," *Appl. Phys. Lett.*, vol. 94, no. 13, p. 132902, Mar. 2009, doi: 10.1063/1.3110968.

[9] H. Arimura *et al.*, "Temperature-dependent La- and Al-induced dipole behavior monitored by femtosecond pump/probe photoelectron spectroscopy," *Appl. Phys. Lett.*, vol. 96, no. 13, p. 132902, Mar. 2010, doi: 10.1063/1.3374883.

[10] J. Fei and K. Kita, "Understanding the impact of interface reaction on dipole strength at MgO/$SiO_2$ and $Y_2O_3$/$SiO_2$ interfaces," *Jpn. J. Appl. Phys.*, vol. 55, no. 4S, p. 04EB11, Mar. 2016, doi: 10.7567/JJAP.55.04EB11.

[11] S. Hibino, T. Nishimura, K. Nagashio, K. Kita, and A. Toriumi, "Counter Dipole Layer

Formation in Multilayer High-*k* Gate Stacks," *Jpn. J. Appl. Phys.*, vol. 51, no. 8R, p. 081303, Aug. 2012, doi: 10.1143/JJAP.51.081303.

[12] T. S. Böscke, J. Müller, D. Bräuhaus, U. Schröder, and U. Böttger, "Ferroelectricity in hafnium oxide thin films," *Appl. Phys. Lett.*, vol. 99, no. 10, p. 102903, Sep. 2011, doi: 10.1063/1.3634052.

[13] R. E. Cohen, "Origin of ferroelectricity in perovskite oxides," *Nature*, vol. 358, no. 6382, pp. 136–138, Jul. 1992, doi: 10.1038/358136a0.

[14] J. Junquera and P. Ghosez, "Critical thickness for ferroelectricity in perovskite ultrathin films," *Nature*, vol. 422, no. 6931, pp. 506–509, Apr. 2003, doi: 10.1038/nature01501.

[15] D. D. Fong *et al.*, "Ferroelectricity in ultrathin perovskite films.," *Science*, vol. 304, no. 5677, pp. 1650–3, Jun. 2004, doi: 10.1126/science.1098252.

[16] M. Pešić *et al.*, "Physical Mechanisms behind the Field-Cycling Behavior of $HfO_2$-Based Ferroelectric Capacitors," *Adv. Funct. Mater.*, vol. 26, no. 25, pp. 4601–4612, Jul. 2016, doi: 10.1002/adfm.201600590.

[17] T. Shimizu *et al.*, "The demonstration of significant ferroelectricity in epitaxial Y-doped $HfO_2$ film," *Sci. Rep.*, vol. 6, no. 1, pp. 1–8, Sep. 2016, doi: 10.1038/srep32931.

[18] K. Katayama *et al.*, "Orientation control and domain structure analysis of {100}-oriented epitaxial ferroelectric orthorhombic $HfO_2$-based thin films," *J. Appl. Phys.*, vol. 119, no. 13, p. 134101, Apr. 2016, doi: 10.1063/1.4945029.

[19] T. Shimizu, K. Katayama, T. Kiguchi, A. Akama, T. J. Konno, and H. Funakubo, "Growth of epitaxial orthorhombic $YO_{1.5}$-substituted $HfO_2$ thin film," *Appl. Phys. Lett.*, vol. 107, no. 3, p. 032910, Jul. 2015, doi: 10.1063/1.4927450.

[20] S. Clima *et al.*, "Identification of the ferroelectric switching process and dopant-dependent switching properties in orthorhombic $HfO_2$: A first principles insight," *Appl. Phys. Lett.*, vol. 104, no. 9, p. 92906, Mar. 2014, doi: 10.1063/1.4867975.

[21] X. Tian, S. Shibayama, T. Nishimura, T. Yajima, S. Migita, and A. Toriumi, "Evolution of ferroelectric $HfO_2$ in ultrathin region down to 3 nm," *Appl. Phys. Lett.*, vol. 112, no. 10, p. 102902, Mar. 2018, doi: 10.1063/1.5017094.

[22] J. Muller, P. Polakowski, S. Muller, and T. Mikolajick, "(Invited) Ferroelectric Hafnium Oxide Based Materials and Devices: Assessment of Current Status and Future Prospects,"

*ECS Trans.*, vol. 64, no. 8, pp. 159–168, Aug. 2014, doi: 10.1149/06408.0159ecst.

[23] S. M. Sze and K. K. Ng, *Physics of Semiconductor Devices*. Hoboken, NJ, USA: John Wiley & Sons, Inc., 2006.

[24] E. H. Nicollian and J. R. Brews, *MOS (metal oxide semiconductor) physics and technology*. Wiley-Interscience, 2003.

[25] "Introducing Mitsubishi Electric Power Device Technologies and Product Trends." https://www.mitsubishielectric.com/semiconductors/triple_a_plus/technology/01/index.html (accessed Aug. 01, 2021).

[26] D. K. Schroder, *Semiconductor Material and Device Characterization: Third Edition*. John Wiley and Sons, 2005.

[27] S. Kobayashi, "X-Ray thin film measurement techniques IV. In-plane XRD measurements," *Rigaku J.*, vol. 26, no. 1, pp. 3–11, 2010.

[28] G. L. Parrish, C. Ortiz, M. Hart, and M. Bellotto, "Grazing incidence synchrotron x-ray diffraction method for analyzing thin films," *J. Mater. Res.*, vol. 2, no. 4, pp. 471–477, Jan. 1987, doi: 10.1557/JMR.1987.0471.

[29] A. D. Hatmanto and K. Kita, "Thermal-oxidation-induced local lattice distortion at surface of 4H-SiC(0001) characterized by in-plane X-ray diffractometry," *Appl. Phys. Express*, vol. 11, no. 1, p. 011201, Jan. 2018, doi: 10.7567/APEX.11.011201.

[30] H. Diamant, K. Drenck, and R. Pepinsky, "Bridge for accurate measurement of ferroelectric hysteresis," *Rev. Sci. Instrum.*, vol. 28, no. 1, pp. 30–33, Dec. 1957, doi: 10.1063/1.1715701.

[31] S. Guha *et al.*, "Examination of flatband and threshold voltage tuning of $HfO_2$/TiN field effect transistors by dielectric cap layers," *Appl. Phys. Lett.*, vol. 90, no. 9, p. 092902, Feb. 2007, doi: 10.1063/1.2709642.

[32] P. D. Kirsch *et al.*, "Dipole model explaining high-*k*/metal gate field effect transistor threshold voltage tuning," *Appl. Phys. Lett.*, vol. 92, no. 9, p. 092901, Mar. 2008, doi: 10.1063/1.2890056.

[33] K. Shimura *et al.*, "Positive and negative dipole layer formation at high-k/SiO2 interfaces simulated by classical molecular dynamics," *Jpn. J. Appl. Phys.*, vol. 55, no. 4S, p. 04EB03, Apr. 2016, doi: 10.7567/JJAP.55.04EB03.

[34] S. Nittayakasetwat and K. Kita, “Anomalous temperature dependence of $Al_2O_3/SiO_2$ and $Y_2O_3/SiO_2$ interface dipole layer strengths,” *J. Appl. Phys.*, vol. 125, no. 8, p. 084105, Feb. 2019, doi: 10.1063/1.5079926.

[35] T. Hamaguchi, S. Nittayakasetwat, and K. Kita, “Study on interface dipole layer strength change by temperature in high-*k*/$SiO_2$ and high-*k*/high-*k* systems and its possible origin,” Sep. 2018, doi: 10.7567/SSDM.2018.B-5-01.

[36] H. Tada *et al.*, “Thermal expansion coefficient of polycrystalline silicon and silicon dioxide thin films at high temperatures,” *J. Appl. Phys.*, vol. 87, no. 9, p. 4189, Apr. 2000, doi: 10.1063/1.373050.

[37] S. Skirl, M. Hoffman, K. Bowman, S. Wiederhorn, and J. Rödel, “Thermal expansion behavior and macrostrain of $Al_2O_3$/Al composites with interpenetrating networks,” *Acta Mater.*, vol. 46, no. 7, pp. 2493–2499, Apr. 1998, doi: 10.1016/S1359-6454(98)80033-5.

[38] R. J. Beals and R. L. Cook, “Directional Dilatation of Crystal Lattices at Elevated Temperatures,” *J. Am. Ceram. Soc.*, vol. 40, no. 8, pp. 279–284, Aug. 1957, doi: 10.1111/j.1151-2916.1957.tb12620.x.

[39] T. S. Böscke *et al.*, “Phase transitions in ferroelectric silicon doped hafnium oxide,” *Appl. Phys. Lett.*, vol. 99, no. 11, p. 112904, Sep. 2011, doi: 10.1063/1.3636434.

[40] J. Müller *et al.*, “Ferroelectricity in simple binary $ZrO_2$ and $HfO_2$,” *Nano Lett.*, vol. 12, no. 8, pp. 4318–4323, Aug. 2012, doi: 10.1021/nl302049k.

[41] M. Hoffmann *et al.*, “Stabilizing the ferroelectric phase in doped hafnium oxide,” *J. Appl. Phys.*, vol. 118, no. 7, p. 072006, Aug. 2015, doi: 10.1063/1.4927805.

[42] P. Polakowski and J. Müller, “Ferroelectricity in undoped hafnium oxide,” *Appl. Phys. Lett.*, vol. 106, no. 23, p. 232905, Jun. 2015, doi: 10.1063/1.4922272.

[43] S. V. Ushakov *et al.*, “Crystallization in hafnia- and zirconia-based systems,” *Phys. Status Solidi Basic Res.*, vol. 241, no. 10, pp. 2268–2278, Aug. 2004, doi: 10.1002/pssb.200404935.

[44] K. Kita, K. Kyuno, and A. Toriumi, “Permittivity increase of yttrium-doped $HfO_2$ through structural phase transformation,” *Appl. Phys. Lett.*, vol. 86, no. 10, pp. 1–3, Mar. 2005, doi: 10.1063/1.1880436.

[45] D. W. Stacy and D. R. Wilder, “The Yttria-Hafnia System,” *J. Am. Ceram. Soc.*, vol. 58, no. 7–8, pp. 285–288, Jul. 1975, doi: 10.1111/j.1151-2916.1975.tb11476.x.

[46] S. V. Ushakov, C. E. Brown, and A. Navrotsky, “Effect of La and Y on crystallization temperatures of hafnia and zirconia,” *J. Mater. Res.*, vol. 19, no. 3, pp. 693–696, 2004, doi: 10.1557/jmr.2004.19.3.693.

[47] A. Navrotsky, “Thermochemical insights into refractory ceramic materials based on oxides with large tetravalent cations,” *J. Mater. Chem.*, vol. 15, no. 19, pp. 1883–1890, May 2005, doi: 10.1039/b417143h.

[48] M. H. Park *et al.*, “Surface and grain boundary energy as the key enabler of ferroelectricity in nanoscale hafnia-zirconia: A comparison of model and experiment,” *Nanoscale*, vol. 9, no. 28, pp. 9973–9986, Jul. 2017, doi: 10.1039/c7nr02121f.

[49] R. Materlik, C. Kunneth, and A. Kersch, “The origin of ferroelectricity in $Hf_{1-x}Zr_xO_2$: A computational investigation and a surface energy model,” *J. Appl. Phys.*, vol. 117, no. 13, p. 134109, Apr. 2015, doi: 10.1063/1.4916707.

[50] R. Batra, H. D. Tran, and R. Ramprasad, “Stabilization of metastable phases in hafnia owing to surface energy effects,” *Appl. Phys. Lett.*, vol. 108, no. 17, p. 172902, Apr. 2016, doi: 10.1063/1.4947490.

[51] L. Xu, T. Nishimura, S. Shibayama, T. Yajima, S. Migita, and A. Toriumi, “Kinetic pathway of the ferroelectric phase formation in doped $HfO_2$ films,” *J. Appl. Phys.*, vol. 122, no. 12, p. 124104, Sep. 2017, doi: 10.1063/1.5003918.

[52] M. H. Park *et al.*, “A comprehensive study on the structural evolution of $HfO_2$ thin films doped with various dopants,” *J. Mater. Chem. C*, vol. 5, no. 19, pp. 4677–4690, May 2017, doi: 10.1039/c7tc01200d.

[53] Y. Mori, T. Nishimura, T. Yajima, S. Migita, and A. Toriumi, “Impacts of doped element on ferroelectric phase stabilization in $HfO_2$ through non-equilibrium PDA,” in *Extended Abstracts of the 2018 International Conference on Solid State Devices and Materials*, Sep. 2018, pp. 1271–1272, doi: 10.7567/SSDM.2018.PS-10-18.

[54] Y. Nakajima, K. Kita, T. Nishimura, K. Nagashio, and A. Toriumi, “Experimental Demonstration of Higher-*k* Phase $HfO_2$ Through Non-Equilibrium Thermal Treatment,” in *ECS Transactions*, Apr. 2019, vol. 28, no. 2, pp. 203–212, doi: 10.1149/1.3372576.

[55] T. Nakayama, K. Arai, Y. Shiraishi, R. Nagasawa, M. Araidai, and K. Shiraishi, "Charging-induced Stabilization of Ferroelectric Orthorhombic $HfO_2$ Phase; Key Growth Processes based on Frist-principles Study," in *Proceedings of the Extended abstract of the 51st IEEE Semiconductor Interface Specialists Conference*, 2020, p. 10.1.

[56] A. S. Foster, V. B. Sulimov, F. L. Gejo, A. L. Shluger, and R. M. Nieminen, "Structure and electrical levels of point defects in monoclinic zirconia," *Phys. Rev. B*, vol. 64, no. 22, p. 224108, Nov. 2001, doi: 10.1103/PhysRevB.64.224108.

[57] A. S. Foster, F. L. Gejo, A. L. Shluger, and R. M. Nieminen, "Vacancy and interstitial defects in hafnia," *Phys. Rev. B*, vol. 65, no. 17, p. 174117, May 2002, doi: 10.1103/PhysRevB.65.174117.

[58] K. Xiong, J. Robertson, M. C. Gibson, and S. J. Clark, "Defect energy levels in $HfO_2$ high-dielectric-constant gate oxide," *Appl. Phys. Lett.*, vol. 87, no. 18, p. 183505, Oct. 2005, doi: 10.1063/1.2119425.

[59] T. Shimizu *et al.*, "Contribution of oxygen vacancies to the ferroelectric behavior of $Hf_{0.5}Zr_{0.5}O_2$ thin films," *Appl. Phys. Lett.*, vol. 106, no. 11, p. 112904, Mar. 2015, doi: 10.1063/1.4915336.

[60] S. Starschich, S. Menzel, and U. Böttger, "Evidence for oxygen vacancies movement during wake-up in ferroelectric hafnium oxide," *Appl. Phys. Lett.*, vol. 108, no. 3, p. 032903, Jan. 2016, doi: 10.1063/1.4940370.

[61] M. H. Park *et al.*, "Study on the internal field and conduction mechanism of atomic layer deposited ferroelectric $Hf_{0.5}Zr_{0.5}O_2$ thin films," *J. Mater. Chem. C*, vol. 3, no. 24, pp. 6291–6300, Jun. 2015, doi: 10.1039/c5tc01074h.

[62] T. Schenk, U. Schroeder, M. Pešić, M. Popovici, Y. V. Pershin, and T. Mikolajick, "Electric field cycling behavior of ferroelectric hafnium oxide," *ACS Appl. Mater. Interfaces*, vol. 6, no. 22, pp. 19744–19751, Nov. 2014, doi: 10.1021/am504837r.

[63] T. Schenk, M. Hoffmann, J. Ocker, M. Pešić, T. Mikolajick, and U. Schroeder, "Complex internal bias fields in ferroelectric hafnium oxide," *ACS Appl. Mater. Interfaces*, vol. 7, no. 36, pp. 20224–20233, Sep. 2015, doi: 10.1021/acsami.5b05773.

[64] K. Carl and K. H. Hardtl, "Electrical After-Effects In $Pb(Ti, Zr)O_3$ Ceramics," *Ferroelectrics*, vol. 17, no. 1, pp. 473–486, Jan. 1977, doi: 10.1080/00150197808236770.

[65] S. Starschich, S. Menzel, and U. Böttger, “Pulse wake-up and breakdown investigation of ferroelectric yttrium doped $HfO_2$,” *J. Appl. Phys.*, vol. 121, no. 15, p. 154102, Apr. 2017, doi: 10.1063/1.4981893.

[66] T. Schenk *et al.*, “About the deformation of ferroelectric hystereses,” *Appl. Phys. Rev.*, vol. 1, no. 4, p. 041103, Dec. 2014, doi: 10.1063/1.4902396.

[67] T. Shimizu *et al.*, “Ferroelectricity mediated by ferroelastic domain switching in $HfO_2$-based epitaxial thin films,” *Appl. Phys. Lett.*, vol. 113, no. 21, p. 212901, Nov. 2018, doi: 10.1063/1.5055258.

[68] S. S. Fields *et al.*, “Phase-Exchange-Driven Wake-Up and Fatigue in Ferroelectric Hafnium Zirconium Oxide Films,” *ACS Appl. Mater. Interfaces*, vol. 12, no. 23, pp. 26577–26585, Jun. 2020, doi: 10.1021/acsami.0c03570.

[69] T. Shimizu *et al.*, “Electric-Field-Induced Ferroelectricity in 5%Y-doped $Hf_{0.5}Zr_{0.5}O_2$ : Transformation from the Paraelectric Tetragonal Phase to the Ferroelectric Orthorhombic Phase,” *Phys. status solidi – Rapid Res. Lett.*, vol. 15, no. 5, p. 2000589, May 2021, doi: 10.1002/pssr.202000589.

[70] E. D. Grimley *et al.*, “Structural Changes Underlying Field-Cycling Phenomena in Ferroelectric $HfO_2$ Thin Films,” *Adv. Electron. Mater.*, vol. 2, no. 9, p. 1600173, Sep. 2016, doi: 10.1002/aelm.201600173.

[71] D. Martin *et al.*, “Ferroelectricity in Si-Doped $HfO_2$ revealed: A binary lead-free ferroelectric,” *Adv. Mater.*, vol. 26, no. 48, pp. 8198–8202, Dec. 2014, doi: 10.1002/adma.201403115.

[72] M. H. Park *et al.*, “Effect of Zr Content on the Wake-Up Effect in $Hf_{1-x}Zr_xO_2$ Films,” *ACS Appl. Mater. Interfaces*, vol. 8, no. 24, pp. 15466–15475, Jun. 2016, doi: 10.1021/acsami.6b03586.

[73] H. J. Kim *et al.*, “A study on the wake-up effect of ferroelectric $Hf_{0.5}Zr_{0.5}O_2$ films by pulse-switching measurement,” *Nanoscale*, vol. 8, no. 3, pp. 1383–1389, Jan. 2016, doi: 10.1039/c5nr05339k.

[74] S. Shibayama, T. Nishimura, S. Migita, and A. Toriumi, “Thermodynamic control of ferroelectric-phase formation in $Hf_xZr_{1-x}O_2$ and $ZrO_2$,” *J. Appl. Phys.*, vol. 124, no. 18, p. 184101, Nov. 2018, doi: 10.1063/1.5028181.

[75] L. Pintilie and M. Alexe, “Ferroelectric-like hysteresis loop in nonferroelectric systems,” *Appl. Phys. Lett.*, vol. 87, no. 11, p. 112903, Sep. 2005, doi: 10.1063/1.2045543.

[76] S. Nittayakasetwat and K. Kita, “Evidence of ferroelectric $HfO_2$ phase transformation induced by electric field cycling observed at a macroscopic scale,” *Solid. State. Electron.*, vol. 184, p. 108086, Oct. 2021, doi: 10.1016/j.sse.2021.108086.

[77] J. Meena, S. Sze, U. Chand, and T.-Y. Tseng, “Overview of emerging nonvolatile memory technologies,” *Nanoscale Res. Lett.*, vol. 9, no. 1, p. 526, 2014, doi: 10.1186/1556-276X-9-526.

[78] S. Nittayakasetwat and K. Kita, “Relationship between the Waking-up Effect and Structural Distortion in Ferroelectric $HfO_2$ characterized by X-ray Diffraction,” in *Extended Abstracts of the 2020 International Conference on Solid-State Device and Materials*, 2020, pp. 13–14.

[79] T. Shiraishi *et al.*, “Impact of mechanical stress on ferroelectricity in $(Hf_{0.5}Zr_{0.5})O_2$ thin films,” *Appl. Phys. Lett.*, vol. 108, no. 26, p. 262904, Jun. 2016, doi: 10.1063/1.4954942.

[80] S. J. Kim *et al.*, “Large ferroelectric polarization of TiN/$Hf_{0.5}Zr_{0.5}O_2$/TiN capacitors due to stress-induced crystallization at low thermal budget,” *Appl. Phys. Lett.*, vol. 111, no. 24, p. 242901, Dec. 2017, doi: 10.1063/1.4995619.

[81] M. H. Park, H. J. Kim, Y. J. Kim, T. Moon, and C. S. Hwang, “The effects of crystallographic orientation and strain of thin $Hf_{0.5}Zr_{0.5}O_2$ film on its ferroelectricity,” *Appl. Phys. Lett.*, vol. 104, no. 7, p. 072901, Feb. 2014, doi: 10.1063/1.4866008.

[82] T. D. Huan, V. Sharma, G. A. Rossetti, and R. Ramprasad, “Pathways towards ferroelectricity in hafnia,” *Phys. Rev. B - Condens. Matter Mater. Phys.*, vol. 90, no. 6, p. 064111, Aug. 2014, doi: 10.1103/PhysRevB.90.064111.

[83] E. D. Grimley, T. Schenk, T. Mikolajick, U. Schroeder, and J. M. LeBeau, “Atomic Structure of Domain and Interphase Boundaries in Ferroelectric $HfO_2$,” *Adv. Mater. Interfaces*, vol. 5, no. 5, p. 1701258, Mar. 2018, doi: 10.1002/admi.201701258.

[84] S. Mueller *et al.*, “Incipient ferroelectricity in Al-doped $HfO_2$ thin films,” *Adv. Funct. Mater.*, vol. 22, no. 11, pp. 2412–2417, Jun. 2012, doi: 10.1002/adfm.201103119.

[85] A. Chernikova, M. Kozodaev, A. Markeev, Y. Matveev, D. Negrov, and O. Orlov, “Confinement-free annealing induced ferroelectricity in $Hf_{0.5}Zr_{0.5}O_2$ thin films,”

*Microelectron. Eng.*, vol. 147, pp. 15–18, Nov. 2015, doi: 10.1016/j.mee.2015.04.024.

[86] T. Nishimura, L. Xu, S. Shibayama, T. Yajima, S. Migita, and A. Toriumi, "Ferroelectricity of nondoped thin $HfO_2$ films in TiN/$HfO_2$/TiN stacks," *Jpn. J. Appl. Phys.*, vol. 55, no. 8S2, p. 08PB01, Jun. 2016, doi: 10.7567/JJAP.55.08PB01.

[87] J. M. Leger and J. Haines, "Relative stability of $ZrO_2$ and $HfO_2$ structural phases," *Phys. Rev. B - Condens. Matter Mater. Phys.*, vol. 60, no. 21, pp. 14485–14488, Dec. 1999, doi: 10.1103/PhysRevB.60.14485.

[88] M. Lederer *et al.*, "Local crystallographic phase detection and texture mapping in ferroelectric Zr doped $HfO_2$ films by transmission-EBSD," *Appl. Phys. Lett.*, vol. 115, no. 22, p. 222902, Nov. 2019, doi: 10.1063/1.5129318.

[89] S. Nittayakasetwat and K. Kita, "Anomalous structural distortion – a possible origin for the waking-up of the spontaneous polarization in ferroelectric $HfO_2$," *Jpn. J. Appl. Phys.*, vol. 60, no. 7, p. 070908, Jul. 2021, doi: 10.35848/1347-4065/ac085c.

[90] X. Zhao and D. Vanderbilt, "First-principles study of structural, vibrational, and lattice dielectric properties of hafnium oxide," *Phys. Rev. B - Condens. Matter Mater. Phys.*, vol. 65, no. 23, pp. 1–4, Jun. 2002, doi: 10.1103/PhysRevB.65.233106.

[91] D. Ceresoli and D. Vanderbilt, "Structural and dielectric properties of amorphous $ZrO_2$ and $HfO_2$," *Phys. Rev. B - Condens. Matter Mater. Phys.*, vol. 74, no. 12, p. 125108, Sep. 2006, doi: 10.1103/PhysRevB.74.125108.

[92] A. Toriumi, K. Kita, K. Tomida, and Y. Yamamoto, "Doped $HfO_2$ for Higher-k Dielectrics," in *ECS Transactions*, 2019, vol. 1, no. 5, pp. 185–197, doi: 10.1149/1.2209268.

[93] M. K. Hudait, Y. Zhu, D. Maurya, and S. Priya, "Energy band alignment of atomic layer deposited $HfO_2$ on epitaxial (110)Ge grown by molecular beam epitaxy," *Appl. Phys. Lett.*, vol. 102, no. 9, p. 093109, Mar. 2013, doi: 10.1063/1.4794838.

[94] M. K. Hudait and Y. Zhu, "Energy band alignment of atomic layer deposited $HfO_2$ oxide film on epitaxial (100)Ge, (110)Ge, and (111)Ge layers," *J. Appl. Phys.*, vol. 113, no. 11, p. 114303, Mar. 2013, doi: 10.1063/1.4795284.

[95] J. Widiez, K. Kita, K. Tomida, T. Nishimura, and A. Toriumi, "Internal Photoemission over $HfO_2$ and $Hf_{(1-x)}Si_xO_2$ High-*k* Insulating Barriers: Band Offset and Interfacial

Dipole Characterization," *Jpn. J. Appl. Phys.*, vol. 47, no. 4, pp. 2410–2414, Apr. 2008, doi: 10.1143/JJAP.47.2410.

[96] S. Guha and V. Narayanan, "Oxygen Vacancies in High Dielectric Constant Oxide-Semiconductor Films," *Phys. Rev. Lett.*, vol. 98, no. 19, p. 196101, May 2007, doi: 10.1103/PhysRevLett.98.196101.

[97] J. L. Gavartin, D. M. Ramo, A. L. Shluger, G. Bersuker, and B. H. Lee, "Negative oxygen vacancies in $HfO_2$ as charge traps in high-k stacks," *Appl. Phys. Lett.*, vol. 89, no. 8, p. 082908, Aug. 2006, doi: 10.1063/1.2236466.

# Publications

## Original Papers for journals with peer-review

- **S. Nittayakasetwat** and K. Kita, ‘Anomalous temperature dependence of $Al_2O_3/SiO_2$ and $Y_2O_3/SiO_2$ interface dipole layer strengths’, *Journal of Applied Physics*. 125, 084105 (2019). (Selected for Editor's Pick)
- **S. Nittayakasetwat** and K. Kita, ‘Evidence of Ferroelectric $HfO_2$ Phase Transformation Induced by Electric Field Cycling Observed at a Macroscopic Scale’, *Solid State Electronic. 184*, 108086 (2021)
- **S. Nittayakasetwat** and K. Kita, ‘Anomalous Structural Distortion – a Possible Origin for the Waking-up of the Spontaneous Polarization in Ferroelectric $HfO_2$’, *Japanese Journal of Applied Physics – Rapid Communication, 60,* 070908 (2021).
- **S. Nittayakasetwat**, H. Momiyama, and K. Kita, ‘Origin of structural distortion – a driving force of the waking-up in the spontaneous polarization’. {In-preparation}
- **S. Nittayakasetwat** and K. Kita, ‘The Origin of Electric Field driven Phase Transformation in Ferroelectric $HfO_2$’. {In-preparation}

# Proceedings for International Conferences with peer-review

- **Siri Nittayakasetwat** and Koji Kita, "Temperatures Induced Anomalous Change in Effective Charges of $Al_2O_3/SiO_2$ Interface Dipole Layer", Oral presentation at International Workshop on Dielectric Thin Films for Future Electron Devices (IWDTF), S5-2 (Nov. 21, 2017, Todaiji Temple Cultural Center, Nara).
- **Siri Nittayakasetwat** and Koji Kita, "Consideration on the Effective Dipole Length in $Al_2O_3/SiO_2$ and $Y_2O_3/SiO_2$ Interface Dipole Layers via Temperature Dependences of their Dipole Strength", poster presentation at International Conference on Solid-State Device and Materials (SSDM), (Sep 9-13, 2018, University. of Tokyo).
- Takashi Hamaguchi**, Siri Nittayakasetwat** and Koji Kita, "Study on Interface Dipole Layer Strength change by Temperature in high-I/$SiO_2$ and high-*k*/high-*k* systems and its Possible Origin", International Conference on Solid-State Device and Materials (SSDM), (Sep 9-13, 2018, University. of Tokyo).
- **Siri Nittayakasetwat**, Takashi Hamaguchi, and Koji Kita, "Experimentally Observed Temperature-Induced Changes in Interface Dipole Layer Strengths in high-*k*/SiO and high-*k*/high-*k* Systems", 21st Conference on Insulating Films on Semiconductors (INFOS), (Jul 1-3, 2019, Clare College, Cambridge University)
- **Siri Nittayakasetwat** and Koji Kita, "Relationship between the Waking-up Effect and Structural Distortion in Ferroelectric $HfO_2$ characterized by X-ray Diffraction", at International Conference on Solid-State Device and Materials (SSDM), (Sep 27-30, 2020, All virtual-conference).
- **Siri Nittayakasetwat**, Haruki Momiyama, and Koji Kita, "Direct Evidence of Ferroelectric $HfO_2$ Phase Transformation Induced by Voltage Cycling and Its Possible Origin", 22nd Conference on Insulating Films on Semiconductors (INFOS), (June 28-July2, 2021, Rende, Italy).

# Proceedings for Domestic Conferences

- **Siri Nittayakasetwat**, Hironobu Kamata and Koji Kita, "Anomalous temperature dependence of dipole layer strength at the $Al_2O_3/SiO_2$ interface", 78th Japan Society of Applied Physic Autumn Meeting, 5p-C11-3 (Sep. 5, 2017, Fukuoka International Conference Center, Fukuoka).
- **Siri Nittayakasetwat**, and Kita Koji, “Consideration of Charge Injection Effect on the Degradation of Ferroelectric $HfO_2$ during Bipolar Voltage Cycling”, 67th Japan Society of Applied Physic Spring Meeting, p-A303-11 (Mar 14, 2020, Yotsuya Campus, Sophia Univ.). (*Cancelled due to COVID-19)
- **Siri Nittayakasetwat**, and Kita Koji, “Direct Evidence of Electric Field driven Phase Transformation in the Waking-up Process of Ferroelectric $HfO_2$ Characterized by Conventional X-ray Diffraction”, 68th Japan Society of Applied Physic Spring Meeting, p16 -Z26-07 (Mar 16, 2-21, All-Virtual Conference)
- Haruki Momiyama, **Siri Nittayakasetwat**, and Kita Koji, “Changing of Structural Sistortion and Stabilization of Ferroelectric Phase in Cap-annealed $HfO_2$ Thin Films Characterized by In-plane and Out-of-plane XRD”, 68th Japan Society of Applied Physic Spring Meeting, p16 -Z26007 (Mar 16, 2-21, All-Virtual Conference)

# Acknowledgment

It has been a period of excitement and hardworking. I realize that I would not be able to accomplish all these works the supports from friends, colleagues, and families. For this reason, I would like to acknowledge and give my sincere gratitude to those that support me through all these years.

First. I would like to sincerely thank my advisor – Associate Professor Koji Kita for his guidance and encouragement during the course. I would like to thank him for allowing me to be in this field since I started my graduate school in 2016. His guidance helped me navigate through challenges and obstacles during my time with him.

I would like to give a special thank you to Dr. Tomonori Nishimura for this technical support on various kinds of experiments I made in this study. It was a joy to have a chance to work with him personally and professionally.

I would like to thank my doctoral dissertation committee members: Prof. Satoshi Watanabe, Prof. Takashi Kondo, Prof. Kosuke Nagashio, Assoc. Prof. Masaharu Kobayashi, for their precious time and meaningful comments for my Ph.D. study.

I would like to acknowledge and thank you Takashi Hamaguchi and Haruki Momiyama for their contribution to this study. The experimental data regarding the spontaneous polarization at $MgO/SiO_2$ and $MgO/Al_2O_3$ interfaces were done by Takashi Hamaguchi. Several preliminary experiments in ferroelectric $HfO_2$ were conducted by Haruki Momiyama.

Finally, I would like to give my sincere thanks to my family: Mr. Jarrus Nittayakasetwat, Ms. Siriporn Nittayakasetwat, Mr. Jerrus Nittayakasetwat, and Ms. Prattana Tanyapanyachon for always having my back and being there for me when I needed the most.